MAGNETIC RESONANCE IMAGING (MRI) TECHNIQUES FOR CONTRAST-ENHANCED CELLULAR AND MOLECULAR IMAGING

PHD THESIS

GRADUATE SCHOOL OF INTEGRATIVE SCIENCES AT THE NATIONAL UNIVERSITY OF SINGAPORE

LEE TECK HOCK

HT061812Y

ACKNOWLEDGEMENTS

The past four years have been the most enlightening part of my life. Having previously worked as a semiconductor engineer for 4 years, the plunge into biomedical research certainly took a great leap of faith. From zero knowledge of magnetic resonance imaging to the ability in exploiting it in the field of cellular and molecular imaging, I sincerely express my gratitude to the following people, without whom this thesis would not be possible. First is my supervisor Sir George Radda, who strongly supported my research and gave me the opportunity to spend a year at his lab in the University of Oxford. That was a very fulfilling experience, both in science and personal development. Many thanks to Professor Xavier Golay for introducing me to MRI and the wonderful opportunities that it presents. His endless stream of novel ideas certainly rubs off onto me. Dr. Damian Tyler led me to the exciting world of hyperpolarized Carbon-13 and opened up opportunities for further postdoctoral research. I also wish to thank Dr. Marie Schroeder, who was a patient mentor and Professor Kieran Clarke for her generosity and encouragement. I am indebted to Dr Zheng Bingwen for imparting his pulse programming skills. Last but not least, I am grateful to my fellow colleagues at the Cardiac Metabolism Research Group (CMRG) in the University of Oxford, Singapore Bioimaging Imagining Consortium (SBIC) at A-STAR and Center for Advanced Biomedical Imaging (CABI) at University College London, who helped me intangibly in these 4 years.

TABLE OF CONTENTS

CHAPTER THREE

SUMMARY

In this thesis, I aimed to demonstrate the capability and versatility of Magnetic Resonance Imaging (MRI) to perform diagnostic imaging at different physical scales, from physiological to cellular and finally at the molecular level. Chapter 2 illustrates the ability of 'Dynamic Contrast Enhanced Magnetic Resonance Imaging' or 'DCE-MRI' to measure an important physiological parameter that is a biomarker of nutrient delivery, which is hemodynamic perfusion. The use of a *T1*-reducing contrast agent in facilitating DCE-MRI in the mouse pancreas is described. A mathematical approach to quantify tracer pharmacokinetics in order to estimate blood flow is also illustrated. The competency of DCE-MRI to distinguish between normal and angiogenesis-impaired pancreas in a STAT3 knock-out mouse model is also be presented.

Chapter 3 ventured higher up the magnification scale into the cellular regime, whereby cellular tracking of exogenous cells transplanted for tissue repair was visualized with positive contrast. Superparamagnetic iron-oxide particles (SPIO) were the selected passive probes that acted as beacons of delivered cells. The superior detection sensitivity offered by a Multiple-Echo Ultrashort Echo Time (MUTE) MRI technique was demonstrated. In addition, I proposed a novel method that provides robust positive contrast with high temporal efficiency to advance cellular tracking technology. The physical principles of positive contrast sensing and factors affecting detection sensitivity are discussed.

Finally, molecular imaging is demonstrated in Chapter 4 via the use of an avant-garde technique that permits real-time dynamic monitoring of carbohydrate metabolism, this is

'Dynamic Nuclear Polarized ^{13}C Magnetic Resonance Spectroscopy (DNP-MRS)'. Here, the biomarkers of interest were also the molecular probes themselves. They are the downstream biomolecules of pyruvate metabolism, including [1-^{13}C] lactate, $^{13}CO_2$, $H^{13}CO_3^-$ and [1-^{13}C] acetyl-carnitine. In addition, the generation and utilization of these substrates were dependent on underlying enzyme activity such as pyruvate dehydrogenase (PDH), carbonic anhydrase (CA) and carnitine acetyltransferase (CAT). By measuring the MR signal amplitude of these reporting probes, I was able to quantify critical biological parameters such as intracellular pH, and track its changes at the onset of ischaemia. I also demonstrated the utilization of this technique to study the dynamic energy storage mechanism of the heart. The potential of [1,4-^{13}C] fumarate as a biomarker of necrosis in the heart was also investigated. Finally, 2-dimensional mapping of metabolic activity was performed with chemical shift imaging (CSI).

LIST OF TABLES

LIST OF FIGURES

LIST OF SYMBOLS

B_0	static magnetic field strength
B_1	RF magnetic field strength
$B_{z,inh}$	local magnetic field inhomogenenity
C_e	tracer concentration in EES
C_p	tracer concentration in plasma
C_t	tracer concentration in tissue
$C(k_x,k_y)$	gridding convolution function
δf	chemical shift
γ	gyromagnetic ratio
G_{ssr}	slice refocusing gradient amplitude
ρ	tissue density
E	tracer extraction fraction in tissue
F	blood flow per unit mass of tissue
K^{trans}	volume transfer constant between v_p and v_e
k_{max}	maximum range in k-space
M_0	longitudinal magnetization at thermal equilibrium
$M(k_x,k_y)$	ideal continuous k-space data
$M_{NC}(k_x,k_y)$	non-Cartesian sampled k-space data
$M_C(k_x,k_y)$	Cartesian sampled k-space data
P	polarization
pR	calculated pH based on Henderson-Hasselbach equation
P_{sa}	point-spread function without transverse signal decay
P_{blur}	point-spread function with transverse signal decay
r_1	longitudinal relaxivity
r_2	transverse relaxivity
ρ	tissue density
S	surface area per unit mass of tissue

$S_{NC}(k_x,k_y)$	non-Cartesian sampling function
$S_C(k_x,k_y)$	2D Cartesian sampling function
S_{spio}	signal intensity of SPIO-labeled cells
S_{ctrl}	signal intensity of unlabeled control cells
σ_{noise}	standard deviation of noise
t_{ssr}	slice refocusing gradient duration
θ_{T1W}	flip angle in T1-weighted DCE-MRI
θ_{PDW}	flip angle in proton density-weighted DCE-MRI
v_e	fractional volume of extravascular extracellular space in tissue
v_p	fractional volume of blood plasma space in tissue
$W(k_x,k_y)$	weighting function

LIST OF ABBREVIATIONS

AIF	arterial input function
ADP	adenosine 5’-diphosphate
ATP	adenosine 5’-triphosphate
BMSC	bone marrow stem cells
CE	contrast enhancement
$CE_{subtract}$	contrast enhancement in subtracted image
CNR	contrast-to-noise ratio
CSI	chemical shift imaging
DCE	dynamic contrast enhancement
DNP	dynamic nuclear polarization
DSC	dynamic susceptibility contrast
EES	extravascular extracellular space
EPI	echo-planar imaging
ETZ	6-ethoxyzolamide
FITC	fluorescein isothiocyanate
FOV	field-of-view
GRE	gradient recalled echo
IAUGC	initial area under the gadolinium curve
IODEX	dextran-coated iron-oxide nanoparticles
IRON	inversion recovery with on-resonant water suppression
MPIO	micron-sized iron-oxide particles
MRI	magnetic resonance imaging
MRS	magnetic resonance spectroscopy
MUTE	multiple-echo ultrashort echo-time
NMR	nuclear magnetic resonance
ORI	off-resonance imaging
PHIP	parahydrogen induced polarization

PCr	phosphocreatine
pH_i	intracellular pH
P_i	inorganic phosphate
PSF	point-spread function
RF	radio-frequency
ROI	region of interest
SLR	shinnar le-roux
SNR	signal-to-noise ratio
SPIO	superparamagnetic iron-oxide nanoparticles
STAT	signal transducers and activators of transcription
STZ	streptozotocin
T_1	longitudinal relaxation time
T_2	transverse relaxation time
TAT	transactivator of transcription peptide
TCA	tricarboxylic acid cycle
TE	echo-time
TR	repetition time
TH	tissue homogeneity model
TK	Tofts-Kermonde model
USPIO	ultra-small superparamagnetic iron-oxide nanoparticles
UTE	ultrashort echo-time
VEGF	vascular endothelial growth factor
VERSE	variable rate selective excitation
WM	white-marker imaging
ZUTE	Z-shimmed ultrashort echo-time

CHAPTER ONE

INTRODUCTION TO CELLULAR AND MOLECULAR IMAGING

1.1 Emergence of Cellular and Molecular Imaging

The development of life is a proficiently orchestrated process of a myriad of distinctive molecules. From DNA to cells to tissues and organs, biomolecules are the building blocks of all life. The ability to probe molecular and cellular processes during mammalian development facilitates the understanding of how aberrant events can lead to disease pathogenesis (1-3). The acme of interventional medicine is the application of ameliorative actions as soon as a molecular aberration occurs or even before the event (4). It is optimistic that by taking such preemptive measures, disease progression could be arrested and physiological injury could be limited, sparing patients of unnecessary duress (5-7). Possible preventive or interventional treatments include gene therapy whereby beneficial genes are transfected for transcription of therapeutic proteins (e.g. SERCA2a gene therapy in heart failure to improve contractility) (8), pharmacological inhibition of specific proteins to block deleterious signaling pathways (e.g. inhibiting matrix metallo-proteinases MMPs to reduce left myocardium wall thinning in heart failure) (9), or tissue repair with exogenous cell therapy (e.g. stem-cell transplantation in infarcted myocardium) (10). With the advances in high throughput screening technology, combinatorial drug chemistry, recombinant protein developments and availability of transgenic models, many more therapeutic targets are being discovered at a rapid pace. Molecular medicine is thus propelling a paradigm shift not only in the way drugs are being developed and customized (11-14), but also the translational relationship between basic biological research and clinical applications (15,16).

The pursuit of molecular medicine encompasses multiple levels of research which begins from basic research at the bench to validation in animal models and finally translation into the clinic. The translational researcher who carries out this arduous task is one who needs to characterize the molecular mechanism underlying the pathology in the laboratory, devise a method to measure that in-situ in the human disease state and develop a beneficial intervention in the clinic (17). He or she would demand a series of imaging modalities to visualize specific molecular and cellular interactions as well as detect physiological response at various experimental stages (3). These imaging paradigms can be broadly categorized into molecular, cellular and physiological imaging (3,18). Cellular imaging has in fact been present since the invention of the optical microscope in the 17th century, when Robert Hooke first described cells in a cork (19). Modern microscopes with much higher magnification and advanced optics now enable detailed visualization of constituents in a cell as well as cellular activity at the microscopic level. Molecular imaging on the other hand, is a contemporary concept involving the detection of molecular events and mechanisms below the microscopic level, encompassing processes such as metabolic activity, reporter gene expression and enzymatic action (20). It is to be noted that visualization of a single biological process can fall into both cellular and molecular imaging regimes. For example apoptosis or programmed cell death can be characterized by morphological changes including plasma membrane blebbing, cell shrinkage, chromatin condensation and formation of apoptotic bodies (21). The visualization of such structural demise is categorized under cellular imaging. But these permutations are initially triggered by a series of biochemical events including activation of initiator caspases and mitochondrial release of 'apoptogens', which can be detected using different fluorescent platforms (22). The apoptotic stage can be assessed by measuring Annexin-V binding to phosphatidylserine (23,24), a protein that gets enhanced exposure on

the external cell membrane during early apoptosis. Visualization of such intracellular and extracellular proteins unique to apoptosis is an application of molecular imaging.

Progress in cellular and molecular imaging is driven primarily by the following demands in molecular medicine research (3): [1] to develop non-invasive in-vivo imaging methods that reflect specific cellular and molecular processes, for example gene expression or more complex molecular interactions such as protein–protein interactions; [2] to monitor multiple molecular events about-simultaneously; [3] to follow cell trafficking; [4] to optimize drug and gene therapy; [5] to assess pathological progression at a molecular level; and [6] to achieve all of the above goals in a rapid, reproducible, and quantitative manner. The emergence of modern molecular and cellular imaging strategies can be attributed to recent unprecedented advances in molecular biology techniques such as polymerase chain reaction (PCR) technology (25), development of transgenic (26-28) and experimental animal models (29,30) as well as successful implementation of small-animal instrumentation (31,32). In addition, the nascent biomedical nanotechnology sector heralds a new paradigm in targeted molecular imaging and therapy by increasing the availability of novel imaging probes and drugs that are highly specific (33-36). For example engineered antibodies attached with radio-nuclides now empower the oncologist to locate specific tumor markers in-vivo and quantify concentration and uptake levels, boosting diagnostic precision (37,38). The operating mode can then be switched from radiology to therapy by increasing the radioactive dose to annihilate the tumor (39,40).

1.2 Cellular and Molecular Imaging Modalities

The foray into molecular medicine is a seemingly daunting task judging from the sheer amount of biological information that has to be extracted and interpreted. As new molecular pathways in pathology are being discovered, more specific and accurate methods of imaging would be demanded, in order to identify potential targets for therapeutic intervention (1). Developments in molecular and cellular imaging can be basically grouped into three categories (41): [1] the physics and engineering of imaging techniques and instruments, [2] the chemical and materials science needs for designing imaging probes and contrast agents, and [3] the biological questions to be answered. It is thus appropriate here to identify the roles of biomarkers, imaging probes and their sensing modalities.

1.2.1 Biomarkers

A biomarker is a biological characteristic that is objectively measured and evaluated as an indicator of normal or pathogenic processes, as well as pharmacological responses to a therapeutic intervention. Typical biomarkers are molecular in nature such as intracellular proteins (e.g. STAT proteins) (42), surface receptors (e.g. Her2 tyrosine kinase receptor in breast cancers) (43), metabolites (e.g. lactate) (44), mRNA expression profiles (e.g. in Huntington's disease) (45) or antibodies (e.g. human immune deficiency). Depending on application, a biomarker might also be cellular morphology change or even behavioral symptom. For example, Parkinson's disease (PD) is characterized by a loss of dopamine producing neurons in the substantia nigra pars compacta (46,47). Molecular biomarkers of this particular neurodegenerative disease include elevated striatal dopamine D1 and D2

receptors (48), increased levels of cytokines such as interleukin-1 (49) and increased iron deposits (50). Cellular biomarkers include decreased number of dopaminergic neurons and presence of Lewy bodies (51). Cognitive and motor impairments such as dementia (52,53), tremor, rigidity and akinesia are some of its physiological biomarkers. Thus a combination of biomarkers at different scales is necessary to confirm diagnosis, monitor disease progression and assess therapeutic efficacy (54). Because a disease might have a plethora of biomarkers which weigh differently in the diagnostic process, the National Institute of Health conjured a classification system to optimize the use of biomarkers in the development and evaluation of novel therapies (55). Since biomarkers are usually the intermittent or end products of a pathological signaling pathway, they are often pharmaceutical targets as well (e.g. protein kinases in cancer therapy) (56). Biomarkers in general play important roles in management and treatment of pathology.

1.2.2 Molecular Imaging Probes

Molecular imaging probes, on the other hand, are molecular compounds that can be sensed by an imaging modality. They include small molecules such as receptor ligands or enzyme substrates, large molecular-weight affinity ligands such as monoclonal antibodies or recombinant proteins. Molecular probes provide the imaging signal or contrast in the imaging assays. They are usually introduced into the biological sample (serum, blood, cells, biopsies etc) or delivered into the subject to visualize specific biological or molecular events. A notable exception is MR Spectroscopy (MRS), where the signal derives from endogenous molecules like ^{1}H, ^{13}C or ^{31}P nuclei.

There are many categories of molecular probes including but not limited to:

[1] ***Activatable or passive*.** Activatable probes are smart sensors that emit a signal (as in PET, fluorescence or bioluminescence) or induce proton relaxation changes (as in MRI) when they interact with their targets, else they remain inactive. An example of an activatable MR probe is the 5-hydroxytryptamide (MPO-Gd) molecule. The biomarker myeloperoxidase is produced during inflammatory phase in the infarcted heart, and this molecule activates the molecular probe which then binds to matrix proteins and becomes trapped in the vicinity, leading to localized enhancement on T_1-weighted MRI (57). Other examples include magnetic nanosensors that can interact with DNA or RNA sequences (58) and activatable paramagnetic chelators (59).

[2] ***Direct/in-direct imaging***. A direct reporting probe is one that emits a signal when the target is reached, or when the biological event of interest occurs (e.g. location of signal voids in MRI are direct indicators of iron-oxide labeled cells). An example of in-direct imaging is 'reporter gene expression', whereby a reporter gene such as GFP is inserted in the same loci as the gene of interest and its expression implies that the targeted gene is expressed as well.

[3] ***Specific/Non-specific Imaging***. In order to be useful as a beacon for a specific molecular process, a probe has to be linked to the biomarker for that particular event. Therefore it usually has a modular design composing of a high affinity ligand that binds to the biomarker and a signaling component for imaging. Specific probes have a distinct set of targets while non-specific ones do not. Specificity is increasingly important as molecular biologists dig deeper into the root causes of pathological diseases, and discover potential pharmaceutical targets along the signalling pathway. Molecular imaging probes with high specificity and targeting potential can be made by attachment of the signalling probe to antibodies, ligands, or substrates that interact only with their respective targets, e.g. magnetic nanocrystals

conjugated to antibody Herceptin specific for Her2/neu surface receptors in breast cancer cells (60). Non-specific probes do not lock-in to certain biological targets but constantly emit detection signals instead, e.g. cell labelling with superparamagnetic iron-oxide nanoparticles for in-vivo tracking (61,62).

Molecular probes consist of a myriad of compounds including radio-labeled ligands in positron emission tomography (PET) (34,63) and single photon emission computed tomography (SPECT) (64), paramagnetic (Gd^{3+}, Mn^{2+}) (65,66) or superparamagnetic (iron-oxides) (61,67) contrast agents for magnetic resonance imaging detection, and fluorescent dyes for optical detection (68,69). Recent advances in probe development explored the potential in multi-modality detection of a molecular event as well as report the location of the event. For example, Josephson et al synthesized a biocompatible, dextran-coated superparamagnetic nanoparticle conjugated to a Tat-peptide with a fluorescent tag (CLIO-TAT-FITC) and demonstrated its affinity to cell membrane receptors which resulted in a high labeling efficiency and enhanced detection sensitivity (70). Its bifunctionality allows it to be detected with MRI and fluorescent microscopy, facilitating in-vivo detection with histological confirmation. Regardless of the type of probe used to visualize the occurrence of the molecular event or cell of interest, it should ideally possess these properties for optimal detection and precision in reporting of biological processes:

[1] High specificity towards the desired ligand or protein biomarker targets

[2] Appropriate amplification strategies exist for heightened sensitivity

[3] Quantifiable relationship between biomarker concentration and frequency or magnitude of event such as pathological severity or therapeutic efficacy

[4] Biocompatiblity and negligible toxicity

[5] Cost-effective and provide robust signals

[6] Imaging modality used for its detection must be sensitive, possesses low background noise and produces images of high spatial and temporal resolution.

As we learn more about the biological mechanisms of major killers such as cancer, heart failure and diabetes and their mutual interactions and effects on one another, the demands for molecular probes are expected to exceed these requirements. We envision the future of reporter probes that not only emit different signals for distinct molecular events in-vivo, but adapt to the detected pathological process and implement immediate corrective actions, e.g. drug release upon identification of a target. Multi-functional molecular probes that integrate imaging, detection, and therapy are a harbinger of this foreseeable future (71).

1.2.3 Molecular Imaging Modalities

The pace of translation from in-vitro to in-vivo experimental models has quickened in recent years resulting in demand for high performance molecular imaging. The technology employed to probe the myriad of biochemical processes from molecular to cellular and physiological scales should ideally incorporate the following characteristics: [1] high sensitivity, [2] excellent spatial/temporal resolution, [3] high signal-to-noise/contrast, [4] wide field-of-view and large penetration depth, [5] minimal radioactivity, [6] minimal invasiveness, [7] speed and [8] cost effectiveness. A wide range of technologies is currently available for in-vitro, ex-vivo and in-vivo molecular imaging. Apart from their reporting

mechanism (i.e. the detection of resonant magnetic frequencies, radio-nuclides, emitted light or ultrasound), these techniques vary in many other aspects, from their invasiveness to cost-effectiveness. The choice of technique depends not only on the molecules or cells one wishes to detect in living subjects, but also be influenced by the number of repeat assessments required and the resulting risks involved (72). Key instruments used in clinical and animal research are positron emission tomography (PET), single-photon emission computed tomography (SPECT), bioluminescence imaging (BLI), optical fluorescence imaging, magnetic resonance imaging (MRI), computed tomography (CT) and ultrasound (US). The preferred imaging modality depends on the translation stage. Optical imaging provides very high spatial and temporal resolution for genomic and proteomic studies, PET and SPECT enables functional imaging while MRI and US contribute the horsepower for in-vivo physiological imaging. Massoud and Gambhir have elegantly summarized the characteristics of these imaging modalities, including spatial resolution, sensitivity, molecular probe, temporal resolution, cost and quantitative degree (3).

Since this thesis primarily utilized MRI as the imaging modality in physiological perfusion measurement, exogenous cell tracking and monitoring real-time metabolic processes, I shall focus on its physical principles to aid understanding of materials in subsequent chapters.

1.3 Physical Principles of Magnetic Resonance Imaging (MRI)

1.3.1 Origin of MRI Signal

Magnetic resonance imaging is based on the interaction of nuclear spins with an external field $\overrightarrow{B_0}$. The dominant nucleus in MRI is the proton in hydrogen and its interaction with the external field results in precession of the proton spin about the field direction (see Fig. 1.1a) with a fixed frequency (known as Larmor Frequency) given by

$$\omega_0 = \gamma B_0 \quad (rad/s) \tag{1.1}$$

$$f_0 = \frac{\gamma}{2\pi} B_0 \quad (Hz) \tag{1.2}$$

where γ is a constant called the gyromagnetic ratio and $\vec{\mu}$ is the magnetic dipole moment vector.

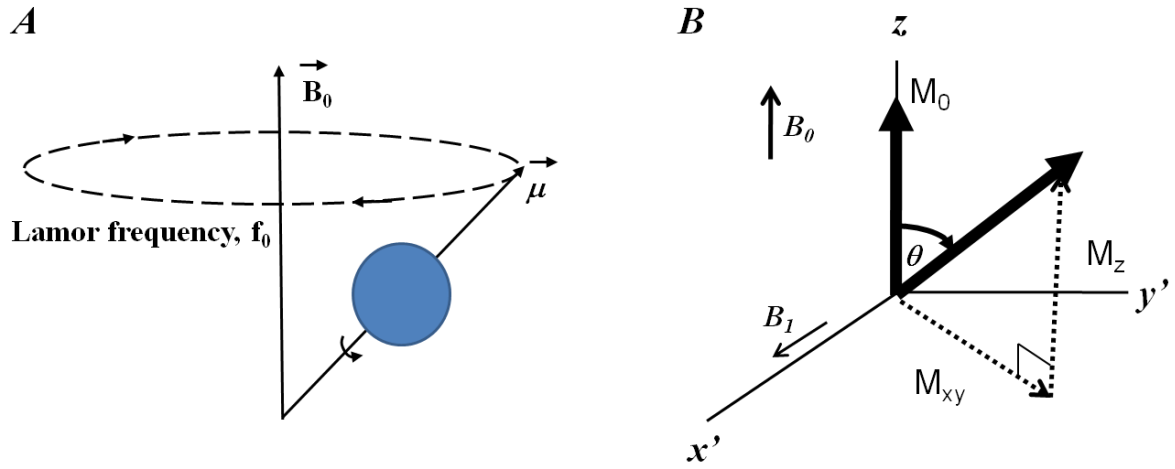

Figure 1.1: A) A spinning nucleus precessing about B_0 at Larmor frequency. B) Thermal equilibrium longitudinal magnetization rotates by excitation angle θ, resulting in the MR signal M_{xy}.

The bulk magnetization is prevented from relaxing fully to an alignment along the external magnetic field $\overrightarrow{B_0}$ because of thermal energy associated with the absolute temperature *T*. At human body temperatures the average thermal energy κT, where κ is the Boltzmann constant (1.38 x 10^{-23} J/K), is millions of times higher than the quantum energy difference between parallel alignment (lower energy, spin-up ↑) and anti-parallel alignment (higher-energy, spin-down ↓). The quantum energy difference ΔE between the two energy states in a spin ½-system is proportional to the Larmor frequency, where *h* is the Planck quantum constant.

$$\Delta E = \hbar\omega_0 \tag{1.3}$$

The Boltzmann's probability for the two spin- ½ states (magnetic number m = ± ½) is

$$P_{\pm} = \frac{e^{\pm u/2}}{e^{u/2} + e^{-u/2}}, u = \frac{\hbar\omega_0}{\kappa T} \tag{1.4}$$

In other words, $P_{\pm}$ is the probability of a nuclear spin with energy $\epsilon = \mp \frac{\hbar\omega_0}{2}$ and parallel / anti-parallel alignment, respectively. The number of spins parallel to the magnetic field $N(\uparrow)$ exceeding the number anti-parallel to that field $N(\downarrow)$, or the 'spin excess', is defined as

$$\begin{aligned} \Delta N &\equiv N(\uparrow) - N(\downarrow) \\ &= N(P_+ - P_-) \\ &\approx \frac{Nu}{2}, \qquad since\ \hbar\omega_0 \ll \kappa T \end{aligned} \tag{1.5}$$

Thus the proton spin excess at a magnetic field strength of 1.5 T is only 5 out of a million spins while it is 32 ppm at 9.4T. Taking into consideration electronic noise and hardware limitations, the number of detectable spins would be even lower. This minuscule spin inequality (also known as *polarization*) is the reason for the low detection sensitivity of MRI

(typically in order of mM) and the technological push for higher magnetic field strength (73,74). Even though the paucity of spin excess might appear disheartening, the detectable NMR signal is actually quite decent because there are Avogadro numbers of protons in a few grams of tissue. We shall explore the intrinsic properties in MRI that affects detection sensitivity. Consider the average magnetic dipole density, or 'longitudinal equilibrium magnetization' $M_0\hat{z}$ (that is the longitudinal component of the sample magnetization $\overrightarrow{M}$) with a magnitude given by

$$M_0 = \frac{\rho_0 \gamma^2 \hbar^2}{4\kappa T} B_0 \tag{1.6}$$

where ρ_0 is the number of protons per unit volume or 'spin density'. Although M_0 is limited by the small spin excess, there exists measurable NMR signal (75,76) because of the large spin density. We also observe that M_0 is proportional to the square of the gyromagnetic ratio γ, and since hydrogen has the largest value among the spin- ½ nuclei (42.58 MHz/T), it is the most prevalent nucleus measured with MRS and MRI. In order to generate an MR signal, the magnetization vector $\overrightarrow{M}$ has to be tipped away from the external field direction $\overrightarrow{B_0}$ in order to set it into precession. This is accomplished by using a transmit coil to apply a short radiofrequency pulse (tens of μs to a few ms duration) at the Larmor frequency ω_0. This is the resonance condition in MR. As illustrated in Figure 1.1B, when a RF pulse is applied along *x'* with magnitude field B_1, the equilibrium magnetization is rotated at a rate corresponding to the frequency

$$\omega_1 = \gamma B_1 \tag{1.7}$$

The angle upon which $M_0\hat{z}$ is rotated depends on both B_1 amplitude and RF duration τ_{rf}:

$$\theta = \gamma \int_0^{\tau_{rf}} B_1 dt \tag{1.8}$$

The transverse magnetization M_{xy} induces a voltage on the receiver coil which is sampled and stored. That is the magnetic resonance or free-induction decay signal that we shall refer to for remainder of the thesis.

1.3.2 Proton Relaxation and Signal Attenuation

In MRI, we are primarily concerned with proton imaging, with the exception of Chemical Shift Imaging in Chapter 4. An image is made up of a matrix of voxels. Each voxel is a volume of proton spins with the same phase ('spin isochromat'). The magnetization of each voxel is thus a summation of magnetic moment of all individual spins as defined in eqn. (1.9) below, assuming a uniform B_0 field across the voxel. When a magnetic moment is immersed in a magnetic field, it will tend to line up parallel to the field in order to reach its minimum energy state. Since each spin is in thermal contact with the lattice of nearby protons, it can exchange energy with the lattice. After spins are excited by a RF pulse, this interaction enables them to relax energetically and gradually re-align to the main magnetic field. The rate of change in longitudinal magnetization M_z, as defined in eqn. (1.10) as a consequent of this relaxation mechanism is characterized by the 'spin-lattice relaxation time' T_1. This characteristic time is a very important parameter in understanding the re-growth of longitudinal magnetization after an excitation, and is crucial in pulse sequence design.

$$\vec{M} = \frac{1}{V} \sum_{protons\ in\ V} \vec{\mu_i} \tag{1.9}$$

$$\frac{dM_z}{dt} = \frac{1}{T_1}(M_0 - M_z) \tag{1.10}$$

The transverse magnetization M_{xy} is affected not only by the amount of longitudinal magnetization present before excitation M_z (t = 0), but also the physical interaction between spins (77). Spins experience the main magnetic field as well as the local fields of their neighbors. When local field variations are present, the effective magnetic field experienced by a spin will be $B_0 \pm \Delta B_{local}(r)$, leading to different local precessional frequencies. As displayed in Figure 1.2, the excited spins will then tend to fan out in time (this process is also known as dephasing). Thus the vector sum of the individual magnetic moments within a voxel would be reduced, decreasing the net transverse magnetization and ultimately the MR signal. The 'spin-spin' relaxation time used to describe this signal decay mechanism is T_2.

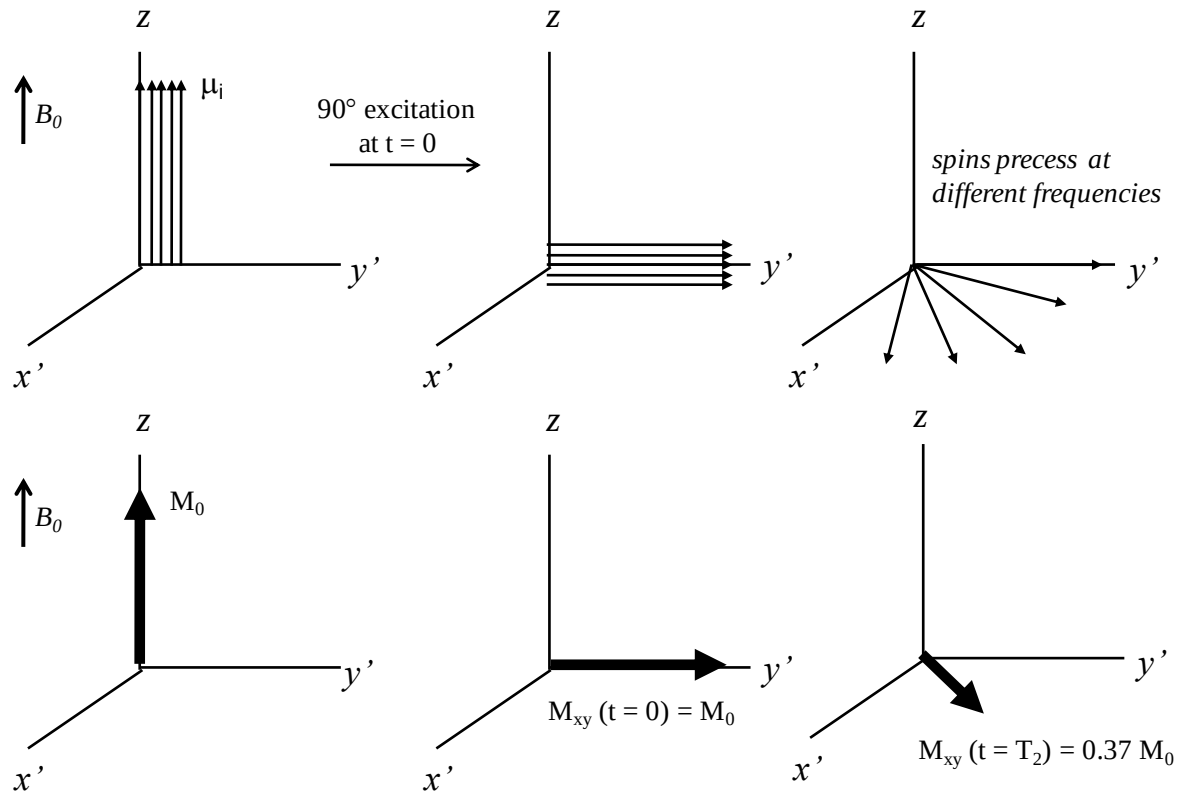

Figure 1.2: The effect of dephasing is illustrated here in the laboratory frame. When a set of spin isochromats is tipped into the *x-y* plane by a 90° RF excitation pulse, each individual spin will precess at a slightly different frequency due to the local field variation induced by spin-spin interactions. The transverse magnetization M_{xy} in the voxel thus attenuates with time.

There is another important component that further attenuates sensitivity in MRI, and that is the spatially dependent external field inhomogeneity $\Delta B_z(\vec{r})$. When a sample or patient is loaded into the magnet, its dielectric inhomogeneity distorts the main magnetic field, causing localized variation in Larmor frequency $\omega_0(\vec{r})$. This results in additional dephasing of the transverse magnetization which further suppresses the MR signal. Incorporating this decay time T_2' yields the effective transverse relaxation time constant T_2^* given by

$$\frac{1}{T_2^*} = \frac{1}{T_2} + \frac{1}{T_2'} \tag{1.11}$$

The overall rate of change in transverse magnetization can thus be included in the equation of precessional motion for interacting spins to become

$$\frac{d\overrightarrow{M_\perp}}{dt} = \gamma \vec{M}_\perp \times \overrightarrow{B_0} - \frac{1}{T_2^*}\vec{M}_\perp \tag{1.12}$$

If we combine the longitudinal and transverse relaxation effects into a single vector equation, we yield the total rate of change in the magnetization vector in eqn. (1.13).

$$\frac{d\vec{M}}{dt} = \gamma \vec{M}_\perp \times \overrightarrow{B_0} + \frac{1}{T_1}(M_0 - M_z)\hat{z} - \frac{1}{T_2^*}\vec{M}_\perp \tag{1.13}$$

In order to ameliorate the detrimental effect of magnetic field inhomogeneities, a mandatory procedure in MRI is gradient shimming. This exercise is extremely important in maintaining a homogenous magnetic field in the desired volume-of-interest and its incompetency adversely impacts the spectral resolution in spectroscopy (78-80) and image quality in imaging (81-83). Sophisticated shimming gradient coils are integrated into the spatial encoding coils with implementation of extensive algorithms to correct field inhomogeneities (84-92). Together with intricate gradient shimming methods (93-97), spin-echo acquisition sequences are also frequently utilized to reverse the signal loss caused by field inhomogeneities (98,99). Note that if $T_2' << T_2$, then T_2^* is substituted by T_2. This occurs when the magnetic field is homogenous after shimming or spin-echoes are acquired.

The effects of relaxation on the magnetization of the system can perhaps be effectively conveyed with the Bloch equation (100), whereby influences of spatial and time varying gradients, $\overrightarrow{G(r,t)} = \begin{pmatrix} G_x(t) \\ G_y(t) \\ G_z(t) \end{pmatrix}$ that encode each position in the sample $\vec{r} = \begin{pmatrix} x \\ y \\ z \end{pmatrix}$, together with the physical effect of the applied $\overrightarrow{B_1}$ field on the magnetization are summarized. This matrix relation is the fundamental physical basis of MRI and its solution could be numerically obtained to optimize either pulse sequences (101-103) or RF pulse designs (104,105). An extremely useful application of the Bloch equation is to measure chemical reaction rates in biochemical processes via saturation transfer techniques (106-108).

$$\frac{d}{dt}\begin{pmatrix} M_{x'} \\ M_{y'} \\ M_z \end{pmatrix} = \begin{pmatrix} -\frac{1}{T_2} & \gamma\vec{G}\cdot\vec{r} & -\gamma B_{1,y} \\ -\gamma\vec{G}\cdot\vec{r} & -\frac{1}{T_2} & \gamma B_{1,x} \\ \gamma B_{1,y} & -\gamma B_{1,x} & -\frac{1}{T_1} \end{pmatrix}\begin{pmatrix} M_{x'} \\ M_{y'} \\ M_z \end{pmatrix} + M_0\begin{pmatrix} 0 \\ 0 \\ \frac{1}{T_1} \end{pmatrix} \quad (1.14)$$

In summary, the transverse magnetization decays at a time-constant of T_2 while the longitudinal component recovers at a T_1-dependent rate upon excitation. Since biological tissues vary in their molecular composition, cellular phenotypes and vasculature, their T_1 and T_2 relaxation time constants are different. Therefore their M_z recovery and M_{xy} signal decay will be dissimilar. This aspect has traditionally been the source of contrast in MR imaging and is the reason for its superiority in in-vivo visualization of soft tissue (109-111). In molecular and cellular imaging, the use of MR contrast agents exploits this feature by increasing either longitudinal or transverse relaxation of targeted molecules or cells to differentiate them from the background. This methodology extends the sensitivity limit of MRI and enables applications beyond routine anatomical imaging. With respect to MR contrast agents, Chapter 2 investigates the use of gadolinium compounds to increase blood vessel signals and facilitate blood flow measurements. Augmenting detection sensitivity of exogenous cells via labeling with T_2^* contrast agents is demonstrated in Chapter 3. Chapter 4 adopts a unique ^{13}C label that is neither a T_1 nor T_2 reducing agent in metabolic studies.

1.4 Chapter References

1. Weissleder R. Molecular imaging: exploring the next frontier. Radiology 1999;212(3):609-614.
2. Blasberg RG. Molecular imaging and cancer. Mol Cancer Ther 2003;2(3):335-343.
3. Massoud TF, Gambhir SS. Molecular imaging in living subjects: seeing fundamental biological processes in a new light. Genes Dev 2003;17(5):545-580.
4. Semsarian C, Seidman CE. Molecular medicine in the 21st century. Intern Med J 2001;31(1):53-59.
5. Massoud TF, Gambhir SS. Integrating noninvasive molecular imaging into molecular medicine: an evolving paradigm. Trends Mol Med 2007;13(5):183-191.
6. Ginsburg GS, McCarthy JJ. Personalized medicine: revolutionizing drug discovery and patient care. Trends Biotechnol 2001;19(12):491-496.
7. Liotta LA, Kohn EC, Petricoin EF. Clinical proteomics: personalized molecular medicine. JAMA 2001;286(18):2211-2214.
8. Vinge LE, Raake PW, Koch WJ. Gene therapy in heart failure. Circ Res 2008;102(12):1458-1470.
9. Mann DL. Mechanisms and models in heart failure: A combinatorial approach. Circulation 1999;100(9):999-1008.
10. Segers VF, Lee RT. Stem-cell therapy for cardiac disease. Nature 2008;451(7181):937-942.
11. Kelloff GJ, Krohn KA, Larson SM, Weissleder R, Mankoff DA, Hoffman JM, Link JM, Guyton KZ, Eckelman WC, Scher HI, O'Shaughnessy J, Cheson BD, Sigman CC, Tatum JL, Mills GQ, Sullivan DC, Woodcock J. The progress and promise of molecular imaging probes in oncologic drug development. Clin Cancer Res 2005;11(22):7967-7985.
12. Jain RK. The next frontier of molecular medicine: delivery of therapeutics. Nat Med 1998;4(6):655-657.
13. Rudin M, Weissleder R. Molecular imaging in drug discovery and development. Nat Rev Drug Discov 2003;2(2):123-131.
14. Gross S, Piwnica-Worms D. Molecular imaging strategies for drug discovery and development. Curr Opin Chem Biol 2006;10(4):334-342.
15. Baumann M, Bentzen SM, Doerr W, Joiner MC, Saunders M, Tannock IF, Thames HD. The translational research chain: is it delivering the goods? Int J Radiat Oncol Biol Phys 2001;49(2):345-351.
16. Workman P, Kaye SB. Translating basic cancer research into new cancer therapeutics. Trends Mol Med 2002;8(4 Suppl):S1-9.
17. Birmingham K. What is translational research? Nat Med 2002;8(7):647.
18. Modo M, Hoehn M, Bulte JW. Cellular MR imaging. Mol Imaging 2005;4(3):143-164.
19. Mazzarello P. A unifying concept: the history of cell theory. Nat Cell Biol 1999;1(1):E13-15.
20. Herschman HR. Molecular imaging: looking at problems, seeing solutions. Science 2003;302(5645):605-608.
21. Makin G, Dive C. Apoptosis and cancer chemotherapy. Trends Cell Biol 2001;11(11):S22-26.
22. Ward TH, Cummings J, Dean E, Greystoke A, Hou JM, Backen A, Ranson M, Dive C. Biomarkers of apoptosis. Br J Cancer 2008;99(6):841-846.
23. Sosnovik DE, Schellenberger EA, Nahrendorf M, Novikov MS, Matsui T, Dai G, Reynolds F, Grazette L, Rosenzweig A, Weissleder R, Josephson L. Magnetic resonance imaging of cardiomyocyte apoptosis with a novel magneto-optical nanoparticle. Magn Reson Med 2005;54(3):718-724.
24. Tait JF. Imaging of apoptosis. J Nucl Med 2008;49(10):1573-1576.
25. Heid CA, Stevens J, Livak KJ, Williams PM. Real time quantitative PCR. Genome Res 1996;6(10):986-994.

26. Gassmann M, Hennet T. From Genetically Altered Mice to Integrative Physiology. News Physiol Sci 1998;13:53-57.
27. Sharpless NE, Depinho RA. The mighty mouse: genetically engineered mouse models in cancer drug development. Nat Rev Drug Discov 2006;5(9):741-754.
28. Tornell J, Snaith M. Transgenic systems in drug discovery: from target identification to humanized mice. Drug Discov Today 2002;7(8):461-470.
29. Edinger M, Sweeney TJ, Tucker AA, Olomu AB, Negrin RS, Contag CH. Noninvasive assessment of tumor cell proliferation in animal models. Neoplasia 1999;1(4):303-310.
30. Beal MF. Experimental models of Parkinson's disease. Nat Rev Neurosci 2001;2(5):325-334.
31. Weissleder R. Scaling down imaging: molecular mapping of cancer in mice. Nat Rev Cancer 2002;2(1):11-18.
32. Herschman HR. Micro-PET imaging and small animal models of disease. Curr Opin Immunol 2003;15(4):378-384.
33. Service RF. New probes open windows on gene expression, and more. Science 1998;280(5366):1010-1011.
34. Gambhir SS. Molecular imaging of cancer with positron emission tomography. Nat Rev Cancer 2002;2(9):683-693.
35. Kaufmann BA, Lindner JR. Molecular imaging with targeted contrast ultrasound. Curr Opin Biotechnol 2007;18(1):11-16.
36. Lee JH, Huh YM, Jun YW, Seo JW, Jang JT, Song HT, Kim S, Cho EJ, Yoon HG, Suh JS, Cheon J. Artificially engineered magnetic nanoparticles for ultra-sensitive molecular imaging. Nat Med 2007;13(1):95-99.
37. Hudson PJ, Souriau C. Engineered antibodies. Nat Med 2003;9(1):129-134.
38. Holliger P, Hudson PJ. Engineered antibody fragments and the rise of single domains. Nat Biotechnol 2005;23(9):1126-1136.
39. Kenanova V, Wu AM. Tailoring antibodies for radionuclide delivery. Expert Opin Drug Deliv 2006;3(1):53-70.
40. Wu AM, Senter PD. Arming antibodies: prospects and challenges for immunoconjugates. Nat Biotechnol 2005;23(9):1137-1146.
41. Cassidy PJ, Radda GK. Molecular imaging perspectives. J R Soc Interface 2005;2(3):133-144.
42. Yu H, Jove R. The STATs of cancer--new molecular targets come of age. Nat Rev Cancer 2004;4(2):97-105.
43. Spigel DR, Burstein HJ. HER2 overexpressing metastatic breast cancer. Curr Treat Options Oncol 2002;3(2):163-174.
44. Albers MJ, Bok R, Chen AP, Cunningham CH, Zierhut ML, Zhang VY, Kohler SJ, Tropp J, Hurd RE, Yen YF, Nelson SJ, Vigneron DB, Kurhanewicz J. Hyperpolarized 13C lactate, pyruvate, and alanine: noninvasive biomarkers for prostate cancer detection and grading. Cancer Res 2008;68(20):8607-8615.
45. Borovecki F, Lovrecic L, Zhou J, Jeong H, Then F, Rosas HD, Hersch SM, Hogarth P, Bouzou B, Jensen RV, Krainc D. Genome-wide expression profiling of human blood reveals biomarkers for Huntington's disease. Proc Natl Acad Sci U S A 2005;102(31):11023-11028.
46. Lang AE, Lozano AM. Parkinson's disease. Second of two parts. N Engl J Med 1998;339(16):1130-1143.
47. Lang AE, Lozano AM. Parkinson's disease. First of two parts. N Engl J Med 1998;339(15):1044-1053.
48. Seeman P, Niznik HB. Dopamine receptors and transporters in Parkinson's disease and schizophrenia. FASEB J 1990;4(10):2737-2744.
49. Rothwell NJ, Luheshi GN. Interleukin 1 in the brain: biology, pathology and therapeutic target. Trends Neurosci 2000;23(12):618-625.

50. Jellinger K, Paulus W, Grundke-Iqbal I, Riederer P, Youdim MB. Brain iron and ferritin in Parkinson's and Alzheimer's diseases. J Neural Transm Park Dis Dement Sect 1990;2(4):327-340.
51. Trojanowski JQ, Lee VM. Aggregation of neurofilament and alpha-synuclein proteins in Lewy bodies: implications for the pathogenesis of Parkinson disease and Lewy body dementia. Arch Neurol 1998;55(2):151-152.
52. Dubois B, Pillon B. Cognitive deficits in Parkinson's disease. J Neurol 1997;244(1):2-8.
53. Emre M. Dementia associated with Parkinson's disease. Lancet Neurol 2003;2(4):229-237.
54. Michell AW, Lewis SJ, Foltynie T, Barker RA. Biomarkers and Parkinson's disease. Brain 2004;127(Pt 8):1693-1705.
55. Biomarkers and surrogate endpoints: preferred definitions and conceptual framework. Clin Pharmacol Ther 2001;69(3):89-95.
56. Adjei AA, Hidalgo M. Intracellular signal transduction pathway proteins as targets for cancer therapy. J Clin Oncol 2005;23(23):5386-5403.
57. Nahrendorf M, Sosnovik D, Chen JW, Panizzi P, Figueiredo JL, Aikawa E, Libby P, Swirski FK, Weissleder R. Activatable magnetic resonance imaging agent reports myeloperoxidase activity in healing infarcts and noninvasively detects the antiinflammatory effects of atorvastatin on ischemia-reperfusion injury. Circulation 2008;117(9):1153-1160.
58. Perez JM, Josephson L, O'Loughlin T, Hogemann D, Weissleder R. Magnetic relaxation switches capable of sensing molecular interactions. Nat Biotechnol 2002;20(8):816-820.
59. Louie AY, Huber MM, Ahrens ET, Rothbacher U, Moats R, Jacobs RE, Fraser SE, Meade TJ. In vivo visualization of gene expression using magnetic resonance imaging. Nat Biotechnol 2000;18(3):321-325.
60. Artemov D, Mori N, Okollie B, Bhujwalla ZM. MR molecular imaging of the Her-2/neu receptor in breast cancer cells using targeted iron oxide nanoparticles. Magn Reson Med 2003;49(3):403-408.
61. Bulte JW, Kraitchman DL. Iron oxide MR contrast agents for molecular and cellular imaging. NMR Biomed 2004;17(7):484-499.
62. Frank JA, Zywicke H, Jordan EK, Mitchell J, Lewis BK, Miller B, Bryant LH, Jr., Bulte JW. Magnetic intracellular labeling of mammalian cells by combining (FDA-approved) superparamagnetic iron oxide MR contrast agents and commonly used transfection agents. Acad Radiol 2002;9 Suppl 2:S484-487.
63. Phelps ME. PET: the merging of biology and imaging into molecular imaging. J Nucl Med 2000;41(4):661-681.
64. Meikle SR, Kench P, Kassiou M, Banati RB. Small animal SPECT and its place in the matrix of molecular imaging technologies. Phys Med Biol 2005;50(22):R45-61.
65. Artemov D, Mori N, Ravi R, Bhujwalla ZM. Magnetic resonance molecular imaging of the HER-2/neu receptor. Cancer Res 2003;63(11):2723-2727.
66. Winter PM, Morawski AM, Caruthers SD, Fuhrhop RW, Zhang H, Williams TA, Allen JS, Lacy EK, Robertson JD, Lanza GM, Wickline SA. Molecular imaging of angiogenesis in early-stage atherosclerosis with alpha(v)beta3-integrin-targeted nanoparticles. Circulation 2003;108(18):2270-2274.
67. Thorek DL, Chen AK, Czupryna J, Tsourkas A. Superparamagnetic iron oxide nanoparticle probes for molecular imaging. Ann Biomed Eng 2006;34(1):23-38.
68. Weissleder R, Tung CH, Mahmood U, Bogdanov A, Jr. In vivo imaging of tumors with protease-activated near-infrared fluorescent probes. Nat Biotechnol 1999;17(4):375-378.
69. Ntziachristos V, Chance B. Probing physiology and molecular function using optical imaging: applications to breast cancer. Breast Cancer Res 2001;3(1):41-46.
70. Josephson L, Tung CH, Moore A, Weissleder R. High-efficiency intracellular magnetic labeling with novel superparamagnetic-Tat peptide conjugates. Bioconjug Chem 1999;10(2):186-191.

71. Cormode DP, Skajaa T, Fayad ZA, Mulder WJ. Nanotechnology in medical imaging: probe design and applications. Arterioscler Thromb Vasc Biol 2009;29(7):992-1000.
72. Pomper MG. Translational molecular imaging for cancer. Cancer Imaging 2005;5 Spec No A:S16-26.
73. Rutt BK, Lee DH. The impact of field strength on image quality in MRI. J Magn Reson Imaging 1996;6(1):57-62.
74. Hu X, Norris DG. Advances in high-field magnetic resonance imaging. Annu Rev Biomed Eng 2004;6:157-184.
75. Bloch F. The Principle of Nuclear Induction. Science 1953;118(3068):425-430.
76. Bloch F. Dynamical Theory of Signal Induction. Physical Review 1955;102:104-135.
77. Soloman I. Relaxation Processes in a System of Two Spins. Physical Review 1955;99(2):559-565.
78. O'Donnell M, Edelstein WA. NMR imaging in the presence of magnetic field inhomogeneities and gradient field nonlinearities. Med Phys 1985;12(1):20-26.
79. Jensen JH, Chandra R. Strong field behavior of the NMR signal from magnetically heterogeneous tissues. Magn Reson Med 2000;43(2):226-236.
80. Yablonskiy DA, Haacke EM. Theory of NMR signal behavior in magnetically inhomogeneous tissues: the static dephasing regime. Magn Reson Med 1994;32(6):749-763.
81. Jezzard P, Clare S. Sources of distortion in functional MRI data. Hum Brain Mapp 1999;8(2-3):80-85.
82. Truong TK, Chakeres DW, Beversdorf DQ, Scharre DW, Schmalbrock P. Effects of static and radiofrequency magnetic field inhomogeneity in ultra-high field magnetic resonance imaging. Magn Reson Imaging 2006;24(2):103-112.
83. Reichenbach JR, Venkatesan R, Yablonskiy DA, Thompson MR, Lai S, Haacke EM. Theory and application of static field inhomogeneity effects in gradient-echo imaging. J Magn Reson Imaging 1997;7(2):266-279.
84. Zeng H, Constable RT. Image distortion correction in EPI: comparison of field mapping with point spread function mapping. Magn Reson Med 2002;48(1):137-146.
85. Seppenwoolde JH, van Zijtveld M, Bakker CJ. Spectral characterization of local magnetic field inhomogeneities. Phys Med Biol 2005;50(2):361-372.
86. Van Leemput K, Maes F, Vandermeulen D, Suetens P. Automated model-based bias field correction of MR images of the brain. IEEE Trans Med Imaging 1999;18(10):885-896.
87. Reinsberg SA, Doran SJ, Charles-Edwards EM, Leach MO. A complete distortion correction for MR images: II. Rectification of static-field inhomogeneities by similarity-based profile mapping. Phys Med Biol 2005;50(11):2651-2661.
88. Truong TK, Clymer BD, Chakeres DW, Schmalbrock P. Three-dimensional numerical simulations of susceptibility-induced magnetic field inhomogeneities in the human head. Magn Reson Imaging 2002;20(10):759-770.
89. Yablonskiy DA, Haacke EM. An MRI method for measuring T2 in the presence of static and RF magnetic field inhomogeneities. Magn Reson Med 1997;37(6):872-876.
90. Wilkins J, Miller S. The use of adaptive algorithms for obtaining optimal electrical shimming in magnetic resonance imaging (MRI). IEEE Trans Biomed Eng 1989;36(2):202-210.
91. Morgan PS, Bowtell RW, McIntyre DJ, Worthington BS. Correction of spatial distortion in EPI due to inhomogeneous static magnetic fields using the reversed gradient method. J Magn Reson Imaging 2004;19(4):499-507.
92. Schmithorst VJ, Dardzinski BJ, Holland SK. Simultaneous correction of ghost and geometric distortion artifacts in EPI using a multiecho reference scan. IEEE Trans Med Imaging 2001;20(6):535-539.
93. Schneider E, Glover G. Rapid in vivo proton shimming. Magn Reson Med 1991;18(2):335-347.

94. Schad L, Lott S, Schmitt F, Sturm V, Lorenz WJ. Correction of spatial distortion in MR imaging: a prerequisite for accurate stereotaxy. J Comput Assist Tomogr 1987;11(3):499-505.
95. Gruetter R. Automatic, localized in vivo adjustment of all first- and second-order shim coils. Magn Reson Med 1993;29(6):804-811.
96. Glover GH. 3D z-shim method for reduction of susceptibility effects in BOLD fMRI. Magn Reson Med 1999;42(2):290-299.
97. Gruetter R, Tkac I. Field mapping without reference scan using asymmetric echo-planar techniques. Magn Reson Med 2000;43(2):319-323.
98. Hahn EL. Spin Echoes. Physical Review 1950;80:580-594.
99. Hennig J, Scheffler K. Hyperechoes. Magn Reson Med 2001;46(1):6-12.
100. Hinshaw WS, Lent AH. An Introduction to NMR Imaging: from the Bloch Equation to the Imaging Equation. Proceedings of the IEEE 1983;71(3):338-354.
101. Carr HY. Steady-State Free Precession in Nuclear Magnetic Resonance. Physical Review 1958;112(5):1693-1701.
102. Saam B, Yablonskiy DA, Gierada DS, Conradi MS. Rapid imaging of hyperpolarized gas using EPI. Magn Reson Med 1999;42(3):507-514.
103. Torrey HC. Bloch Equations with Diffusion Terms. Physical Review 1956;104(3):563-565.
104. Garwood M, DelaBarre L. The return of the frequency sweep: designing adiabatic pulses for contemporary NMR. J Magn Reson 2001;153(2):155-177.
105. Pauly J, Le Roux P, Nishimura D, Macovski A. Parameter relations for the Shinnar-Le Roux selective excitation pulse design algorithm [NMR imaging]. IEEE Trans Med Imaging 1991;10(1):53-65.
106. McConnell HM. Reaction Rates by Nuclear Magnetic Resonance. Journal of Chemical Physics 1958;28(3):430-431.
107. Bittl JA, Ingwall JS. Reaction rates of creatine kinase and ATP synthesis in the isolated rat heart. A 31P NMR magnetization transfer study. J Biol Chem 1985;260(6):3512-3517.
108. Brindle KM. NMR methods for measuring enzyme kinetics in vivo. Progress in Nuclear Magnetic Resonance Spectroscopy 1988;20(3):257-293.
109. Aisen AM, Martel W, Braunstein EM, McMillin KI, Phillips WA, Kling TF. MRI and CT evaluation of primary bone and soft-tissue tumors. AJR Am J Roentgenol 1986;146(4):749-756.
110. Ng SH, Chang TC, Ko SF, Yen PS, Wan YL, Tang LM, Tsai MH. Nasopharyngeal carcinoma: MRI and CT assessment. Neuroradiology 1997;39(10):741-746.
111. Blum U, Buitrago-Tellez C, Mundinger A, Krause T, Laubenberger J, Vaith P, Peter HH, Langer M. Magnetic resonance imaging (MRI) for detection of active sacroiliitis--a prospective study comparing conventional radiography, scintigraphy, and contrast enhanced MRI. J Rheumatol 1996;23(12):2107-2115.
112. Leach MO, Brindle KM, Evelhoch JL, Griffiths JR, Horsman MR, Jackson A, Jayson GC, Judson IR, Knopp MV, Maxwell RJ, McIntyre D, Padhani AR, Price P, Rathbone R, Rustin GJ, Tofts PS, Tozer GM, Vennart W, Waterton JC, Williams SR, Workman P. The assessment of antiangiogenic and antivascular therapies in early-stage clinical trials using magnetic resonance imaging: issues and recommendations. Br J Cancer 2005;92(9):1599-1610.
113. Parker GJ, Suckling J, Tanner SF, Padhani AR, Revell PB, Husband JE, Leach MO. Probing tumor microvascularity by measurement, analysis and display of contrast agent uptake kinetics. J Magn Reson Imaging 1997;7(3):564-574.
114. Schroeder MA, Atherton HJ, Ball DR, Cole MA, Heather LC, Griffin JL, Clarke K, Radda GK, Tyler DJ. Real-time assessment of Krebs cycle metabolism using hyperpolarized 13C magnetic resonance spectroscopy. FASEB J 2009;23(8):2529-2538.

115. Ardenkjaer-Larsen JH, Fridlund B, Gram A, Hansson G, Hansson L, Lerche MH, Servin R, Thaning M, Golman K. Increase in signal-to-noise ratio of > 10,000 times in liquid-state NMR. Proc Natl Acad Sci U S A 2003;100(18):10158-10163.

CHAPTER TWO

DYNAMIC PERFUSION STUDY WITH T1-WEIGHTED DYNAMIC CONTRAST ENHANCEMENT (DCE) MRI IN MOUSE PANCREAS – A POTENTIAL BIOMARKER OF GLUCOSE SENSING

2.1 Overview

Dynamic contrast enhanced magnetic resonance imaging (DCE-MRI) is an established technique used for characterization of microvasculature in oncology. Its sensitivity to physiological biomarkers such as blood flow, transendothelial permeability and volume of extracellular space enables differentiation between pathological states and assists in therapeutic assessment. In this chapter, we exploit the strengths of DCE-MRI to probe the microvasculature in the mouse pancreas, which is a critical organ maintaining glucose homeostasis via insulin secretion. Semi-quantitative analysis comparing the pancreatic hemodynamics between STAT3-deficient and healthy mice is first presented, in order to demonstrate its potential as a biomarker to probe angiogenesis impairment. Subsequently, quantitative pancreatic blood flow is deduced via pharmacokinetic modeling and rapid imaging techniques in order to achieve a biomarker with direct physiological relevance. Such an endeavor has not yet been attempted by the scientific community because of intricate challenges.

2.2 Why image blood flow in the pancreas?

Insulin secretions by beta-cells in the pancreatic islets of Langerhans are critical in maintaining blood glucose homeostasis. A rise in blood glucose level (e.g. after a meal) under normal physiological condition triggers insulin secretion, which in turn signals for increased glucose uptake in tissues. Defects in the insulin secretion mechanism create a metabolic disorder of multiple etiologies characterized by chronic hyperglycemia with disturbances of carbohydrate, fat and protein metabolism (1). This pathological condition that affects more than 220 million people worldwide is known as diabetes mellitus (2). All forms of diabetes have very serious effects on health. There are a number of long-term complications

associated with the disease. These include cardiovascular, peripheral vascular, ocular, neurologic and renal abnormalities, which are responsible for morbidity, disability and premature death in young adults (3-5). Furthermore, the disease is associated with reproductive complications causing problems for both mothers and their children (6). The American Diabetes Association estimates that the mortality rate doubles in diabetics. Cost to the American health care system is estimated to be $174 billion in 2007, of which $116 billion was for direct care of diabetes, $58 billion for treatment of diabetes complications and the rest due to increased incidence of other diseases such as heart failure (7). Although improved glycemic control may decrease the risk of developing these complications, diabetes remains a very significant cause of social, psychological and financial burdens in populations worldwide (8,9).

There are two major types of diabetes, Type 1 and 2. Type-1 diabetes, previously known as insulin-dependent diabetes mellitus or IDDM, is characterized by the specific autoimmune recognition and destruction of insulin-generating beta-cells (10,11), leading to absolute insulin deficiency. The mechanism is hypothesized to be the triggering of an inflammation response by T-lymphocytes in the islets, provoking destruction of the β-cells by leukocytes, a condition known as insulitis (12). Figure 2.1 illustrates this hypothetical inflammation process in a pictorial representation. Type-1 diabetes accounts for about 10% of clinical cases.

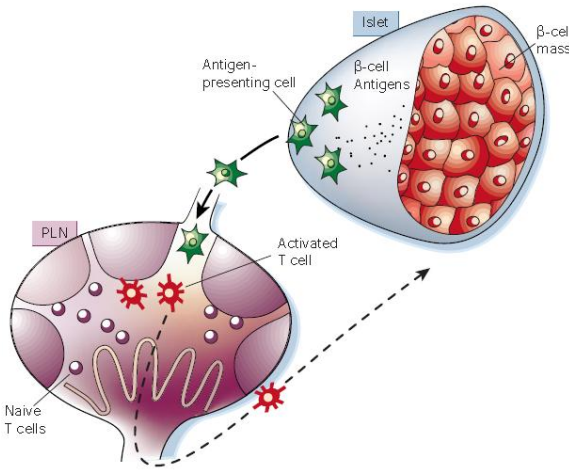

Figure 2.1: Proposed scheme for the initiation of type 1 diabetes (12). Antigen presenting cells trigger the influx of T-lymphocytes, provoking a destructive autoimmune process against β-cells.

The majority of diabetic patients though suffer from Type-2 diabetes (also known as non-insulin dependent diabetes mellitus NIDDM), which is a chronic metabolic disorder arising from defects in insulin secretion and insulin action (13,14). They create multiple disturbances in glucose homeostasis, including: (1) impaired insulin secretion; (2) insulin resistance in muscle, liver, and adipocytes; and (3) abnormalities in splanchnic glucose uptake (15). Type-2 diabetes is also associated with several other metabolic abnormalities such as central obesity, hypertension, and dyslipidemia, contributing to the very high rate of cardiovascular morbidity and mortality (16). The onset of diabetes mellitus is thus attributed to a convolution of factors ranging from genetic predisposition (17,18) to the environment (19,20). It is obvious that diabetes is an intricate collection of diseases, originating from various causes with different progression paths. Since these pathologies appear to converge and develop into hyperglycemia, insulin production by β-cells is therefore a very important biological process in the development of the disease.

The central role of β-cells in the pathogenesis of diabetes has attracted great interest in the use of molecular and cellular imaging techniques for in-vivo detection of their function and physiology. A host of molecular probes are being developed to sense the occurrence of

important processes that seek to destroy β-cells or seriously disrupt their function. Tracking the homing of lymphocytes labeled with anionic magnetic nanoparticles for instance, offers a real-time monitor of the auto-immune destruction of β -cells in the diabetic pancreas (21). Specific targeting of the auto-reactive lymphocytes via a molecular probe of high affinity (e.g. NRP-V7 peptide conjugated to a cross-linked superparamagnetic iron-oxide nanoparticle) enables identification of an explicit lymphocyte population that triggers the auto-immune destruction of β-cells (CD8+ T-cells in this example) (22). Although cellular tracking allows a probe into the inflammatory response in the pancreatic islets, it is at the end-point and affected β-cells will still be eliminated subsequently. It is perhaps more useful to study the processes that precede the islet destruction and implement preventive actions. Accumulating evidence suggests that vascular endothelium is of crucial importance for the development of inflammatory reactions (23). The roles of endothelial and leukocyte surface receptors in the homing of inflammatory cells to the pancreatic islets are becoming more evident, shedding light on their participation in the origin of insulitis and IDDM (24-26). Furthermore, changes in vascular permeability of islet blood vessels during the development of IDDM have been described in diabetic rodent models (27,28). Notwithstanding its role in facilitating autoimmune destruction of β-cells, the microvascular network in the islets is also a key infrastructure in transmission of information pertaining to the blood glucose level, which regulates insulin production, and in transportation of the secreted hormone (29). This information highway is extremely crucial in glucose sensing and maintaining homeostasis (30,31). It is thus not surprising that the microvasculature of the pancreatic islets is an intricate network of arterioles and capillaries (32), which receive a significant 10-20% of the total pancreatic arteriolar blood flow (33), despite their relatively minute composition (1.7% mass) in the whole pancreas. It is thus intuitive that in-vivo detection of blood flow, blood volume and vessel permeability of the pancreas could serve as biomarkers of islet viability

and function (34). Obtaining real-time macroscopic information pertaining to the hemodynamic properties of the pancreas would then herald pathogenesis and perturbations in the glucose balancing mechanism.

2.3 Pancreatic Perfusion Quantification Methods

2.3.1 Pancreas Morphology

Accomplishing this goal of measuring pancreatic perfusion quantitatively with DCE-MRI is a tremendous challenge owing to the unique cellular composition and structure of the pancreas. The pancreas consists of the endocrine and exocrine glands, consisting of the islets of Langerhans and the pancreatic acini, respectively. Pancreatic islets are small organ-like entities dispersed throughout the pancreas at a low density and account for only 1.7% of the pancreatic volume (35). It is a complex structure comprising four types of secretory endocrine cells, namely the insulin-containing β-cells, the glucagon-containing α-cells, the somatostatin-containing δ-cells and the pancreatic polypeptide-producing (PP) cells (36). In humans, the cellular composition appears to depend on the region in the pancreas; with β-cells contributing between 48% and 59% of total cell population, α-cells between 33% and 46%, and δ-cells between 8% and 12% (37). Islet cellular composition also varies widely in healthy and diabetic patients (38), further convoluting the microcirculation morphology. Thus subject variability is expected to be substantial in the quantified pharmacokinetic parameters. Nonetheless, the advantages offered by DCE-MRI to probe pancreatic microcirculation propel us to develop a protocol for non-invasive blood flow measurements in a very important small animal model, the laboratory mouse.

2.3.2 Microsphere Technique for Blood Flow Measurement

Pancreatic blood flow in small animals has traditionally been measured with the invasive method of polystyrene microspheres injection into a carotid cannula with simultaneous blood withdrawal for quantification reference. The rate of blood flow per sphere is then assumed to equal the rate of withdrawal divided by the number of spheres in the withdrawn blood volume. By dissecting the pancreatic tissue and counting the number of spheres in the microvasculature, the blood flow (ml min^{-1}) and perfusion (ml $min^{-1}g^{-1}$) can be deduced (35,39). Distribution of islet blood flow can subsequently be mapped out according to islet size. In a rodent, the distribution of islet blood flow ranges from 3% to 64% of total islet blood flow, depending on islet diameter (25 – 300μm) (40). Although this method permits quantification of blood flow down to the tens of μm in spatial resolution, it is a terminal procedure and does not allow longitudinal assessment of hemodynamics in the pancreas.

2.3.3 Appeal of DCE-MRI in Perfusion Studies

A more appealing method for in-vivo perfusion measurement is the non-invasive dynamic contrast enhanced magnetic resonance imaging technique, whereby either a T_1 or T_2 reducing agent is infused into the blood stream to create signal enhancement or depletion in perfused tissues, respectively (41,42). If a low molecular weight contrast agent is used, its molecules are transiently confined within blood vessels during first passage and then rapidly diffused through the fenestrated capillaries into the extravascular extracellular space (EES). The rate of extravasation depends upon the endothelial permeability, surface area, tracer's particle size and blood flow. The flux of the contrast agent back into the microcirculation will occur subsequently at a rate dependent on the endothelial permeability. By measuring the temporal changes in tissue signal intensity, the concentration of the exogenous contrast agent in the

tissue can be derived, divulging its diffusion kinetics into the tissue extracellular space. The tracer's bio-distribution provides information on perfusion and microvessel characteristics, such as endothelial permeability, volume of the plasma space and interstitial volume (41,43-45). These parameters have proven valuable in the assessment of tumor vasculature and function (46,47), as well as in the analysis of tumor response to therapeutic drugs such as anti-angiogenesis inhibitors (48-50). A clinical example would be the comparison of pharmacokinetic parametric maps between treated and untreated tumors, such as K^{trans} (volume transfer constant), in order to determine the arrest efficiency of the therapeutic agent (51,52).

2.4 Probing of Pancreatic Microvasculature with DCE-MRI

2.4.1 Novelty in Mouse Pancreas DCE-MRI

Very little literature exists on the quantitative perfusion of the mouse pancreas. In fact we found only one in PubMed that measures T_1 in the pancreas and not perfusion per se (i.e. semi-quantitative only) (53). There are a couple of reasons for such scarcity. First is the complex structure of the mouse pancreas, which is a thin film of tissue (~1 mm) that stretches across the abdomen in an irregular fashion in-between gastrointestinal structures. Therefore, dedicated small animal MRI system is necessary to achieve the required resolution and precision. Second, it is extremely difficult to obtain the arterial input function (AIF) in mice because of its rapid cardiac cycle. Yet the AIF is fundamental for quantitative blood flow deduction. High temporal resolution is thus essential and that stresses the gradient performance of the system. To appreciate the technical challenges faced and limitations in the physiological interpretation of quantities obtained with DCE-MRI, we will have to

understand the quantification process including the difficulties encountered in magnetic resonance imaging of the mouse pancreas.

2.4.2 Roadmap to Mouse Pancreatic Perfusion Quantification

We begin this journey by comparing DCE-MRI techniques that could measure MR signal changes dynamically. Identification of the different T_1-reducing exogenous contrast agents available and a description of their distinct pharmacokinetics in tissue perfusion are then presented. A systematic approach for consistent mouse pancreas MR imaging then follows. Semi-quantitative T_1 DCE-MRI analysis is performed on a STAT3 knockout model to search for abnormalities in pancreatic microvessel development. As we progress to quantitative perfusion measurements, an introduction of contrast agent mass transport kinetics and the relevant physiological parameters affecting their pharmacokinetic properties will be made, using a two-compartment model (54). We shall seek to derive tissue perfusion information by fitting dynamic concentration curves into this model. Finally, a quantitative treatment of the dynamic signal enhancement with the two-compartment model, upon infusion of a low molecular weight T_1-reducing contrast agent, is performed to extract blood flow and volume percentage of extracellular space in the mouse pancreas.

2.4.3 Pharmacokinetic Modeling with DCE-MRI

Types of DCE-MRI

DCE-MRI has proven its potential to distinguish the vasculatures of normal and pathological tissues in oncology. Semi-quantitative and quantitative analysis further makes it appealing as a potent biomarker for non-invasive grading of tumor (55-57). The pharmacokinetic

properties that can be derived in a DCE-MRI experiment depend on the applied methodology. DCE-MRI sequences can be designed to be sensitive to the vascular phase of contrast medium delivery (so-called *dynamic susceptibility contrast* which reflects on tissue perfusion and blood volume). In this technique, a rapid injection of high-concentration contrast agent is infused (a 'bolus'), giving rise to magnetic field inhomogeneities that decrease the MRI signal (58). This effect is most pronounced during the first passage through the tissue, after which signal quickly recovers to its equilibrium value. The real-time changes in tissue signal intensity has to be tracked rapidly using a fast imaging sequence, with a typical temporal resolution of 1-2 seconds over a period of 60 seconds post-injection. Generally, a gradient-echo or spin-echo sequence is used, with the latter providing greater sensitivity to microvessels (59). To increase sensitivity to blood flow and reduce dependency on tracer molecule diffusion into the tissue extracellular space, a blood-pool agent is preferred. Semi-quantitative analysis of the signal changes may be performed to obtain parameters indirectly related to physiology (60) . Alternatively, if contrast agent concentration is known together with knowledge of the arterial input function (AIF), parametric maps of tissue blood flow F (ml $g^{-1}min^{-1}$), tissue blood volume tBV (ml g^{-1}) and mean transit time *MTT* (the average time taken for the tracer to pass through the vascular bed within the voxel; units are in minutes) can be generated from the time-course of the MRI signal changes by applying kinetic analysis (61,62). Since its initial maximum peak enhancement ('first pass') usually occurs within 10 seconds upon infusion in mice and is substantially completed in half that time (63), some technical requirements must therefore be fulfilled to ensure accuracy in bolus tracking experiments. High spatial resolution for accurate derivation of the arterial input function, together with a high temporal resolution to capture the peak enhancement during the bolus phase (64) are essential conditions. A typical mouse has a blood volume of about 2 mL and a cardiac output of 11 mL min^{-1} (65), and thus its circulation period is only about 11 seconds.

A healthy human being on the other hand has approximately 5 liters of blood and an output of 5.5 L min^{-1}, resulting in a period of 55 seconds. Thus if the first pass in the mouse is to be captured with sufficient temporal resolution, ultra-fast imaging techniques must be adopted without sacrificing accuracy in quantification.

Alternatively, T_1-weighted sequences can be employed to create signal enhancement. If a low molecular weight tracer is used in conjunction, these techniques become sensitive to the presence of contrast medium in the EES, which reflect microvessel perfusion, endothelium permeability and extracellular leakage volume. T_1-weighted DCE-MRI is what we have adopted in this work because of the interest in studying the microvascular characteristics in the pancreas and thus its utilization will be further discussed in subsequent sections. A brief overview comparing T_2^*- and T_1- weighted DCE-MRI techniques are presented in Table 2.1 (66,67).

	T_2^*-weighted imaging	T_1-weighted imaging
Tissue signal intensity change	Darkening	Enhancement
Temporal resolution	1 – 2s	2 – 25s
Duration on imaging	60 – 90s	5 – 10min
Magnitude of effect	Small	Larger
Type of contrast agent	Blood-pool agents (molecular weight MW > 70kDa preferred)	Low to moderate MW agents that diffuse into the EES
Optimal contrast medium dose	> 0.2 mmol/kg body weight	0.1 - 0.2 mmol/kg b.w.
Quantification method used	Relative more than absolute	relative and absolute
Physiological property measured	Perfusion / blood volume	Trans-endothelial permeability, capillary surface area, tissue leakage space
Kinetic parameters derived	Blood volume and flow, transit time	Transfer and rate constants, leakage space
Pathological correlates	Tumor grade and microvessel density	microvessel density
Clinical MR applications	Lesion characterization - breast, liver and brain Directing brain tumor grading Directing brain autopsy Determining brain tumor prognosis Monitoring treatment, e.g. radiotherapy	Vascular endothelial growth factor (VEGF) inhibition Lesion detection and characterization Improving accuracy of tumor staging Predicting response to treatment Monitoring response to treatment Novel therapies including anti-angiogenic drugs Detecting tumor relapse
Special technical requirements for small animal imaging	Ultra-fast sequence to capture first-passage of contrast medium in the tissue	Good slice profile for very thin slices of ~ 0.50 mm Very short echo-time to minimize T_2^*-effect at high magnetic field

Table 2.1: Comparison of T_2^*- and T_1- weighted dynamic contrast enhanced MRI techniques.

Requirements unique to small animal DCE-MRI at high magnetic field are also included.

2.4.4 Contrast Agents for T1-weighted DCE-MRI

There are essentially two types of exogenous contrast agents for T_1-weighted DCE-MRI, namely low molecular weight (< 1000 Da) and moderate molecular weight contrast media (> 10000 Da). The appropriate tracer to use depends on the desired application. Low molecular weight (or *extravascular*) contrast agents allow probing of microvascular properties such as transendothelial permeability P, capillary surface area S, transfer and rate constants K^{trans}, micro-vessel density, fractional volume of extracellular extravascular space v_e, and plasma space v_p (68). These microvascular characteristics directly impact tracer uptake and clearance in the tissue and alter the MRI signal in the tissue. These properties are dependent on the current physiological state, and thus tracking their changes could benefit pathodiagnosis and disease staging. Numerous clinical studies have demonstrated their utility in measuring or assessing therapeutic response of tumors in the bladder, breast, brain, cervix and bone in patients (69-73). However, there are instances in which only the blood flow and volume are desired. Then the contrast medium preferably remains in the blood circulation with minimal loss into the tissue interstitial space and low molecular weight contrast agents will not be suitable for this task. This requirement can be met by attaching low molecular weight contrast media to macromolecules such as peptides. The resulting macromolecular contrast agents possess limited ability to diffuse through the capillary endothelium, enabling diminished tissue uptake and slower clearance from the blood pool. This category of tracers is clinically termed *intravascular* contrast agents, because of their prolonged plasma lifetimes. Their excretion is also retarded, yielding flatter arterial input functions. The slower kinetics allows for higher dynamic range in quantification of vascular leakage and acquisition of much higher-resolution images (74). To achieve intravascular retention, several paramagnetic chelates have been proposed and tested. These included Gd-DTPA-albumin (75), Gd-DTPA-dextran (76) and Gd-DTPA-polylysine (77), with molecular weights ranging from 48 to

150kDa. Molecular size is a critical factor determining the retention of these compounds in the intravascular compartment as well as its relaxivity. Although they are most commonly used in bolus tracking experiments with T_2^*-weighted MRI, I adapted their utilization in prolonged perfusion imaging with T_1-weighted DCE-MRI by gradual infusion at low concentration. By doing so, I could perform semi-quantitative analysis on the resulting signal enhancement curve (see section 2.6). The availability of low molecular and macromolecular weight contrast agents thus facilitates the investigation of microvascular dynamics as well as offers a probe into the endothelial membrane integrity.

2.4.5 Definition of Semi-Quantitative DCE-MRI Parameters

When a contrast agent is delivered into the systemic circulation, it is carried in the blood plasma and delivered throughout the body. A portion is initially absorbed into the tissue extracellular extravascular space (EES) via diffusion through the capillary endothelium. There is also back-diffusion from the EES into the plasma space before equilibrium is established. Subsequently as more tracer molecules are excreted, contrast agent concentration in the blood plasma will diminish. The concentration gradient changes polarity and the tracer begins to wash-out from the tissue EES. The whole process from infusion to absorption and finally clearance describes the pharmacokinetics of the contrast agent and indirectly reports on the pathophysiological status of the targeted tissue. The blood circulation at the capillary level, or microcirculation, is driven by the metabolic activity of the tissue. In pathological processes, such as tumorigenesis, this microcirculation becomes altered and leads to an increase in microvascular density resulting from the growth of new capillary networks as well as vasodilation of existing vessels (78). To describe the impact of these physiological metamorphoses on the MR signal, a series of terminology has been proposed including the

initial area under the Gadolinium curve (IAUGC), *maximum enhancement gradient* and *enhancement* (79). Such semi-quantitative DCE-MRI has benefitted disease prognosis and been particularly useful in the investigation of tumor angiogenesis (80). It enables the study of microcirculation in a number of diseases including breast metastases in which a highly vascularized carcinoma is characterized by a rapid upslope, high signal enhancement and clear washout phase (81), in bone sarcoma where necrotic, semi-necrotic, proliferating and viable regions of the bone displayed distinct tracer pharmacokinetics (69), and in the evaluation of the use of an inhibitor of VEGF receptor tyrosine kinase to retard angiogenesis in metastatic liver lesions (82). Rate of tracer uptake and clearance have also been employed as biomarkers to gauge blood-brain barrier breakdown in neurodegenerative diseases such as multiple sclerosis (83,84), which indirectly report the rate of axon demyelination. Regardless of the contrast agent's principal relaxation mechanism (T_1- or T_2- shortening), the induced signal changes can be chronologically measured with dynamic MRI. Before pioneering quantification work from Tofts (45), Brix (85) and Parker (86), semi-quantitative DCE-MRI provided the pragmatic information to distinguish between necrotic and viable tissues (87-89), merely from the comparison of their signal enhancement curves. This is a valuable diagnostic tool in MRI that has been extensively used in the past two decades and remains so. To exploit its advantages, I defined the parameters that are commonly used in the clinic to describe the dynamic signal enhancement data. Furthermore, to showcase an application of this semi-quantitative methodology in the investigation of pancreatic vasculature, I measured these parameters in a study comparing the signal enhancement curves between a wild-type and a STAT3 knock-out mouse, and attempted to interpret the physiological relationship between their dissimilar signal enhancement evolution and microvascularity differences (see section 2.6).

A starting point in semi-quantitative analysis is to look at a typical T_1-weighted dynamic contrast enhancement signal intensity curve illustrated in Figure 2.2. There are normally three distinct phases in the signal enhancement time evolution; the upslope, maximum enhancement and washout (66). It is generally recognized that the upslope is highly dependent on tissue perfusion and permeability, with perfusion dominating principally due to high blood volume and high first pass extraction. Maximum enhancement is related to the total uptake concentration of the contrast medium in the interstitial space and washout rate is associated with a decrease in the concentration of the tissue contrast agent. The latter two phases are strongly coupled to vascular permeability. Semi-quantitative analysis of signal intensity changes with respect to these three phases and provides insight into the pharmacokinetics of the contrast agent, which is influenced by the underlying physiology. Thus it offers a fast and convenient method to aid in diagnosis. Parameters for description of tracer kinetics include the following and are shown in Figure 2.2 (86):

1. Onset time: defined as the time period between the midpoint of the tracer injection and the point on the enhancement curve at which signal is 10% of its maximum.
2. Maximum signal intensity: defined as the peak level of relative signal intensity within the tissue of interest, within the dynamic measurement method.
3. Initial gradient: defined as the rate of change in relative signal intensity at the 10% point on the uptake curve.
4. Mean gradient: defined as the average rate of change in relative signal intensity between the 10% point and the 90% point on the enhancement curve.
5. Washout gradient: defined as the average rate of change in signal intensity between the point of maximum enhancement and the end of the dynamic scanning period, if a maximum is reached during the time.

6. Initial area under the gadolinium curve (IAUGC): Integral area under the signal enhancement curve from tracer delivery till after the first pass. Commonly used as an endpoint in assessment of blood flow, vascular permeability and interstitial space (90).

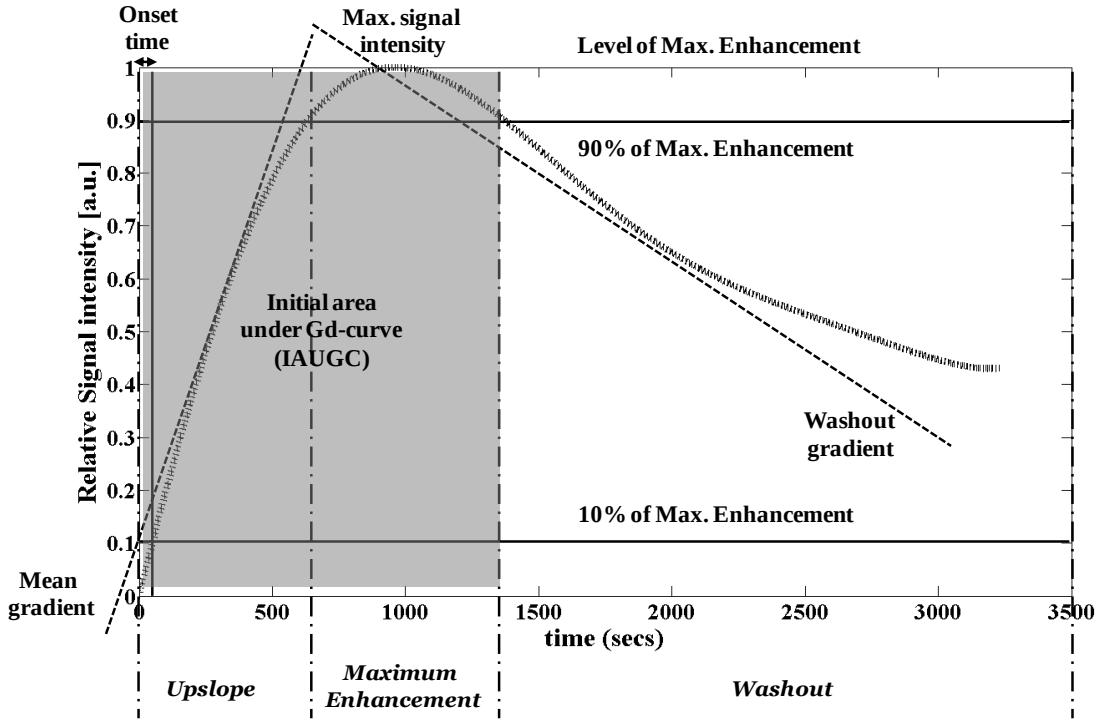

Figure 2.2: Relative signal intensity of wild-type mouse in a T_1-weighted DCE-MRI experiment after an intravenous injection of 0.2 mmol kg^{-1} Vasovist® (intravascular contrast agent) at time t = 0 s. Relative signal intensity is defined as $\frac{[S(t)-S(0)]}{\max(S(t)-S(0))}$, where *S(t)* is the absolute signal at time t, *S(0)* is the baseline signal and max[S(t)] is the maximum signal intensity.

2.4.6 Pharmacokinetics of Low Molecular Weight Extracellular Contrast Agents

Low molecular contrast media available in the clinic, such as gadopentetate dimeglumine (Gd-DTPA) with a molecular weight of 590 Da, diffuse from the blood plasma pool into the EES of the pancreas at a rate determined by the blood flow into the tissue *F*, the permeability

of the capillaries *P* and the surface area of the perfusing vessels *S*. The contrast agent molecules do not cross cell membranes and hence its volume distribution is effectively the extracellular extravascular space, as shown in Figure 2.3. On T_1-weighted images, the shortened T_1-relaxation times of the blood pool and extracellular water, induced by the tracer in the plasma and interstitial spaces, respectively, result in positive enhancement. The early phase in contrast enhancement, which is equivalent to the first-pass in a bolus injection, involves the arrival of the contrast medium in the pancreas via the arterial supply, and lasts several cardiac cycles. The contrast agent subsequently diffuses back into the vasculature and is excreted via the reticuloendothelial system (RES). When these influx and outflux processes are limited in poorly perfused regions, it is reflected in the lower volume transfer parameter K^{trans} (91). This discrepancy in tracer uptake and clearance between normal and pathological tissues could be used as biomarkers in treatment diagnosis and disease staging (92). In order to obtain accurate quantitative information from DCE-MRI for sensible correlation to physiology, we will need to model the in-vivo pharmacokinetics of the contrast agent.

The rate of accumulation and wash-out of a contrast agent into the interstitial space, assuming it is homogenous in the vascular plasma space v_p and well-mixed in the EES, can be described by the steady-state mass transfer equation from Kety (93):

$$v_e \frac{dC_e(t)}{dt} = K^{trans}\left[C_p(t) - C_e(t)\right] \qquad (2.1)$$

where v_e is the volume of the EES per unit volume of tissue, C_e (mM) is the concentration of the agent in v_e, v_p is the blood plasma volume per unit volume of tissue, C_p (mM) is the concentration of agent in v_p, and K^{trans} is the volume transfer constant between v_p and v_e (41)

(see Figure 2.3). The transfer constant depends on the equilibrium between capillary permeability and blood flow in the tissue of interest. In a highly-permeable membrane, the flux across the endothelium is flow-limited and K^{trans} is equal to the blood plasma flow per unit volume of tissue according to Eqn. (2.2). F is the perfusion of whole blood per unit mass of tissue (ml $g^{-1}min^{-1}$), ρ is tissue density (g ml^{-1}), Hct is the hematocrit, P is the total permeability of the capillary wall (cm min^{-1}) and S is the surface area per unit mass of tissue (cm^2 g^{-1}).

$$Flow - limited\ regime: \quad K^{trans} = F\rho(1 - Hct) \quad (PS \gg F) \qquad (2.2)$$

In the reversed scenario of low permeability limiting tracer flux, the transfer constant is equal to the permeability surface area product between blood plasma and EES per unit volume of tissue, i.e.

$$Permeability - limited\ regime: \quad K^{trans} = PS\rho \quad (PS \ll F) \qquad (2.3)$$

In the general mixed perfusion- and permeability-limited regime, K^{trans} becomes equal to $EF\rho$ *(1-Hct)*, where E is the extraction fraction of the tracer (i.e. the fraction of tracer that is extracted from v_p into v_e in a single capillary transit). Thus $E = 1$ in a flow-limited situation while $E = PS / [F(1-Hct)]$ in a permeability-limited regime.

$$K^{trans} = EF\rho(1 - Hct) \qquad (2.4)$$

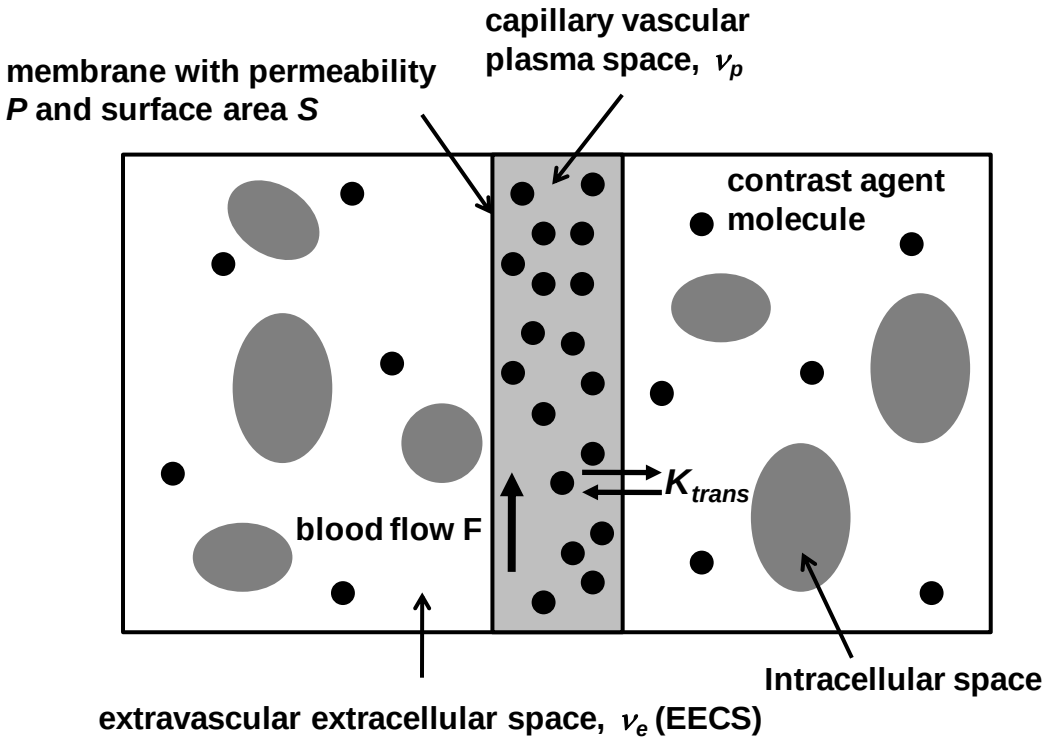

Figure 2.3: Major compartments involved in the distribution of a contrast agent tracer

C_t is the tracer concentration in the tissue that is indirectly measured in DCE-MRI. If we ignore the contribution of intravascular tracer to the tissue concentration, then it is defined as (41)

$$C_t(t) = v_e C_e(t) \tag{2.5}$$

Substituting this into Eqn. (2.1), the resulting 1st order differential equation to solve would be

$$\frac{dC_t(t)}{dt} = K^{trans}\left[C_p(t) - C_t(t)/v_e\right] \tag{2.6}$$

The problem with this *Tofts-Kermode (TK)* model is the assumption that the observed contrast agent concentration changes in a voxel is entirely caused by the leakage of tracer molecules into the EES. In reality signal enhancement, upon induced T_1-relaxation with

contrast media, occurs in both capillary vascular plasma space v_p and the EES v_e (assuming no cellular uptake). The flawed assumption leads to erroneously high K^{trans} values caused by intravascular contrast agent and inflates vascular permeability estimates (94,95). This artifact has therefore been referred to as "pseudo-permeability' (54). To rectify the modeling error, the total contrast agent concentration in the tissue voxel should reflect the component of intravascular tracer and thus eqn. (2.5) is modified to become eqn. (2.7). Putting this into eqn. (2.1), we obtain the total tissue concentration per voxel according to eqn. (2.8).

$$C_t(t) = v_p C_p(t) + v_e C_e(t) \tag{2.7}$$

$$C_t(t) = v_p C_p(t) + K^{trans} \int_0^t C_p(t') \times exp\left[\frac{-K^{trans}(t-t')}{v_e}\right] dt' \tag{2.8}$$

$C_t(t)$ may also be expressed in the form presented in eqn. (2.9), where $H(t)$ is the impulse function given by eqn. (2.10) and $\otimes$ denotes the convolution operation. This is known as the *modified TK* model.

$$C_t(t) = v_p C_p(t) + C_p(t) \otimes H(t) \tag{2.9}$$

$$H(t) = K^{trans} exp\left(\frac{-K^{trans} t}{v_e}\right) \tag{2.10}$$

Tracer concentration in the blood plasma changes with regard to the pharmacokinetics of the contrast agent in the pancreas, hemodynamics of the animal and excretion. Its effect on T_1-enhancement is mixed with that in the EES and is not easily extracted from the measured MR signal. Tofts and Kermode approximated this arterial input function (AIF) by a bi-exponential function that was scaled according to the administered dose of contrast agent D (mmol kg^{-1} body weight) , with the constants a_1, a_2, m_1, m_2 and A (41,96):

$$C_p(t) = D[a_1 exp(-m_1 t) + a_2 exp(-m_2 t)] + A \tag{2.11}$$

Determination of the AIF is a critical component in the quantitative process. The easiest way to introduce an AIF to a DCE-MRI kinetic modeling experiment is to assume one derived from the time course of the mean vascular concentration measured in blood samples from healthy subjects (97). Although this simple method is convenient, it does not consider the actual AIF of the subject and would most likely introduce parametric errors in the model. To avoid such detrimental consequences, we prefer to measure the AIF for each subject, using an MRI procedure if possible. In this thesis, we used the abdominal aorta as the source of arterial input function to fit into eqn. (2.11) and estimate $C_p(t)$. Together with the measured tracer concentration in the pancreas, $C_t(t)$, the modified TK model is fitted to the dynamic MR concentration data using nonlinear least squares estimation to obtain values for K^{trans}, v_e and v_p in eqn. (2.9). Pancreatic blood flow is then extracted from K^{trans} according to eqn. (2.2), assuming a pancreatic tissue density of ρ =1.05 g ml^{-1} and a haematocrit of 0.49.

2.4.7 Dynamic T_1 Quantification

It is apparent that the contrast agent concentration in the tissue C_t and plasma C_p are key parameters in the determination of tissue uptake rate, capillary permeability and blood flow. The determination of C_t and C_p is perhaps the most challenging step in the quantitative characterization of tracer pharmacokinetics. Since MRI does not measure concentration per se, it will have to be extracted from the MR signal. A straightforward approach is to assume that the change in signal intensity is directly proportional to tracer concentration according to eqn. (2.12). T_{10} is the baseline tissue longitudinal relaxation time before infusion of contrast agent (i.e. at t = 0) while $T_1(t)$ are the dynamic values upon tracer delivery. Tracer relaxivity r_1 depends on the field strength, the chemical nature of the contrast agent and the physicochemical properties of the tissue. T_1 depends on the inherent tissue properties such as

proton density content and the microenvironment of the various proton pools. When contrast agent particles enter the circulation, some will diffuse into the extracellular extravascular space of the pancreas while others remain in the blood plasma or are excreted via the kidneys. These Gd-complexes hasten relaxation of juxtaposed proton pools in the blood plasma as well as in the EES, resulting in the voxel signal becoming an ensemble of relaxation effects from different compartments. This weighted signal inclines towards either the EES or vascular space compartment as spatial resolution improves. It is intuitive from eqn. (2.12) that if we measure T_1 variation with time, an estimate of contrast agent concentration in tissue could be obtained (96).

$$C_t(t) = \frac{\left[\frac{1}{T_1(t)} - \frac{1}{T_{10}}\right]}{r_1} \tag{2.12}$$

Measurement of T_1 in DCE-MRI requires accuracy and sufficient signal-to-noise ratio over a wide range of values (i.e. good dynamic range). This is because the T_1 of the mouse pancreas can vary from about 650 ms pre-contrast to 194 ms upon infusion at 9.4T field strength (53). Therefore the measurement method must be rigorously validated over a wide range of T_1 values. In order to obtain a sufficient in-plane spatial resolution (~150 × 150 μm^2) within a reasonable time, and to minimize the transverse relaxation effect of the contrast agent, the most common approach to dynamic T_1 measurements is to employ a rapid gradient echo-based sequence such as Snap-Shot Flash (98). This technique possesses a number of advantages including speed and ease of T_1 estimation. The MR signal S from a spoiled-gradient echo image with echo time, TE is

$$S = \frac{S_0 \sin\theta\left[1 - e^{-TR/T_1}\right]}{1 - \cos\theta e^{-TR/T_1}} e^{-TE/T_2^*} \tag{2.13}$$

where *TR* is the repetition time, θ is the RF flip angle used, and S_0 is the relaxed signal for a 90° pulse when $TR >> T_1$ and $TE << T_2^*$ (i.e. the proton-density signal). By making multiple acquisitions with different repetition times and/or different flip angles, it is possible to estimate the T_1 of the tissue. For quantitative DCE-MRI, a straightforward protocol involves a single heavily proton density-weighted acquisition, prior to contrast agent administration, followed by numerous T_1-weighted acquisitions over time (see Figure 2.4) (86,99,100). This could be achieved by choosing a low θ_{PDW} for *PD*-weighted acquisition and a higher θ_{T1W} for dynamic T_1-weighted acquisitions. If their respective flip angles sum up to 90°, i.e.

$$\theta_{T_1W} + \theta_{PDW} = 90^{\circ} \tag{2.14}$$

then the expected ratio of the T_1-weighted signal, S_A, to the proton density weighted signal, S_B, is:

$$\frac{S_A}{S_B} = \tan\theta \frac{\left(1 - exp(-TR_A/T_1)\right)}{\left(1 - exp(-TR_B/T_1)\right)} \frac{\left(1 - \sin\theta\, exp(-TR_B/T_1)\right)}{(1 - \cos\theta\, exp(-TR_A/T_1))} \tag{2.15}$$

where $\theta = \theta_{T_1W}$, TR_A is the repetition time of the T_1-weighted sequence and TR_B is that for the proton density weighted sequence. As the proton density – weighted image is only recorded once, the temporal resolution of the T_1 measurement in the dynamic study is the time taken to acquire one T_1-weighted image (86).

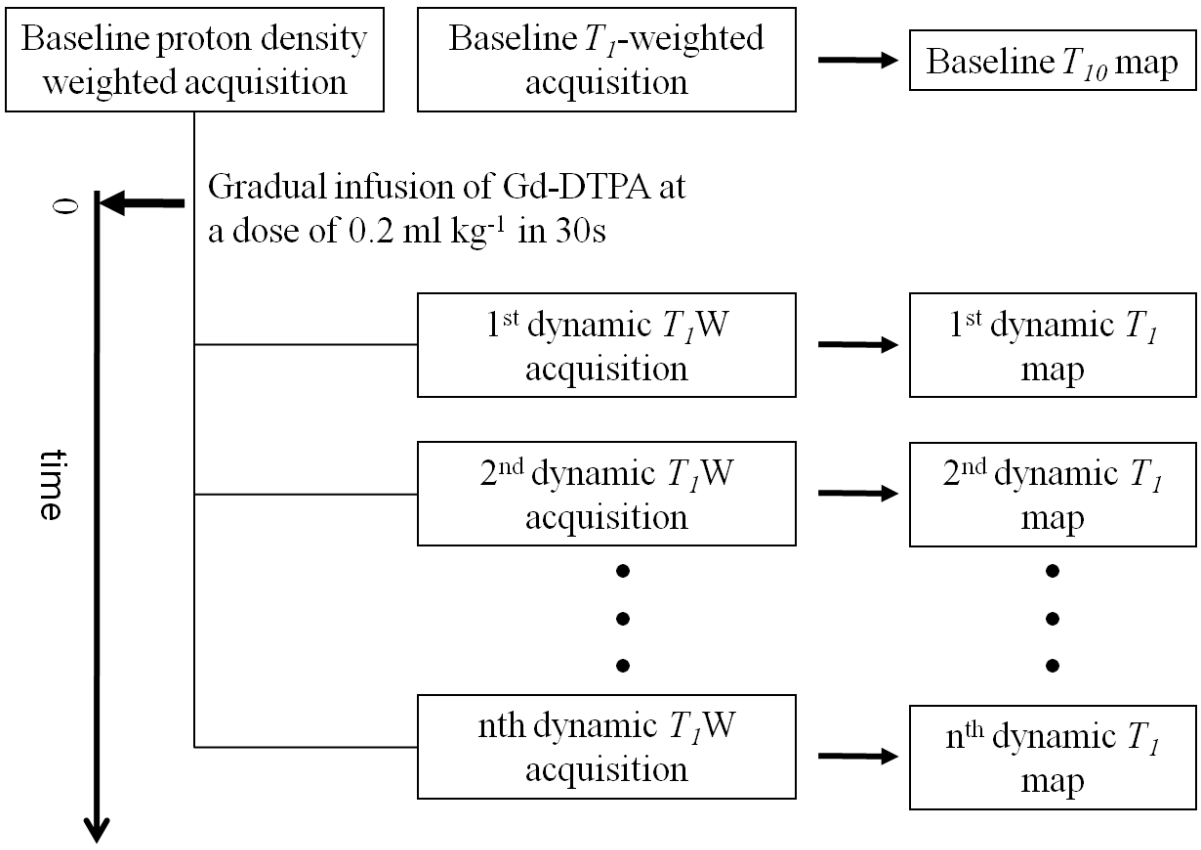

Figure 2.4: Schematic of a typical DCE-MRI acquisition protocol. T_1 maps at each time-point are calculated by relating the signal intensity in the dynamic T_1-weighted series to the baseline PD-weighted data set, which is acquired prior to infusion of contrast agent.

2.5 Rapid Localization of the Mouse Pancreas with MRI

The delineation of the mouse pancreas is not a trivial task because it is a very thin piece of tissue (~1 mm) that is spread out between the spleen, stomach and kidney. There is no single oblique slice that could capture the whole pancreas in an MR image because of its dispersed distribution across the abdomen. After some trial and error attempts, I established an imaging protocol for quick localization of the mouse pancreas and identification of an optimal slice for quantification. Initially, multiple coronal slices (using rapid T_1W- gradient echo imaging) are taken along the abdomen to locate the stomach and spleen, which act as landmarks. The

tail of the pancreas is closely adjacent to the spleen and stomach. The spleen appears as a triangular shape structure in coronal view, as shown in Figure 2.5a; the stomach is an oval structure with a low signal lumen, continuing to the right into the duodenum and lying adjacent to the right lobe of the liver. The pancreas tail is usually situated distal to the stomach, medial to and partly covering the spleen and also the upper pole of the left kidney, filling a triangular-shaped space between the stomach, kidney and spleen. Following the tail of the pancreas to the right allows easy delineation of the pancreas body, which lies immediately adjacent to the duodenum. In order to identify the pancreatic structures it is crucial to obtain thin adjacent slices of 1 mm or less in thickness without any gap between them, in order to allow the differentiation of the pancreatic tissue from adjacent gut structures (101). The next step is to acquire oblique slices that cover a major area of the pancreas with T_2-weighted MRI as shown in Figure 2.5b. The pancreas (bordered in red) can then be distinguished from other abdominal structures. The stringent requirement of thin slices demands high gradient strengths, which are usually available only in preclinical MRI scanners. Fortunately the scanner in our facility is a 9.4 T small animal system with a gradient strength of 40 gauss cm^{-1} at a rise time of 130 μs and has the capability to perform a minimum slice thickness of 0.25 mm in routine scans.

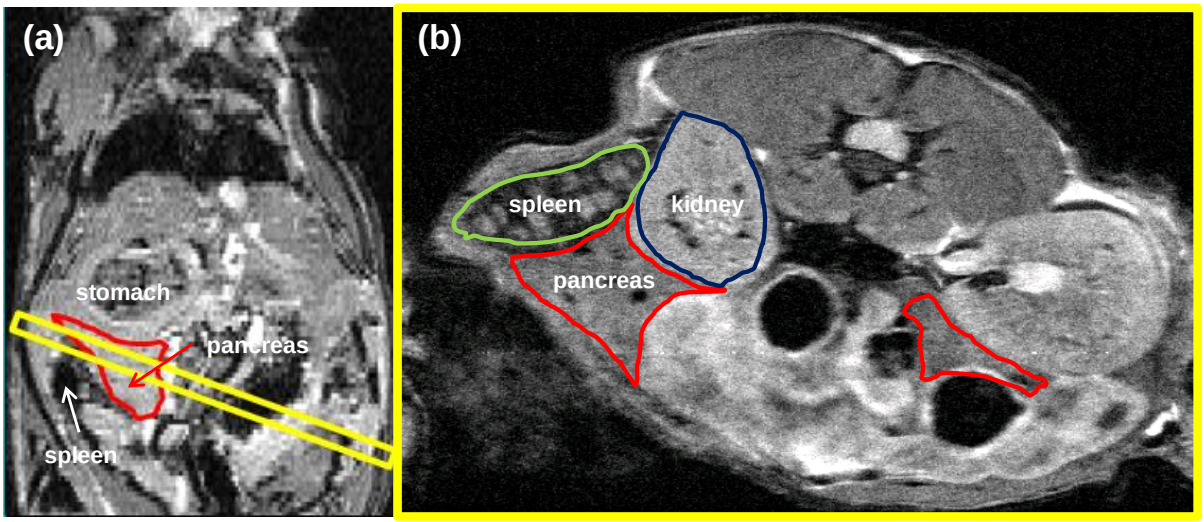

Figure 2.5: A quick method to locate the pancreas in less than 2 minutes: (a) Fast gradient-echo images in the coronal direction with 5 averages and no respiratory gating. (b) A T_2-weighted oblique slice below the stomach and across the spleen provides a lucid view of the pancreas. This slice orientation is subsequently applied in T_1-weighted dynamic MRI. Both images are thin 0.5mm slices with an in-plane spatial resolution of approximately 150x150μm^2 and 75 x 75μm^2 respectively.

2.6 Semi-Qualitative DCE-MRI Perfusion Study in a STAT3 Knockout Mouse with a Blood Pool Contrast Agent (MS-325)

2.6.1 Signal transducers and activators of transcription (STAT3) Knockout Mouse

Signal transducers and activators of transcription (STAT) proteins are a family of latent cytoplasmic transcription factors that are produced in many cell types and that are activated by tyrosine phosphorylation and dimerization in response to a wide variety of extracellular ligands, such as cytokines and growth factors (102). STAT3 in particular is a ubiquitous transcription factor that is indispensible during early embryogenesis and is one of the potential mediators for multiple growth factors acting on the pancreatic β-cells, including

hepatocyte growth factor, betacellulin and heparin-blinding EGF-like growth factor. STAT3 plays an important role in β-cell insulin secretion, maintaining normal islet morphology and glucose tolerance (103). When the STAT3 gene is disrupted in mice β-cells, islet architecture is impaired together with a 45% reduction of vascular endothelial growth factor (VEGF) expression (104). One in particular is VEGF-A, which induces capillary networks in the pancreatic islet that are essential for optimized blood glucose regulation (105,106). Originally discovered as a vascular permeability factor (107), VEGF-A induces vessel fenestration that increases vascular permeability and regulates the transport of solutes across to the extracellular space (108). Its importance becomes apparent when we consider the formation of the pancreatic islet, which occurs in two sequential steps: the first step involves the signaling from blood vessel endothelium to induce islet formation adjacent to the vessels. In the second step, the newly formed islets reciprocally signal to the adjacent endothelial cells, via VEGF-A, to induce formation of a dense network of fenestrated capillaries (109). Mice with disrupted VEGF-A gene specifically in beta cells has been shown to possess reduced islet vascular density with impaired formation of endothelial fenestration. With regard to β-cells function, their insulin release mechanism is impaired, resulting in glucose intolerance (110). Thus STAT3 regulation of VEGF-A is crucial in the development of microvascularization in the pancreatic islets and ultimately their glucose sensing ability. Furthermore, the observation that MRI kinetic parameters can detect suppression of vascular permeability after anti-VEGF antibody (111) and after the administration of inhibitors of VEGF signaling (112) lends weight to the important role of VEGF in determining MRI enhancement. We therefore expect to detect differences in signal enhancement between the wild-type and STAT3 knockout mice.

2.6.2 Materials and Methods

Intravascular Contrast Agent for Semi-quantitative DCE-MRI

In this section, I used a blood pool agent MS-325 (gadofosveset trisodium, Vasovist®), which is the first gadolinium-based blood pool MR agent to be approved by the FDA for clinical use, to probe the microenvironment of the pancreas. When intravenously injected into the blood circulation, the low molecular weight contrast agent binds strongly but reversibly with serum albumin in the plasma to result in a 90 kDa macromolecule. Protein binding reduces extravasation of the chelates from the vasculature, leading to an increased plasma half-life of 2-3h (113). In addition, Vasovist® is a negatively charged hydrophilic compound which makes it unlikely to diffuse across the lipid bilayer of cell membranes. Thus even if it diffuses across the epithelium, it would most likely remain in the extracellular space. The reduced tumbling rate of albumin-bound MS-325 also enables large r_1 relaxivity, providing superior positive contrast in MR angiography studies (114-117).

DCE-MRI of STAT3 Knockout and Wild-type Mice

Wild-type and STAT3 knockout phenotype mice were anaesthetized with 1.5% isoflurane and ventilated with 1 L min^{-1} of air/oxygen mixture, in accordance with local IACUC. MRI with respiratory monitoring was conducted in a 9.4T preclinical Varian scanner. Localization of the pancreas was accomplished by multi-slice gradient echo imaging to locate the spleen, and then followed by a T_2-weighted fast-spin-echo sequence to identify the pancreas, a procedure mentioned in section 2.5. Once a suitable slice of the pancreas is found, a dynamic T_1-weighted fast spin-echo pulse (FSE) sequence is applied in the semi-quantitative investigation of contrast agent pharmacokinetics. Echo-train length was 8, giving a temporal

resolution of 12 seconds per image. Critical MR parameters were: TR = 0.81 s, TE = 11.8 ms, Matrix = 128 x 128, FOV = 23 x 16 mm, slice thickness = 0.5 mm, spatial resolution = 180 x 125 μm^2. A 10 ul (0.1 mmol kg^{-1}) bolus volume of Vasovist® was injected intravenously within 10 s, via a catheter inserted into the tail vein, after 3 mins of baseline scan.

2.6.3 Results and Discussion

Figure 2.6 displays the baseline image at time t = 0, defined as the instant of tracer delivery, and the dynamic image at t = 30 min in the wild-type mouse. Notice the considerable signal reduction in the kidney. Its signal intensity curve, which is derived from the mean intensity at the drawn region-of-interest (ROI), illustrates the excretion of MS-325 upon infusion. Because MS-325 is only 80% reversibly bound to albumin in rodents compared to 95% in humans (118), a significant unbound portion (with molecular weight of only 957 Da) is present in the blood plasma and that is rapidly cleared by the renal system. Signal attenuation with time is seen instead of enhancement due to the high concentration of unbound MS-325 in the kidney, resulting in a dominant T_2-shortening effect.

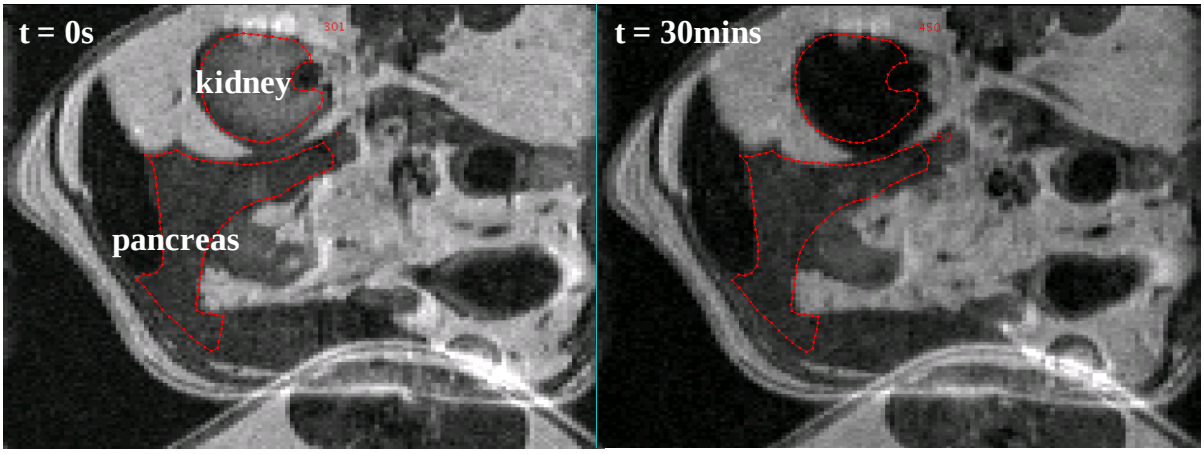

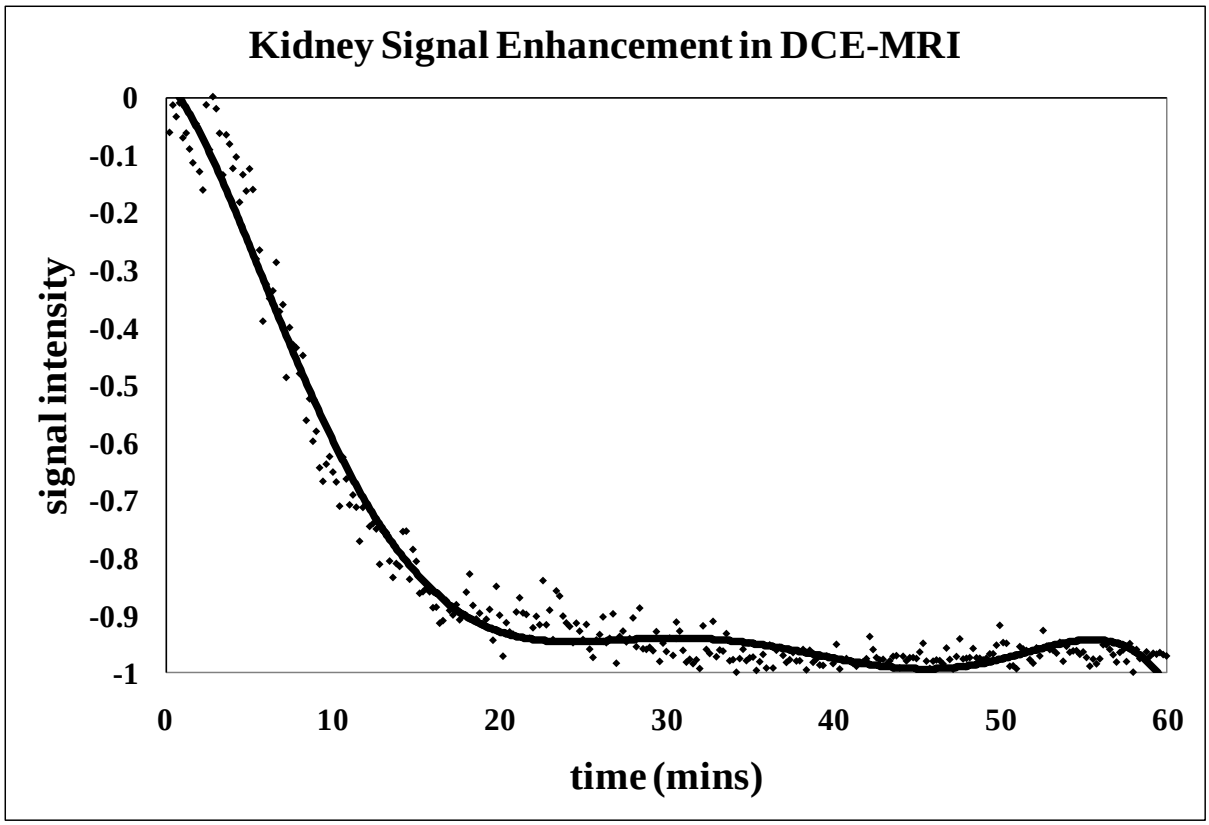

Figure 2.6: T_1-weighted DCE-MRI images at time t = 0 min (beginning of MS-325 intravenous injection) and at t = 30 min. Hypointensed kidney is caused by the clearance of unbound tracer molecules. Excretion in the kidney serves as an indicator of successful infusion via the mouse tail-vein.

Figure 2.7 illustrates the relative signal enhancement at the pancreas in the wild-type and STAT3 knockout mice. Their semi-quantitative parameters are summarized in Table 2.2. The onset time occurs 6 times earlier in the STAT3-deficient mouse which might be attributed to lower capillary blood flow, a less developed capillary network, or reduced endothelial membrane permeability. The uptake and wash-out gradients are also much reduced, corroborating the hypothesis on impaired capillary fenestration. The maximum enhancement phase is significantly longer, which we attribute to the saturation of the EES with tracer molecules and their slow outflux. Maximum intensity is approximately equal in both

phenotypes, which indicates unchanged interstitial volume. This is consistent with the finding that β-cell mass is comparable between mutant and control mice (104).

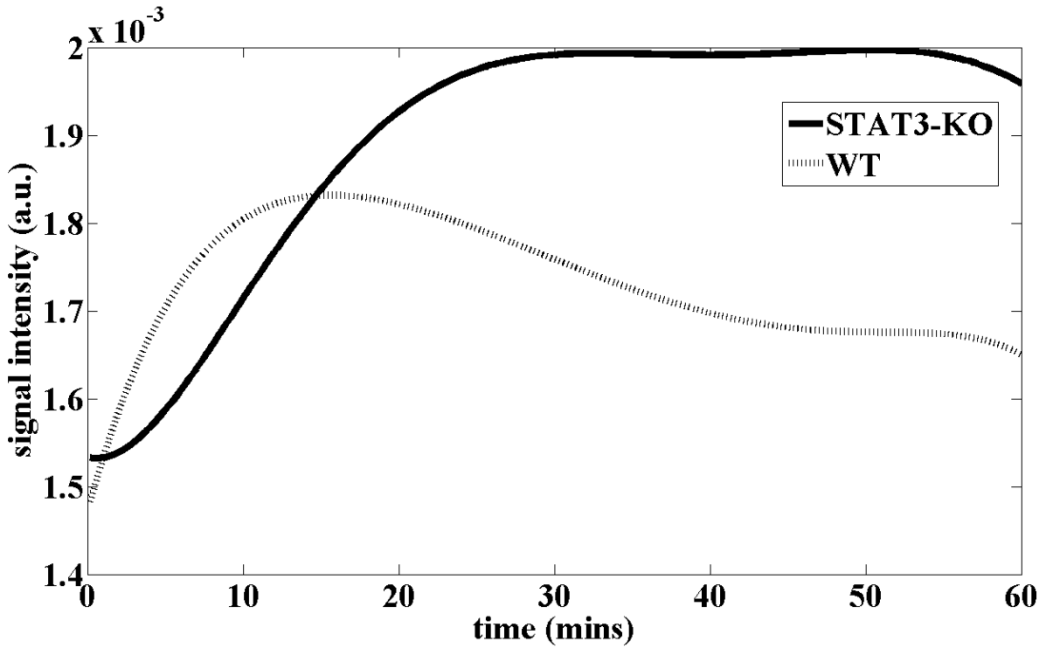

Figure 2.7: Signal intensity curve comparing tracer uptake between control and STAT3 knock-out mice.

Semi-quantitative parameter	Wild-type	Stat3 knockout
Onset time (mins)	0.8	4.7
Time-to-maximum intensity (mins)	15	30
Max. signal intensity	0.0018	0.002
Duration of max. enhancement phase (mins)	13	35
Initial gradient	5.88E-05	2.05E-05
Mean gradient	3.40E-05	2.12E-05
Washout gradient	-4.05E-06	-1.35E-06
IAUGC	0.0259	0.058

Table 2.2: Semi-quantitative parameters used in the comparison of MS-325 pharmacokinetics between wild-type mouse and the conditional STAT3-knockout phenotype

Although semi-quantitative analysis offers a convenient and often reliable gauge in pathodiagnosis, the biological relevance behind the parameters is not clearly defined. Absolute or relative changes in the semi-quantitative parameters can neither be directly translated into physiological properties nor interpreted as occurrence of specific biological events. For example, it has been initially suggested that IAUGC is related to blood flow, vascular permeability and the fraction of interstitial space, but there was no qualification of that relationship (99). Subsequently Walker et al. showed, via pharmacokinetic simulations, that IAUGC is actually a mixed parameter that is correlated with K^{trans}, v_p and v_e and it has an intractable relationship with all three (119). Therefore, quantification of these pharmacokinetic parameters is necessary to truly characterize the underlying pathological mechanism as well as isolate noise caused by intra- and inter-subject variability.

2.6.4 Conclusion

The slow uptake, prolonged enhancement and retarded tracer washout could perhaps serve as a biomarker of arrested microvessel development in the pancreatic islets, and measure the degree of debilitation in microvascular perfusion. Semi-quantitative DCE-MRI permits an easy and convenient method to compare hemodynamics in small animal models.

2.7 Quantitative Pancreatic Blood Flow Measurement with DCE-MRI

Using the modified Tofts-Kermode model illustrated in section 2.4.6, we aim to quantify the blood flow in a mouse pancreas with a clinical low molecular weight contrast agent Gadobutrol (also known as Gadovist®, relaxivity r1 = 3.9 $mM^{-1}s^{-1}$ at 9.4 T).

2.7.1 Materials and Methods

Animal Preparation

The wild-type mice (n = 2) were anaesthetized with 1.5% Isoflurane and ventilated with a mixture of medical air and oxygen at a flow rate of 1 L min^{-1}. A proton-density weighted baseline image was first acquired with the following settings with a normal spoiled gradient-echo sequence: TR = 500 ms, TE = 1.9ms, Matrix = 192 x 192, FOV = 30 x 30mm^2, slice thickness = 0.5 mm, in-plane resolution = 156 × 156 μm^2, number of averages = 3, θ_{PDW} = 20° and no respiratory gating was applied.

DCE-MRI

At the beginning of the dynamic T_1-weighted scan with the Snapshot FLASH sequence, approximately 3 min of baseline scan was acquired followed by a 10 µl (0.1 mmol kg^{-1}) intravenous injection of Gadovist® into the tail-vein in under a minute. Successful infusion is immediately known from the almost instantaneous signal decay in the kidney. Scan parameters for the dynamic T_1-weighted MRI were: TR = 10 ms, TE = 1.9 ms, Matrix = 192 × 192, FOV = 30 x 30 mm^2, slice thickness = 0.5 mm, in-plane resolution = 156 x 156 μm^2, number of averages = 3, θ_{T1W} = 70°, temporal resolution = 9 s, number of dynamic scans =

300 and no respiratory gating was applied. The mean intensities of the respective ROIs at the abdominal aorta and pancreas were used in the model fit.

Pharmacokinetics Modeling

The pharmacokinetics quantification process began with the estimation of dynamic T_1 values in the pancreas and aorta using eqn. (2.15). Then the concentrations of the contrast agent in these respective compartments are derived from the T_1 values using eqn. (2.12). Step three involves the estimation of the arterial input function according to a bi-exponential model similar to eqn. (2.11). Inputs into the AIF model consist of ROI mean intensity of the aorta, dosage D (0.1mmol/kg) and acquisition time t. The calculated AIF is then fitted into the *TK* model to yield K^{trans}, v_p and v_e. Assuming the perfusion situation is flow-limited, i.e. $PS >> F$, pancreatic blood flow can be extracted according to eqn. (2.2).

2.7.2 Results and Discussion

Figure 2.8 displays the *PD*-weighted image and a dynamic T_1-weighted image with the pancreas and abdominal aorta delineated for region-of-interest (ROI) analysis. The fitted arterial input function $C_p(t)$ is displayed in Figure 2.9a. Our quantitative treatment results in a pancreatic blood flow of approximately 0.465ml/min/g, which is almost equivalent to the value of 0.54ml/min/g obtained by Carlsson et al., who used the microspheres injection technique (35). Unfortunately, we cannot verify the authenticity of v_p and v_e because of the absence of literature regarding quantitative MRI perfusion studies in the mouse pancreas. Although Hathout et al. evaluated the in-vivo dynamic contrast enhancement time-course of transplanted islets in mice and claimed they could quantify changes in vascularization; their

study was in fact only semi-quantitative and they merely used IAUGC and tissue concentration C_t as biomarkers of angiogenesis (120), without further pharmacokinetics quantification. Nonetheless, the pharmacokinetic values measured in the pancreas of other mammals could serve as a guide. Yu et al. assessed the pancreatic microcirculation in type-2 diabetic patients and healthy controls with DCE-MRI and observed a significant difference between their fractional interstitial space v_e (0.141 vs 0.103) (121); the latter being similar to our measured value of 0.101 in the mice. In addition, Bolender carried out a detailed morphological analysis of the guinea pig pancreas and found the fractional volume of the EES (which he called extra-exocrinocytic spaces) to be 0.0838 (122), again quite similar to our value. It is to be noted though that DCE-MRI measures total tracer concentration including that in the islets, acinar tissue and blood vessels. Thus the blood flow obtained in the pharmacokinetic modeling is a wholesome perfusion measurement of the pancreas. Although the pancreatic islets form only 1-2% of pancreatic mass, they receive 10-20% of total pancreatic blood supply; therefore we believe that abnormalities in microvascular development of the pancreatic islets should be sufficiently captured in such quantitative perfusion measurement. The ability to characterize microcirculation in the mouse pancreas is an invaluable asset that could be exploited to investigate alterations in microvasculature in the endocrine (e.g. insulitis) or in the exocrine systems (e.g. pancreatitis). An application could be the investigation of angiogenesis induced by pancreatic islet transplantation. An adequate revascularization is crucial for islet survival and function after transplantation which implicates islet graft metabolism and insulin secretion (123). It has been suggested that vascular density is dramatically reduced in grafted islets in mice and the reduced blood flow could potentially undermine the transplantation success (124). DCE-MRI possesses the capability to probe this physiological property in-vivo and in real-time, and might enable

longitudinal monitoring of vascular development, improve islet delivery strategies and optimize the transplantation procedure.

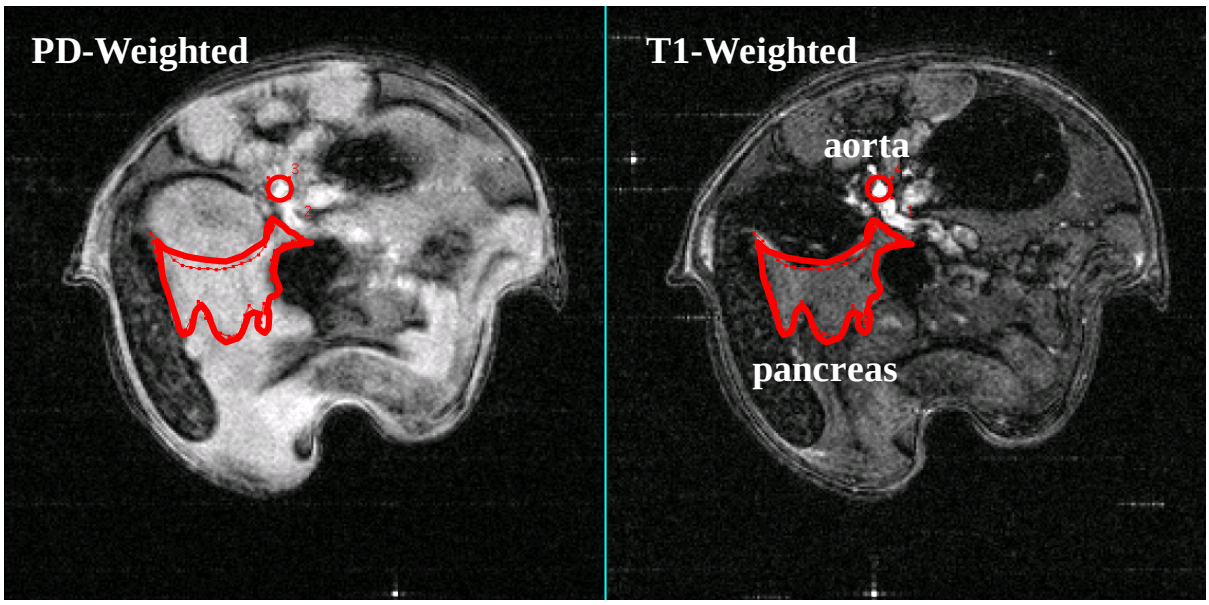

Figure 2.8: Baseline proton-density weighted and dynamic T_1-weighted MRI images acquired in the quantitative DCE-MRI of the mouse pancreas.

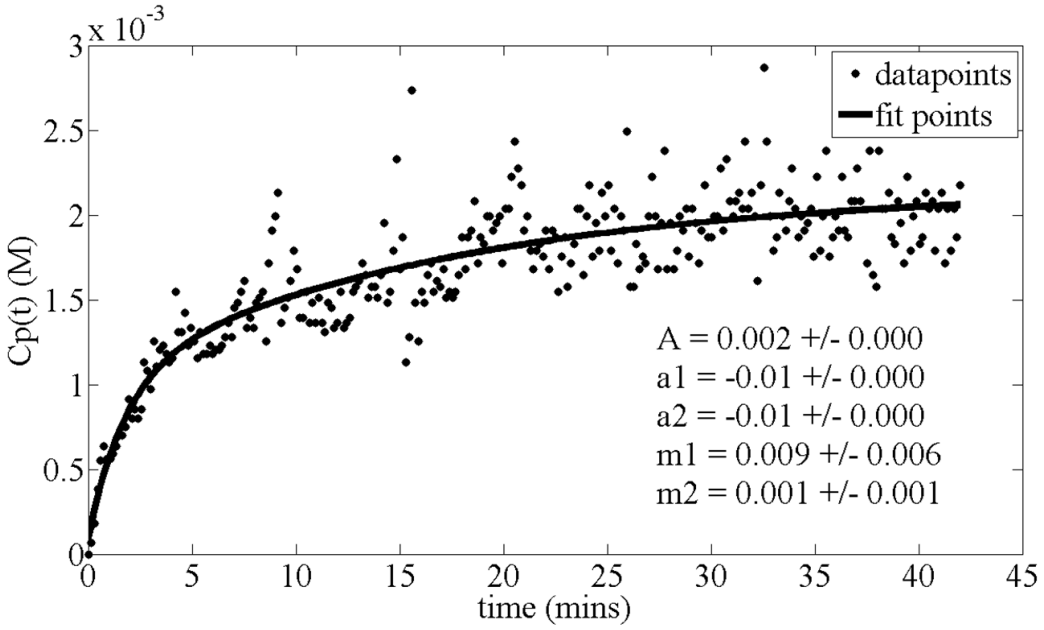

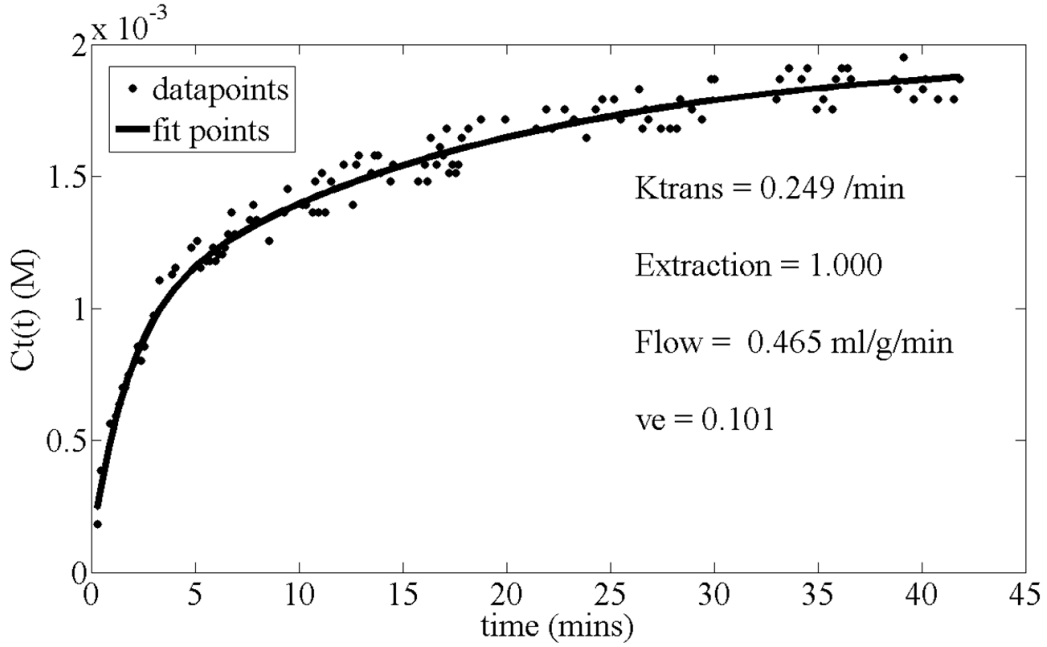

Figure 2.9: (a) Dynamic contrast agent concentration in the blood plasma (arterial input function), fitted into a bi-exponential model according to eqn. (3.11). (b) Quantified pharmacokinetic parameters, blood flow F, v_p and v_e in the mouse pancreas.

2.7.3 Conclusion

I have demonstrated the capability of T_1-weighted DCE-MRI to quantify important physiological information such as blood flow and fractional interstitial volume in the mouse pancreas, in which there was no precedence. Technical challenges in pancreas localization and rapid T_1-weighted imaging to capture mouse hemodynamics were overcome. This technology enables future studies in pancreatic vascular development and perhaps serves as an indirect biomarker of glucose response.

2.8 Limitations in Dual Compartment Model, Mouse Pancreas MRI and T_1 Estimation

In this work, I have made quite a few assumptions in order to quantify the contrast agent pharmacokinetics and characterize microvasculature in the mouse pancreas including representation of microenvironment with a two-compartment model, uniform tracer distribution in the blood plasma, negligible echo-time, perfectly spoiled gradient-echo signal, negligible motion and insignificant effect of anesthesia on perfusion. Actual experimental conditions deviate from ideality and reduce precision of quantified parameters. Challenges in DCE-MRI include selection of an appropriate kinetic model, optimal choice of imaging protocol for high accuracy in real-time T_1 quantification, precision of measurements and relevance to physiology. In this section, I discuss the impact of aberrations and suggest methods to ameliorate their detrimental effects.

2.8.1 Dual-Compartment Model

The tissue voxel scenario adopted in the estimation of the pharmacokinetic parameters is an oversimplified two-compartment model (i.e., pancreatic interstitium and blood plasma only). In reality, contrast agent molecules are delivered throughout the body via the circulation system, resulting in tracer diffusion into the extracellular space of multiple organs. A more comprehensive model that could be used is displayed in Figure 2.10 below, which includes clearance from kidney and loss of tracer into non-pancreatic EES (96). In addition, contrast agent pharmacokinetic is complex in pathological tissues due to morphological changes and a more comprehensive multi-compartment model would be essential for improved physiological interpretation (125). For example, contrast agent molecules might permeate into necrotic β-cells, be captured in the interstitial space due to protein binding or phagocytized by macrophages (126), resulting in an overestimation of v_e. I adopted the

modified TK model in this work to account for the impact of tracer concentration in the blood plasma in T_1 relaxation. However this model assumes that the tracer is well-mixed with uniform biodistribution in each of the compartments it occupies, which could result in consistent underestimation of v_p and overestimation of K^{trans} (127). To overcome this fallacy, St Lawrence and Lee (127,128) adapted the *tissue homogeneity model (TH)* introduced by Johnson and Wilson (129), via an adiabatic approximation, and defined the plasma tracer concentration as a function that varies along the capillary length and time, i. e. $C_p = C_p(x,t)$. This model allows the assessment of blood flow and extraction simultaneously. Although the *TK, modified TK* and *TH* models have been adopted for use in the clinical assessment of blood flow and characterization of microvasculature, it must be noted that they are still only simple models that attempt to correlate pharmacokinetic quantities to the complex physiology. Thus the interpretation is flawed to some extent. For example, flow heterogeneity is not considered in the models at all (130). Flow heterogeneity differs between regions and individuals and may not remain constant, as assumed in this study, but could change as a function of pathology (131). Additionally, the fitted kinetic parameters are estimates that depend on the fitting algorithm and imposed conditions (e.g., initial guesses in the fitting routine). It is important to address these uncertainties because it is only after the model parameters have been accurately estimated that the diagnostic or prognostic efficacy of specific quantitative physiological parameters can be properly tested (132).

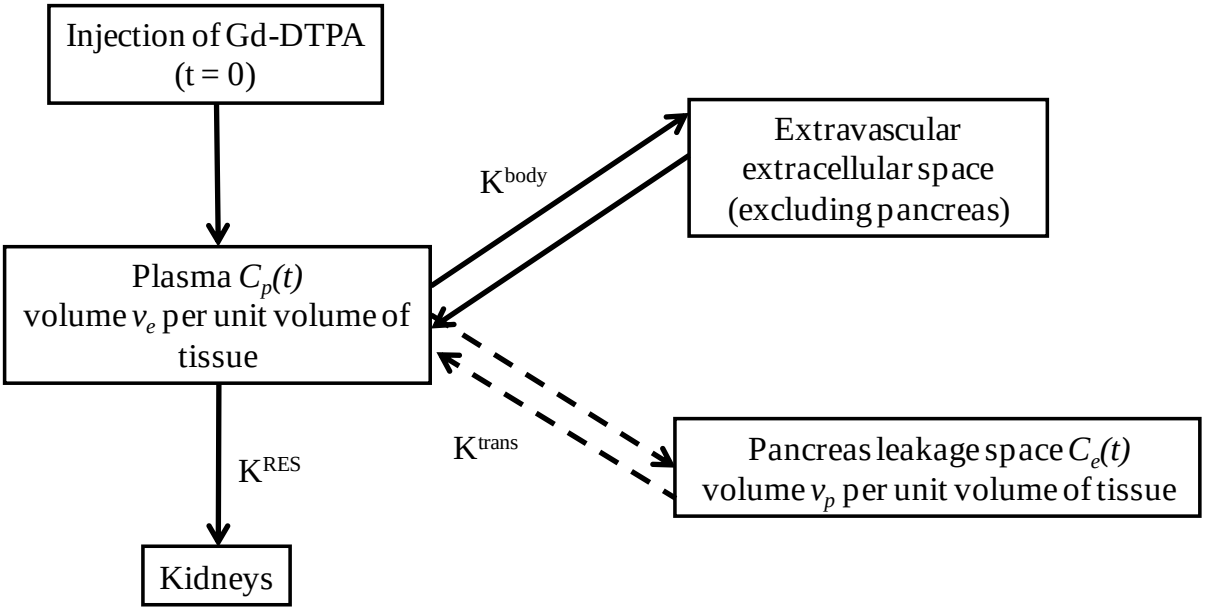

Figure 2.10: Compartmental model of DTPA tracer distribution. The conventional compartments (plasma, whole-body extracellular space and kidneys) are represented with solid lines. The leakage into the pancreas extravascular extracellular space is drawn with dotted lines. Leakage rate constants K^{RES} and K^{body} characterize tracer excretion in the kidneys and influx into the EES at rest of body respectively.

2.8.2 Sensitivity to Contrast Agent Concentration and Precision in T1 measurements

Sensitivity to contrast agent concentration in real-time is very dependent on the accuracy of the dynamic T_1 quantification. A compromise between precision, spatial resolution and imaging speed is essential. In this thesis we have adopted the rapid Snapshot FLASH sequence for dynamic measurements in order to acquire the arterial input function with sufficient temporal resolution. However, this technique tends to underestimate T_1 values at very short repetition times and its accuracy deteriorates with shorter *TR*. A calibration factor or full analysis of signal evolution would be necessary to rectify the discrepancies (133,134). Additionally, the requirement for very thin slices of approximately 0.5 mm in the pancreas

stresses the uniformity of the RF field. Imperfection in the transmitted B_1 field causes flip angle inhomogeneity within the slice and leads to significant deviations in calculated T_1 values from the true values (135). Parker et al. proposed a methodology which explicitly corrected for the shape of the RF pulse and for spatial variations in transmitted RF field intensity. Including these factors in the derivation of T_1 gives a substantial improvement in accuracy and precision of T_1 measurements in the presence of RF non-uniformity and non-ideal pulse profiles (136). The thin slices also increase the risk of motion artifacts, exacerbated by the respiratory motion at the abdomen, as well as elevate partial volume effects. Respiratory-gated acquisition and motion correction could partially alleviate these artifacts (137-139). Alternatively, 3D acquisition could be utilized with an added advantage of augmented SNR (140).

The requirements for high temporal resolution are related to the studied pathology and the adopted pharmacokinetics model. A high temporal resolution is required for DCE-MRI in many conditions, especially for bolus tracking in tissues with leaky vasculature. Simulations have suggested that the arterial input function would have to be sampled every second in order to limit errors in model parameters within 10% (141). Although Snapshot FLASH offers imaging speed, its signal-to-noise ratio is a fraction $1/\sqrt{2}$ of spin-echo techniques (142). The low SNR characteristic of ultrafast gradient-echo techniques poses a challenge in fitting the noisy data to the model and handicaps the accuracy of kinetic parameters. Alternatively, spin-echo approaches for rapid T_1 measurements such as EPI–based sequences like Look-Locker (143,144) possess the advantage of acquiring entire T_1 measurements at every time point within the series with high SNR. Thus the appropriate imaging sequence has to be adopted for improved sensitivity to the investigated vasculature.

Another factor that could corrupt T_1 measurement is the application of user-defined regions-of-interest (ROI) analysis. ROI methods yield enhancement curves with good SNR, but lack the spatial resolution and are prone to partial volume averaging errors. Furthermore, the placements of ROI vary between users and that could incur inconsistencies on the outcome of the analysis. ROI analysis could also be detrimental because heterogeneous regions of enhancement might actually be indicating changes in microvessel density, VEGF expression or highlighting pathological processes like necrosis (145,146). Selecting an ROI would then average these events and mask their significance. To minimize errors incurred with ROI analysis, Evelhoch et al. has recommended a DCE-MRI protocol for accurate T_1 measurements (99). Alternatively, pixel mapping of pharmacokinetic parameters could be adopted to depict quantitative enhancement information exactly co-registered with anatomic images on a pixel-by-pixel basis. In this manner, information pertaining to tissue heterogeneity is completely preserved and the need for ROI placement is eliminated (54,147).

We have assumed that the echo-time is negligible compared to the T_2^* attenuation effect on the MRI signal (i.e. $TE << T_2^*(t)$). As illustrated in the previous chapter, all exogenous contrast agents exert both longitudinal and transverse relaxation effects. The ratio r_1/r_2 usually decreases with magnetic field strength, and thus spin-spin relaxation influence is augmented and cannot be ignored, especially in the preclinical environment. This signifies a necessity to include the signal decay factor $e^{-TE\cdot\left(\frac{1}{T_2^*(t)}-\frac{1}{T_{20}^*}\right)}$ into eqn. (2.15), where $T_2^*(t)$ is the changing transverse relaxation time during the dynamic scans and T_{20}^* is that at baseline. Thus there is a need for a pulse sequence that could measure the T_2^* simultaneously with T_1.

Heilmann et al. accomplished this feat by combining a saturation recovery turbo-FLASH technique with a multiple gradient-echo sequence and using it for AIF assessment (63,148).

2.8.3 Physiological Relevance and Validation of DCE-MRI Parameters

Semi-quantitative analysis of signal enhancement provides a convenient and easy method to compare between physiological states and hints at the pathogenesis. However, it is important to realize that semi-quantitative diagnostic criteria cannot be simply transferred across imaging centers. The extracted parameters are profoundly affected by experimental conditions such as dosage, pulse sequences used, scanner field strength, acquisition parameters etc. Quantification techniques aim to minimize such variability and allow comparison between patients and between different imaging centers. Besides, quantification derives kinetic parameters that are based on physiological processes and thus can provide insights into tissue biology (80). Validation is an important step in establishing the authenticity of derived pharmacokinetic parameters and confirming their relevance to the underlying physiology. Although our hypothesis of impaired vascular development in STAT3-deficient mice appeared to agree with the semi-quantitative results, no histological validation on the islet morphology was performed. Available methods to validate DCE-MRI measurements in blood flow and capillary permeability include fluorescent microsphere technique (149,150), autoradiography (151) and the use of radio-labeled probes (152).

Besides validating kinetic parameters obtained with DCE-MRI, there is also a need to verify their relationship to glucose sensing in the pancreas. We could perhaps reference this by looking at blood flow in other tissue types. In healthy patients, insulin-mediated increases in

skeletal muscle blood flow leads to increased glucose uptake. But this mechanism is defective in insulin-resistant patients. It has been proposed that constitutive reductions in capillary density or insufficient blood flow alters insulin and glucose delivery into muscles, causing insulin resistance (153). Thus reduced perfusion might act as a biomarker of insulin-resistance. There is also a need to distinguish the hemodynamics between species with respect to insulin secretion. In the perfused rat pancreas, insulin secretion upon glucose infusion appears to occur in two distinct phases - an early, or rapid, release of insulin which subsided within approximately 2 min, followed by a late or slow release phase which continually increased in rate until termination of the glucose infusion (154). Mice seem to have a different insulin release dynamics characterized by a constant 2^{nd} phase (155). Thus their hemodynamic responses to glucose might differ.

2.9 Chapter Conclusion

In this chapter, I have showcased the possibility of non-invasive in-vivo measurement of pancreatic blood flow with DCE-MRI. Semi-quantitative kinetic parameters facilitate a convenient means of comparison between contrast enhancements in wild-type and STAT3-deficient mice. The derived quantities appear to corroborate with the impaired fenestration of capillaries in the latter phenotype, giving reduced uptake and slower clearance. Quantitative pharmacokinetic parameters were derived from a modified Toft-Kermode model that compartmentalized the plasma and extracellular spaces. With the AIF, which was estimated by a bi-exponential function, the dynamic contrast agent concentration in the extravascular extracellular and plasma spaces were fitted into the model to derive blood flow F. Although aberrations exist in the modeling and errors are incurred in the T_1 measurements, this is the first quantitative perfusion study to be implemented in mouse pancreas as far as I know, and

this technique possesses potential as a biomarker to probe insulin secretion and glucose homeostasis.

2.10 References

1. Saltiel AR, Kahn CR. Insulin signalling and the regulation of glucose and lipid metabolism. Nature 2001;414(6865):799-806.
2. Alberti KG, Zimmet PZ. Definition, diagnosis and classification of diabetes mellitus and its complications. Part 1: diagnosis and classification of diabetes mellitus provisional report of a WHO consultation. Diabet Med 1998;15(7):539-553.
3. Kannel WB, McGee DL. Diabetes and cardiovascular disease. The Framingham study. JAMA 1979;241(19):2035-2038.
4. Luchsinger JA, Tang MX, Stern Y, Shea S, Mayeux R. Diabetes mellitus and risk of Alzheimer's disease and dementia with stroke in a multiethnic cohort. Am J Epidemiol 2001;154(7):635-641.
5. Perneger TV, Brancati FL, Whelton PK, Klag MJ. End-stage renal disease attributable to diabetes mellitus. Ann Intern Med 1994;121(12):912-918.
6. Linne Y. Effects of obesity on women's reproduction and complications during pregnancy. Obes Rev 2004;5(3):137-143.
7. National Diabetes Fact Sheet, American Diabetes Association, http://www.diabetes.org/diabetes-statistics/national-diabetes-factsheet.jsp. 2007.
8. Organisation WH. Genetics and Diabetes. Fact sheet 312 November 2009.
9. Brandle M, Zhou H, Smith BR, Marriott D, Burke R, Tabaei BP, Brown MB, Herman WH. The direct medical cost of type 2 diabetes. Diabetes Care 2003;26(8):2300-2304.
10. Kloppel G, Lohr M, Habich K, Oberholzer M, Heitz PU. Islet pathology and the pathogenesis of type 1 and type 2 diabetes mellitus revisited. Surv Synth Pathol Res 1985;4(2):110-125.
11. Bach JF. Insulin-dependent diabetes mellitus as an autoimmune disease. Endocr Rev 1994;15(4):516-542.
12. Mathis D, Vence L, Benoist C. beta-Cell death during progression to diabetes. Nature 2001;414(6865):792-798.
13. DeFronzo RA. Pharmacologic therapy for type 2 diabetes mellitus. Ann Intern Med 1999;131(4):281-303.
14. Ratner RE. Type 2 diabetes mellitus: the grand overview. Diabet Med 1998;15 Suppl 4:S4-7.
15. DeFronzo RA. Pathogenesis of type 2 diabetes mellitus. Med Clin North Am 2004;88(4):787-835, ix.
16. Edelman SV. Type II diabetes mellitus. Adv Intern Med 1998;43:449-500.
17. Pociot F, McDermott MF. Genetics of type 1 diabetes mellitus. Genes Immun 2002;3(5):235-249.
18. Kahn CR, Vicent D, Doria A. Genetics of non-insulin-dependent (type-II) diabetes mellitus. Annu Rev Med 1996;47:509-531.
19. Hu FB, Manson JE, Stampfer MJ, Colditz G, Liu S, Solomon CG, Willett WC. Diet, lifestyle, and the risk of type 2 diabetes mellitus in women. N Engl J Med 2001;345(11):790-797.
20. Neel JV. Diabetes mellitus: a "thrifty" genotype rendered detrimental by "progress"? Am J Hum Genet 1962;14:353-362.

21. Billotey C, Aspord C, Beuf O, Piaggio E, Gazeau F, Janier MF, Thivolet C. T-cell homing to the pancreas in autoimmune mouse models of diabetes: in vivo MR imaging. Radiology 2005;236(2):579-587.
22. Moore A, Grimm J, Han B, Santamaria P. Tracking the recruitment of diabetogenic CD8+ T-cells to the pancreas in real time. Diabetes 2004;53(6):1459-1466.
23. Pober JS, Cotran RS. The role of endothelial cells in inflammation. Transplantation 1990;50(4):537-544.
24. Hanninen A, Jalkanen S, Salmi M, Toikkanen S, Nikolakaros G, Simell O. Macrophages, T cell receptor usage, and endothelial cell activation in the pancreas at the onset of insulin-dependent diabetes mellitus. J Clin Invest 1992;90(5):1901-1910.
25. Hanninen A, Taylor C, Streeter PR, Stark LS, Sarte JM, Shizuru JA, Simell O, Michie SA. Vascular addressins are induced on islet vessels during insulitis in nonobese diabetic mice and are involved in lymphoid cell binding to islet endothelium. J Clin Invest 1993;92(5):2509-2515.
26. Faveeuw C, Gagnerault MC, Lepault F. Modifications of the expression of homing and adhesion molecules in infiltrated islets of Langerhans in NOD mice. Adv Exp Med Biol 1994;355:137-142.
27. De Paepe ME, Corriveau M, Tannous WN, Seemayer TA, Colle E. Increased vascular permeability in pancreas of diabetic rats: detection with high resolution protein A-gold cytochemistry. Diabetologia 1992;35(12):1118-1124.
28. Sandler S, Jansson L. Vascular permeability of pancreatic islets after administration of streptozotocin. Virchows Arch A Pathol Anat Histopathol 1985;407(4):359-367.
29. Olerud J, Johansson Å, Carlsson P-O. Vascular niche of pancreatic islets. Expert review of endocrinology and metabolism 2009;4(5):484-491.
30. Ballian N, Brunicardi FC. Islet vasculature as a regulator of endocrine pancreas function. World J Surg 2007;31(4):705-714.
31. Weir GC, Bonner-Weir S. Islets of Langerhans: the puzzle of intraislet interactions and their relevance to diabetes. J Clin Invest 1990;85(4):983-987.
32. Konstantinova I, Lammert E. Microvascular development: learning from pancreatic islets. Bioessays 2004;26(10):1069-1075.
33. Bonner-Weir S, Orci L. New perspectives on the microvasculature of the islets of Langerhans in the rat. Diabetes 1982;31(10):883-889.
34. Laughlin MR. Why Image the Pancreatic Beta Cell? Current medicinal chemistry Immunology, endocrine & metabolic agents 2004;4:251-252.
35. Carlsson PO, Andersson A, Jansson L. Pancreatic islet blood flow in normal and obese-hyperglycemic (ob/ob) mice. Am J Physiol 1996;271(6 Pt 1):E990-995.
36. Orci L, Unger RH. Functional subdivision of islets of Langerhans and possible role of D cells. Lancet 1975;2(7947):1243-1244.
37. Stefan Y, Orci L, Malaisse-Lagae F, Perrelet A, Patel Y, Unger RH. Quantitation of endocrine cell content in the pancreas of nondiabetic and diabetic humans. Diabetes 1982;31(8 Pt 1):694-700.
38. Rahier J, Goebbels RM, Henquin JC. Cellular composition of the human diabetic pancreas. Diabetologia 1983;24(5):366-371.
39. Lifson N, Kramlinger KG, Mayrand RR, Lender EJ. Blood flow to the rabbit pancreas with special reference to the islets of Langerhans. Gastroenterology 1980;79(3):466-473.
40. Lifson N, Lassa CV, Dixit PK. Relation between blood flow and morphology in islet organ of rat pancreas. Am J Physiol 1985;249(1 Pt 1):E43-48.
41. Tofts PS, Brix G, Buckley DL, Evelhoch JL, Henderson E, Knopp MV, Larsson HB, Lee TY, Mayr NA, Parker GJ, Port RE, Taylor J, Weisskoff RM. Estimating kinetic parameters from dynamic contrast-enhanced T(1)-weighted MRI of a diffusable tracer: standardized quantities and symbols. J Magn Reson Imaging 1999;10(3):223-232.

42. Tofts PS. Modeling tracer kinetics in dynamic Gd-DTPA MR imaging. J Magn Reson Imaging 1997;7(1):91-101.
43. Tofts PS. Optimal detection of blood-brain barrier defects with Gd-DTPA MRI-the influences of delayed imaging and optimised repetition time. Magn Reson Imaging 1996;14(4):373-380.
44. Tofts PS, Wicks DA, Barker GJ. The MRI measurement of NMR and physiological parameters in tissue to study disease process. Prog Clin Biol Res 1991;363:313-325.
45. Tofts PS, Kermode AG. Blood brain barrier permeability in multiple sclerosis using labelled DTPA with PET, CT and MRI. J Neurol Neurosurg Psychiatry 1989;52(8):1019-1020.
46. Padhani AR. Dynamic contrast-enhanced MRI in clinical oncology: current status and future directions. J Magn Reson Imaging 2002;16(4):407-422.
47. Choyke PL, Dwyer AJ, Knopp MV. Functional tumor imaging with dynamic contrast-enhanced magnetic resonance imaging. J Magn Reson Imaging 2003;17(5):509-520.
48. Leach MO, Brindle KM, Evelhoch JL, Griffiths JR, Horsman MR, Jackson A, Jayson GC, Judson IR, Knopp MV, Maxwell RJ, McIntyre D, Padhani AR, Price P, Rathbone R, Rustin GJ, Tofts PS, Tozer GM, Vennart W, Waterton JC, Williams SR, Workman P. The assessment of antiangiogenic and antivascular therapies in early-stage clinical trials using magnetic resonance imaging: issues and recommendations. Br J Cancer 2005;92(9):1599-1610.
49. Magnon C, Galaup A, Rouffiac V, Opolon P, Connault E, Rose M, Perricaudet M, Roche A, Germain S, Griscelli F, Lassau N. Dynamic assessment of antiangiogenic therapy by monitoring both tumoral vascularization and tissue degeneration. Gene Ther 2007;14(2):108-117.
50. Zwick S, Strecker R, Kiselev V, Gall P, Huppert J, Palmowski M, Lederle W, Woenne EC, Hengerer A, Taupitz M, Semmler W, Kiessling F. Assessment of vascular remodeling under antiangiogenic therapy using DCE-MRI and vessel size imaging. J Magn Reson Imaging 2009;29(5):1125-1133.
51. O'Connor JP, Jackson A, Parker GJ, Jayson GC. DCE-MRI biomarkers in the clinical evaluation of antiangiogenic and vascular disrupting agents. Br J Cancer 2007;96(2):189-195.
52. Maxwell RJ, Wilson J, Prise VE, Vojnovic B, Rustin GJ, Lodge MA, Tozer GM. Evaluation of the anti-vascular effects of combretastatin in rodent tumours by dynamic contrast enhanced MRI. NMR Biomed 2002;15(2):89-98.
53. Medarova Z, Castillo G, Dai G, Bolotin E, Bogdanov A, Moore A. Noninvasive magnetic resonance imaging of microvascular changes in type 1 diabetes. Diabetes 2007;56(11):2677-2682.
54. Harrer JU, Parker GJ, Haroon HA, Buckley DL, Embelton K, Roberts C, Baleriaux D, Jackson A. Comparative study of methods for determining vascular permeability and blood volume in human gliomas. J Magn Reson Imaging 2004;20(5):748-757.
55. Ludemann L, Grieger W, Wurm R, Wust P, Zimmer C. Glioma assessment using quantitative blood volume maps generated by T1-weighted dynamic contrast-enhanced magnetic resonance imaging: a receiver operating characteristic study. Acta Radiol 2006;47(3):303-310.
56. Palmowskia M, Schifferdeckerc I, Zwickd S, Macher-Goeppingere S, Lauef H, Haferkampg A, Kauczorc H-U, Kiessling F, Hallscheidtc P. Tumor perfusion assessed by dynamic contrast-enhanced MRI correlates to the grading of renal cell carcinoma: Initial results. European Journal of Radiology 2009;Article in Press.
57. Tuncbilek N, Karakas HM, Altaner S. Dynamic MRI in indirect estimation of microvessel density, histologic grade, and prognosis in colorectal adenocarcinomas. Abdom Imaging 2004;29(2):166-172.
58. Thomas DL, Lythgoe MF, Pell GS, Calamante F, Ordidge RJ. The measurement of diffusion and perfusion in biological systems using magnetic resonance imaging. Phys Med Biol 2000;45(8):R97-138.

59. Simonsen CZ, Ostergaard L, Smith DF, Vestergaard-Poulsen P, Gyldensted C. Comparison of gradient- and spin-echo imaging: CBF, CBV, and MTT measurements by bolus tracking. J Magn Reson Imaging 2000;12(3):411-416.
60. Zahra MA, Hollingsworth KG, Sala E, Lomas DJ, Tan LT. Dynamic contrast-enhanced MRI as a predictor of tumour response to radiotherapy. Lancet Oncol 2007;8(1):63-74.
61. Barbier EL, Lamalle L, Decorps M. Methodology of brain perfusion imaging. J Magn Reson Imaging 2001;13(4):496-520.
62. Rosen BR, Belliveau JW, Buchbinder BR, McKinstry RC, Porkka LM, Kennedy DN, Neuder MS, Fisel CR, Aronen HJ, Kwong KK, et al. Contrast agents and cerebral hemodynamics. Magn Reson Med 1991;19(2):285-292.
63. Heilmann M, Walczak C, Vautier J, Dimicoli JL, Thomas CD, Lupu M, Mispelter J, Volk A. Simultaneous dynamic T1 and T2* measurement for AIF assessment combined with DCE MRI in a mouse tumor model. MAGMA 2007;20(4):193-203.
64. Evelhoch JL. Key factors in the acquisition of contrast kinetic data for oncology. Journal of Magnetic Resonance Imaging 1999;10:254-259.
65. Schneider JE, Cassidy PJ, Lygate C, Tyler DJ, Wiesmann F, Grieve SM, Hulbert K, Clarke K, Neubauer S. Fast, high-resolution in vivo cine magnetic resonance imaging in normal and failing mouse hearts on a vertical 11.7 T system. J Magn Reson Imaging 2003;18(6):691-701.
66. Padhani AR. MRI for assessing antivascular cancer treatments. Br J Radiol 2003;76 Spec No 1:S60-80.
67. Cheng HL. Dynamic contrast-enhanced MRI in oncology drug development. Curr Clin Pharmacol 2007;2(2):111-122.
68. Padhani AR. MRI for assessing antivascular cancer treatments The British Journal of Radiology 2003;76:S60-S80.
69. Reddick WE, Taylor JS, Fletcher BD. Dynamic MR imaging (DEMRI) of microcirculation in bone sarcoma. J Magn Reson Imaging 1999;10(3):277-285.
70. Knopp MV, Weiss E, Sinn HP, Mattern J, Junkermann H, Radeleff J, Magener A, Brix G, Delorme S, Zuna I, van Kaick G. Pathophysiologic basis of contrast enhancement in breast tumors. J Magn Reson Imaging 1999;10(3):260-266.
71. Mayr NA, Hawighorst H, Yuh WT, Essig M, Magnotta VA, Knopp MV. MR microcirculation assessment in cervical cancer: correlations with histomorphological tumor markers and clinical outcome. J Magn Reson Imaging 1999;10(3):267-276.
72. Barentsz JO, Engelbrecht M, Jager GJ, Witjes JA, de LaRosette J, van Der Sanden BP, Huisman HJ, Heerschap A. Fast dynamic gadolinium-enhanced MR imaging of urinary bladder and prostate cancer. J Magn Reson Imaging 1999;10(3):295-304.
73. Hawighorst H, Libicher M, Knopp MV, Moehler T, Kauffmann GW, Kaick G. Evaluation of angiogenesis and perfusion of bone marrow lesions: role of semiquantitative and quantitative dynamic MRI. J Magn Reson Imaging 1999;10(3):286-294.
74. Kroft LJ, de Roos A. Blood pool contrast agents for cardiovascular MR imaging. J Magn Reson Imaging 1999;10(3):395-403.
75. Farace P, Merigo F, Fiorini S, Nicolato E, Tambalo S, Daducci A, Degrassi A, Sbarbati A, Rubello D, Marzola P. DCE-MRI using small-molecular and albumin-binding contrast agents in experimental carcinomas with different stromal content. Eur J Radiol 2009.
76. Wang SC, Wikstrom MG, White DL, Klaveness J, Holtz E, Rongved P, Moseley ME, Brasch RC. Evaluation of Gd-DTPA-labeled dextran as an intravascular MR contrast agent: imaging characteristics in normal rat tissues. Radiology 1990;175(2):483-488.
77. Schuhmann-Giampieri G, Schmitt-Willich H, Frenzel T, Press WR, Weinmann HJ. In vivo and in vitro evaluation of Gd-DTPA-polylysine as a macromolecular contrast agent for magnetic resonance imaging. Invest Radiol 1991;26(11):969-974.

78. Radjenovic A, Dall BJ, Ridgway JP, Smith MA. Measurement of pharmacokinetic parameters in histologically graded invasive breast tumours using dynamic contrast-enhanced MRI. Br J Radiol 2008;81(962):120-128.
79. Galbraith SM, Lodge MA, Taylor NJ, Rustin GJ, Bentzen S, Stirling JJ, Padhani AR. Reproducibility of dynamic contrast-enhanced MRI in human muscle and tumours: comparison of quantitative and semi-quantitative analysis. NMR Biomed 2002;15(2):132-142.
80. Padhani AR, Husband JE. Dynamic contrast-enhanced MRI studies in oncology with an emphasis on quantification, validation and human studies. Clin Radiol 2001;56(8):607-620.
81. Su MY, Cheung YC, Fruehauf JP, Yu H, Nalcioglu O, Mechetner E, Kyshtoobayeva A, Chen SC, Hsueh S, McLaren CE, Wan YL. Correlation of dynamic contrast enhancement MRI parameters with microvessel density and VEGF for assessment of angiogenesis in breast cancer. J Magn Reson Imaging 2003;18(4):467-477.
82. Morgan B, Thomas AL, Drevs J, Hennig J, Buchert M, Jivan A, Horsfield MA, Mross K, Ball HA, Lee L, Mietlowski W, Fuxuis S, Unger C, O'Byrne K, Henry A, Cherryman GR, Laurent D, Dugan M, Marme D, Steward WP. Dynamic contrast-enhanced magnetic resonance imaging as a biomarker for the pharmacological response of PTK787/ZK 222584, an inhibitor of the vascular endothelial growth factor receptor tyrosine kinases, in patients with advanced colorectal cancer and liver metastases: results from two phase I studies. J Clin Oncol 2003;21(21):3955-3964.
83. Kermode AG, Tofts PS, Thompson AJ, MacManus DG, Rudge P, Kendall BE, Kingsley DP, Moseley IF, du Boulay EP, McDonald WI. Heterogeneity of blood-brain barrier changes in multiple sclerosis: an MRI study with gadolinium-DTPA enhancement. Neurology 1990;40(2):229-235.
84. Larsson HB, Stubgaard M, Frederiksen JL, Jensen M, Henriksen O, Paulson OB. Quantitation of blood-brain barrier defect by magnetic resonance imaging and gadolinium-DTPA in patients with multiple sclerosis and brain tumors. Magn Reson Med 1990;16(1):117-131.
85. Brix G, Semmler W, Port R, Schad LR, Layer G, Lorenz WJ. Pharmacokinetic parameters in CNS Gd-DTPA enhanced MR imaging. J Comput Assist Tomogr 1991;15(4):621-628.
86. Parker GJ, Suckling J, Tanner SF, Padhani AR, Revell PB, Husband JE, Leach MO. Probing tumor microvascularity by measurement, analysis and display of contrast agent uptake kinetics. J Magn Reson Imaging 1997;7(3):564-574.
87. Krestin GP, Steinbrich W, Friedmann G. Adrenal masses: evaluation with fast gradient-echo MR imaging and Gd-DTPA-enhanced dynamic studies. Radiology 1989;171(3):675-680.
88. Erlemann R, Reiser MF, Peters PE, Vasallo P, Nommensen B, Kusnierz-Glaz CR, Ritter J, Roessner A. Musculoskeletal neoplasms: static and dynamic Gd-DTPA--enhanced MR imaging. Radiology 1989;171(3):767-773.
89. Edelman RR, Siegel JB, Singer A, Dupuis K, Longmaid HE. Dynamic MR imaging of the liver with Gd-DTPA: initial clinical results. AJR Am J Roentgenol 1989;153(6):1213-1219.
90. Evelhoch JL, LoRusso PM, He Z, DelProposto Z, Polin L, Corbett TH, Langmuir P, Wheeler C, Stone A, Leadbetter J, Ryan AJ, Blakey DC, Waterton JC. Magnetic resonance imaging measurements of the response of murine and human tumors to the vascular-targeting agent ZD6126. Clin Cancer Res 2004;10(11):3650-3657.
91. Jansen JF, Schoder H, Lee NY, Wang Y, Pfister DG, Fury MG, Stambuk HE, Humm JL, Koutcher JA, Shukla-Dave A. Noninvasive Assessment of Tumor Microenvironment Using Dynamic Contrast-Enhanced Magnetic Resonance Imaging and (18)F-Fluoromisonidazole Positron Emission Tomography Imaging in Neck Nodal Metastases. Int J Radiat Oncol Biol Phys 2009.
92. Hayes C, Padhani AR, Leach MO. Assessing changes in tumour vascular function using dynamic contrast-enhanced magnetic resonance imaging. NMR Biomed 2002;15(2):154-163.
93. Kety SS. The theory and applications of the exchange of inert gas at the lungs and tissues. Pharmacol Rev 1951;3(1):1-41.

94. Haroon HA, Buckley DL, Patankar TA, Dow GR, Rutherford SA, Baleriaux D, Jackson A. A comparison of Ktrans measurements obtained with conventional and first pass pharmacokinetic models in human gliomas. J Magn Reson Imaging 2004;19(5):527-536.
95. Henderson E, Sykes J, Drost D, Weinmann HJ, Rutt BK, Lee TY. Simultaneous MRI measurement of blood flow, blood volume, and capillary permeability in mammary tumors using two different contrast agents. J Magn Reson Imaging 2000;12(6):991-1003.
96. Tofts PS, Kermode AG. Measurement of the blood-brain barrier permeability and leakage space using dynamic MR imaging. 1. Fundamental concepts. Magn Reson Med 1991;17(2):357-367.
97. Weinmann HJ, Laniado M, Mutzel W. Pharmacokinetics of GdDTPA/dimeglumine after intravenous injection into healthy volunteers. Physiol Chem Phys Med NMR 1984;16(2):167-172.
98. Haase A. Snapshot FLASH MRI. Applications to T1, T2, and chemical-shift imaging. Magn Reson Med 1990;13(1):77-89.
99. Evelhoch JL. Key factors in the acquisition of contrast kinetic data for oncology. J Magn Reson Imaging 1999;10(3):254-259.
100. Li KL, Zhu XP, Waterton J, Jackson A. Improved 3D quantitative mapping of blood volume and endothelial permeability in brain tumors. J Magn Reson Imaging 2000;12(2):347-357.
101. Grimm J, Potthast A, Wunder A, Moore A. Magnetic resonance imaging of the pancreas and pancreatic tumors in a mouse orthotopic model of human cancer. Int J Cancer 2003;106(5):806-811.
102. Bromberg J, Darnell JE, Jr. The role of STATs in transcriptional control and their impact on cellular function. Oncogene 2000;19(21):2468-2473.
103. Cui Y, Huang L, Elefteriou F, Yang G, Shelton JM, Giles JE, Oz OK, Pourbahrami T, Lu CY, Richardson JA, Karsenty G, Li C. Essential role of STAT3 in body weight and glucose homeostasis. Mol Cell Biol 2004;24(1):258-269.
104. Gorogawa S, Fujitani Y, Kaneto H, Hazama Y, Watada H, Miyamoto Y, Takeda K, Akira S, Magnuson MA, Yamasaki Y, Kajimoto Y, Hori M. Insulin secretory defects and impaired islet architecture in pancreatic beta-cell-specific STAT3 knockout mice. Biochem Biophys Res Commun 2004;319(4):1159-1170.
105. Lammert E, Gu G, McLaughlin M, Brown D, Brekken R, Murtaugh LC, Gerber HP, Ferrara N, Melton DA. Role of VEGF-A in vascularization of pancreatic islets. Curr Biol 2003;13(12):1070-1074.
106. Brissova M, Shostak A, Shiota M, Wiebe PO, Poffenberger G, Kantz J, Chen Z, Carr C, Jerome WG, Chen J, Baldwin HS, Nicholson W, Bader DM, Jetton T, Gannon M, Powers AC. Pancreatic islet production of vascular endothelial growth factor--a is essential for islet vascularization, revascularization, and function. Diabetes 2006;55(11):2974-2985.
107. Bates DO, Harper SJ. Regulation of vascular permeability by vascular endothelial growth factors. Vascul Pharmacol 2002;39(4-5):225-237.
108. Roberts WG, Palade GE. Increased microvascular permeability and endothelial fenestration induced by vascular endothelial growth factor. J Cell Sci 1995;108 (Pt 6):2369-2379.
109. Senger DR, Galli SJ, Dvorak AM, Perruzzi CA, Harvey VS, Dvorak HF. Tumor cells secrete a vascular permeability factor that promotes accumulation of ascites fluid. Science 1983;219(4587):983-985.
110. Iwashita N, Uchida T, Choi JB, Azuma K, Ogihara T, Ferrara N, Gerber H, Kawamori R, Inoue M, Watada H. Impaired insulin secretion in vivo but enhanced insulin secretion from isolated islets in pancreatic beta cell-specific vascular endothelial growth factor-A knock-out mice. Diabetologia 2007;50(2):380-389.
111. Pham CD, Roberts TP, van Bruggen N, Melnyk O, Mann J, Ferrara N, Cohen RL, Brasch RC. Magnetic resonance imaging detects suppression of tumor vascular permeability after

administration of antibody to vascular endothelial growth factor. Cancer Invest 1998;16(4):225-230.
112. Padhani AR. Dynamic contrast-enhanced MRI studies in human tumours. Br J Radiol 1999;72(857):427-431.
113. Parmelee DJ, Walovitch RC, Ouellet HS, Lauffer RB. Preclinical evaluation of the pharmacokinetics, biodistribution, and elimination of MS-325, a blood pool agent for magnetic resonance imaging. Invest Radiol 1997;32(12):741-747.
114. Grist TM, Korosec FR, Peters DC, Witte S, Walovitch RC, Dolan RP, Bridson WE, Yucel EK, Mistretta CA. Steady-state and dynamic MR angiography with MS-325: initial experience in humans. Radiology 1998;207(2):539-544.
115. Lauffer RB, Parmelee DJ, Dunham SU, Ouellet HS, Dolan RP, Witte S, McMurry TJ, Walovitch RC. MS-325: albumin-targeted contrast agent for MR angiography. Radiology 1998;207(2):529-538.
116. Goyen M, Edelman M, Perreault P, O'Riordan E, Bertoni H, Taylor J, Siragusa D, Sharafuddin M, Mohler ER, 3rd, Breger R, Yucel EK, Shamsi K, Weisskoff RM. MR angiography of aortoiliac occlusive disease: a phase III study of the safety and effectiveness of the blood-pool contrast agent MS-325. Radiology 2005;236(3):825-833.
117. Hartmann M, Wiethoff AJ, Hentrich HR, Rohrer M. Initial imaging recommendations for Vasovist angiography. Eur Radiol 2006;16 Suppl 2:B15-23.
118. Straub V, Donahue KM, Allamand V, Davisson RL, Kim YR, Campbell KP. Contrast agent-enhanced magnetic resonance imaging of skeletal muscle damage in animal models of muscular dystrophy. Magn Reson Med 2000;44(4):655-659.
119. Walker-Samuel S, Leach MO, Collins DJ. Evaluation of response to treatment using DCE-MRI: the relationship between initial area under the gadolinium curve (IAUGC) and quantitative pharmacokinetic analysis. Phys Med Biol 2006;51(14):3593-3602.
120. Hathout E, Sowers L, Wang R, Tan A, Mace J, Peverini R, Chinnock R, Obenaus A. In vivo magnetic resonance imaging of vascularization in islet transplantation. Transpl Int 2007;20(12):1059-1065.
121. Yu CW, Shih TT, Hsu CY, Lin LC, Wei SY, Lee CM, Lee YT. Correlation between pancreatic microcirculation and type 2 diabetes in patients with coronary artery disease: dynamic contrast-enhanced MR imaging. Radiology 2009;252(3):704-711.
122. Bolender RP. Stereological analysis of the guinea pig pancreas. I. Analytical model and quantitative description of nonstimulated pancreatic exocrine cells. J Cell Biol 1974;61(2):269-287.
123. Brissova M, Powers AC. Revascularization of transplanted islets: can it be improved? Diabetes 2008;57(9):2269-2271.
124. Mattsson G, Jansson L, Carlsson PO. Decreased vascular density in mouse pancreatic islets after transplantation. Diabetes 2002;51(5):1362-1366.
125. Port RE, Knopp MV, Hoffmann U, Milker-Zabel S, Brix G. Multicompartment analysis of gadolinium chelate kinetics: blood-tissue exchange in mammary tumors as monitored by dynamic MR imaging. J Magn Reson Imaging 1999;10(3):233-241.
126. Kiessling F, Morgenstern B, Zhang C. Contrast agents and applications to assess tumor angiogenesis in vivo by magnetic resonance imaging. Curr Med Chem 2007;14(1):77-91.
127. St Lawrence KS, Lee TY. An adiabatic approximation to the tissue homogeneity model for water exchange in the brain: I. Theoretical derivation. J Cereb Blood Flow Metab 1998;18(12):1365-1377.
128. St Lawrence KS, Lee TY. An adiabatic approximation to the tissue homogeneity model for water exchange in the brain: II. Experimental validation. J Cereb Blood Flow Metab 1998;18(12):1378-1385.
129. Johnson JA, Wilson TA. A model for capillary exchange. Am J Physiol 1966;210(6):1299-1303.

130. Kroll K, Wilke N, Jerosch-Herold M, Wang Y, Zhang Y, Bache RJ, Bassingthwaighte JB. Modeling regional myocardial flows from residue functions of an intravascular indicator. Am J Physiol 1996;271(4 Pt 2):H1643-1655.
131. Ostergaard L, Chesler DA, Weisskoff RM, Sorensen AG, Rosen BR. Modeling cerebral blood flow and flow heterogeneity from magnetic resonance residue data. J Cereb Blood Flow Metab 1999;19(6):690-699.
132. Buckley DL. Uncertainty in the analysis of tracer kinetics using dynamic contrast-enhanced T1-weighted MRI. Magn Reson Med 2002;47(3):601-606.
133. Jivan A, Horsfield MA, Moody AR, Cherryman GR. Dynamic T1 measurement using snapshot-FLASH MRI. J Magn Reson 1997;127(1):65-72.
134. Fram EK, Herfkens RJ, Johnson GA, Glover GH, Karis JP, Shimakawa A, Perkins TG, Pelc NJ. Rapid calculation of T1 using variable flip angle gradient refocused imaging. Magn Reson Imaging 1987;5(3):201-208.
135. Brookes JA, Redpath TW, Gilbert FJ, Needham G, Murray AD. Measurement of spin-lattice relaxation times with FLASH for dynamic MRI of the breast. Br J Radiol 1996;69(819):206-214.
136. Parker GJ, Barker GJ, Tofts PS. Accurate multislice gradient echo T(1) measurement in the presence of non-ideal RF pulse shape and RF field nonuniformity. Magn Reson Med 2001;45(5):838-845.
137. Sourbron SP, Michaely HJ, Reiser MF, Schoenberg SO. MRI-measurement of perfusion and glomerular filtration in the human kidney with a separable compartment model. Invest Radiol 2008;43(1):40-48.
138. Hedley M, Yan H, Rosenfeld D. Motion artifact correction in MRI using generalized projections. IEEE Trans Med Imaging 1991;10(1):40-46.
139. Kerwin WS, Cai J, Yuan C. Noise and motion correction in dynamic contrast-enhanced MRI for analysis of atherosclerotic lesions. Magn Reson Med 2002;47(6):1211-1217.
140. Liu G, Rugo HS, Wilding G, McShane TM, Evelhoch JL, Ng C, Jackson E, Kelcz F, Yeh BM, Lee FT, Jr., Charnsangavej C, Park JW, Ashton EA, Steinfeldt HM, Pithavala YK, Reich SD, Herbst RS. Dynamic contrast-enhanced magnetic resonance imaging as a pharmacodynamic measure of response after acute dosing of AG-013736, an oral angiogenesis inhibitor, in patients with advanced solid tumors: results from a phase I study. J Clin Oncol 2005;23(24):5464-5473.
141. Henderson E, Rutt BK, Lee TY. Temporal sampling requirements for the tracer kinetics modeling of breast disease. Magn Reson Imaging 1998;16(9):1057-1073.
142. Haacke EM, Tkach JA. Fast MR imaging: techniques and clinical applications. AJR Am J Roentgenol 1990;155(5):951-964.
143. Gowland P, Mansfield P, Bullock P, Stehling M, Worthington B, Firth J. Dynamic studies of gadolinium uptake in brain tumors using inversion-recovery echo-planar imaging. Magn Reson Med 1992;26(2):241-258.
144. Freeman AJ, Gowland PA, Mansfield P. Optimization of the ultrafast Look-Locker echo-planar imaging T1 mapping sequence. Magn Reson Imaging 1998;16(7):765-772.
145. Matsubayashi R, Matsuo Y, Edakuni G, Satoh T, Tokunaga O, Kudo S. Breast masses with peripheral rim enhancement on dynamic contrast-enhanced MR images: correlation of MR findings with histologic features and expression of growth factors. Radiology 2000;217(3):841-848.
146. Yamashita Y, Baba T, Baba Y, Nishimura R, Ikeda S, Takahashi M, Ohtake H, Okamura H. Dynamic contrast-enhanced MR imaging of uterine cervical cancer: pharmacokinetic analysis with histopathologic correlation and its importance in predicting the outcome of radiation therapy. Radiology 2000;216(3):803-809.
147. Grenier N, Pedersen M, Hauger O. Contrast agents for functional and cellular MRI of the kidney. Eur J Radiol 2006;60(3):341-352.

148. Heilmann M, Dimicoli J, Thomas C, Walczak C, Volk A. Saturation-recovery multi-gradient-echo snapshot technique for simultaneous measurement of *R*1 and *R*∗2 at high spatial and temporal resolution in dynamic MRI of tumor microvasculature. Magnetic Resonance Materials in Physics, Biology and Medicine 2005;18(S1):176-307.
149. Glenny RW, Bernard S, Brinkley M. Validation of fluorescent-labeled microspheres for measurement of regional organ perfusion. J Appl Physiol 1993;74(5):2585-2597.
150. Van Oosterhout MF, Willigers HM, Reneman RS, Prinzen FW. Fluorescent microspheres to measure organ perfusion: validation of a simplified sample processing technique. Am J Physiol 1995;269(2 Pt 2):H725-733.
151. Ferrier MC, Sarin H, Fung SH, Schatlo B, Pluta RM, Gupta SN, Choyke PL, Oldfield EH, Thomasson D, Butman JA. Validation of dynamic contrast-enhanced magnetic resonance imaging-derived vascular permeability measurements using quantitative autoradiography in the RG2 rat brain tumor model. Neoplasia 2007;9(7):546-555.
152. Bol A, Melin JA, Vanoverschelde JL, Baudhuin T, Vogelaers D, De Pauw M, Michel C, Luxen A, Labar D, Cogneau M, et al. Direct comparison of [13N]ammonia and [15O]water estimates of perfusion with quantification of regional myocardial blood flow by microspheres. Circulation 1993;87(2):512-525.
153. Baron AD, Brechtel-Hook G, Johnson A, Hardin D. Skeletal muscle blood flow. A possible link between insulin resistance and blood pressure. Hypertension 1993;21(2):129-135.
154. Curry DL, Bennett LL, Grodsky GM. Dynamics of insulin secretion by the perfused rat pancreas. Endocrinology 1968;83(3):572-584.
155. Berglund O. Different dynamics of insulin secretion in the perfused pancreas of mouse and rat. Acta Endocrinol (Copenh) 1980;93(1):54-60.

CHAPTER THREE

IN VIVO TRACKING OF EXOGENOUS CELL DELIVERY WITH POSITIVE CONTRAST

3.1 Overview

With the discovery of pluripotent stem cells in humans, an entire new research field in cellular therapy has emerged. It is anticipated that therapeutic stem cell repair could rejuvenate damaged tissues and organs that would otherwise deteriorate and malfunction. A key consideration in the success of any stem cell therapy is the precision of cell delivery to the targeted site. Stem cells labeled with exogenous MR sensitive contrast agents have been actively pursued in the past decade to provide in vivo information on cell delivery and migration. Labeled with either positive or negative contrast agents, proton relaxation is altered in these cells and that phenomenon facilitates its distinction from native cells. In-vitro cell labeling with super-paramagnetic iron-oxide nanoparticles (SPIOs) coupled with T_2^*-weighted MRI is currently the most popular cell tracking methodology. The resultant hypointensities present in the MR image however are convoluted with other undesired effects such as susceptibility artifacts, partial volume and local magnetic field inhomogeneities, leading to confused interpretation of labeled cells. An elegant solution is to turn iron-induced hypointensities into hyperintensities. For this chapter, I primarily explored the potential to generate positive contrast in SPIO-labeled cells with a Multiple Ultra-short Echo Time (MUTE) pulse sequence. A summary of current positive contrast enhancement techniques is first discussed with their strengths and weaknesses highlighted. Then I considered MUTE and illustrated its superior positive contrast generating mechanism. With a clever combination of MUTE and the White-marker technique, the potential of Z-shimmed UTE (ZUTE) to boost positive contrast enhancement by up to 100% is finally presented.

3.2 Types of Contrast Agents for Cell Labeling

Therapeutic regeneration and repair of pathological tissues and organs with exogenous stem cells have been actively investigated in the last decade. Transplantation of pluripotent cells such as embryonic and mesenchymal stem cells (1) promises rejuvenation in a myriad of degenerative diseases, including myocardial infarction and central nervous system disorders. Regardless of their ameliorative mechanisms, central to the success of such corrective cell therapy are the ability to track their migration from the site of implantation to relevant foci of disease, and survival for sufficient periods of time to exhibit their regenerative properties (2). MRI cell tracking provides a non-invasive method to observe the migration dynamics of transplanted cells and their residence time in the targeted tissue or organ, with high temporal and spatial resolution. However, because MRI cannot distinguish between exogenous and intrinsic native cells due to their almost similar T_1 and T_2 values, transplanted cells must be labeled with an MR-sensitive contrast agent. Key issues that must be answered in MRI tracking of labeled cells include: 1) the physical attachment between the contrast agent particles and the cells, i.e., are they attached on the surface receptors or incorporated into the cells; 2) the minimum amount of contrast agent required per cell for obvious MRI visualization; 3) biocompatibility and intracellular stability of the synthetic complexes in the cells; 4) possibility to link functionalized groups and ligands for molecular targeting; 5) quantification of in vivo detected cells; and 6) impact of contrast agent particles on cell function. The ideal label should exhibit high detection sensitivity at low concentration, homogenous incorporation in all cells, high stability without toxicity concerns, flexible ligand-binding on the coating for molecular sensing, distinct relationship between MR signal and concentration for quantification, as well as minimal detrimental impact on normal cellular function such as differentiation and proliferation.

3.2.1 T_1-weighted Cellular and Molecular Targeting

T_1-weighted contrast agents such as Gd^{3+}-chelates and Mn^{2+} - based nanoparticles attenuate proton relaxation to provide positive contrast, i.e., labeled cells appear as hyperintense spots or regions. Gadopentetate dimeglumine (Gd-DTPA) has been demonstrated to be easily incorporated into mouse embryonic and neuronal stem cells via gene transfection agents such as lipofectamine or calcium phosphate, yielding a labeling efficiency of up to 83% and doubling of longitudinal relaxation rate (3). MR signal amplification is the essence of high detection sensitivity and that could be accomplished by manipulating the interaction between Gd-chelates and surrounding protons. Aime et al. introduced a Gd-loaded apoferritin complex in which several Gd-HPDO3A units are trapped within the large cavity in apoferritin (4). The interaction between the paramagnetic centers and the high number of protein hydration water molecules and mobile protons induces further exchange with the bulk solvent, amplifying the presence of the Gd^{3+} ions by 20 times compared to free Gd-HPDO3A in water.

Another paramagnetic label that has been explored for cellular labeling is Manganese. Mn^{2+} is an essential heavy metal ion that can enter cells through voltage-gated calcium channels, enabling active brain regions (5) and changes in inotropic status in the heart to be monitored by MRI (6). In vivo tract tracing of neuronal pathways facilitated by anterograde transport of Mn^{2+} has also been demonstrated (7,8). Success in physiological imaging with manganese enhanced MRI (MEMRI) prompted the investigation of $MnCl_2$ as a positive contrast cellular biomarker. In-vitro cell labeling with $MnCl_2$ for detection with MRI was first demonstrated by Aoki et al. in blood lymphocytes (9). Subsequently Yamada and co-workers proved its feasibility in human embryonic and bone marrow stem cells for in-vivo tracking (10).

Although proton relaxation induced by paramagnetic centers such as Gd^{3+} and Mn^{2+} produces positive contrast and enables in-vivo cellular tracking, some major drawbacks exist and impede their clinical implementation. One concern is biotoxicity, and emerging evidence suggests that gadolinium induces a rare disorder known as 'nephrogenic systemic fibrosis (NSF)' in patients with renal failure (11-13). A number of studies have shown that Mn^{2+} uptake in the heart causes a delayed augmentation of contractility, induced by its inhibition of cell-surface Na-Ca exchange activity (14,15). In addition, it is well known that chronic exposure to manganese leads to a neurological disorder resembling Parkinson's disease (16).

3.2.2 T_2 / T_2^* -Weighted Cellular and Molecular Probes

Due to their lower detection sensitivity and biotoxicity at high doses, gadolinium and manganese compounds are much less popular compared to their T_2/T_2^*-weighted counterpart, superparamagnetic nanoparticles, also known as SPIOs. Iron oxide nanoparticles composed of maghemite and magnetite (Fe_2O_3, Fe_3O_4) stabilized by various coating agents (17) are characterized by a large magnetic moment in the presence of a static external magnetic field, which makes them suitable as MR contrast agents. This large magnetic moment is caused by a crystal ordering that induces cooperation between the individual paramagnetic domains (~ 30 nm), which consequently do not show any magnetic remanence (i.e. restoration of the induced magnetization to zero upon removal of the external magnetic field), unlike ferromagnetic materials (18). SPIOs possess suitable properties that make them attractive for cell labeling; 1) they provide the most signal change per unit of metal, appearing as hypointensities that extend beyond their spatial dimensions (19). This feature is the most important characteristic of SPIOs and it effectively determines their detection sensitivity. Hence it will be discussed thoroughly in the next section. 2) SPIOs typically have dextran

coatings that are biodegradable, releasing the submicron iron crystal cores (~5-30 nm diameter) that can be absorbed into the body via the normal iron metabolic pathways (20,21). 3) The dextran surface coating permits linkage to functional groups and ligands and enables specific molecular targeting (e.g. the cross-linked iron oxide (CLIO) nanoparticle platform that could conjugate to a wide range of hetero-bifunctional linkers such as transferrin, annexin V or twin-arginine-translocase (TAT) peptides (22,23). 4) Histological verification of cell incorporation is easily performed with optical staining such as Prussian blue (24). 5) Iron content per cell can be easily quantified with inductively coupled plasma mass spectrometry (ICP-MS); and 6) their effect on proton relaxation can be manipulated according to size (25). 7) Labeling protocols such as transfection have been optimized for some mammalian cell lines (26-28). With such attractive physiochemical properties, it is natural that SPIO–based particles are currently the most popular contrast agent used for in-vivo cellular tracking in preclinical models and in the clinic.

3.2.3 Negative Contrast Generation Mechanism with SPIOs

Both T_1 and T_2 (or T_2^*) relaxation times are shortened by iron-oxide particles. The magnetic susceptibility effect of SPIOs is generally dominant over longitudinal relaxation to give a much greater r_2/r_1 ratio (r_1 and r_2 are longitudinal and transverse relaxivities, respectively) than paramagnetic molecules such as Gd-DTPA, i.e. signal dephasing from reduced T_2 or T_2^* is greater than signal enhancement due to shorter T_1 (17). The observed effect on MR signal intensity depends on various factors, including particle composition, particle size, concentration of particles within an imaging voxel and data acquisition parameters (29). At preclinical field strengths, r_1 is much lower than r_2 (e.g., for SHU555C/Resovist®, r_1 ~ 1

$mM^{-1}s^{-1}$ and r_2 ~ 256 $mM^{-1}s^{-1}$ at 9.4 T) (30), thus signal voids are often interpreted as SPIO-labeled cells (2).

A collection of SPIO labeled cells will superimpose a field pattern onto the static magnetic field, resulting in a locally perturbed field. For a small paramagnetic particle, the field perturbation $B_{z,inh}$ outside the particle can be described by a dipole and it depends on the magnetic susceptibility difference $\Delta\chi$ between the SPIO and its surroundings, radius a of the SPIO (assumed spherical), radial distance r from the iron core and the angle θ relative to the main magnetic field $\boldsymbol{B_0}$ as given by eqn. (3.1) below. It is also commonly expressed as eqn. (3.2), where $\Delta\chi V$ characterizes the local magnetic dose of the marker as the product of the difference of volume susceptibilities to the environment and the marker volume.

$$B_{z,inh}(r,\theta) = \frac{\Delta\chi B_0}{3}\left(\frac{a}{r}\right)^3 (3cos^2\theta - 1) \tag{3.1}$$

$$B_{z,inh}(x,y,z) = c\frac{x^2 + y^2 - 2z^2}{(x^2 + y^2 + z^2)^{\frac{5}{2}}} \quad with \quad c = \frac{B_0\Delta\chi V}{4\pi} \tag{3.2}$$

The localized field inhomogeneities induced by the superparamagnetic centers cause field variations within imaging voxels, resulting in spins within the voxels to precess at different frequencies according to the Larmor equation. For gradient-echo sequences without refocusing RF pulses, the voxel signal will decay because of irreversible intravoxel dephasing and gives rise to an average voxel signal given by:

$$S_{voxel} = \frac{1}{V}\int_V \rho(r)exp(-i\varphi)d^3r \tag{3.3}$$

$$where\ \varphi = \gamma B_{z,inh}(x,y,z)TE \tag{3.4}$$

Where φ is the additional phase resulting from an inhomogenous magnetic field distortion $B_{z,inh}$ in the z-direction, $\rho(r)$ is the spin density, V is the voxel volume (mm^3), TE is the echo time (ms), and γ is the proton gyromagnetic ratio.

For a single slice, signal loss owing to dephasing in the slice direction will be dominant. Integration of eqn. (3.3) over the slice thickness d results in the normalized complex signal per voxel, as given by eqn. (3.5). The resultant signal amplitude varies spatially as shown in figure (3.1), effectively creating a 'blooming' artifact which acts as a negative contrast biomarker of labeled cells in a T_2^*-weighted image. This typical dipole susceptibility effect extends way beyond the SPIO size, and is the reason why SPIOs offer much higher sensitivity than Gd (III) or Mn^{2+} contrast agents. When a congregation of cells occurs, their dephasing effects can be summed together, which further enhances detection sensitivity (31).

$$S(x,y) = \int_{-\frac{d}{2}}^{\frac{d}{2}} \rho(x,y,z)\exp\left(-i\gamma B_{z,inh}(x,y,z)TE\right)dz \qquad (3.5)$$

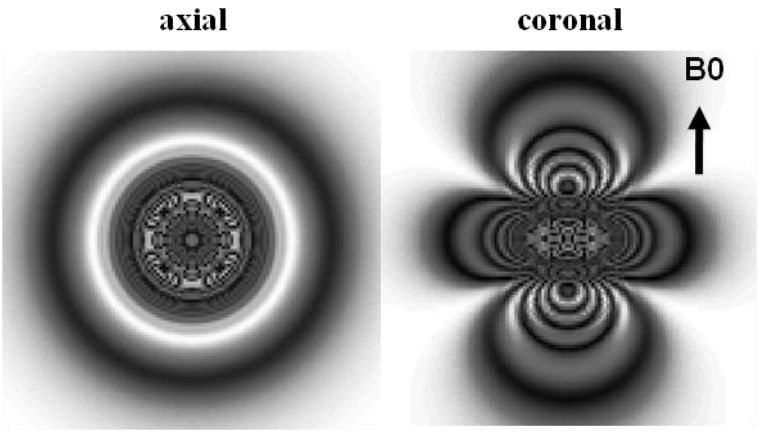

Figure 3.1: Simulation of susceptibility effect of a superparamagnetic biomarker at 9.4 T in a 1 mm^3 voxel. Assumed parameters are ρ = 1x10^{10}, $\Delta\chi V$ = 1x10^{-7} mm^3 and TE = 10 ms.

3.3 Review of Positive Contrast Techniques for Cellular Tracking

In this section, I review positive contrast techniques that have been demonstrated recently for cell tracking in the clinic, namely off-resonance imaging (ORI), inversion recovery with on-resonance water suppression (IRON) and white-marker (WM). The physical basis of these methods relies chiefly on the susceptibility effect of SPIOs, which are exploited in different schemes to generate positive contrast. I briefly explain the underlying principles of each technique and highlight their strengths and weaknesses, emphasizing on their suitability in the preclinical environment.

3.3.1 Off-Resonance Imaging (ORI)

Off-resonance imaging was proposed recently by Cunningham et al. (32) to generate positive contrast of intracellular superparamagnetic particles. It exploits the shift in resonance frequencies of protons surrounding the nanoparticle caused by its susceptibility effect according to eqn. (3.6). To illustrate this phenomenon, Figure 3.2A displays the simulated spatial variation in resonance frequency shift δf (Hz) of spins surrounding a SPIO nanoparticle at 9.4 T. Its dipole behavior is obvious in that protons in the North and South poles (parallel to the static field $\boldsymbol{B_0}$) have positive chemical shifts while those at the East and West regions have negative chemical shifts. The largest magnitude chemical shift is observed to be at the immediate vicinity of the SPIO nanoparticle, and decreases radially.

$$\delta f = \gamma B_{z,inh}(x, y, z) \tag{3.6}$$

The chemical shifts essentially broaden the on-resonance water peak and induces a spread of off-resonance protons. By selectively exciting a small spectral range of protons at off-resonance (see Figure 3.2B), we can highlight specific regions either on the East-West or

North-South axes. Since only selected off-resonance spins are excited, while the rest do not give rise to any signal, the emanated MR signal without background signal provides positive contrast of the cells.

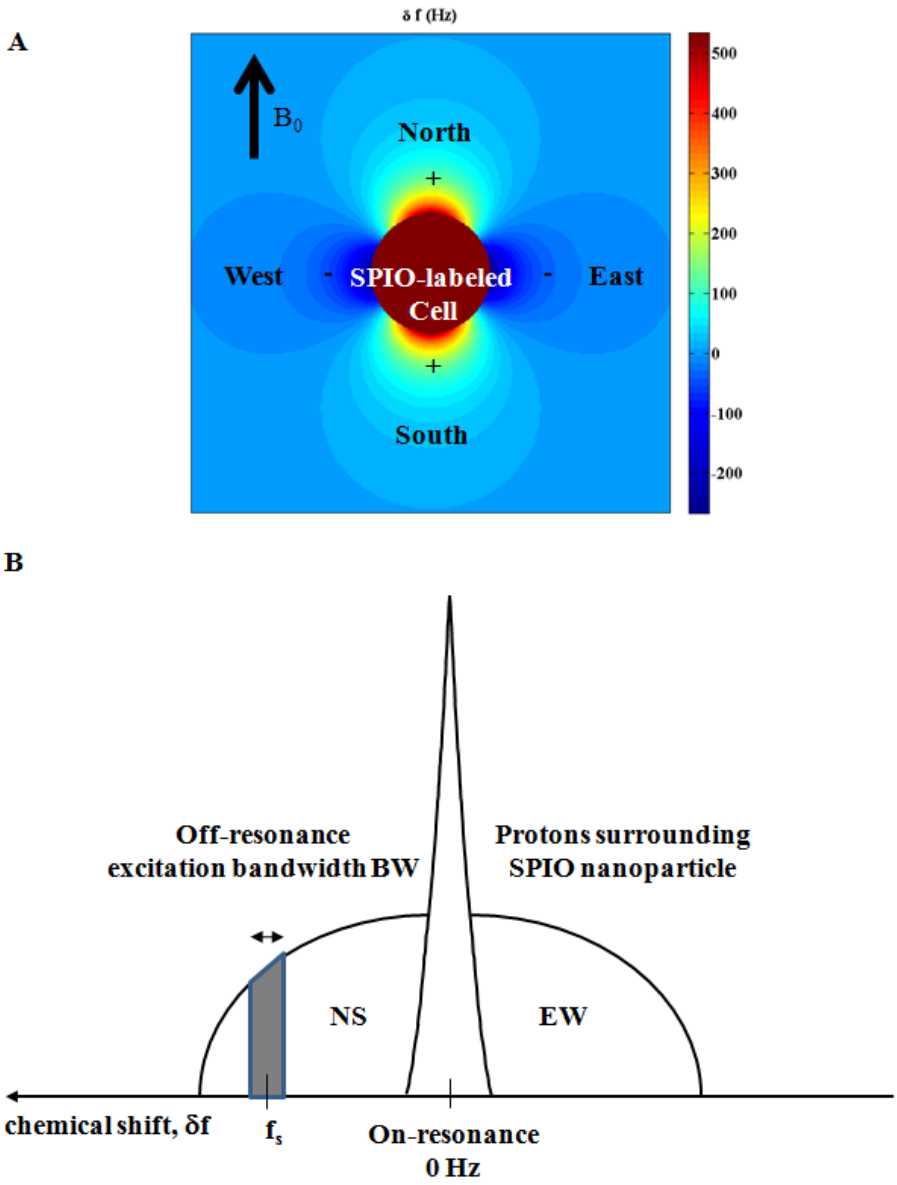

Figure 3.2: (A) Spatial variation in proton resonance frequency surrounding a superparamagnetic nanoparticle. Chemical shift polarity is indicated by '+' and '-'. (B) Off-resonance RF excitation at f_s selects the protons within the spectral window bandwidth BW, while others including on-resonance spins are not excited. In this illustration, the spins in the North-South poles with resonance frequency $f = f_s \pm BW/2$ will give rise to MR signal.

In-vitro studies have demonstrated the potential of off-resonance imaging in cell quantification based on a nonlinear relationship between measured signal and cell number (32). ORI also offers high contrast-to-noise ratio (CNR) since the background signal (i.e. from on-resonant protons) is almost non-existent. Feasibility studies have been demonstrated in the positive contrast visualization of SPIO-labeled embryonic stem cells in mouse limbs (32,33), tracking infiltration of macrophages in the infarcted mouse heart (34) and in rabbit hind-limbs implanted with much larger micron-sized SPIOs (35). ORI has also been used to visualize MR-compatible passive devices such as intra-myocardial needles (36). However, there are a few technical constraints regarding this positive contrast technique which retard their adoption in the preclinical environment. First, specially designed RF saturation pulses have to be calculated since only unique off-resonance frequencies with certain bandwidths are desired. For optimal excitation at a fixed frequency offset, the bandwidth has to be narrow and that in turn reduces signal amplitude. Thus ORI requires spin-echo refocusing in order to obtain sufficient signal-to-noise ratio, which prolongs scan time. A recent study by Farrar and co-workers modeled and compared the sensitivity, specificity and linearity of ORI at two preclinical field strengths of 4.7 T and 14 T in the detection of different concentration of monocrystalline iron oxide nanoparticles (MION) solutions (34). Since different iron contents give rise to different off-resonance profiles, in addition to wider on-resonance linewidth at high magnetic field strength, the diagnostic ability of ORI relies on the capability to differentiate MION-shifted resonances from on-resonance water; this stresses the robustness of the designed RF pulse because on-resonance protons must be suppressed effectively without affecting off-resonance water. The situation becomes more complex at the air/tissue interface, where the field inhomogeneity is most pronounced and further distorts the chemical shift distribution, compromising specificity as a result. Since iron concentration linearly

correlates with the induced chemical shift, care must be taken in the choice of labeling concentration to prevent an overlap in off resonance frequencies between iron-induced and air/tissue susceptibility effects. Second major hurdle to ORI is the nonlinear relationship between signal intensity and iron concentration (34). Beyond a MION concentration of approximately 150 μg ml^{-1}, T_2-induced decay dominates and signal intensity decreases. Thus an ultra-short echo time sequence might be necessary to ensure $TE << T_2$. Third obstacle to preclinical translation is the degradation of specificity due to wider on-resonance linewidth (34). Therefore shimming is a very critical procedure that could determine the diagnostic accuracy of ORI at high magnetic field strength. Finally, ORI is not a signal efficient method because only the positive or negative frequencies (i.e., NS or EW regions) are excited. Hence detection sensitivity might be low. In summary, the optimal performance of ORI will likely be seen at low fields, with moderate MION concentrations and with sequences that could perform very short echo-times. Its performance in the small animal environment would require extremely uniform shims and high performance gradient systems for short TE.

Demonstration of Off-Resonance Imaging Potential at 9.4 T

As a demonstration of ORI's potential at 9.4 T when the above conditions are partially met, i.e. reasonable shimming and short echo-time, I prepared a phantom consisting of water and 2.56 mM of SPIO solution (SHU555C, Resovist®) and compared images acquired with T_2^*-weighted and ORI. After extensive 3D-volume shimming, the on-resonance linewidth achieved was 0.1 ppm or 40 Hz. Parameters used in the acquisition were: TR = 50 ms, TE = 2.3 ms, excitation flip angle = 60°, matrix = 128 × 128, field-of-view = 16 × 30 mm^2, frequency offset = 500 Hz, spectral selective RF bandwidth = 100 Hz (sinc). The imaging results are displayed in Figure 3.3. We observe that off-resonance excitation enables positive

contrast of SPIO solution, but the image appeared noisy partially due to the narrow RF excitation bandwidth of 0.25 ppm and the acquisition of gradient echoes instead of spin-echoes.

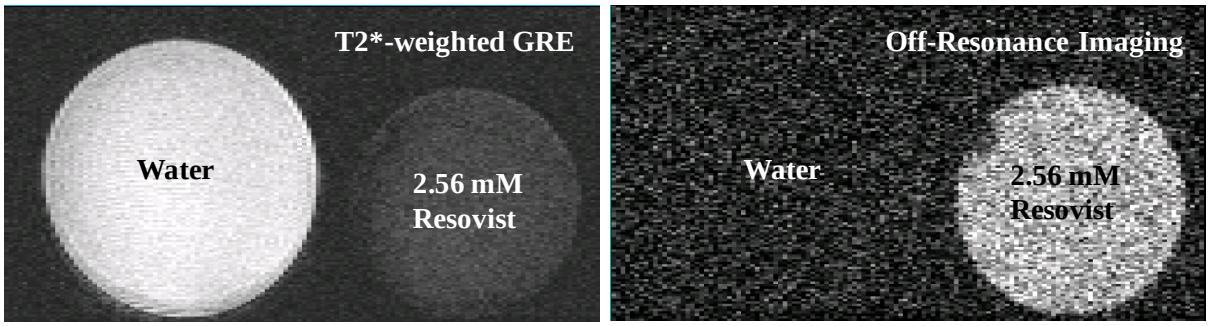

Figure 3.3: Proof-of-principle that off-resonance imaging has the potential to provide positive contrast of SPIO at 9.4 T. Phantom consisted of water and a 2.56 mM solution of SHU-555C (Resovist®).

3.3.2 Inversion Recovery with On-Resonant water suppression (IRON)

Stuber and co-workers invented this inversion recovery technique that nulls both fat and on-resonance water signals, while exciting the remaining off-resonance protons with a broadband RF excitation (37,38). Figure 3.4 illustrates this concept whereby on-resonance saturation destroys the longitudinal magnetization of protons distant from the SPIO nanoparticle. By choosing the appropriate delay times (T_{d1} *and* T_{d2}), fat can be simultaneously nulled. The text in the figure explains the physical principles of IRON. This technique has been demonstrated to produce positive contrast visualization of SPIO-labeled mesenchymal stem cells implanted in rabbit hind-limbs (37), MIONs injected into lymph nodes (38), evaluation of macrophage-rich vulnerable plaques (39) and in MR angiography (40).

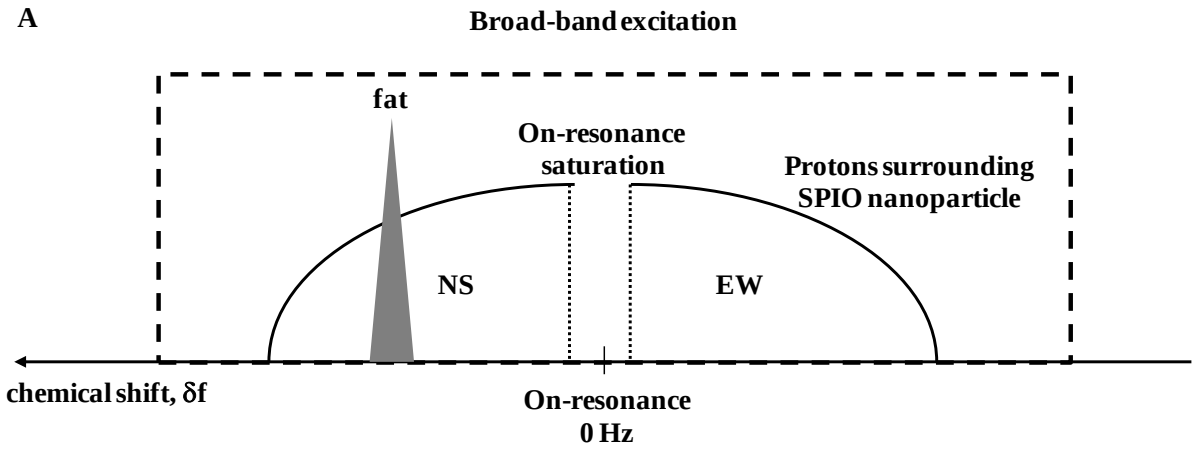
A
Broad-band excitation
fat
On-resonance saturation
Protons surrounding SPIO nanoparticle
NS
EW
chemical shift, δf
On-resonance 0 Hz

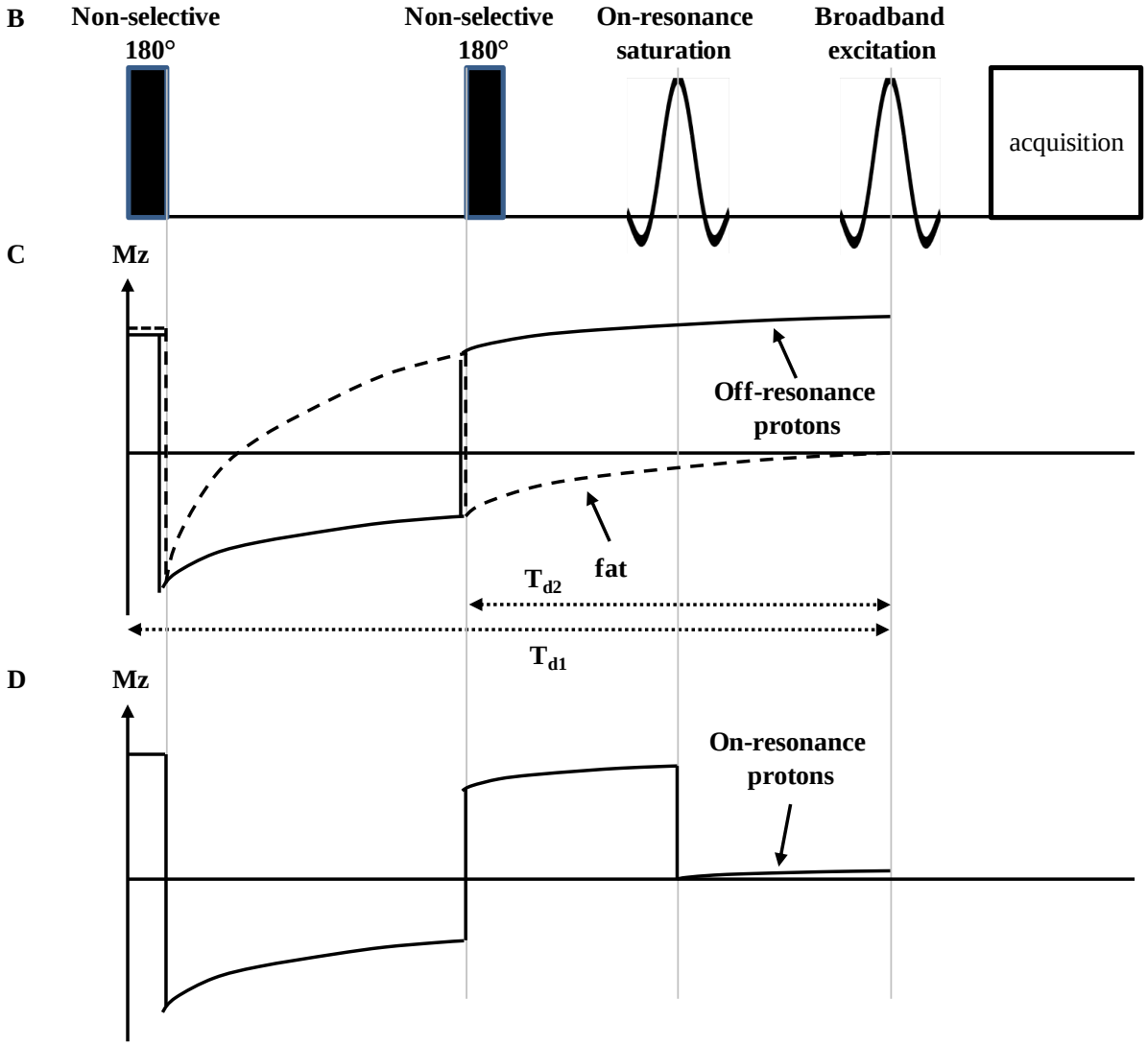
B
Non-selective 180°
Non-selective 180°
On-resonance saturation
Broadband excitation
acquisition
C
Mz
Off-resonance protons
fat
T_{d2}
T_{d1}
D
Mz
On-resonance protons

Figure 3.4: Physical principle of IRON. (A) The spectral distribution of fat, off- and on-resonance water. The on-resonance protons are saturated, effectively eliminating background signal. Broadband excitation encompasses a wide spectrum. (B) To suppress the fat signal, dual non-selective inversion pulses (180°) are applied. (C) The first 180° pulse inverts all proton pools, including fat. Since the T_1 of fat is low, its longitudinal magnetization $M_{z,fat}$ will recover faster than other tissue protons. The second inversion pulse will cause the magnetization to invert once more, while flipping that of off- and on- resonance protons ($M_{z,off}$ and $M_{z,on}$ respectively) to positive polarity. Subsequently an on-resonance saturation pulse destroys the longitudinal magnetization of background water, followed by the usual signal acquisition. The delays T_{d1} and T_{d2} have to consider the T_1 relaxation times of fat and the different proton pools, and are timed accordingly for successful fat nulling. (D) The longitudinal magnetization evolution of on-resonance protons in the IRON sequence. We observe from the temporal evolution of longitudinal magnetization that the fat signal is suppressed while on-resonance protons contribute minimal signal compared to off-resonance water.

Advantages and Disadvantages of IRON Imaging

The application of broad–band excitation in IRON eliminates the need for a robust spectrally selective RF pulse as seen in ORI. In addition, there is no fat signal corrupting the image. The biggest gain in IRON is perhaps all off-resonance protons surrounding the SPIO are excited by the broadband RF, and that increases sensitivity compared to ORI. Thus it is a more signal-efficient technique. A minimum of 125,000 cells could be detected in-vivo and there appears to be a linear correlation between signal enhancement and cell concentration, thus quantification might be possible (37). Disadvantages of IRON are very similar to that in off-

resonance imaging, including the stringent requirement for a homogenous magnetic field. Thus at high magnetic field strength in preclinical systems, implementation is expected to be challenging. Alternative sources of off-resonance signal inevitably lead to positive signal that might not necessarily be related to the presence of the susceptibility-generating SPIO-labeled cells, especially at tissue borders, air-tissue interfaces with local $\boldsymbol{B_0}$ inhomogeneities (37).

3.3.3 Gradient Echo Acquisition for Superparamagnetic Particles with Positive Contrast (GRASP) or White-Marker Imaging

The physical principle of White-Marker imaging is based on phase compensation with gradient application in the slice direction (41,42). A typical slice selection involves excitation of a slice of thickness d followed by a refocusing gradient to undo its accumulated phase. This results in on-resonance protons with null phases. In the presence of an SPIO nanoparticle however, its susceptibility effect causes surrounding protons to accrue additional phase according to eqn. (3.4). If that phase can somehow be nulled during slice refocusing, some off-resonance protons would be refocused completely while on-resonance protons remain dephased, thus the MR signal arising from the former proton pool will dominate. White-marker imaging achieves that goal by adding a fraction α of the slice refocusing gradient amplitude G_{ssr}, which has duration τ_{ssr} during the slice refocusing process. The effective phase at the echo-time is then given by eqn. (3.7) with resulting voxel signal according to eqn. (3.8). $\rho(x, y, z)$ being the spatial spin distribution surrounding the SPIO. Maximum signal will arise from protons that satisfy the condition $\varphi(x, y, z, TE) = 0$.

$$\varphi(x, y, z, TE) = \gamma B_{z,inh}(x, y, z)TE + \alpha G_{ssr}\tau_{ssr}z \qquad (3.7)$$

$$S(x,y) = \frac{1}{d}\int_{-\frac{d}{2}}^{\frac{d}{2}} \rho(x,y,z)\exp\left[-i\gamma\left(B_{z,inh}(x,y,z)TE + \alpha G_{ssr}\tau_{ssr}z\right)\right]dz \qquad (3.8)$$

White-marker at 9.4 T

To prove that this method is theoretically feasible at 9.4 T, we ran a simulation with the following parameters: a 1 mm^3 voxel with thickness d = 1 mm, $\rho = 10^{10}$, $\Delta\chi V = 10^{-7}$ mm^3, B_0 = 9.4 T, TE = 10 ms, G_{ssr} = 0.5 T/m and t_{ssr} = 0.15 ms. Results comparing T_2^*-weighted (α = 0) and white-marker (α = 0.45) imaging are shown in Figure 3.5. In the latter, background signal is subdued because of incomplete phase compensation, whereas off-resonance protons juxtaposition to the superparamagnetic marker emanate strong MR signal.

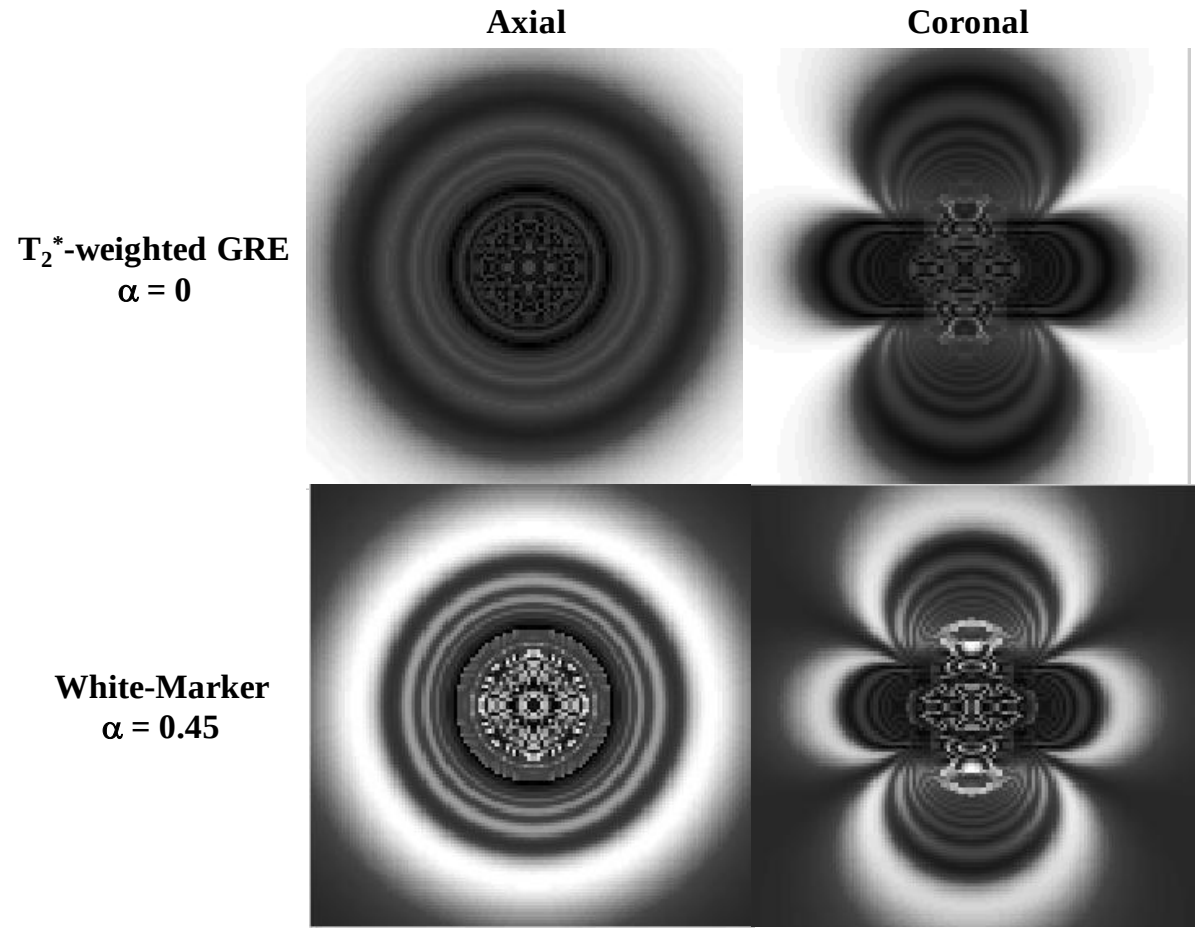

Figure 3.5: Simulation to illustrate negative and positive contrast of a superparamagnetic marker at 9.4 T. White-marker suppresses background signal and compensates phase accrued by surrounding protons in the slice direction.

To explore experimentally the potential of white-marker, we tested its ability to produce positive contrast on biological samples. An excised mouse brain injected with SPIOs nanoparticles was embedded in agarose and placed in a 9.4 T horizontal bore MRI scanner. Acquisition with typical T_2^*-weighted gradient echo is first carried out with 100 % slice refocusing gradient (i.e. $\alpha = 0$), followed by White-marker imaging with 60% ($\alpha = 0.4$) refocusing. Relevant scan parameters were: TR = 120 ms, TE = 4 ms, excitation flip angle = 30°, matrix = 128 × 128, field-of-view = 20 × 20 mm^2.

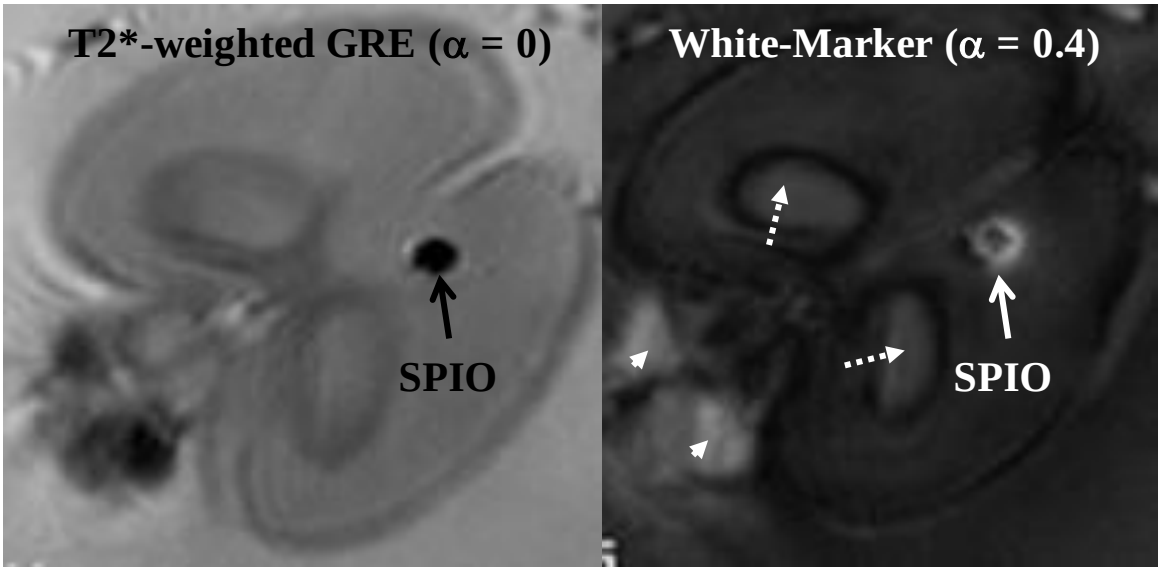

Figure 3.6: Negative and positive contrast of SPIOs in an excised mouse brain. Arrowheads depict non-SPIO regions that display positive contrast due to coincidental phase compensation. Although the phases of ventricles (dashed arrows) are not sufficiently compensated, they still exhibit substantial signal because of their high proton density.

The SPIOs are conspicuously visible in both gradient-echo and white-marker images. The signal in the unlabeled contralateral region is 112 units and 38 units for T_2^*-GRE and White-marker, respectively. Thus we can see that background signal is suppressed in White-marker due to incomplete gradient refocusing in the slice axis. Contrast-to-noise ratio, which is defined in eqn. (3.9), is - 48 and + 36, respectively based on region-of-interest (ROI) analysis. The reason for the lower contrast magnitude in white-marker is the T_2^*-effect of SPIO. A method to overcome such signal decay is the use of very short echo-times, which can be achieved with an ultra-short echo time (UTE) pulse sequence. This is the topic in the next section.

$$Contrast - to - noise\ ratio, CNR = \frac{S_{spio} - S_{ctrl}}{\sigma_{noise}} \qquad (3.9)$$

Where S_{spio} is the signal intensity in SPIO region-of-interest, S_{ctrl} is that in the contralateral region and σ_{noise} is the standard deviation of noise.

Advantages and disadvantages of White-Marker Imaging (WM)

The White-marker technique possesses some practical qualities that are absent in ORI and IRON sequences, which are high sensitivity, ease of implementation and high imaging speed (since gradient-echo imaging can be used). A mere multiplication factor has to be added to the slice-refocusing gradient amplitude in WM to achieve robust positive contrast (41). A recent comparison between IRON and White-marker imaging demonstrated the latter's higher sensitivity in detection of SPIO-labeled glioma cells *in vivo* (43). Its feasibility has been demonstrated in applications including the detection of ferritin deposition in *in-vivo*

thrombi (44) and cell tracking during stem cell therapy of the infarcted myocardium (45). There are a few limitations in the visualization of SPIO-labeled cells with White-marker though. First, dephasing appears to be relatively ineffective for voxels that are only partly occupied by observable spins. This partial volume effect could give rise to edge enhancement artifacts (46). Second, wherever the local field inhomogeneity is compensated, i.e., $\varphi(x, y, z, TE) = 0$, hyperintensity will result. Thus accidental local compensation of susceptibility-induced field gradients, e.g. in air-tissue interface or tissue boundaries, could be confused with actual SPIO-labeled cells. In addition, even though on-resonance protons are insufficiently refocused, they could still display signal if their spin density is sufficiently large. An example can be seen in Figure 3.6, whereby the ventricles in the brain display positive contrast, even though there is no SPIO-induced susceptibility effect. Therefore specificity is not optimal in White-Marker imaging. Third, since the SPIO-induced $\boldsymbol{B_0}$ field inhomogeneities are spatially varied in x, y and z directions, and only phases in the slice direction are compensated, not all surrounding spins would be refocused completely. This effect has already been predicted in the simulation (see Figure 3.5), whereby only specific protons exhibit positive contrast.

3.4 Positive Contrast with Multiple-Echoes Ultrashort-echo Time (MUTE)

In this section, we introduce a pulse sequence that would improve specificity and provide robust positive contrast of SPIO-labeled cells, which is the *Multiple-Echoes Ultrashort Echo Time (MUTE)*. To understand the positive contrast generating mechanism with MUTE, we shall first describe the signal evolution of SPIO-labeled cells and how they can be segregated from native tissue with positive contrast. Then the pulse sequence of MUTE is explained in detail including changes I adopted to cater for high field applications. As a demonstration of

MUTE's superiority in specificity and contrast, a comparative study was carried out with white-marker imaging. The effect of iron content per cell on detection sensitivity is also discussed.

3.4.1 Simulation Study of Positive Contrast Enhancement with MUTE

An expression for the spoiled steady-state incoherent (SSI) signal (also known as Fast Low Angle Shot or FLASH) (47) is:

$$S = \frac{kM_0\left(1 - exp\left(\frac{-TR}{T_1}\right)\right)\sin\theta}{1 - exp\left(\frac{-TR}{T_1}\right)\cos\theta} exp\left(\frac{-TE}{T_2^*}\right) \tag{3.10}$$

where M_0 is the magnitude of longitudinal magnetization at thermal equilibrium, k is a constant dependent on scanner performance and θ is the excitation flip angle.

We adopt a simple relaxation mechanism whereby SPIO lowers the T_1 and T_2^* of surrounding protons according to eqn. (3.11) and (3.12). T_1 and T_2^* are the respective observed longitudinal and transverse relaxation times of SPIO-labeled cells. T_{10} and T_{20}^* are that of unlabeled myocardium. r_1 and r_2 are the respective longitudinal and transverse relaxivities ($mM^{-1}sec^{-1}$) and [SPIO] is the concentration of iron-oxide nanoparticles (mM).

$$\frac{1}{T_1} = \frac{1}{T_{10}} + r_1[SPIO] \tag{3.11}$$

$$\frac{1}{T_2^*} = \frac{1}{T_{20}^*} + r_2[SPIO] \tag{3.12}$$

The cell of interest in the simulation is healthy rat myocardium, which has approximate relaxation times T_{10} = 950 ms and T_{20}^{*} = 36 ms at 9.4 T. To input an experimentally relevant concentration [SPIO], we assume an iron content of 16 pg per cell (26) and an intra-myocardial injection of 1 million cells in 20 μl (48), resulting in a total concentration of 14.3 mM. Together with the measured longitudinal and transverse relaxivities r_1 (1.21 $mM^{-1}sec^{-1}$) and r_2 (262 $mM^{-1}sec^{-1}$) of SPIO solution at 9.4 T (49), we calculated the signal intensity of labeled (S_{spio}) and unlabeled myocardium (S_{myo}) within an echo-time range of 0 to 10 ms, in 0.2 ms steps and at a *TR* of 150 ms. We also define contrast enhancement (CE) as the normalized signal intensity difference between S_{spio} and S_{myo}, according to eqn. (3.13). Assumed parameters in the simulation are M_0 = 1, k = 1 and θ = 60°.

$$CE = S_{spio} - S_{myo} \tag{3.13}$$

Figure 3.7A shows the simulation result, which illustrates the rapid signal decay of SPIO-labeled cells compared to the unlabeled myocardium. For typical gradient-echo sequences with echo-times of a few milliseconds, SPIO-labeled cells would translate as signal voids due to transverse relaxation effect. The plot also suggests that positive contrast (CE > 0) can be achieved if echo-time is kept below 0.35 ms. But in order to exploit the T_1-shortening effect of SPIO and maximize positive contrast, echo-time should ideally be as close to zero as possible. However, this might not be feasible because of hardware limitations such as gradient slew rate and amplitude (50). A more attractive alternative is to enhance positive contrast with a subtraction between the absolute FID and subsequent ECHO signal intensities (51). The difference signal intensity $S_{subtract}$ is given by eqn. (3.14). Post-subtraction contrast ($CE_{subtract}$) between labeled ($S_{subtract,spio}$) and unlabeled cells ($S_{subtract,myo}$) is then calculated

according to eqn. (3.15). In this simulation, we assumed that FID is acquired at TE = 0 ms and the echo-time of the ECHO is varied from 0 to 10 ms.

$$S_{subtract} = S_{fid} - S_{echo} \tag{3.14}$$

$$CE_{subtract} = S_{subtract,spio} - S_{subtract,myo} \tag{3.15}$$

Figure 3.7B plots the signal intensities and contrast after subtraction between FID (TE = 0 ms) and ECHO signals (TE = 0 – 10ms). Due to the dominant T_2^* shortening effect of SPIO, labeled cells had a much greater signal difference than unlabeled myocardium. This is advantageous because it implies high positive contrast is possible in SPIO-labeled cells with a subtraction between FID and the ECHO. We also observe that the contrast peaks at TE = 1.7 ms, beyond which no more detectable signal manifests from SPIO-labeled cells and contrast decreases gradually.

The minimum echo-time available for FID signal acquisition depends on the width of the excitation RF, and *k*-space sampling strategy (centric, spiral or Cartesian). To obtain maximum positive contrast via subtraction between FID and ECHO signals, the T_1 relaxation effect of SPIO must be exploited. In other words, the echo-time of FID has to be a minimum. Figure 3.7C illustrates the effect in contrast enhancement at different FID echo-times. The simulated results show that positive contrast increases to a maximum and decreases gradually for all the curves. The most significant observation is that maximum positive contrast decreases exponentially as FID echo-time increases (Figure 3.7D), owing to failure in exploiting T_1-shortening effect of SPIO.

This simulation highlights the potential of MUTE to generate and optimize positive contrast from SPIO-labeled cells. Three key conclusions are derived from this simulation study: 1) In order to maximize positive contrast with this technique, echo-time of FID has to be as low as possible. Thus RF excitation and refocusing gradients have to be very short, including utilization of centric *k*-space sampling, 2) subtraction between FID and ECHO signals could yield much higher positive contrast than mere reliance on FID, because it exploits the T_2^* dephasing effect of SPIO, and 3) ECHO acquisition must be carried out at optimal echo-time in order to obtain maximum positive contrast. This implies that meticulous timing considerations in the pulse sequence are necessary.

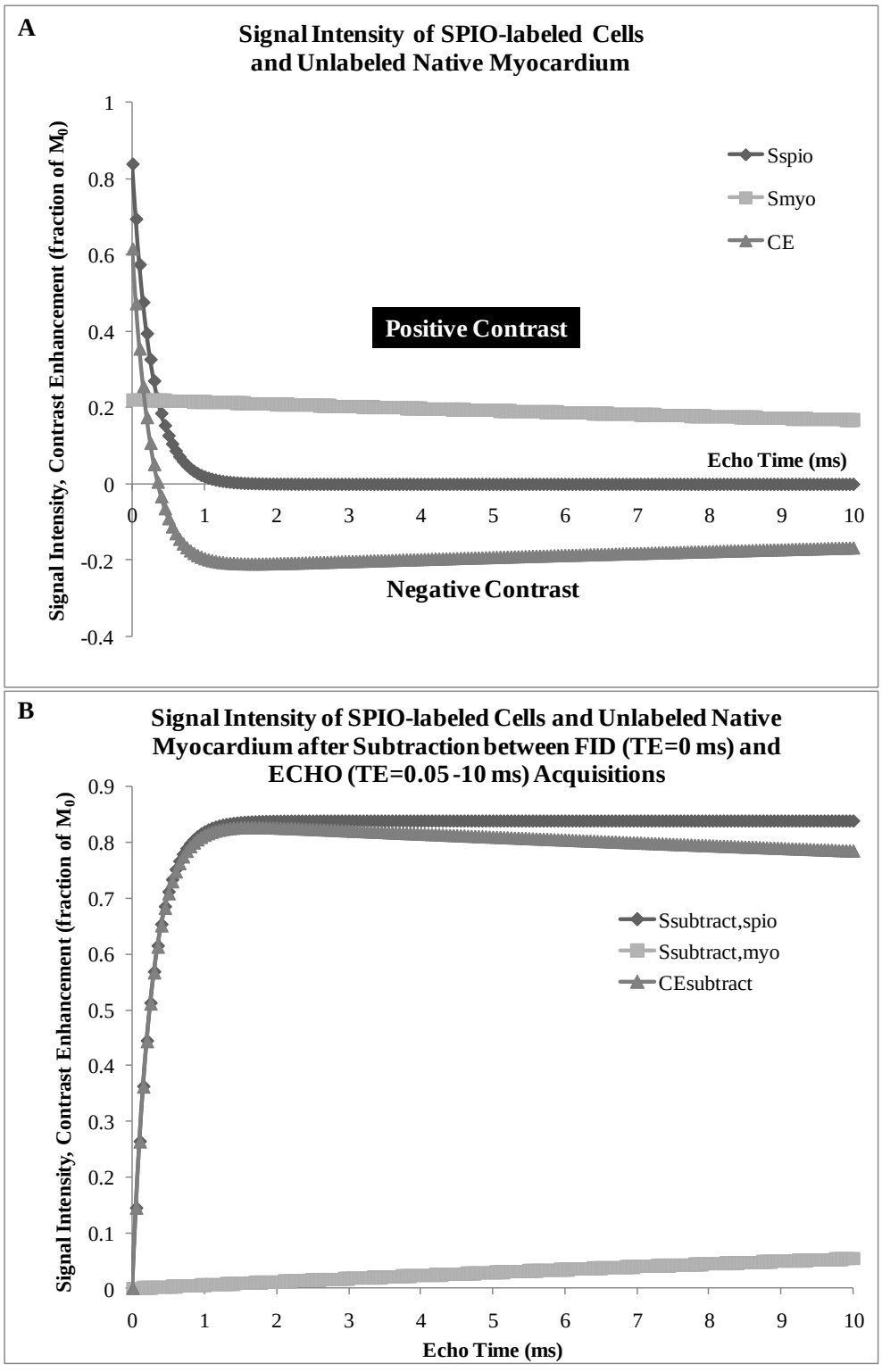

Figure 3.7: (A) Signal intensity of SPIO-labeled cells and unlabeled myocardium with echo-time. Positive contrast could be obtained if TE was shorter than 0.35 ms. (B) Subtracted signal intensity between FID and ECHO collected at different echo-times. Positive enhancement reaches a maximum 1.7 ms after excitation.

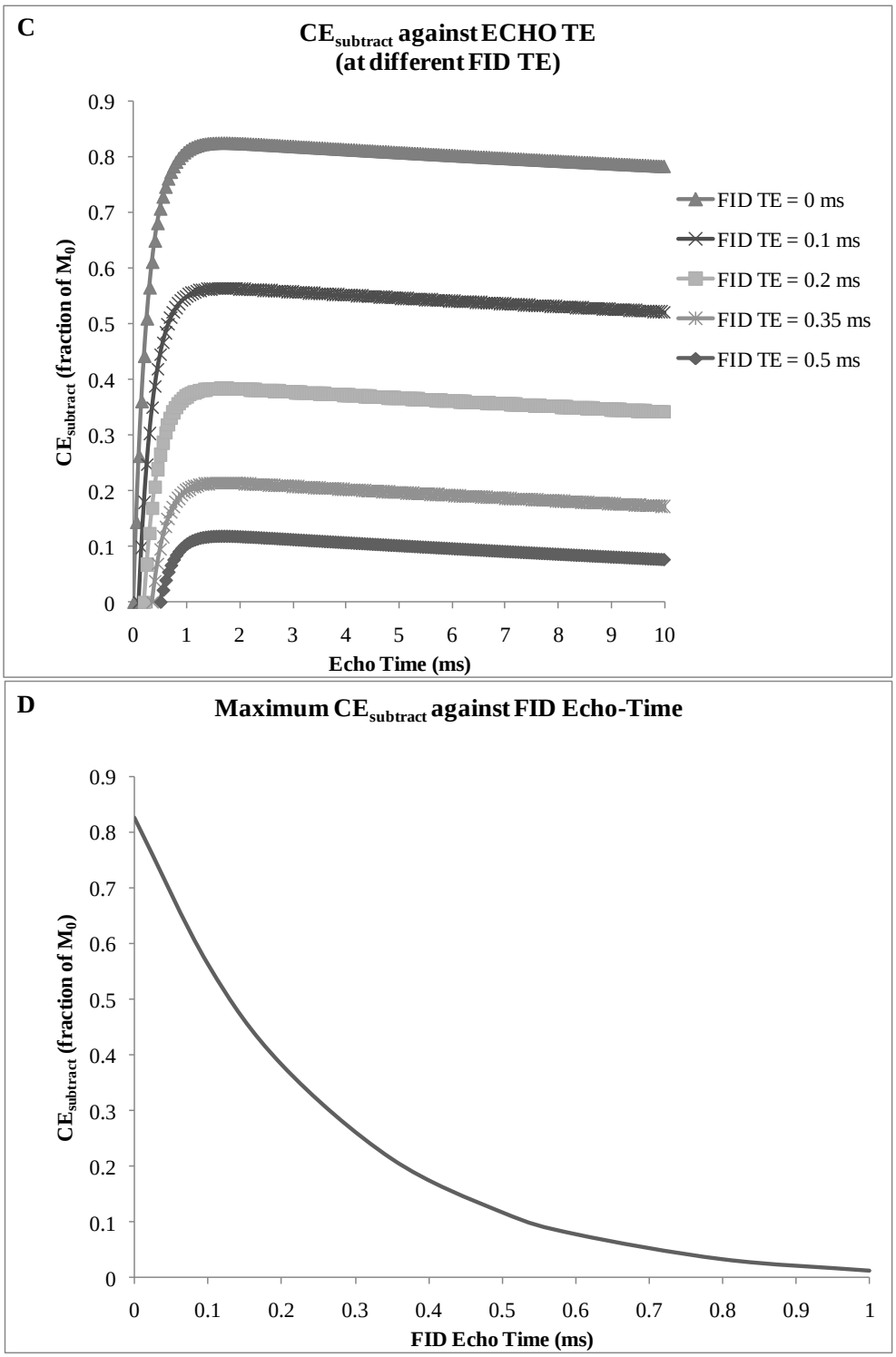

Figure 3.7: (C) Contrast enhancement curves as echo-time of FID is increased. (D) Exponential reduction in maximum positive contrast is seen as the FID echo-time increases.

3.4.2 MUTE Pulse Sequence

The multiple-echo ultrashort echo time (MUTE) pulse sequence was recently implemented in the clinic to visualize tissues with very short T_2 relaxation times, such as ligaments, tendons and bone (52-57). Its key feature is the ability to acquire MR signal at very short echo-times, potentially as low as 70 μs (58). Figure 3.8 displays the schematic diagram of a typical MUTE pulse sequence, comprising principle characteristics such as: 1) preparation pulses for fat saturation or inversion recovery to suppress long T_2 tissue components (59,60); 2) 2D or 3D excitation with dual polarity sinc pulses (61) or non-selective hard pulse (51,62); 3) slice or slab refocusing (for selective excitation only); 4) non-cartesian (spiral or radial) centric readout with high bandwidth for rapid acquisition of free induction decay signal (61,62); and 5) gradient refocusing readout to acquire subsequent echoes (51).

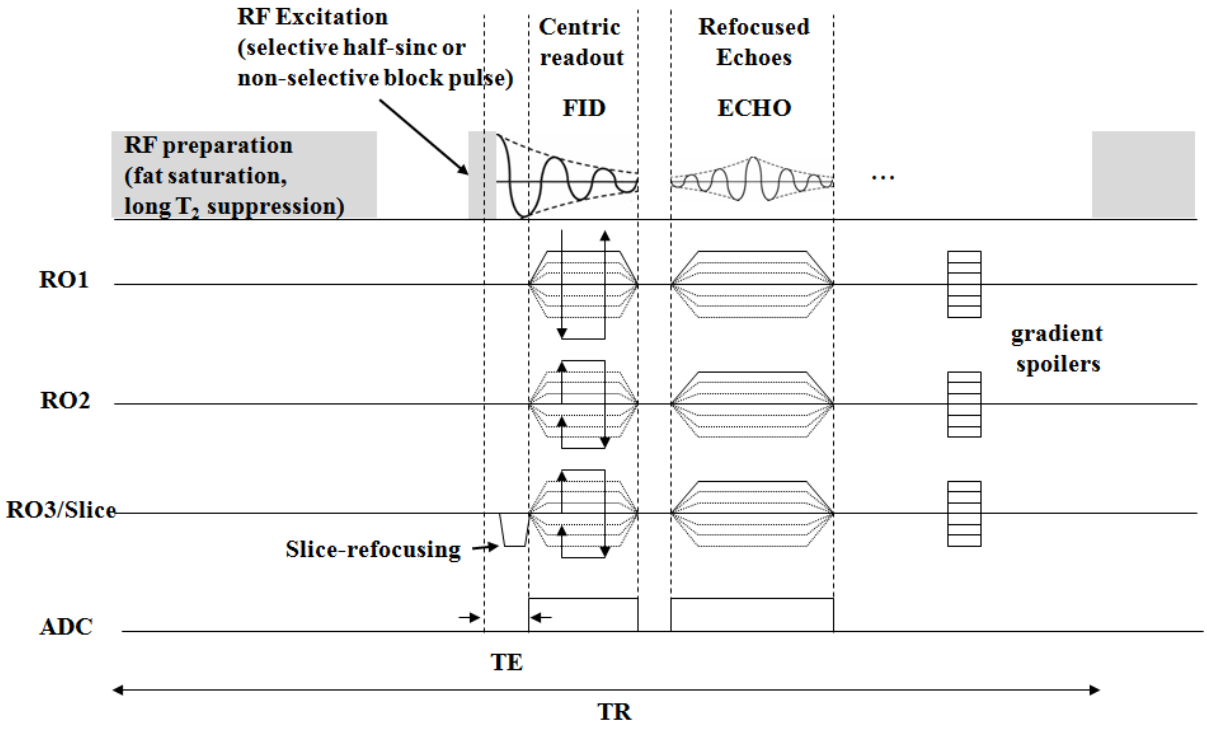

Figure 3.8: Schematic diagram of a MUTE pulse sequence. The essence of the technique is to enable the minimum echo-time allowed by the hardware.

Minimum Phase Shinnar Le-Roux – VERSE RF Excitation

The above pulse sequence characteristics work together to achieve the minimum allowable echo-time and enhance positive contrast of very short T_2 tissue components. Most of these features can be adapted in preclinical scanners with the exception of half-sinc excitation. This slice-selection scheme is particularly sensitive to gradient imperfections and eddy currents (63), resulting in poor slice profile at high magnetic field strength. In addition, two acquisitions with opposing slice gradient polarity are required to attenuate out-of-slice signal (61), doubling imaging time. To overcome this obstacle, I implemented a minimum phase Shinnar Le-Roux (SLR) pulse in our 9.4 T preclinical scanner instead (64). This excitation pulse induces minimum phase within the slice, demanding a shorter slice refocusing gradient that in turn directly reduces echo-time. In addition, the minimum phase SLR pulse enables slice selection with a single gradient polarity, unlike its half-sinc counterpart, therefore achieving similar scan efficiency as a normal T_2*-weighted sequence. As we strive towards even lower echo-time, the minimum phase SLR pulse is combined with the Variable-Rate-Selective Excitation (VERSE) algorithm to synchronize RF excitation pulse and slice selection gradient (60,65). This scheme is illustrated in Figure 3.9A, in which the time from RF peak amplitude to end of slice selection gradient (t_a) is 0.188 ms, compared to 0.572 ms in a SINC pulse with similar 1 ms duration. In our 9.4 T MRI preclinical scanner, the echo-time for a typical T_2^*-weighted gradient-echo sequence is approximately 2.46 ms, assuming field-of view of 30 mm, matrix size of 256 × 256, receiver bandwidth of 100 kHz and a symmetric SINC excitation pulse of 1 ms duration. In addition, the pulse induces a phase that is only about a third of that by the SINC pulse, as seen in Figure 3.9B. Thus the duration of the slice refocusing gradient can also be significantly trimmed. In summary, a minimum echo-time of 0.292 ms is achievable with our setup. Figure 3.9C compared the profiles of a 1 mm slice between typical SINC and minimum phase SLR-VERSE excitations. We observe that the

latter attenuates out-of-slice signal more effectively with diminished in-slice rippling as well, while preserving slice profile integrity.

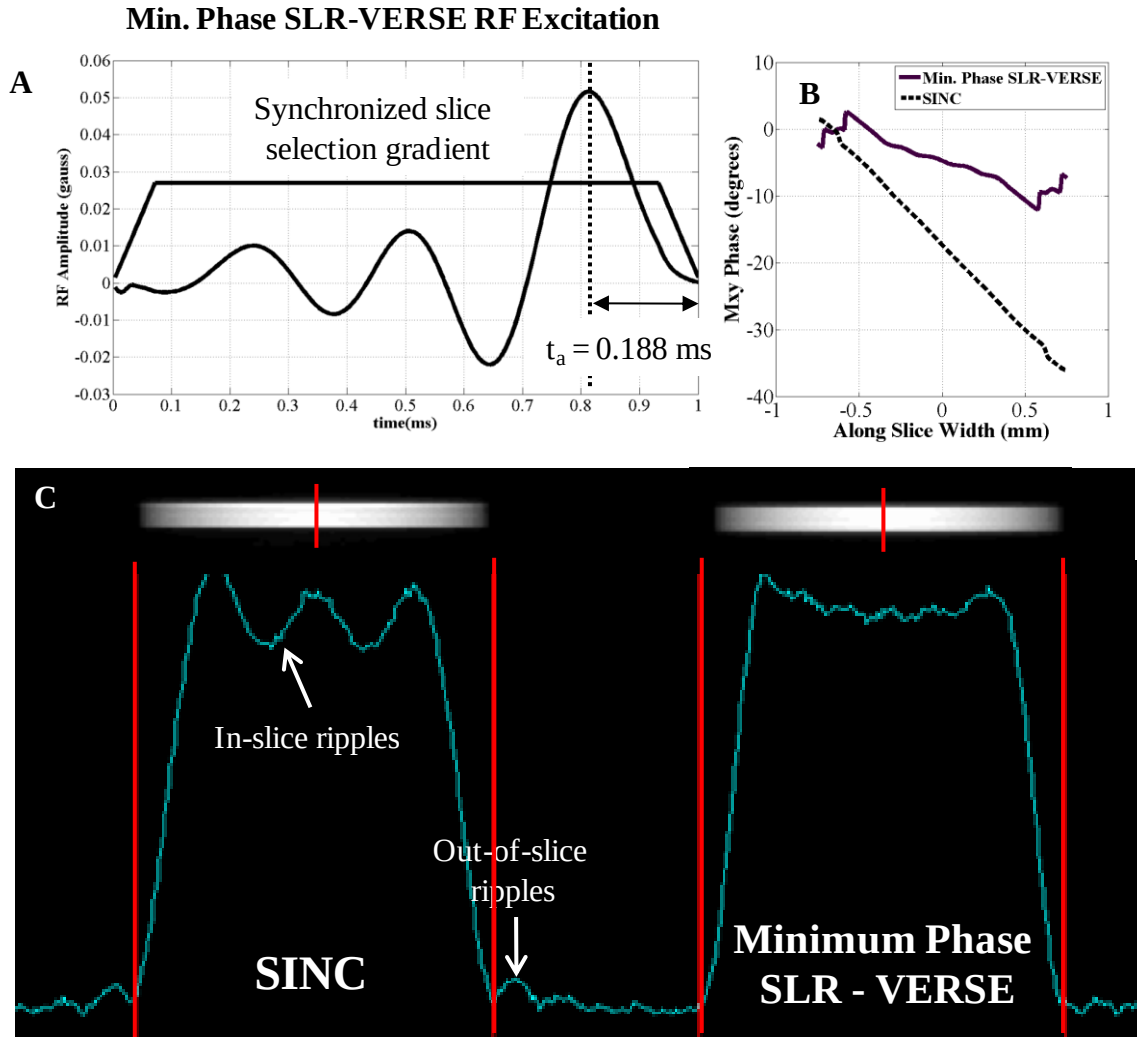

Figure 3.9: (A) Synchronized minimum phase SLR-VERSE excitation and slice selection gradient. (B) Phase accrued across slice that is subsequently nulled with slice refocusing gradient. (C) Profile comparison across a 1 mm slice between the two excitation pulses.

3.4.3 Radial Sampling

In order to minimize *TE* and T_2^* decay, center-out *k*-space sampling strategies are employed in UTE sequences (i.e. 1st data point is at $k = 0$). Popular sampling trajectories include radial (62,66,67), spiral (68-70) or their combination (61,71). In this thesis, we have employed a radial acquisition strategy because of its favorable intrinsic properties. First, it is robust against motion-induced artifacts (72-74). Second, the oversampling of *k*-space origin increases signal-to-noise ratio. Third, image reconstruction can be implemented using established filtered back-projection and regridding techniques. For 2D-MUTE imaging, the gradients involved in radial readouts are calculated according to:

$$G_x = G\cos\theta \tag{3.16}$$

$$G_y = G\sin\theta \tag{3.17}$$

$$G = \frac{BW_{receiver}}{\left(\frac{\gamma}{2\pi}\right)\cdot FOV} \tag{3.18}$$

Where G is the gradient amplitude applied during readout (in T m^{-1}), θ is the projection angle, $BW_{receiver}$ is the receiver bandwidth (in Hz) and FOV is the isotropic field-of-view (in m). Figure 3.10A illustrates this sampling strategy in *k*-space. In order to prevent aliasing and satisfy Nyquist sampling criteria, the following condition must be met (75):

$$n_r \geq 2k_{max}\cdot FOV \tag{3.19}$$

Where n_r is the number of radial readouts and k_{max} is the extent of occupied *k*-space. For 3D-MUTE, we adopted the stack-of-radial trajectory, as shown in Figure 3.10B, instead of spiral trajectory that is favored in the clinic (62,76). One of the reasons is the latter requires a large number of radial projections to meet the Nyquist sampling criteria. For example, a typical number of spiral projections for a spatial resolution of 8 mm^3 (FOV = 200 × 200 × 200 mm^3)

is ~ 31,000, leading to a total acquisition time of ~26 min (77), whereas only 15,700 radial projections are required with the stack of radials. In addition, we aim to implement MUTE for cell tracking in a rodent heart, which implies that very fast imaging and switching of gradients are necessary. Such scan conditions might induce eddy currents and cause mis-trajectories in *k*-space, leading to image artifacts (69,78). Since stack-of-radials consists of radial trajectories only on a plane, mis-trajectories can be more easily corrected than that in a 3D spiral.

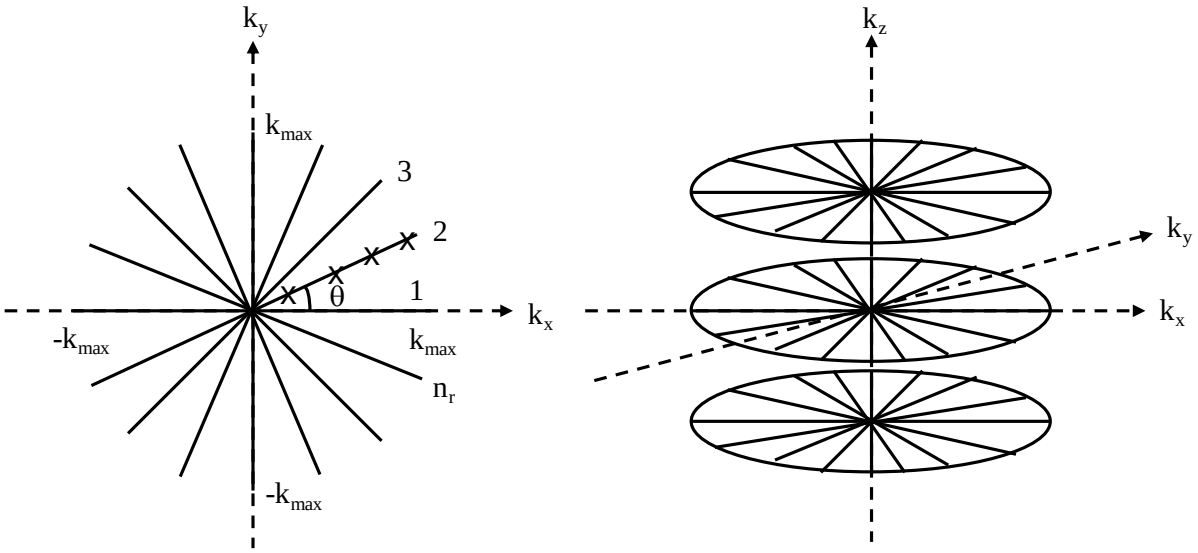

Figure 3.10: 2D-radial and 3D stack-of-radial sampling in MUTE. Crosses denote locations whereby sampled data are placed in *k*-space.

Point Spread Function (PSF)

A quantitative approach to describe image artifacts and to judge the effect of polar sampling is to calculate the point-spread-function (PSF). Ideally the PSF should consist of one delta function in the center of image space. However, real-world image artifacts induced by field inhomogeneities and gradient non-linearity occur and their cumulative effects can perhaps best be described by the broadening of the central peak (blurring), or side lobes (ghosts and aliasing). To understand the radial effects of polar sampling, the PSF can be broken up into two separate components, namely the PSF without decay $P_{sa}(r)$ and the blurring function induced by T_2^* relaxation $P_{blur}(r)$ (62). $P_{sa}(r)$ is essentially the behavior of the main lobe in the principal polar PSF profile (79) as given in eqn (3.20). When normalized to the unit pixel size π/k_{max}, its full-wdith half-maximum (FWHM) Δr_{sa} is 1.41 times an equivalent Cartesian acquisition (62). The blurring function on the other hand considers the impact of the short T_2^* with respect to the readout acquisition time T_{AQ} according to eqn. (3.21). Its normalized FWHM is then $0.49T_{AQ}/T_2^*$, therefore radial blurring becomes significant when readout time is much longer than T_2^*. Although very fast readout then becomes necessary to record the FID signal from SPIO-labeled cells, a caveat exists in that the required receiver bandwidth will be very large, resulting in lower signal-to-noise ratio, because SNR is proportional to $1/\sqrt{BW_{receiver}}$ (80). Fortunately, the center of *k*-space is oversampled and that could compensate the SNR. Numerical treatment of the blurring function suggests an optimal $T_{AQ} = 0.81 \cdot T_2^*$ for maximum SNR (62). As an example, the mean T_2^* of 16 million SPIO-labeled glioma cells is ~ 2 ms at 3 T (58), which would translate to an optimal T_{AQ} at 1.62 ms. The effective point spread function $PSF(r)$ is a convolution of these two components and is illustrated in Figure 3.11 together with $P_{sa}(r)$ and $P_{blur}(r)$. The resultant FWHM is

approximately 1 pixel unit. In summary, radial sampling results in imaging blurring which could be ameliorated at the expense of SNR.

$$P_{sa}(r) = 2\frac{J_1(k_{max}r)}{(k_{max}r)} \tag{3.20}$$

$$P_{blur}(r) = \frac{2\left(\frac{T_2}{T_{AQ}}\right)^2}{\left(1+\left(rk_{max}\frac{T_2}{T_{AQ}}\right)^2\right)^{3/2}} \tag{3.21}$$

$$PSF(r) = P_{sa}(r) \otimes P_{blur}(r) \tag{3.22}$$

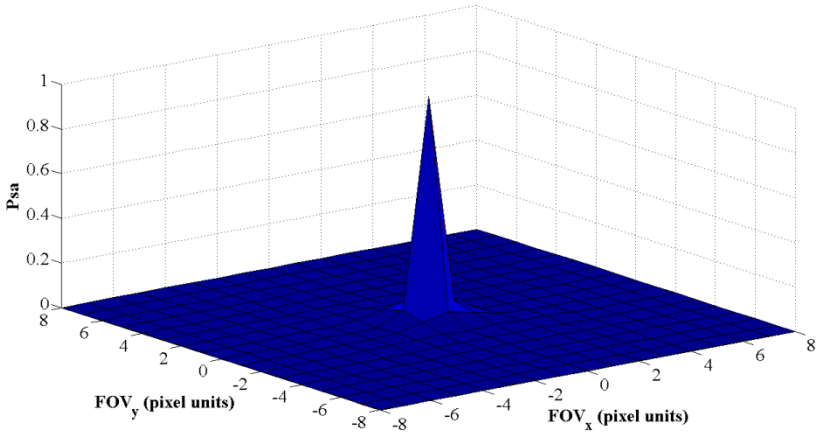

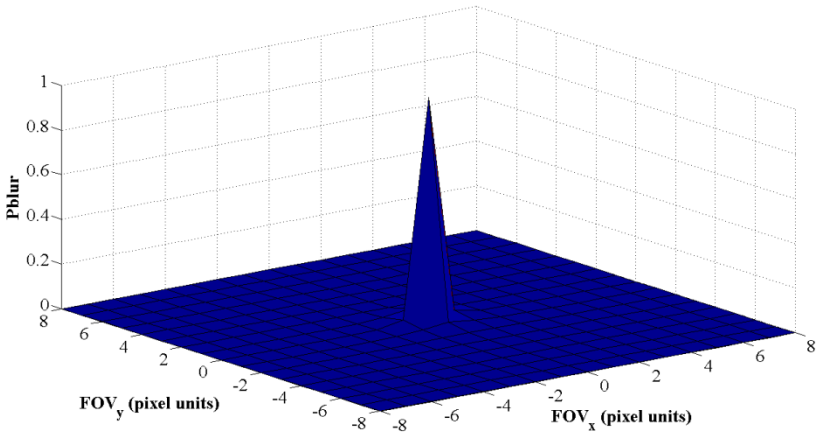

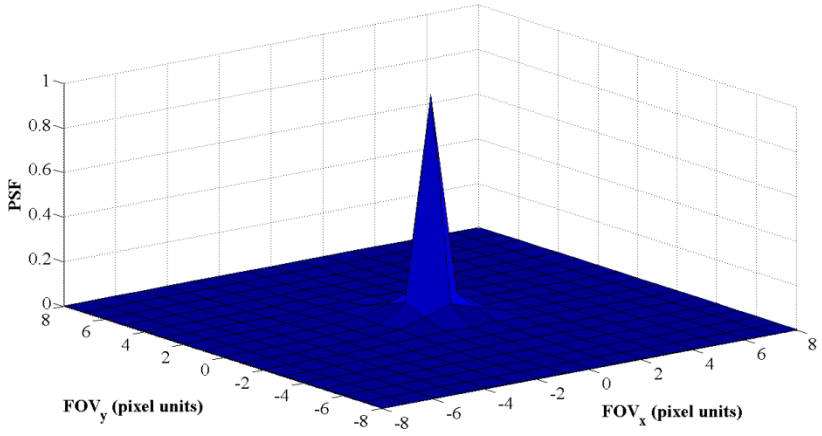

Figure 3.11: Point-spread-functions illustrate blurring of a single point in the center of image space as a result of radial sampling. $P_{sa}(r)$ is the PSF without decay, $P_{blur}(r)$ is that with T_2^* decay and PSF is the effective point-spread-function.

Disadvantages of Polar Sampling and Possible Remedies

There are a couple of disadvantages associated with radial sampling when compared to Cartesian acquisition. First, there is a 57 % increase in total scan time in accordance with Nyquist criteria. Under-sampling of k-space can be adopted though to improve scan efficiency without major artifacts (81). Streaking artifacts common in under-sampled radial data can also be reduced with iterative reconstruction (82). Second, gradient timing errors skew the k-space trajectory and introduce image artifacts (83), while magnetic field inhomogeneities distort image geometry (84). Measuring the actual k-space trajectory to correct for gradient non-linearity and eddy current effects can be applied (85). Third, image blurring in the point-spread-function is proportional to the T_{AQ}/T_2 ratio as illustrated above. Therefore ultrafast gradients are required to image SPIO-labeled cells with very short T_2^* (e.g. high cellular iron content or aggregated cell cluster). Fourth, such non-Cartesian sampling does not permit direct 2D Fourier Transform image reconstruction but rather via a technique

known as regridding. Regridding is a critical aspect in MUTE because it directly impacts the image quality and will therefore be discussed in detail in the following section.

3.4.4 Non-Cartesian Regridding

When the entire MR data set is acquired along a uniformly sampled rectilinear k-space trajectory, the image can be reconstructed using FFT. It is more complex to reconstruct non-Cartesian trajectories such as spiral and radial. Although non-rectilinear sampled *k*-space can be reconstructed with a straightforward extension of discrete fourier transform (DFT) (86), it is too slow for practical use. Alternatively, the data could be resampled into a regular Cartesian grid via convolution with a smoothing function, and then Fourier transformed to form an image. This technique is known as regridding (87,88) and is the most popular interpolation method employed because of its speed and adequate image quality.

The basic idea of regridding (89) is to convolve each data point with an appropriate gridding kernel, which is chosen to be wide enough to extend to neighboring grid points while maintaining reasonable computation time (90). This algorithm accumulates the contribution of each data sample to the surrounding grid points on the Cartesian mesh. After all samples have been processed, the regridded data are FFTed to produce a reconstructed image. Because convolution with the gridding kernel results in multiplication of the image by its FT, substantial shading will be present. This undesired artifact is eliminated by dividing the image by the FT of the kernel. Figure 3.12A illustrates the sampling procedure. In summary, the steps required for regridding are displayed in a flowchart presented in Figure 3.12B (91).

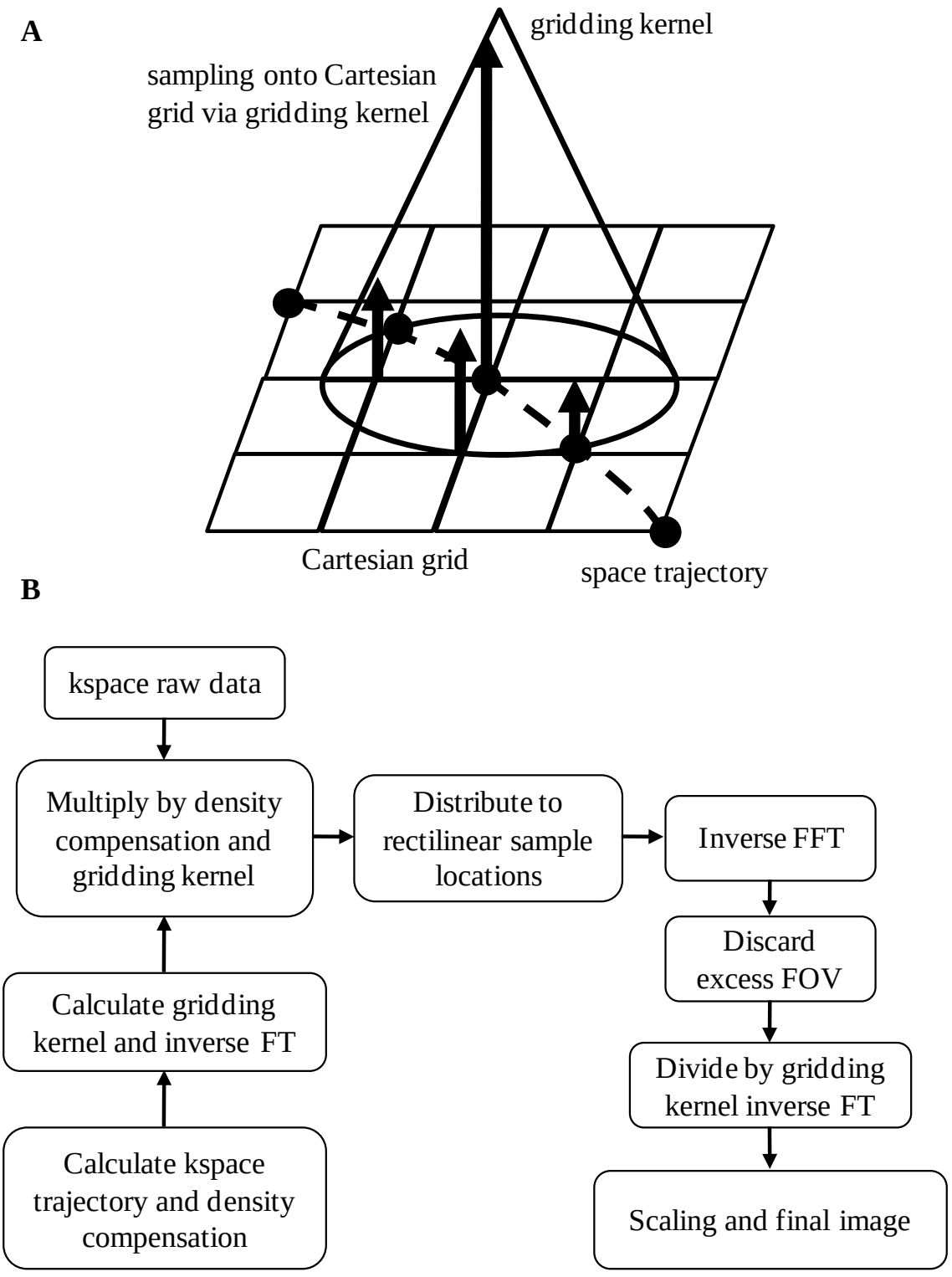

Figure 3.12: (A) Scheme of a 2D gridding procedure. The data samples lie on an arbitrary trajectory through k-space (dashed line). The sampled data points are convolved with a gridding kernel and resampled onto a rectilinear Cartesian grid. (B) Flow chart illustrating the regridding process.

Mathematical Description of 2D Regridding

The 2D version of regridding that has been implemented in this thesis can be described mathematically. The ideal continuous *k*-space data are $M(k_x,k_y)$. During acquisition, these data are sampled in a non-Cartesian fashion by a sampling function $S_{NC}(k_x,k_y)$ given by:

$$S_{NC}(k_x, k_y) = \sum_i \delta\left((k_x - k_{x,i}), (k_y - k_{y,i})\right) \tag{3.23}$$

where δ denotes the delta function. The resulting non-Cartesian data $M_{NC}(k_x,k_y)$ recorded are given in eqn. (3.24).

$$M_{NC}(k_x, k_y) = M(k_x, k_y) \cdot S_{NC}(k_x, k_y) \tag{3.24}$$

The regridding process begins by first defining a 2D Cartesian sampling function $S_C(k_x,k_y)$:

$$S_C(k_x, k_y) = \sum_p \delta(k_x - p\Delta k_x)\,\Delta k_x \sum_q \delta(k_y - q\Delta k_y)\Delta k_y \tag{3.25}$$

Where the k-space sampling distances are given by:

$$\Delta k_x = \Delta k_y = \xi / FOV \tag{3.26}$$

ξ is the k-space oversampling factor (ξ > 1) and FOV is the field-of-field, assumed to be the same in both *x* and *y* directions. Second, a gridding kernel $C(k_x,k_y)$ is defined and is usually either a SINC (87) or Kaiser-Bessel function (90) (more about the kernel function in the next section). $M_{NC}(k_x,k_y)$ is then convolved with the gridding kernel and sampled onto the Cartesian grid to yield the Cartesian sampled data $M_C(k_x,k_y)$:

$$M_c(k_x, k_y) = \left[M_{NC}(k_x, k_y) \otimes C(k_x, k_y)\right] \cdot S_c(k_x, k_y) \tag{3.27}$$

After 2D Fourier transform of the resampled Cartesian data, the resultant image obtained $m_c(x,y)$ is given by:

$$m_c(x,y) = \left[\left(m(x,y) \otimes s_{Nc}(x,y)\right) \cdot\ c(x,y)\right] \otimes s_C\left(\frac{x}{FOV_x}, \frac{y}{FOV_y}\right) \qquad (3.28)$$

Effects of regridding in image space

The effects of the various operations in eqn. (3.28) on the ideal image *m(x,y)* can be interpreted as follows: First, convolution with the radial sampling function $s_{NC}(x,y)$ induces image blurring. In addition, sidelobes are usually created due to the pattern of the samples in k-space. Second, the image is apodized by the transform of the gridding kernel. While this has the undesirable effect of producing shading in the image, it also has the advantage of suppressing the sidelobes that were generated by the convolution with the sampling function. Third, the rectilinear sampling in k-space creates replication in image space. Sidelobes from the first replication might interfere with the desired image. A 1D illustration of these effects on an ideal image is given in Figure 3.13.

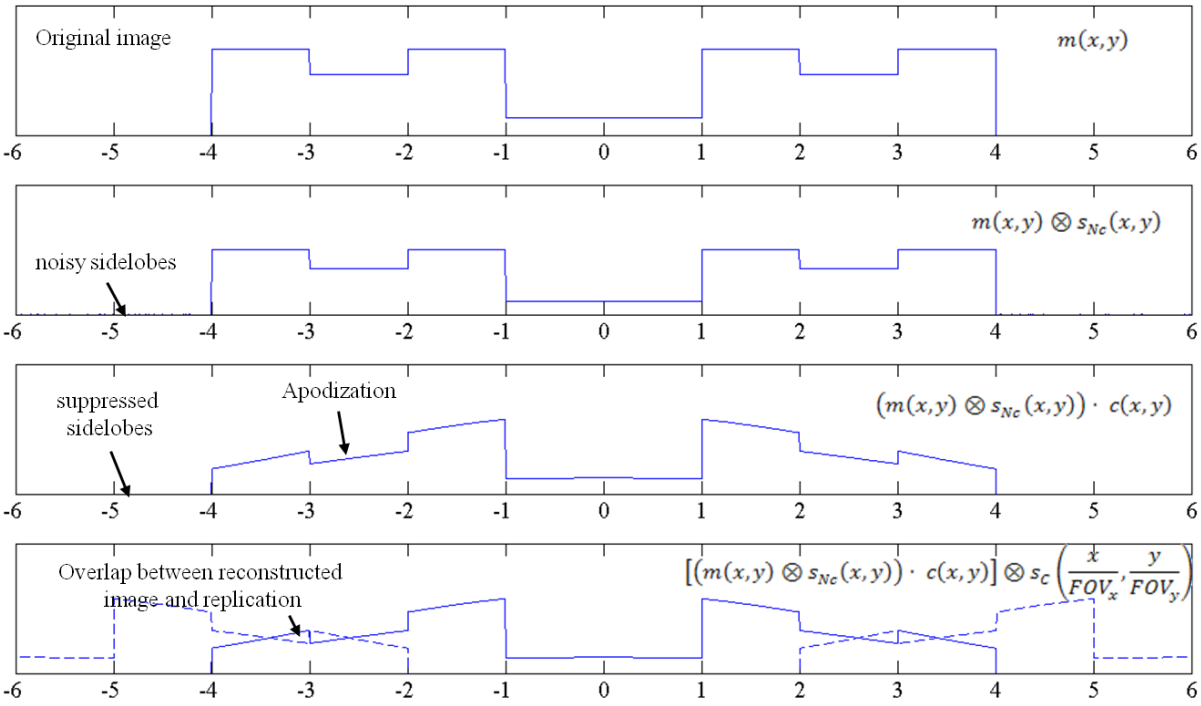

Figure 3.13: Effects of various terms in image regridding process given by eqn. (3.28)

Apodization and C(k_x,k_y)

The apodization function *c(x,y)* is the Fourier transform of the gridding kernel *C(k_x,k_y)*, and it causes undesired shading of the image upon multiplication. This function could be determined numerically and can be used to correct the artifact. Deapodization occurs by dividing the image by the ideal apodization function. In practice, however, it is preferred to divide out only part of the apodization in order to preserve the sidelobes attenuation. Hence in this thesis, the deapodization function applied has an attenuation factor *a* included:

$$d(x,y) = \frac{1}{c(x,y) + a} \tag{3.29}$$

The overall image reconstruction process then becomes:

$$m_c(x,y) = \frac{\left\{\left[\left(m(x,y) \otimes s_{Nc}(x,y)\right) \cdot\ c(x,y)\right] \otimes s_C\left(\frac{x}{FOV_x}, \frac{x}{FOV_y}\right)\right\}}{c(x,y) + a} \tag{3.30}$$

The selection of the gridding kernel has been addressed in the literature (87,88,90). The optimal gridding kernel is one whose Fourier transform is rectangular and band-limited like a sinc function, as given below.

$$Gridding\ Kernel, C\left(k_x, k_y\right) = sinc\left(\frac{k_x}{\Delta k_x}\right) sinc\left(\frac{k_y}{\Delta k_y}\right) \tag{3.31}$$

$$Apodization\ function, c(x,y) = rect\left(\frac{x}{FOV_x}\right) rect\left(\frac{y}{FOV_y}\right) \tag{3.32}$$

However, the infinite extent of a sinc function would prohibit efficient computation and hence a windowed sinc function is normally utilized instead (87). But convolution with a truncated sinc function will contribute side lobes, which are aliased back into the image after sampling onto the Cartesian grid. Therefore a compromise has to be met between computation time and aliasing artifacts. Jackson et al. has optimized this tradeoff, by

designing a Kaiser-Bessel convolution function (90). This 2D Kaiser-Bessel function is based on J_0, the zero-order modified Bessel function of the first kind. The separable gridding kernel used in this thesis, i.e. $C_{KB}(k_x) = C_{KB}(k_y) = C_{KB}(k_r)$, is thus:

$$C_{KB}(k_r) = \frac{1}{W_k} J_0 \left[\beta \sqrt{1 - \left(\frac{2k}{W_k} \right)^2} \right] \tag{3.33}$$

Where W_k denotes the kernel width and β is a free design parameter to achieve the best possible performance. The corresponding apodization function in the image domain is also separable such that $c_{KB}(x) = c_{KB}(y) = c_{KB}(r)$ and it is described by eqn. (3.34) .

$$c_{KB}(r) = \frac{sin\left(\sqrt{\pi^2 {W_k}^2 r^2 - \beta^2} \right)}{\sqrt{\pi^2 {W_k}^2 r^2 - \beta^2}} \tag{3.34}$$

As illustrated in Figure 3.13, subsequent sampling onto the Cartesian grid creates aliasing artifacts, thus oversampling is routinely implemented to resolve that, albeit an increase in computation time. One of the difficulties in designing a gridding solution is that a different gridding kernel (or β) must be chosen for each choice of oversampling ratio α and kernel width W_k. Beatty and co-workers have devised a formula to optimize the regridding process without major aliasing artifacts or loss in computation efficiency (88). That is to calculate β according to eqn. (3.35). With an oversampling ratio of 2 and a kernel width of 4, β is equal to 8.9962. The corresponding gridding kernel and apodization functions are illustrated in Figure (3.14).

$$\beta = \pi \sqrt{\frac{{W_k}^2}{\alpha^2} \left(\alpha - \frac{1}{2} \right)^2 - 0.8} \tag{3.35}$$

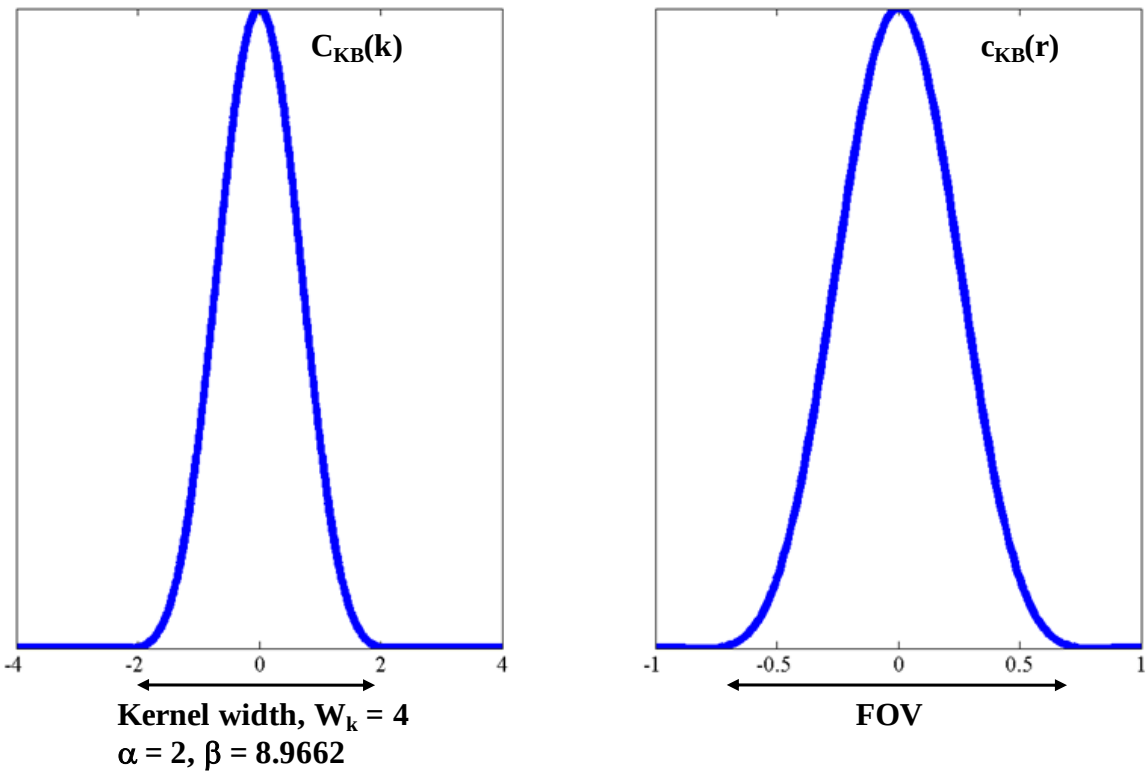

Figure 3.14: Kaiser-Bessel convolution function $C_{KB}(k)$ with kernel width W_k = 4, oversampling ratio α = 2 and free design parameter β = 8.9662. Next to it is the corresponding apodization function calculated according to eqn. (3.34).

Density Compensation

As shown in Figure 3.10, sampled data are placed along each radial spoke in *k*-space. Thus the sampling density is non-uniform, unlike a Cartesian acquisition, and must be corrected in order to minimize reconstruction error (92). An important first step in the gridding process is therefore weighting the data before interpolation to compensate for non-uniform sampling density. A weighting function $W(k_x,k_y)$ is multiplied with the radially sampled data before convolution with the gridding kernel, as described in eqn. (3.36).

$$M_c(k_x, k_y) = \left[\left(M_{NC}(k_x, k_y) \cdot W(k_x, k_y)\right) \otimes C(k_x, k_y)\right] \cdot S_c(k_x, k_y) \qquad (3.36)$$

The appropriate weighting function is proportional to the k-space area that is associated with each data sample. The area could be numerically approximated by the spacing of samples along the trajectory multiplied by the spacing between trajectories. Rasche et al. described an efficient algorithm to solve this problem known as a Voronoi diagram (93). Figure 3.15 displays the Voronoi diagram of the radial sampling pattern. A density estimate for each data point would be the area of each of the cells. This approach has the significant advantage that it only depends on the sampling pattern itself and not on the acquisition order. This allows the application to this technique even in cases where trajectories intersect (94).

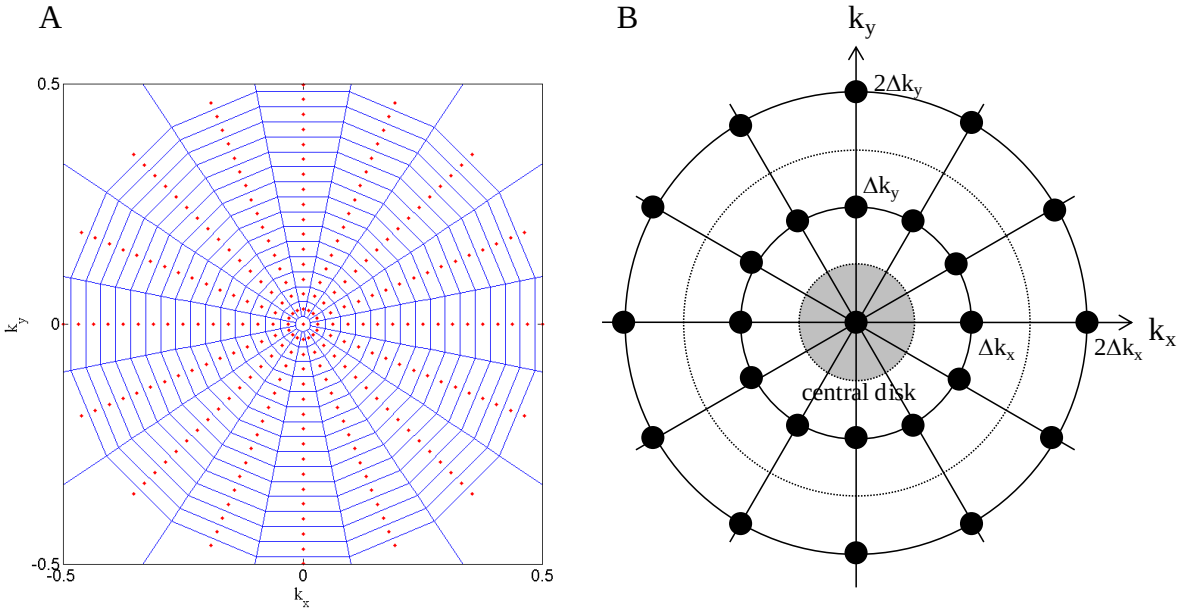

Figure 3.15: (A) Voronoi diagram divides the plane into regions that are closest to any individual point. The inverse area associated with each sample is its weighting. (B) Calculation of density compensation function for a projection data set.

An alternative method to obtain a weighting function is to assume an ideal isotropic 2D radial sampling pattern and calculate the area associated with each sample geometrically (89). This technique is straightforward and especially suitable for simple *k*-space trajectories such as radial projection. Referring to Figure 3.15B, samples are located along radii at multiples of $\Delta k_x = \Delta k_y = \Delta k_r$. The weighting to apply is the inverse of the sampling density $\rho(k_x,k_y)$, i.e.

$$W(k_x, k_y) = \frac{1}{\rho(k_x, k_y)} \tag{3.37}$$

If there are *N* projections, then the central sample is acquired *N* times. For this sample the weighting is *1/N* multiplied by the area of the central disk that is closest to the origin.

$$W_0 = \frac{1}{N}\pi\left(\frac{\Delta k_r}{2}\right)^2 \tag{3.38}$$

The weighting for the first sample is given by the area in the next annular ring outside the disk divided by the number of samples.

$$W_1 = \frac{1}{N}\pi\left[\left(\frac{3\Delta k_r}{2}\right)^2 - \left(\frac{\Delta k_r}{2}\right)^2\right] = \frac{2\pi}{N}(\Delta k_r)^2 \tag{3.39}$$

For samples that lie on subsequent annular rings, i.e., n > 1,

$$W_n = \frac{2\pi n}{N}(\Delta k_r)^2 \tag{3.40}$$

In this thesis, both Voronoi diagram and projection density estimation techniques are employed and would be specified in subsequent results where appropriate.

3.5 A Multi-Echo Technique for In-Vivo Positive Contrast Detection of SPIO-Labeled Cells in the Rat Heart at 9.4 T

We present here a multi-echo ultrashort echo-time technique that exploits the T_1-relaxation effect of iron-oxide to achieve positive contrast of SPIO-labeled cells with high sensitivity in a beating rat heart.

3.5.1 Introduction

Heart failure is the leading cause of death worldwide. The majority of such deaths are caused by ischaemic heart disease, which originates from obstruction of blood supply in the coronary arteries. Heart muscles then die giving rise to myocardial infarction and a loss of cardiac function. To compensate for the contractile loss in the infarct region, they are stressed harder, compounding the pathological condition. Although it has been suggested that endogenous regenerative mechanisms exist to repair the infarcted tissue, such as division of existing cardiomyocytes, bone-marrow stem cell mobilization into the injured myocardium and resident cardiac stem cells activation, it is found that the adult mammalian heart is severely limited in these aspects. Insufficient proliferation, inadequate mobilization, limited differentiation and restricted multi-potency are hurdles to myocardium self-renewal (95). To overcome this handicap, therapeutic cell treatment has been proposed. A myriad of stem cell phenotypes have been investigated for cardiac therapy such as embryonic stem cells, cardiac-derived stem cells (96) and endothelial progenitor cells (97). The precise amelioration mechanisms of these variant cell phenotypes, their functional integration and long-term physiological impact are currently being aggressively pursued in both animal models and human clinical trials.

Cell delivery to the infarcted myocardium critically impacts the success rate of the therapy. Many methods exist, each with their own strengths and weaknesses. Intravenous injection is minimally-invasive and convenient, but it suffers from homing issues. Intra-myocardial delivery directly positions the cells into the injured myocardium, but it requires invasive open chest surgery. Since cell number is a key factor in the mitigation of myocardial damage, a reliable and non-invasive imaging modality is essential to study the migration of transplanted cells as well as assess functional improvement.

A caveat to a negative contrast detection scheme is the misinterpretation of signal voids as transplanted cells. MR signal can be nulled by an array of factors including local magnetic field inhomogeneities, susceptibility artifacts and partial volume effects. The heart is especially vulnerable to such aberration because of its juxtaposition with lungs. Recently, we have demonstrated the use of ultra-short echo time imaging (UTE) to obtain positive contrast of SPIO-labeled mesenchymal stem cells injected into a mouse brain (98). By incorporating multiple-echoes and multiple-frame capabilities into the sequence, I was able to exploit both the T_1 and T_2 relaxation effects of iron-oxide to obtain high contrast-to-noise ratio of SPIO-labeled cells in the beating rat heart.

3.5.2 Materials & Methods

Multiple-echo Ultra-short Echo Time Pulse Sequence (MUTE)

An image was acquired at the shortest possible echo-time (hereby known as FID or UTE image). Subsequent refocused gradient echoes are collected by alternating gradient amplitude polarity and are referred to as ECHO. A cine-UTE sequence with multiple-frame acquisition

capability was also implemented whereby only the FID image was recorded for each frame in the cardiac cycle. The maximum number of frames possible in that setup was 20. Image reconstruction was carried out offline in Matlab with regridding. A Kaiser-Bessel interpolation scheme was employed with an oversampling factor of 2, free-design parameter β of 8.9962 and gridding kernel width of 4. The Voronoi scheme is used for density compensation in this study.

Cell isolation and labeling

Human mononuclear cells (MNCs) were collected by leukapheresis from peripheral blood of G-CSF-stimulated donors. They were washed twice with PBS, centrifugated for 10 min, plated in DMEM (Gibco, UK) and incubated at 37°C and 5% CO_2. After 2 h, non-adhered cells were discarded with the media replaced with fresh DMEM and 10% fetal calf serum (Invitrogen, UK). Cells were subsequently labeled with SPIOs (Endorem, Guerbet Laboratories, UK) by incubation with 45 μl ml^{-1} media for 24h. They were then trypsinized, washed twice with PBS and re-suspended.

Animal Preparation

All animal procedures were approved by the University College London Ethics Committee and the Home Office (London, UK), and conducted under the Animal (Scientific Procedures) Act 1986.

1 male Wistar rat (Charles River Ltd, U.K.) aged 7 - 8 weeks was anaesthetized with intra-peritoneal injection of Hypnovel-Hypnorm-water mixture (1:1:2, 2.5 ml kg^{-1}, Roche U.K., VetaPharma U.K.). Each animal had its body temperature monitored and maintained at 37°C during the surgery. They were then artificially ventilated with pure oxygen (Respirator, Harvard Apparatus Ltd, U.K.) at 1 L min^{-1}. A thoracotomy was performed in the 4th intercostal space following blunt dissection of the chest muscles to expose the heart. 5 x 10^5 and 2.5 x 10^5 of MNCs, were directly injected into the left myocardium wall at the apex and mid-ventricle, respectively. The chest was closed and spontaneous breathing was re-established. Animals were subsequently kept anaesthetized at 2% isoflurane for MRI.

Each anaesthetized animal was rested on a heating blanket in the animal cradle adopting the supine position. An electrocardiogram (ECG) was obtained via subcutaneous insertion of needle electrodes into the front limbs. Cardiac and respiratory monitoring and gating were performed using an MR-compatible system (SA Instruments, NY). Cardiac MRI was performed using a 9.4T (400 MHz) horizontal bore system (Varian Inc. Palo Alto, CA) with a shielded gradient system (strength = 400 mT m^{-1}, slew rate = 2667 mT m^{-1} ms^{-1}). A 72 mm quadrature volume coil was used for transmission and a cardiac phased array coil (Rapid Biomedical GmbH, Germany) was placed over its chest for reception.

Ex-vivo Sample Preparation

The rats were sacrificed after MRI. Their hearts were excised, perfused with PBS and followed by 24 h fixation in 4% PFA at 5°C. They were then placed in increasing sucrose gradients (10, 20, and 30 %) and finally embedded in 1 % agarose.

In-vivo Tracking of SPIO-Labeled Cells with Cine-UTE

An axial slice across the left ventricle where the SPIO-labeled cells were injected was acquired with cine-UTE. A corresponding gradient-echo image (GRE) was also acquired using the lowest possible echo-time and typical sequential Cartesian readout. Region-of-interest analysis was implemented in ImageJ in which an area of 5.4 mm^2 enclosing the SPIO-labeled cells was chosen in each image, and its mean amplitude recorded as S_{spio}. Similar ROI measurement was performed in the unlabeled myocardium to yield S_{myo}. The standard deviation of noise σ_{noise} was obtained for the muscle. All three regions are indicated in Figure 3.16A. These values were then used to calculate the contrast-to-noise ratio (CNR) according to eqn. (3.9).

Critical scan parameters were: TR = 7.5 ms, TE = 0.26 ms (cine-UTE) and 1.22 ms (GRE), regridded matrix size = 256 x 256, number of radial projections in cine-UTE = 403 (satisfying Nyquist criteria), Field-of-view (FOV) = 55 × 55 mm, in-plane image resolution = 215 × 215 μm, receiver bandwidth = 50 kHz, flip angle = 12°, slice thickness = 1.5 mm, number of frames = 15, number of averages = 3, total scan time = 2 min.

Ex-vivo MRI with MUTE

A more powerful gradient insert (strength = 1000 mT/m, slew rate = 7700 mT/m/ms) was utilized in this experiment to reduce echo time. Long axis left-ventricle views of the excised heart were acquired with a MUTE pulse sequence. ROI analysis was subsequently carried out on the two injected sites, namely LV and APEX. Each ROI was about 30 mm^2 and standard

deviation of noise was measured in the agar embedding the sample. Contrast-to-noise ratio was calculated according to eqn. (3.9). Critical scan parameters were: TE = 0.18 ms (FID), echo-interval = 2.79 ms, TR = 20 ms, number of echoes = 3, regridded matrix size = 256 × 256, number of radial projections = 403, FOV = 40 x 40 mm, in-plane image resolution = 156 × 156 μm, receiver bandwidth = 100 kHz, slice thickness = 1.0 mm, number of averages = 3, scan time = 24 s per slice. A 40 mm quadrature volume coil was used for transmit and receive. Images were cropped to 29 mm × 18 mm for display.

3.5.3 Results

In-vivo Tracking of SPIO-Labeled Cells with Cine-UTE

Figure 3.16A displays the FID image at the 7th frame of the cine-UTE MRI, i.e., during mid-diastole, in which the SPIO-labeled cells at the apex were distinctly identified with positive contrast. UTE imaging exploited the attenuated-T_1 relaxation time of SPIO-labeled cells to provide a superior contrast-to-noise ratio of + 21.1. For the Cartesian GRE image on the other hand, although the minimum allowed echo-time was chosen, it is still insufficiently short to give positive contrast, resulting in a signal void.

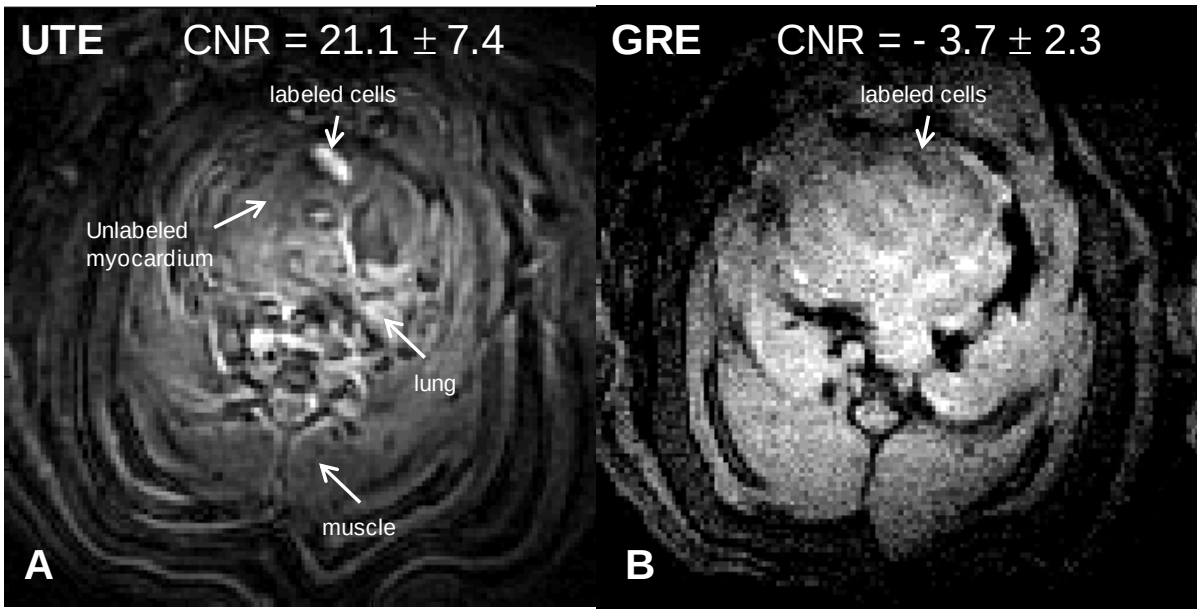

Figure 3.16: The selected slice is near the apex of the heart where the cells were injected. (A) UTE, and (B) GRE images of the 7th frame in the cine-MRI. Regions-of-interest are chosen at the labeled cells, unlabeled myocardium and muscle. Contrast-to-noise ratios were calculated according to eqn. (3.9). Lung is visible in the UTE image as a direct consequence of the ultrashort echo-time.

Ex-vivo MRI with MUTE

Figure 3.17 illustrates the FID, ECHOs (acquired at TE = 2.56 ms and 5.12 ms, respectively) and their subtracted images in the excised heart. Table 3.1 presents the measured contrast-to-noise ratio at the injected regions labeled as *LV* and *APEX* respectively. At the LV region, positive contrast in the FID image (TE = 0.18 ms) was +0.2, against the negative contrast ECHOs of -4.9/-8.9 at echo time of 2.56/5.12 ms respectively. When subtraction is performed between FID and the 1st ECHO, positive contrast is significantly boosted to 2.5 and 4.5 at the mid-left ventricle and apex sites respectively. When the same subtraction procedure is performed with the 2nd ECHO, enhancement is further boosted to 19.6 and 22.7, respectively.

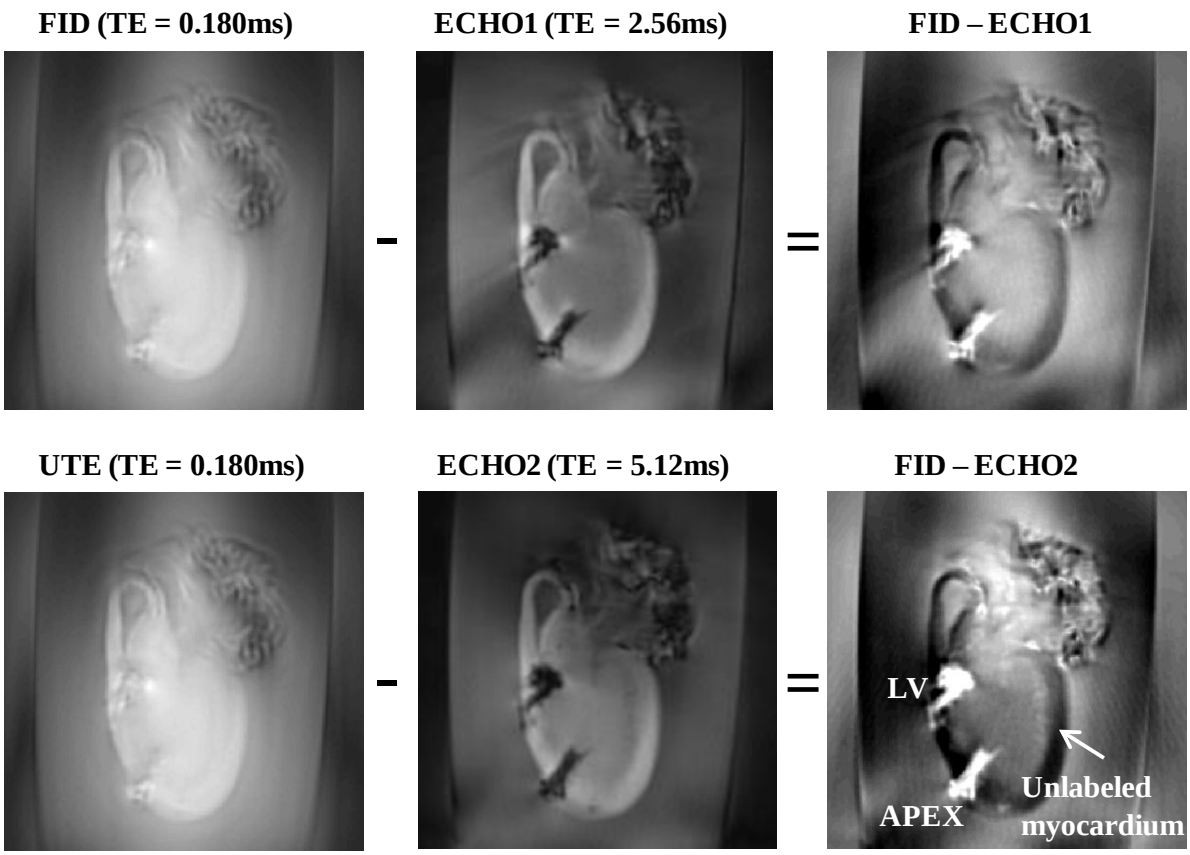

Figure 3.17: MUTE MRI of the excised rat heart depicting the FID, ECHO and their subtracted images. LV and APEX are regions in the left ventricle where the SPIO-labeled mononuclear cells were injected.

Contrast-to-Noise Ratio	LV	APEX
UTE (TE = 0.208ms)	0.2	0.1
ECHO1 (TE = 2.56ms)	-4.9	-9.3
ECHO2 (TE = 5.12ms)	-8.9	-10.6
UTE-ECHO1	2.5	4.5
UTE-ECHO2	19.6	22.7

Table 3.1: Contrast-to-noise ratios of injected SPIO-labeled cells in the rat myocardium showcase the boost in positive contrast upon subtraction between a UTE image and that of a subsequent ECHO.

3.5.4 Discussion

This is the first report of visualization of SPIO-labeled cells with positive contrast in a beating rat heart. The high contrast-to-noise ratio of 21.1 ± 7.4 illustrated the good sensitivity of UTE in the in-vivo detection of iron-labeled cells. We also observe that the image quality in UTE is higher than that in the Cartesian gradient-echo image, and this is attributed to its oversampling of *k*-space origin. An added advantage of our UTE sequence is that the built-in multiple-frame capability could facilitate cardiac function measurements (99), enabling simultaneous cell tracking and functional studies. At first glance, it would appear that ex-vivo UTE MRI of the excised heart displayed disappointing positive contrast enhancement in the FID image, especially at the injected site with 5 x 10^5 cells. A couple of factors contributed to this dismal performance. First, the echo-time was not short enough leading to failure in exploiting T_1-relaxivity effect of SPIOs. The importance of achieving very short echo-time has already been described in Figure 3.7A, especially in high iron content environment (49). Second, a higher cell concentration at the apex implied elevated iron–oxide content and hence a more severe T_2^* decay is present, evident from its more negative contrast (-9.3 at APEX versus -4.9 at LV). At high field, r_2/r_1 ratio is large (100), and thus transverse relaxation outcompetes its longitudinal counterpart when echo-time is insufficiently short. This resulted in reduced signal and diminished positive contrast. At a longer echo time of 5.12 ms, the hypointensities escalated and increased negative contrast. Fortunately, one of the MUTE features is the exploitation of increased T_2^* effect via a subtraction between the FID image, which is heavily T_1-weighted and an ECHO image, which is heavily T_2^*-weighted. As evident in Table 3.1, this method propelled the achievable positive contrast by as much as 12 and 45 times at the LV and APEX, respectively. Further exploitation of T_2^* effect of SPIOs was achieved by subtracting FID and the later ECHO. That further boosted the positive contrast by 98 and 227 times, respectively. Thus higher cell concentration resulted in greater contrast

enhancement with MUTE. That could perhaps serve as a cell number quantification measure. Simulations in Figure 3.7D suggested that FID echo time should be as close to zero as possible to maximize positive contrast. To attain that goal, we could utilize 3D MUTE acquisition with a non-selective hard pulse (62), albeit at a cost to total scan time and image reconstruction computation time. Advancement in gradient hardware with higher slew rates and faster ramp times could ultimately lower echo-time too.

Although cardiac infarction therapy with stem cells is usually detected with T_2^*-weighted MRI, it is difficult to discern between the infarcted region and delivered cells since they both appear as hypointensities (101,102). However, since only SPIO-labeled cells exhibit enhanced T_1-relaxivity but not infarcted tissue, MUTE could possibly separate these two entities. Increasing intracellular SPIO concentration by employing nanoparticles of higher relaxivities, increasing SPIO incubation time or more efficient transfection would introduce larger changes in R_1 and R_2^*, aiding delineation of labeled cells (26,103). Discovering cellular viability and function in-vivo is also a profound task that cell therapists covet (104). Unfortunately, current MRI cell tracking techniques do not provide such information. Passive cell labeling with SPIOs would have to be substituted with SPIO agents that target or report viable cells such as overexpression of endogenous ferritin (105,106). MUTE could then be employed to differentiate between viable and apoptotic cells, for example.

3.5.5 Limitations of the Study

Although cell number is key information in monitoring therapeutic cell treatment efficacy, no attempt has been made in this work to quantify cell population with MUTE. Cell

quantification in T_2^*-weighted MRI usually relies on a inverse relationship between changes in transverse relaxation R_2^* and cell number (107). But this is confounded when cell concentration is too high and T_2^* becomes excessively low. Liu and co-workers have recently demonstrated the ability of UTE to measure very short T_2^* of SPIO-labeled cells and displayed a qualitative relationship between T_2^* and cell concentration at 3T (58). Thus MUTE possesses the potential for in-vivo cell quantification. Even though positive contrast detection of SPIOs was successful in this study, their biological microenvironment was unknown. MUTE only sensed the presence of SPIOs but could not differentiate between intracellular SPIOs, extracellular nanoparticles that were not washed out during cell labeling processes or cells that die upon injection into the myocardium and are subsequently taken up by macrophages (108). In addition, free iron could also be found at injected sites where hemorrhage is often present, and that would confuse detection of labeled cells (109). It has been suggested that the compartment (intra- or extracellular) that SPIOs reside in affects their R_2 relaxation rates and this physical parameter could perhaps be utilized to distinguish between free iron and intracellular SPIOs (110). Another limitation is that the rats were sacrificed immediately after MRI and longitudinal scans were not performed. As cells divide and proliferate, the iron content would become diluted and reduced detection sensitivity. Thus the minimal iron content for in-vivo positive contrast detection with MUTE would have to be investigated to facilitate prolonged studies.

3.5.6 Conclusion

This is the first study that enabled in-vivo positive contrast visualization of infused SPIO-labeled cells in a beating rat heart with a multiple-echo UTE technique. Subtraction between images acquired at ultrashort and long echo-times could boost contrast by as much as 227-

fold. Higher cell number increased transverse relaxation rate and stressed the importance of very short echo time to exploit the T_1-effect of SPIOs.

3.6 In-Vivo Positive Contrast Tracking of Bone Marrow Stem Cells with Superparamagnetic Iron Oxide Particles: Is Bigger also Better?

Bone marrow-derived mesenchymal stem cells (BMSCs) possess tremendous therapeutic potential because of their capacity to differentiate into multiple functional lineages including chondrocytes, osteocytes, adipocytes and myocytes (1). To assess the efficacy of BMSCs cell therapy, MRI methods are being developed to monitor their bio-distribution in longitudinal therapeutic studies. Superparamagnetic particles are currently the most popular magnetic sensors incorporated into exogenous cells. They could also be supplemented with fluorescent dyes for optical detection. One of the pivotal design parameters of such particles is the amount of iron content, which would determine their detection sensitivity. In this work, we compared the in-vivo positive contrast that could be achieved between BMSCs labeled with ultra-small IODEX-TAT-FITC nanoparticles (20 nm in diameter) and micron-sized iron-oxide particles (MPIO, 0.96 μm), using a multiple-echo ultrashort echo time (MUTE) technique.

3.6.1 Introduction

Adult bone marrow stem cells are multipotent biological entities that have the potential to differentiate into a myriad of phenotypes. Two populations of bone marrow cells exist, namely hematopoietic stem cells (HSCs) which give rise to mature lineages of blood, and mesenchymal stem cells (MSCs). Studies have investigated the plasticity of BMSCs and

found that they possess the ability to differentiate into cardiac muscle, endocrine cells as well as central nervous system phenotypes such as neurons and glial cells (111). Their therapeutic potential has been demonstrated in many repair and regeneration studies including myocardial infarction (112,113) and neurodegenerative diseases (114). Their ability to migrate extensively across the brain has also led to suggestions of a vehicular role in cell and gene therapy (115).

In order to develop effective cell therapies, the location, distribution and long-term viability of the implanted cells must be determined in a non-invasive manner. Superparamagnetic iron oxide particles are non-toxic and biocompatible intracellular labels that act as beacons in MRI. They could be easily incorporated into BMSCs via incubation (116) or transfection (117). There are many different types of SPIO particles that are distinguished by their physicochemical properties such as size, coating, proton relaxivities, biocompatibility, stability and biotoxicity (18). As far as MR sensitivity is concerned, the iron content per cell determines its ease of detection (118). Successful infiltration with a transfection agent could yield an iron content as high as 30 pg per cell (26). Ultra-small SPIOs (USPIOs) have very small iron cores of ~ 15-30 nm and are easily incorporated into the cells via endocytosis. In fact, their accumulation in cells gives rise to such a high iron concentration that as low as 3 - 50 cells detection is possible in-vivo (119,120). A particular attractive USPIO particle is that of an iron-oxide core with a dextran coating that is conjugated to HIV-derived transactivator of transcription (TAT) peptide (121). TAT-peptide has been demonstrated to promote cellular uptake of a myriad of biomolecules and its use as a transfection system enables high labeling efficiency with minimal incubation time (22). The peptide also includes fluorescein isothiocyanate or FITC, which serves as a fluoroprobe for in-vitro detection. Such dual-labeled contrast agent permits identification of the cell population in-vivo as well as at the

microscopic cellular level. A major drawback of USPIOs is that each nanoparticle has very low iron content and millions of particles would have to be present within a voxel for detectability. Thus cells must either be heavily loaded with USPIOs, which might undermine their migration and viability, or an aggregation of cells must be present within the voxel, which decreases sensitivity. In addition, cellular division might dilute the label below the detection limit. An alternative compound is the much larger micron-sized iron oxide particles (MPIOs). They have a range of diameters from 0.96 to 5.8 μm and are able to achieve an intracellular iron content of approximately 100 pg, which is three-fold higher than USPIOs (25). This has created a new frontier in single cell detection with high resolution MRI (122). BMSCs are highly proliferative cells and it has been demonstrated that they are equally distributed between two daughter cells during division (123) and thus could be tracked for prolonged periods of time. For example, bone marrow stem cells labeled with MPIOs and injected into infarcted myocardium have been shown to be detectable with MRI beyond 16 weeks (124).

This study aimed to compare the in-vivo positive contrast generation between the two types of SPIOs injected into a rat brain, USPIO – bifunctional contrast agent dextran-coated iron-oxide nanoparticles (IODEX-TAT-FITC) of diameter 15 nm (121) and MPIO - an aggregate of iron oxide magnetite mixed with a fluorophore and encased within an inert polymer shell with a much larger diameter of 0.96 μm (123).

3.6.2 Materials and Methods

BMSC Culture

Bone marrow-derived BMSCs were harvested from femurs and tibias of adult male Wistar rats. The cells were seeded in high-glucose Dulbecco's modified Eagle's medium with L-glutamine supplemented with 10% foetal bovine serum and 25 μg mL^{-1} gentamicin on poly-L-lysine coated flasks. Culture media was replaced every 2 days. Haematopoietic and other non-adherent cells were removed during medium changes. After 10 to 14 days of primary cultivation, the adherent cells were nearly 80% confluent and were dissociated with 0.25% trypsin and 1 mM EDTA and re-plated to expand the cells through successive passages.

In-Vitro Labeling with IODEX-TAT-FITC

TAT-peptide derivatized ultra-small superparamagnetic iron oxide (USPIO) nanoparticles coated with dextran (IODEX-TATFITC; 15–20 nm) were prepared in our laboratory by Dr. Bhakoo Kishore using the method described by Josephson et al. (125). Briefly, the dextran coated USPIO nanoparticles were synthesized and subsequently conjugated with TAT-fluorescein isothiocyanate (FITC) peptide. TAT-FITC was synthesized by the using FMOC-protected amino acid (2-(1-H-Benzotriazol-2-yl)-1,1,3,3-tetramethyluronium hexafluorophosphate; HBTU) activation chemistry. The final iron concentration was 2.5 mg mL^{-1} and the solution was sterilized by γ-irradiation prior to use. A group of BMSCs were labeled at passages 4–6 with IODEX-TAT-FITC by incubation for a minimum of 4–6 h with 10 μg/10^5 cells of the iron-oxide nanoparticles per ml of culture medium (121). The final iron concentration was 21 pg /10^5 cells (Olympus Diagnostic Iron Kit, UK). The BMSCs were

dissociated from the cell culture dishes with 0.25% trypsin in 1 mM EDTA and re-suspended in PBS.

In-Vitro Labeling with MPIO

Superparamagnetic divinyl benzene inert polymer microspheres were obtained from Bangs Laboratories (Fishers, IN). The average size of each micro-particle is 0.96 μm. The particles contain a magnetite iron oxide component (63.4%) as well as a fluorescein-5-isothiocyanate analogue (Dragon Green) component trapped within the polymer matrix (480-nm excitation, 520-nm emission). BMSCs were incubated with 150 μL of iron particles (2 μL mL^{-1}) for 18 h. Each particle contained 0.125 pg of iron. The labeled BMSCs were removed from culture using trypsin / EDTA (5 minutes at 37°C in 5% CO_2), pelleted by centrifugation, and resuspended at 10^7 cells mL^{-1} in phosphate buffered saline (PBS) at 4°C ready for transplantation.

Proliferation Assay of MPIO-labeled BMSCs

Labeled BMSC viability was assessed by in-vitro proliferation using a modified MTT assay (3-[4,5-dimethylthiazol-2-yl]-2,5-diphenyl tetrazolium bromide) (Roche Diagnostics, Indianopolis, IN). Briefly, 1000 BMSCs per well of a 24-well plate were seeded at early passage (P3-P5) and growth curves established after overnight labeling with a range of particle concentrations (0.5-2.5 μL mL^{-1}). Particles were either removed by repeated washing and replaced with fresh media or left in the media for the duration of the assay.

Transplantation of BMSCs

Healthy adult (250–300 g) male Wistar rats were maintained under anesthesia using isoflurane (2%) and oxygen (2 L min^{-1}). Stereotactic surgery took place on a Kopf small animal stereotactic frame. Thermoregulation was monitored with a rectal probe and the temperature kept constant at 37°C. Prior to surgery, a single-cell suspension was prepared in DMEM supplemented with 0.04 mg mL^{-1} Bovine Pancreas DNase to prevent 'clumping' of the cells. 50,000 cells in a volume of 5 μL were injected at a rate of 1 μL min^{-1}. The stereotactic co-ordinates for injection were based on Rat Brain Atlas (126) with reference to the bregma; anterior–posterior = 0.0 mm, lateral–medial = −2.0 mm, dorsal–ventral = −6.3 mm. The needle (26G, outer diameter = 0.46 mm) was kept in situ 2 min before and 5 min after cell-injection to allow for intra-cranial pressure equalization. Subcutaneous buprenorphine (0.1 mg kg^{-1}) was given as analgesia, with intra-peritoneal saline injection and post-op warming to aid recovery.

In-Vivo Positive Contrast Detection with Multiple-Echo Ultrashort Echo Time (MUTE)

Injected rats were maintained in an anaesthetized state with 1.5% isoflurane during MRI measurement. Positive contrast detection of BMSCs was carried out with MUTE at 9.4 T, with a single loop surface receiver coil for reception. Image reconstruction was carried out offline in Matlab with regridding. A Kaiser-Bessel interpolation scheme was employed with an oversampling factor of 2, free-design parameter β of 8.9962 and gridding kernel width of 4. Scan parameters were: TR = 100 ms, TE = 0.3 ms (FID), Echo-interval = 2.56 ms, number of echoes = 8, flip angle = 45°, FOV = 30 × 30 mm, regridded matrix = 256 × 256. Regions-of-interest were drawn at the labeled cells and at the unlabeled contralateral position. Using

the measured signal intensities, contrast-to-noise ratio was calculated according to eqn. (3.9) and compared between FID, ECHO and subtracted (FID-ECHO) images.

3.6.3 Results

Figure 3.18A displays a fluorescent microscopic image of IODEX-TAT-FITC labeled BMSCs with DAPI (nuclei) staining. Green fluorescence indicates the presence of particles, which have been efficiently transfected. Figure 3.18B-D displays the FID, ECHO and their subtracted MUTE images respectively. Figure 3.19A is an overlay between fluorescent and bright-field optical images indicating the successful incorporation of MPIOs into BMSCs after 18 h incubation. B-D displays the corresponding reconstructed images of MPIO-labeled cells in the rat brain. Table 3.2 compares the contrast-to-noise ratio between IODEX-TAT-FITC and MPIOs labeled MSCs, based on ROI analysis. Positive contrast of 50,000 labeled-cells was prominent in the FID images for both particles with contrast enhancement of + 27.9 and + 49.0 respectively. At an echo-time of 18.2 ms, the T_2^* relaxation effect of iron-oxide dominates over T_1-attenuation effect, resulting in signal voids and negative contrast of -12.6 and -48.3 for IODEX-TAT-FITC and MPIO –labeled cells respectively. MUTE exploits the transverse relaxation of both iron-oxide particles and boosts the positive contrast of the cells upon subtraction between FID and ECHO images. IODEX-TAT-FITC-labeled MSCs saw an increase of 30 % in positive contrast to 35.6, while the larger MPIOs yielded an additional 78 % in contrast to 87.0. Another significant difference is that the area of enhancement in the cells labeled with the large 0.96 μm MPIOs is 10.1 mm^2, whereas it is 4.05 mm^2 for that labeled with the much smaller (15 nm) USPIOs.

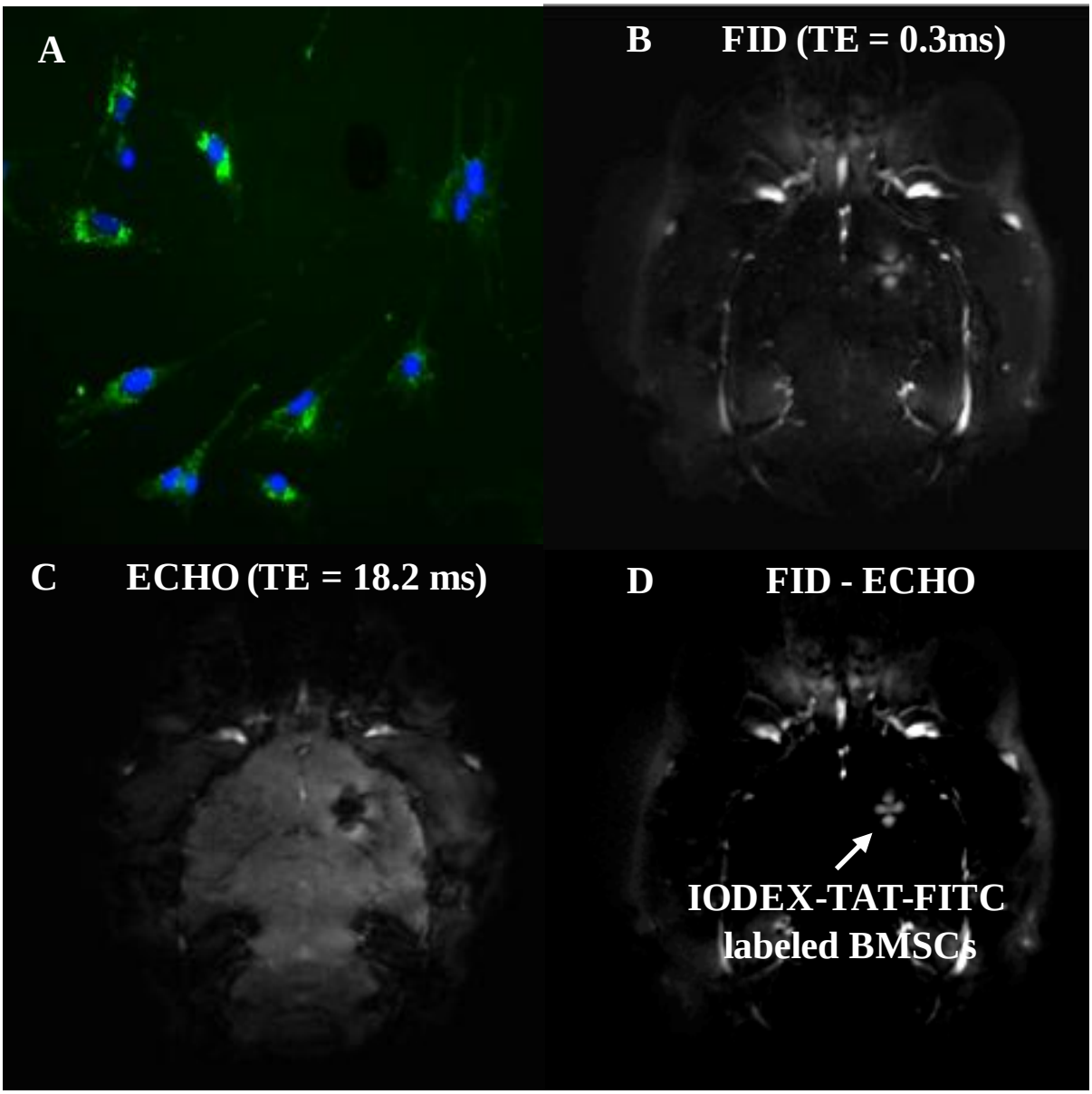

Figure 3.18: (A) Fluorescent microscopic image of the FITC label showed the successful transfection of IODEX-TAT-FITC nanoparticles into the bone marrow cells. MUTE images acquired at TE = 0.3 ms (B) and 18.2 ms (C). (D) Subtraction between FID and ECHO images resulted in higher positive contrast.

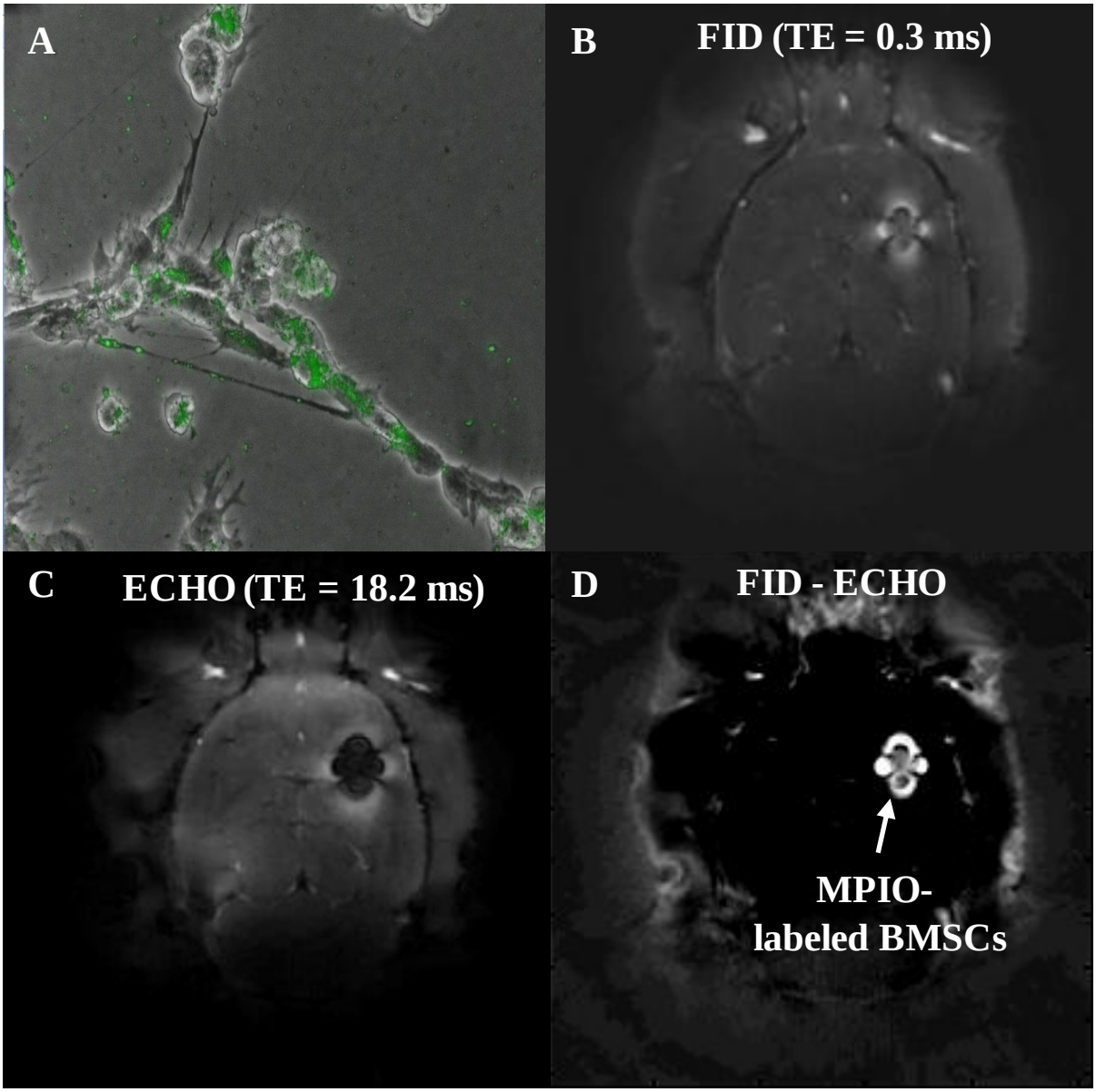

Figure 3.19: (A) Overlay between green fluorescence and bright-field optical images depicting successful endocytosis of MPIOs into BMSCs. (B-C) illustrated the regridded MUTE images at various echo-times (TE = 0.3 ms and 18.2 ms) while D displays their subtraction. The signature 'blooming' artifact of iron-oxide is conspicuous.

	Contrast - to Noise Ratio (CNR)	
	IODEX-TAT-FITC	**MPIO**
FID (TE = 0.3 ms)	27.4 ± 17.9	49.0 ± 36.8
ECHO (TE = 18.2 ms)	-12.6 ± 32.2	-48.3 ± 17.2
FID - ECHO	35.6 ± 31.8	87.0 ± 38.1
% increase in positive contrast after subtraction	30 %	78 %
Area of positive enhancement (mm^2)	4.05	10.10

Table 3.2: Contrast-to-noise ratio comparison between IODEX-TAT-FITC and MPIO – labeled MSCs in the rat brain.

Figure 3.20 illustrates the results of the MTT proliferation assay, in which an inverse relationship exists between cell division capability and labeling concentration. At the current labeling concentration of 2 μL mL^{-1}, there was 40% impairment in cell division.

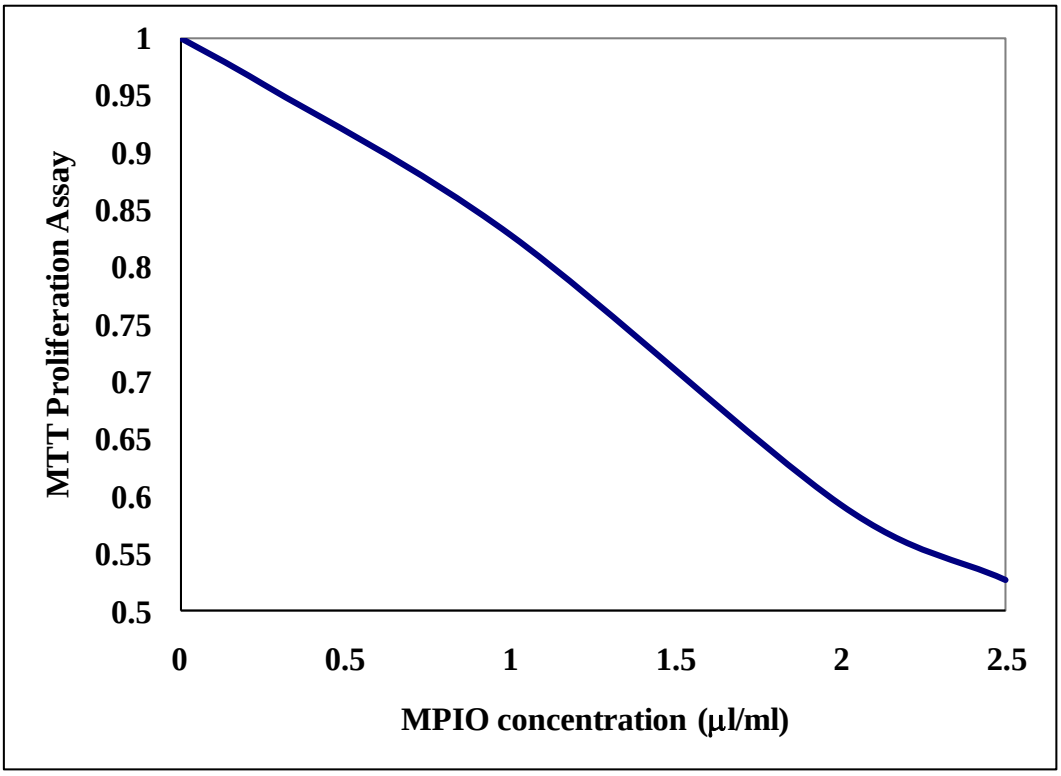

Figure 3.20: MTT proliferation assay depicting the effect of higher MPIO labeling concentration on cell division capability.

3.6.4 Discussion

This is the first demonstration of positive contrast detection of IODEX-TAT-FITC –labeled BMSCs in the preclinical arena. By utilizing a multiple-echo UTE sequence, we were able to achieve high positive contrast in the FID image. When we loaded the cells with much larger MPIOs, it was further elevated (from + 27.4 to + 49.0). This is attributed to the augmented T_1-relaxivity of MPIOs-labeled cells. It is to be clarified that MPIOs do not necessarily have larger longitudinal relaxivity (127); rather it was the total iron content per cell that contributed to the heightened T_1-relaxation, as evident from eqn. (3.11). The difference in R_2^*-relaxation, on the other hand, is much more pronounced between USPIOs and MPIOs because the latter have at least 50% higher iron content (123). An obvious manifestation of this discrepancy is the negative contrast in ECHO images, in which MPIO-labeled cells are four times more hypointensed than the IODEX-TAT-FITC ones. This discrimination is the reason why single cell detection is possible with MPIOs (122,128). And when that was exploited with MUTE, subtraction between FID and ECHO propelled positive contrast of MPIO-labeled cells to new heights, achieving 78% increment compared to 30% for USPIOs. Another conspicuous characteristic is that MPIOs created a larger area of positive enhancement, which was more than twice that in IODEX-TAT-FITC cells. This phenomenon effectively boosted detection sensitivity by 250%. That feature could very well determine the detection success of labeled-cells in situations such as low resolution images or sparse cell clusters (25). The amount of MPIOs incorporated in each cell was not quantified though, and its more pronounced transverse relaxation could be due to higher intracellular concentration as well as r_2^* relaxivity (see eqn. (3.12). The adverse effect of MPIO labeling on cell proliferation was a concern that had to be addressed. Even though a previous study claimed that MPIO labeling of up to 10 μL mL^{-1} for 18h had no impact on cell proliferation (25), those were porcine mesenchymal stem cells and not murine, thus the biological influence of

iron-oxide on cell activity might differ. A recent study comparing various MPIO labeling strategies into endogenous mouse neural progenitor cells also found a significant reduction in $BrdU^+$ (proliferating) cells after injection with MPIOs, albeit a larger particle (1.63 μm) was utilized (129). Nonetheless a cardiac repair study which utilized higher MPIO labeling concentration (2.7 μL mL^{-1} versus 2 μL mL^{-1} used in this study) and longer incubation (24 h against 18 h) on rat BMSCs claimed that there was no significant reduction in cell viability and proliferation (124). The main difference between the studies was BMSC culture conditions and that requires further investigation.

3.6.5 Limitations of Study

Although the positive contrast obtained is phenomenal in both USPIO and MPIO – labeled BMSCs, there were several weaknesses in this study that should be addressed. First, we did not quantify the iron content per cell for both particles. Nonetheless a previous study that labeled similar rat bone marrow cells with IODEX-TAT-FITC achieved an iron content of ~9.5 pg per cell (121), and we did not expect ours to deviate significantly from that since we adopted similar culture and label procedures. Iron content in MPIO-labeled cells however would have to be quantified in order to determine the minimal iron load required to achieve optimal sensitivity, without inhibiting cellular function. Second, functional assessment such as cell viability, toxicity and differentiation capability were not carried out. Since dextran-coated particles can be degraded by the microenvironment of the lysosome, there is a danger that excessive loading of cells with dextran–coated particles may induce cell death due to iron-load or at least incapacitate normal cell activity (130). In addition, a well-labeled cell comprising of ~15 pg of iron presents an extremely high cellular concentration of 250 mM. Most studies to date have not detected significant toxicity, but this remains a major concern.

Particles coated with an inert matrix, such as the MPIOs described here, potentially can prevent this (25). Third, no longitudinal scan was implemented, thus the loss in sensitivity due to cell division could not be verified. It is expected that the MPIOs outperform the USPIOs in this aspect, purely based on its richer iron content. Larger MPIOs could also be utilized to further enhance the sensitivity (25).

3.6.6 Conclusion

In this study, I demonstrated that both IODEX-TAT-FITC and MPIO-labeled bone marrow stem cells could be detected with high sensitivity and visualized as hyperintensities *in vivo*. The multiple-echo ultrashort echo time technique employed here exploited the proton relaxation of USPIOs and MPIOs to raise positive contrast by 30 % and 78 %, respectively, upon subtraction between FID and ECHO images. MPIOs were twice more sensitive to detection than USPIOs, on the basis of their larger enhancement area. Cell proliferation appeared to be impaired with MPIOs and further characterization of its biological impact on cellular activity is necessary.

3.7 Z-Shimmed Ultrashort Echo Time - A New Positive Contrast Detection Scheme

We have shown that UTE could visualize SPIO-labeled cells with high sensitivity which could be further augmented with multiple echo acquisition and subtraction. To fully realize the potential of MUTE however, T_2^* decay must be exploited to yield maximum positive contrast. That imply either a long echo-time or heavily iron-loaded cells are essential. The former is sensitive to motion and susceptibility effects, whereas the latter faces the risk of cellular toxicity. Therefore an alternative method is desirable. Instead of relying on T_2^* to

generate positive contrast, I introduced a technique that takes advantage of the T_1-relaxation effect of SPIOs as well as the off-resonance that they induce, i.e., a hybrid of UTE and White-Marker imaging. In this section, the strengths posed by this technique are presented, notwithstanding the challenges involved, which are also discussed.

3.7.1 Z-shimmed Ultrashort Echo Time Pulse Sequence (ZUTE)

Z-shimmed UTE is a single image acquisition technique that records only the FID signal at very short echo-times. Its pulse sequence is very similar to MUTE, with modification made to the slice-refocusing gradient amplitude and disabling of the multiple-echo functionality. Displayed in Figure 3.21 is the ZUTE pulse sequence which basically incorporates minimum phase SLR-VERSE RF excitation, variable slice refocusing gradient amplitude and radial sampling for minimal echo-time.

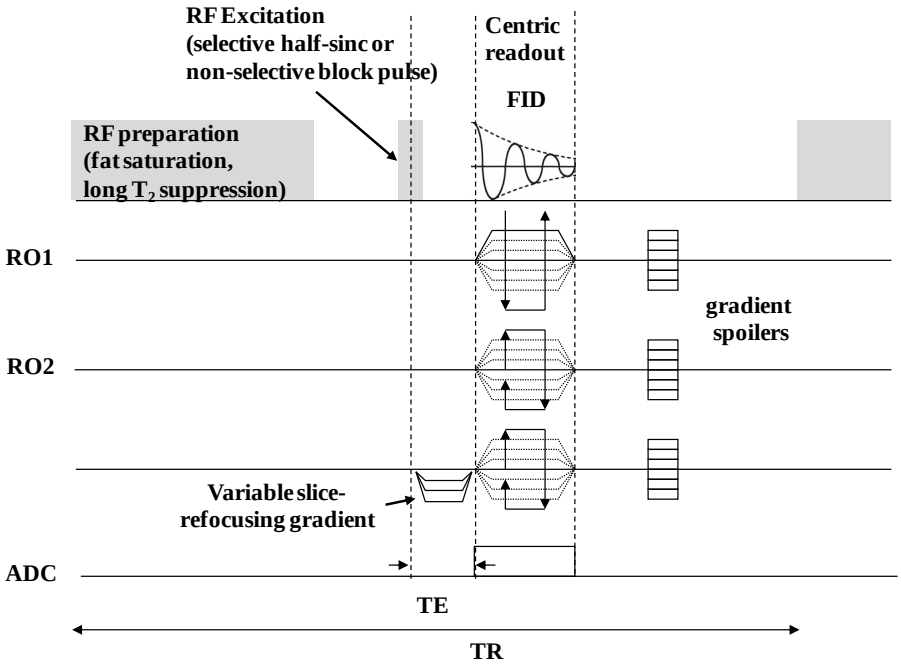

Figure 3.21: Pulse sequence of Z-shimmed Ultrashort Echo Time (ZUTE), a hybrid between UTE and white-marker techniques. Key feature is the variable slice refocusing gradient.

3.7.2 Positive Contrast Enhancement Simulation with ZUTE

The theoretical principles behind ZUTE are similar to that presented in Section 3.2.3. The main difference is that the echo-time is very short (TE < 0.3 ms), which results in a smaller accrued phase for protons surrounding the SPIO. That implies less compensation is required to null that phase. We refer to eqn. (3.8) with the following parameters: a 1 mm^3 voxel with thickness d = 1 mm; ρ = 1; $\Delta\chi V = 10^{-6}$ mm^3; B_0 = 9.4 T, TE = 0.192 ms; G_{ssr} = 0.5 T/m and t_{ssr} = 0.15 ms. Simulation results comparing T_2^*-weighted (α = 0) and ZUTE (α = 0.45) imaging are displayed in Figure 3.22.

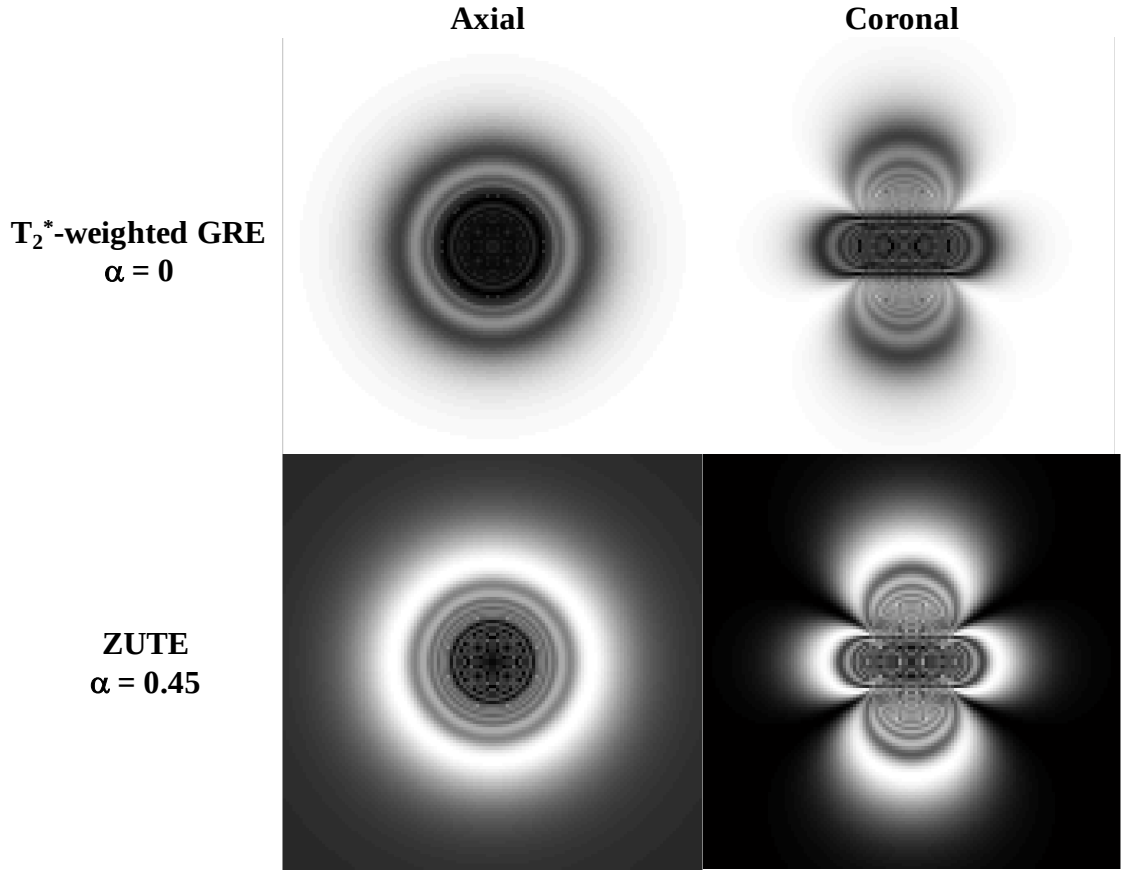

Figure 3.22: Simulated positive contrast achievable with Z-shimmed UTE technique. Echo-time was 0.192 ms. Reducing the slice refocusing gradient amplitude by 45% enables phase compensation along the slice direction, giving rise to positive contrast. Equation (3.8) was used in the simulation.

3.7.3 Positive Contrast Comparison between MUTE and ZUTE

In order to demonstrate the capability of ZUTE, I first put theory into practice and quantified the positive contrast that it offered. An excised rat heart transplanted with SPIO-labeled cells was chosen for the first trial, and then its positive contrast superiority was confirmed *in vivo*.

Ex vivo Sample Preparation

All animal procedures were approved by the University College London Ethics Committee and the Home Office (London, UK), and conducted under the Animal (Scientific Procedures) Act 1986.

1 male Wistar rat (Charles River Ltd, U.K.) aged 7 - 8 weeks was anaesthetised with an intra-peritoneal injection of Hypnovel-Hypnorm-water mixture (1:1:2, 2.5ml/kg, Roche U.K., VetaPharma U.K.). The animal had its body temperature monitored and maintained at 37°C during the surgery. They were then artificially ventilated with pure oxygen (Respirator, Harvard Apparatus Ltd, U.K.) at 1 L min^{-1}. A thoracotomy procedure was performed in the 4th intercostal space following blunt dissection of the chest muscles to expose the heart. 5×10^5 of MNCs were directly injected into the left myocardium wall at the mid-ventricle. The chest was closed and spontaneous breathing was re-established. The rat was sacrificed after 2 hours and its heart was subsequently excised, perfused with PBS and followed by 24 h fixation in 4% PFA at 5°C. It was then placed in increasing sucrose gradients (10, 20, and 30%) and finally embedded in 1% agarose.

Ex vivo MRI with ZUTE

A powerful gradient insert (strength = 1000 mT m^{-1}, slew rate = 7700 mT m^{-1} ms^{-1}) was used for *ex vivo* MRI to reduce echo time. Sagittal slices of the excised heart were acquired with a MUTE pulse sequence. ROI analyses were subsequently carried out with selected areas displayed in the ECHO image. Each ROI was about 30 mm^2 and standard deviation of noise was measured in the agar embedding the sample. The slice-refocusing gradient amplitude was multiplied with a factor α, decreasing from 1 to 0, in steps of 0.1. This indicated a shift in *k*-space from 0 to 41.8 cm^{-1} in the slice direction. Corresponding T_2^*-weighted gradient-echo and White-Marker images were acquired for comparison. Region-of-interest analysis with an area of 10.7 mm^2 was executed on the labeled cells and unlabeled myocardium, with contrast-to-noise ratio calculated according to eqn. (3.9). Other scan parameters were: TR = 150 ms; TE = 0.192 ms (FID); 3.4 ms (GRE/WM); number of echoes = 1; regridded matrix = 256 × 256; number of radial projections = 403 (UTE/ZUTE); FOV = 40 x 40 mm; in-plane image resolution = 156 × 156 μm; receiver bandwidth = 100 kHz; slice thickness = 1.0 mm; number of averages = 3; scan time = 120 sec per slice; flip angle = 45°; G_{ssr} = 49.3 G cm^{-1} (ZUTE) / 35.0 G/cm (WM) and τ_{ssr} = 0.156 ms (ZUTE) / 0.28 ms (WM). A 40 mm quadrature volume coil was used for transmit and receive.

In vivo Sample Preparation and MRI with ZUTE

A rat that has been stereotactically injected with 50,000 bone marrow stem cells, which were labeled with 0.96 μm MPIOs as described previously in section 3.5.2, was inducted with 2-3% isoflurane and maintained at 1.5% with 1L min^{-1} air mixture. Positive contrast detection of BMSCs was carried out with ZUTE at 9.4 T, with a single loop surface receiver coil for reception. Image reconstruction was carried out offline in Matlab with regridding. A Kaiser-

Bessel interpolation scheme was employed with an oversampling factor of 2, free-design parameter β of 8.9962 and gridding kernel width of 4. Scan parameters were: TR = 100 ms; TE = 0.192 ms (FID); number of echoes = 1; flip angle = 45°; FOV = 30 × 30 mm; regridded matrix = 256 × 256; G_{ssr} = 19.7 G cm^{-1} (ZUTE) and τ_{ssr} = 0.28 ms (ZUTE); α ranges from 0 to 1. Regions-of-interest were drawn at the labeled cells and at the unlabeled contralateral position. Using the measured signal intensities, the contrast-to-noise ratio was calculated according to eqn. (3.9) and compared between FID images acquired at different values of α. For each value of α, the compensated slice gradient amplitude was converted into units of mT s^{-1} using eqn. (3.41) below, where G_{ssr} was the slice refocusing gradient amplitude and τ_{ssr} was its duration.

$$\delta G_z = \alpha\, G_{ssr} \tau_{ssr} \qquad (3.41)$$

3.7.4 Results

Ex vivo MRI with ZUTE

After ROI measurements at the injected site and unlabeled myocardium region, as indicted in Figure 3.24, CNR was calculated and compared between white-marker and ZUTE. The CNR plots are displayed in Figure 3.23A and B, respectively. white-marker imaging induced rephasing of protons surrounding SPIO-labeled cells to give a maximum positive enhancement of + 7.1. Without slice refocusing compensation, i.e., at α = 0 or δG_z = 0 mT s^{-1}, SPIOs created a hypointensity with CNR of -9.5. ZUTE on the other hand increased the hyperintensity from +11.7 (α = 0) to a peak of + 21.6 (α = 0.5). Figure 3.24 compares the MR images obtained with gradient-echo (α = 0), White-Marker (α = 0.2), UTE (α = 0) and ZUTE (α = 0.5). The positive contrast enabled with UTE already surpassed that of WM

(+11.7 versus + 7.1). Suppressing the background signal with ZUTE further enhanced contrast to +21.6.

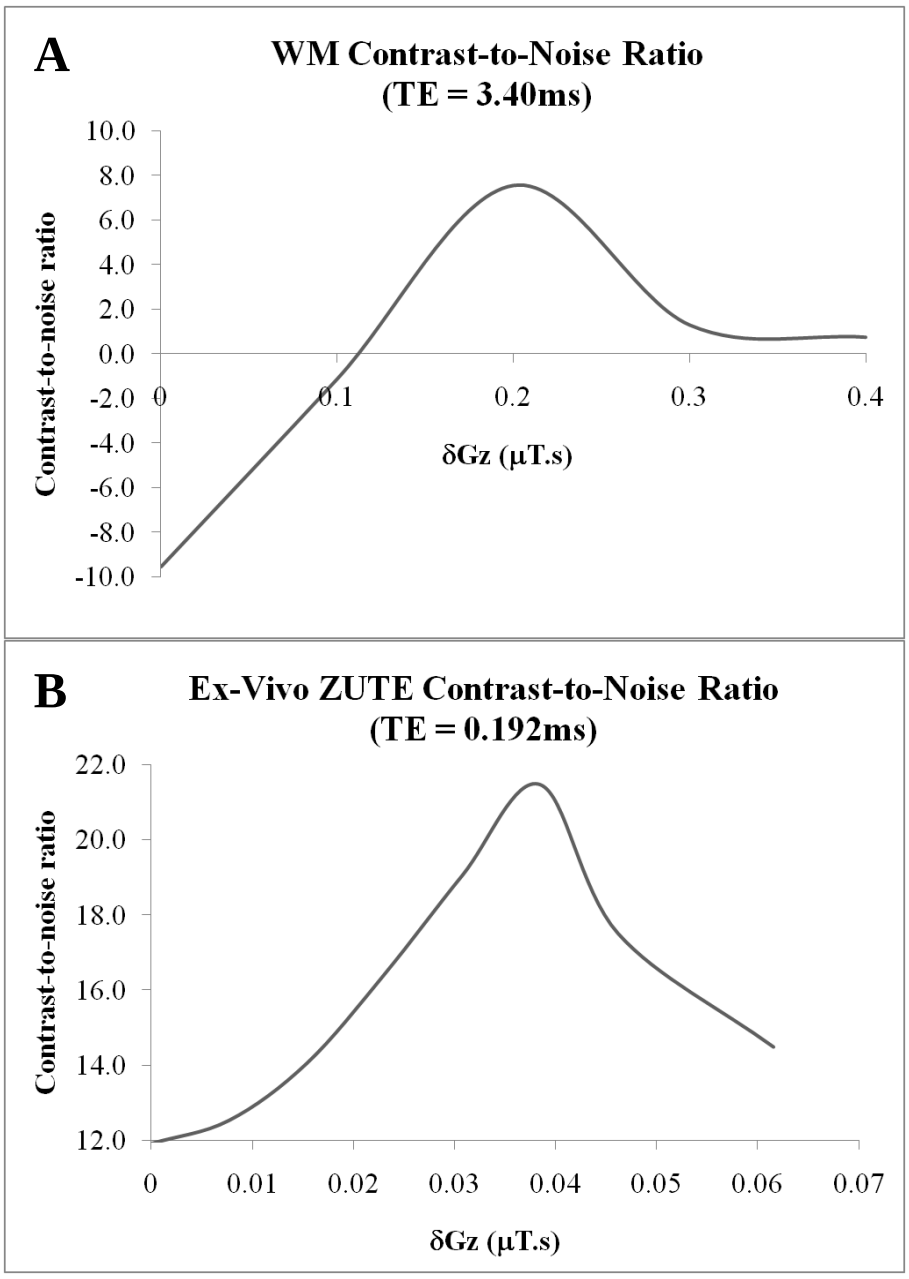

Figure 3.23: CNR comparison between (A) White-Marker and (B) ZUTE as accrued phase within the slice was rephased with a small gradient amplitude during slice refocusing.

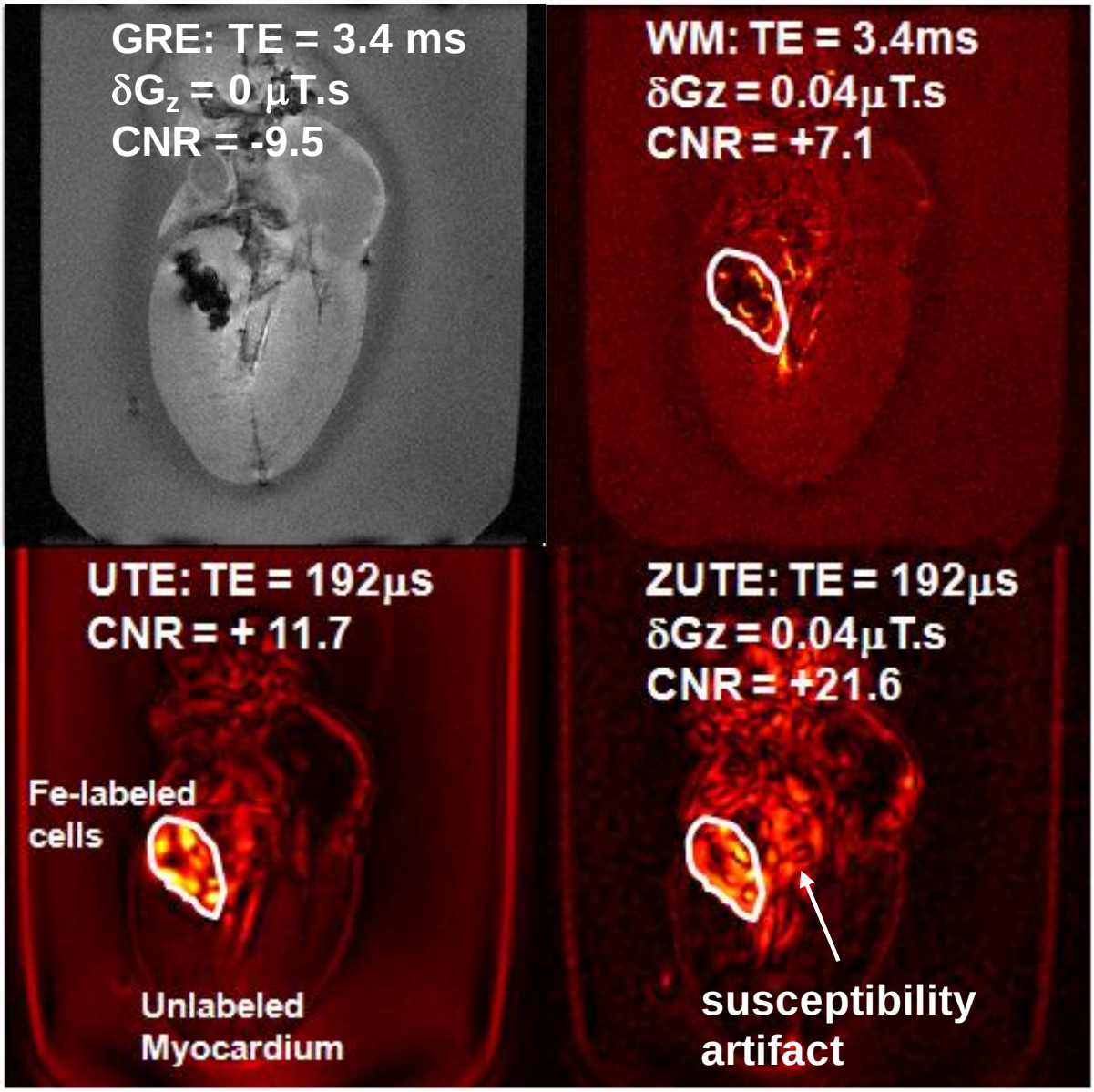

Figure 3.24: MR images comparing negative and positive contrast derived from T_2^*-weighted gradient echo, White-Marker, UTE and ZUTE imaging. Only images with maximum enhancement are displayed for WM, UTE and ZUTE.

In-Vivo MRI with ZUTE

Figure 3.25A illustrates the increase in in-vivo positive contrast of 50,000 MPIO-labeled cells with ZUTE imaging. The routine UTE image in (B) gave rise to a CNR of + 40.2, whereas the maximum available with ZUTE (C) is + 57.9, an improvement of 44 %. As the phase became over-compensated, contrast began to decrease.

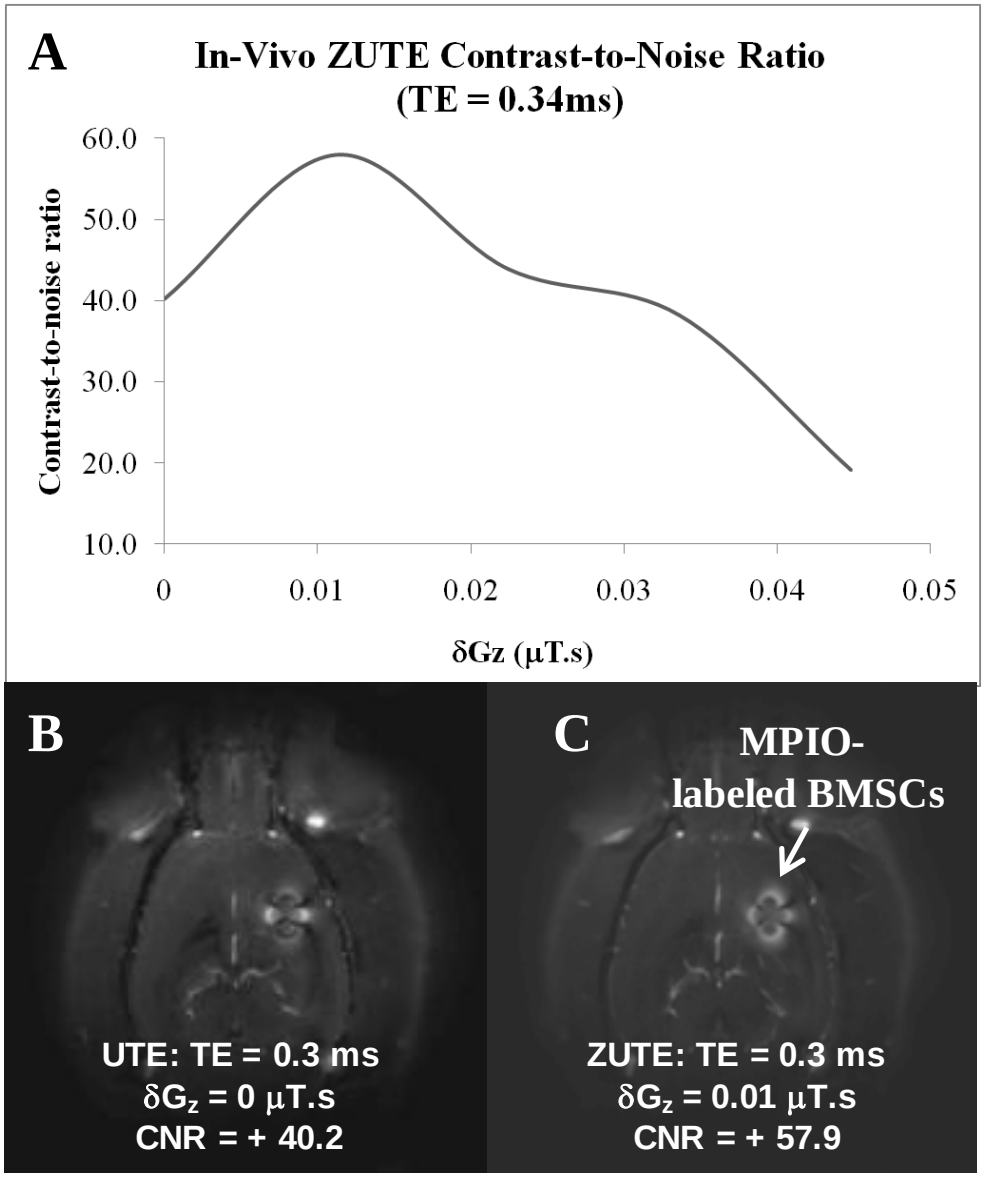

Figure 3.25: (A) CNR depicting the gradual increase in positive contrast as phase within the excited slice was compensated with ZUTE. (B) UTE image at $\alpha = 0$; and (C) ZUTE image at $\alpha = 0.2$.

3.7.5 Discussion

I demonstrated the phenomenal boost in positive contrast that could be achieved with ZUTE. In both ex-vivo excised hearts and in-vivo rat brain, the hyperintensity increased in magnitude with respect to its surroundings as the phase induced by SPIO-labeled cells became compensated. A maximum value was reached when nulling of that phase occurred, as evident from eqn. (3.7) and (3.8). This is consistent with the White-Marker technique (42), which is essentially ZUTE but with much longer echo-time. Obviously UTE already outperformed White-Marker imaging in the excised heart (+11.7 versus +7.1, respectively) because it exploited T_1-relaxation of SPIOs as well as minimized T_2^* decay due to its very short echo-time (as discussed in section 3.5). With phase compensation, the positive contrast was nearly doubled. It is again emphasized here that the principle of ZUTE relies on rephasing specific protons surrounding SPIO, while dephasing distant ones. Therefore a 'blooming' marker was observed in Figure 3.25 B and C, which appeared very similar to the simulated SPIO biomarker in Figure 3.22. The much larger MPIOs (in rat brain) had a more pronounced T_1-relaxation effect and thus generated a more augmented positive contrast than the SPIOs (in excised heart). Close scrutiny reveals a difference between maximum positive contrasts enabled by ZUTE and MUTE (+57.9 and +87.0 respectively, see Table 3.2). There is a reason for this discrepancy. The MPIOs used here had large transverse relaxivity which facilitated large contrast enhancement in the subtraction of FID and ECHO images. ZUTE does not rely on T_2^*-decay because it is heavily T_1-weighted. In fact, T_2^* decay would reduce the signal because of a finite readout time. The almost equivalent CNR when USPIOs are used in the excised hearts, +21.6 (ZUTE) against +22.7 (MUTE, see Table 3.1), corroborates this hypothesis. Since ZUTE rephases protons in the excited slice, its weaknesses are akin to White-Marker's, including partial volume effects and sensitivity to local magnetic susceptibility changes. The latter artifact was actually quite prominent in Figure 3.24.

3.7.6 Conclusion

I demonstrated an alternative method to generate positive contrast from SPIO-labeled cells that could be used *in vivo* as well as *ex-vivo*. Although ZUTE performance was slightly deficient compared to MUTE, in terms of maximum contrast enhancement, it offers some advantages such as single image acquisition and regridding, as well as ease of implementation without major concern of skewed *k*-space trajectories in the echoes. In addition, it is superior to White-Marker imaging and I demonstrated its capability in the preclinical environment.

3.8 Chapter Conclusion

For this chapter, I explored the feasibility of multiple-echoes UTE in in-vivo tracking of SPIO-labeled cells in the preclinical environment. Its superior positive contrast characteristics compared to current clinical techniques placed it at the forefront of cellular tracking in animal disease models. I also proposed a hybrid method that incorporated the high sensitivity of UTE and robust contrast offered by White-Marker imaging to meet demanding requirements in sensitivity, specificity and imaging speed. I am optimistic that these two positive contrast techniques will contribute significantly in understanding migration dynamics in future cellular repair and regeneration endeavors.

3.9 Chapter References

1. Jiang Y, Jahagirdar BN, Reinhardt RL, Schwartz RE, Keene CD, Ortiz-Gonzalez XR, Reyes M, Lenvik T, Lund T, Blackstad M, Du J, Aldrich S, Lisberg A, Low WC, Largaespada DA, Verfaillie CM. Pluripotency of mesenchymal stem cells derived from adult marrow. Nature 2002;418(6893):41-49.
2. Bulte JW, Kraitchman DL. Iron oxide MR contrast agents for molecular and cellular imaging. NMR Biomed 2004;17(7):484-499.
3. Rudelius M, Daldrup-Link HE, Heinzmann U, Piontek G, Settles M, Link TM, Schlegel J. Highly efficient paramagnetic labelling of embryonic and neuronal stem cells. Eur J Nucl Med Mol Imaging 2003;30(7):1038-1044.
4. Aime S, Frullano L, Geninatti Crich S. Compartmentalization of a gadolinium complex in the apoferritin cavity: a route to obtain high relaxivity contrast agents for magnetic resonance imaging. Angew Chem Int Ed Engl 2002;41(6):1017-1019.
5. Lin YJ, Koretsky AP. Manganese ion enhances T1-weighted MRI during brain activation: an approach to direct imaging of brain function. Magn Reson Med 1997;38(3):378-388.
6. Hu TC, Pautler RG, MacGowan GA, Koretsky AP. Manganese-enhanced MRI of mouse heart during changes in inotropy. Magn Reson Med 2001;46(5):884-890.
7. Koretsky AP, Silva AC. Manganese-enhanced magnetic resonance imaging (MEMRI). NMR Biomed 2004;17(8):527-531.
8. Pautler RG, Silva AC, Koretsky AP. In vivo neuronal tract tracing using manganese-enhanced magnetic resonance imaging. Magn Reson Med 1998;40(5):740-748.
9. Aoki I, Takahashi Y, Chuang KH, Silva AC, Igarashi T, Tanaka C, Childs RW, Koretsky AP. Cell labeling for magnetic resonance imaging with the T1 agent manganese chloride. NMR Biomed 2006;19(1):50-59.
10. Yamada M, Gurney PT, Chung J, Kundu P, Drukker M, Smith AK, Weissman IL, Nishimura D, Robbins RC, Yang PC. Manganese-guided cellular MRI of human embryonic stem cell and human bone marrow stromal cell viability. Magn Reson Med 2009;62(4):1047-1054.
11. Khurana A, Runge VM, Narayanan M, Greene JF, Jr., Nickel AE. Nephrogenic systemic fibrosis: a review of 6 cases temporally related to gadodiamide injection (omniscan). Invest Radiol 2007;42(2):139-145.
12. Deo A, Fogel M, Cowper SE. Nephrogenic systemic fibrosis: a population study examining the relationship of disease development to gadolinium exposure. Clin J Am Soc Nephrol 2007;2(2):264-267.
13. Collidge TA, Thomson PC, Mark PB, Traynor JP, Jardine AG, Morris ST, Simpson K, Roditi GH. Gadolinium-enhanced MR imaging and nephrogenic systemic fibrosis: retrospective study of a renal replacement therapy cohort. Radiology 2007;245(1):168-175.
14. Agata N, Tanaka H, Shigenobu K. Effect of Mn2+ on neonatal and adult rat heart: initial depression and late augmentation of contractile force. Eur J Pharmacol 1992;222(2-3):223-226.
15. Tanaka H, Ishii T, Fujisaki R, Miyamoto Y, Tanaka Y, Aikawa T, Hirayama W, Kawanishi T, Shigenobu K. Effect of manganese on guinea pig ventricle: initial depression and late augmentation of contractile force. Biol Pharm Bull 2002;25(3):323-326.
16. Huang CC, Chu NS, Lu CS, Wang JD, Tsai JL, Tzeng JL, Wolters EC, Calne DB. Chronic manganese intoxication. Arch Neurol 1989;46(10):1104-1106.
17. Jung CW, Jacobs P. Physical and chemical properties of superparamagnetic iron oxide MR contrast agents: ferumoxides, ferumoxtran, ferumoxsil. Magn Reson Imaging 1995;13(5):661-674.
18. Wang YX, Hussain SM, Krestin GP. Superparamagnetic iron oxide contrast agents: physicochemical characteristics and applications in MR imaging. Eur Radiol 2001;11(11):2319-2331.

19. Schenck JF. The role of magnetic susceptibility in magnetic resonance imaging: MRI magnetic compatibility of the first and second kinds. Med Phys 1996;23(6):815-850.
20. Briley-Saebo K, Bjornerud A, Grant D, Ahlstrom H, Berg T, Kindberg GM. Hepatic cellular distribution and degradation of iron oxide nanoparticles following single intravenous injection in rats: implications for magnetic resonance imaging. Cell Tissue Res 2004;316(3):315-323.
21. Briley-Saebo K, Hustvedt SO, Haldorsen A, Bjornerud A. Long-term imaging effects in rat liver after a single injection of an iron oxide nanoparticle based MR contrast agent. J Magn Reson Imaging 2004;20(4):622-631.
22. Josephson L, Tung CH, Moore A, Weissleder R. High-efficiency intracellular magnetic labeling with novel superparamagnetic-Tat peptide conjugates. Bioconjug Chem 1999;10(2):186-191.
23. Schellenberger EA, Bogdanov A, Jr., Hogemann D, Tait J, Weissleder R, Josephson L. Annexin V-CLIO: a nanoparticle for detecting apoptosis by MRI. Mol Imaging 2002;1(2):102-107.
24. Jendelova P, Herynek V, DeCroos J, Glogarova K, Andersson B, Hajek M, Sykova E. Imaging the fate of implanted bone marrow stromal cells labeled with superparamagnetic nanoparticles. Magn Reson Med 2003;50(4):767-776.
25. Shapiro EM, Skrtic S, Koretsky AP. Sizing it up: cellular MRI using micron-sized iron oxide particles. Magn Reson Med 2005;53(2):329-338.
26. Frank JA, Miller BR, Arbab AS, Zywicke HA, Jordan EK, Lewis BK, Bryant LH, Jr., Bulte JW. Clinically applicable labeling of mammalian and stem cells by combining superparamagnetic iron oxides and transfection agents. Radiology 2003;228(2):480-487.
27. Arbab AS, Bashaw LA, Miller BR, Jordan EK, Bulte JW, Frank JA. Intracytoplasmic tagging of cells with ferumoxides and transfection agent for cellular magnetic resonance imaging after cell transplantation: methods and techniques. Transplantation 2003;76(7):1123-1130.
28. Arbab AS, Bashaw LA, Miller BR, Jordan EK, Lewis BK, Kalish H, Frank JA. Characterization of biophysical and metabolic properties of cells labeled with superparamagnetic iron oxide nanoparticles and transfection agent for cellular MR imaging. Radiology 2003;229(3):838-846.
29. Jung CW. Surface properties of superparamagnetic iron oxide MR contrast agents: ferumoxides, ferumoxtran, ferumoxsil. Magn Reson Imaging 1995;13(5):675-691.
30. Roch A, Muller RN. Theory of proton relaxation induced by superparamagnetic particles. Journal of Chemical Physics 1999;110(11):5403-5411.
31. Pintaske J, Mueller-Bierl B, Schick F. Numerical simulation of magnetic field distortions caused by cells loaded with SPIO nanoparticles. Proc 14th Annual Meeting ISMRM 2006 2006:1811.
32. Cunningham CH, Arai T, Yang PC, McConnell MV, Pauly JM, Conolly SM. Positive contrast magnetic resonance imaging of cells labeled with magnetic nanoparticles. Magn Reson Med 2005;53(5):999-1005.
33. Suzuki Y, Cunningham CH, Noguchi K, Chen IY, Weissman IL, Yeung AC, Robbins RC, Yang PC. In vivo serial evaluation of superparamagnetic iron-oxide labeled stem cells by off-resonance positive contrast. Magn Reson Med 2008;60(6):1269-1275.
34. Farrar CT, Dai G, Novikov M, Rosenzweig A, Weissleder R, Rosen BR, Sosnovik DE. Impact of field strength and iron oxide nanoparticle concentration on the linearity and diagnostic accuracy of off-resonance imaging. NMR Biomed 2008;21(5):453-463.
35. Foltz WD, Cunningham CH, Mutsaers AJ, Conolly SM, Stewart DJ, Dick AJ. Positive-contrast imaging in the rabbit hind-limb of transplanted cells bearing endocytosed superparamagnetic beads. J Cardiovasc Magn Reson 2006;8(6):817-823.
36. Dharmakumar R, Koktzoglou I, Tang R, Harris KR, Beohar N, Li D. Off-resonance positive contrast imaging of a passive endomyocardial catheter in swine. Phys Med Biol 2008;53(13):N249-257.

37. Stuber M, Gilson WD, Schar M, Kedziorek DA, Hofmann LV, Shah S, Vonken EJ, Bulte JW, Kraitchman DL. Positive contrast visualization of iron oxide-labeled stem cells using inversion-recovery with ON-resonant water suppression (IRON). Magn Reson Med 2007;58(5):1072-1077.
38. Korosoglou G, Tang L, Kedziorek D, Cosby K, Gilson WD, Vonken EJ, Schar M, Sosnovik D, Kraitchman DL, Weiss RG, Weissleder R, Stuber M. Positive contrast MR-lymphography using inversion recovery with ON-resonant water suppression (IRON). J Magn Reson Imaging 2008;27(5):1175-1180.
39. Korosoglou G, Weiss RG, Kedziorek DA, Walczak P, Gilson WD, Schar M, Sosnovik DE, Kraitchman DL, Boston RC, Bulte JW, Weissleder R, Stuber M. Noninvasive detection of macrophage-rich atherosclerotic plaque in hyperlipidemic rabbits using "positive contrast" magnetic resonance imaging. J Am Coll Cardiol 2008;52(6):483-491.
40. Korosoglou G, Shah S, Vonken EJ, Gilson WD, Schar M, Tang L, Kraitchman DL, Boston RC, Sosnovik DE, Weiss RG, Weissleder R, Stuber M. Off-resonance angiography: a new method to depict vessels--phantom and rabbit studies. Radiology 2008;249(2):501-509.
41. Mani V, Briley-Saebo KC, Itskovich VV, Samber DD, Fayad ZA. Gradient echo acquisition for superparamagnetic particles with positive contrast (GRASP): sequence characterization in membrane and glass superparamagnetic iron oxide phantoms at 1.5T and 3T. Magn Reson Med 2006;55(1):126-135.
42. Seppenwoolde JH, Viergever MA, Bakker CJ. Passive tracking exploiting local signal conservation: the white marker phenomenon. Magn Reson Med 2003;50(4):784-790.
43. Liu W, Dahnke H, Jordan EK, Schaeffter T, Frank JA. In vivo MRI using positive-contrast techniques in detection of cells labeled with superparamagnetic iron oxide nanoparticles. NMR Biomed 2008;21(3):242-250.
44. Mani V, Briley-Saebo KC, Hyafil F, Fayad ZA. Feasibility of in vivo identification of endogenous ferritin with positive contrast MRI in rabbit carotid crush injury using GRASP. Magn Reson Med 2006;56(5):1096-1106.
45. Mani V, Adler E, Briley-Saebo KC, Bystrup A, Fuster V, Keller G, Fayad ZA. Serial in vivo positive contrast MRI of iron oxide-labeled embryonic stem cell-derived cardiac precursor cells in a mouse model of myocardial infarction. Magn Reson Med 2008;60(1):73-81.
46. Bakker CJ, Seppenwoolde JH, Vincken KL. Dephased MRI. Magn Reson Med 2006;55(1):92-97.
47. Haase A. Snapshot FLASH MRI. Applications to T1, T2, and chemical-shift imaging. Magn Reson Med 1990;13(1):77-89.
48. Lee P, Riegler J, Price A, Lythgoe MF, Golay X. A multi-echo technique for positive contrast detection of SPIO-labeled cells at 9.4T. Proc Intl Soc Mag Reson Med 2010.
49. Coolen BF, Lee P, Golay X. Optimized MRI parameters for positive contrast detection of iron-oxide labeled cells using double-echo Ultra-short echo time (d-UTE) sequences. Proc Intl Soc Mag Reson Med 2007.
50. Tyler DJ, Robson MD, Henkelman RM, Young IR, Bydder GM. Magnetic resonance imaging with ultrashort TE (UTE) PULSE sequences: technical considerations. J Magn Reson Imaging 2007;25(2):279-289.
51. Rahmer J, Blume U, Bornert P. Selective 3D ultrashort TE imaging: comparison of "dual-echo" acquisition and magnetization preparation for improving short-T 2 contrast. MAGMA 2007;20(2):83-92.
52. Robson MD, Gatehouse PD, So PW, Bell JD, Bydder GM. Contrast enhancement of short T2 tissues using ultrashort TE (UTE) pulse sequences. Clin Radiol 2004;59(8):720-726.
53. Gatehouse PD, He T, Puri BK, Thomas RD, Resnick D, Bydder GM. Contrast-enhanced MRI of the menisci of the knee using ultrashort echo time (UTE) pulse sequences: imaging of the red and white zones. Br J Radiol 2004;77(920):641-647.
54. Robson MD, Bydder GM. Clinical ultrashort echo time imaging of bone and other connective tissues. NMR Biomed 2006;19(7):765-780.

55. Techawiboonwong A, Song HK, Leonard MB, Wehrli FW. Cortical bone water: in vivo quantification with ultrashort echo-time MR imaging. Radiology 2008;248(3):824-833.
56. Hall-Craggs MA, Porter J, Gatehouse PD, Bydder GM. Ultrashort echo time (UTE) MRI of the spine in thalassaemia. Br J Radiol 2004;77(914):104-110.
57. Robson MD, Benjamin M, Gishen P, Bydder GM. Magnetic resonance imaging of the Achilles tendon using ultrashort TE (UTE) pulse sequences. Clin Radiol 2004;59(8):727-735.
58. Liu W, Dahnke H, Rahmer J, Jordan EK, Frank JA. Ultrashort T2* relaxometry for quantitation of highly concentrated superparamagnetic iron oxide (SPIO) nanoparticle labeled cells. Magn Reson Med 2009;61(4):761-766.
59. Larson PE, Conolly SM, Pauly JM, Nishimura DG. Using adiabatic inversion pulses for long-T2 suppression in ultrashort echo time (UTE) imaging. Magn Reson Med 2007;58(5):952-961.
60. Larson PE, Gurney PT, Nayak K, Gold GE, Pauly JM, Nishimura DG. Designing long-T2 suppression pulses for ultrashort echo time imaging. Magn Reson Med 2006;56(1):94-103.
61. Nielsen HT, Gold GE, Olcott EW, Pauly JM, Nishimura DG. Ultra-short echo-time 2D time-of-flight MR angiography using a half-pulse excitation. Magn Reson Med 1999;41(3):591-599.
62. Rahmer J, Bornert P, Groen J, Bos C. Three-dimensional radial ultrashort echo-time imaging with T2 adapted sampling. Magn Reson Med 2006;55(5):1075-1082.
63. Wansapura JP, Daniel BL, Pauly J, Butts K. Temperature mapping of frozen tissue using eddy current compensated half excitation RF pulses. Magn Reson Med 2001;46(5):985-992.
64. Pauly J, Le Roux P, Nishimura D, Macovski A. Parameter Relations for the Shinnar-Le Roux Selective Excitation Pulse Design Algorithm. IEEE TRANSACTIONS ON MEDICAL IMAGING 2001;10(1):53-65.
65. Conolly S, Nishimura D, Macovski A. Variable-rate selective excitation. Journal of Magnetic Resonance 1998;78:440-458.
66. Techawiboonwong A, Song HK, Wehrli FW. In vivo MRI of submillisecond T(2) species with two-dimensional and three-dimensional radial sequences and applications to the measurement of cortical bone water. NMR Biomed 2008;21(1):59-70.
67. Bucholz E, Ghaghada K, Qi Y, Mukundan S, Johnson GA. Four-dimensional MR microscopy of the mouse heart using radial acquisition and liposomal gadolinium contrast agent. Magn Reson Med 2008;60(1):111-118.
68. Qian Y, Boada FE. Acquisition-weighted stack of spirals for fast high-resolution three-dimensional ultra-short echo time MR imaging. Magn Reson Med 2008;60(1):135-145.
69. Du J, Bydder M, Takahashi AM, Chung CB. Two-dimensional ultrashort echo time imaging using a spiral trajectory. Magn Reson Imaging 2008;26(3):304-312.
70. Rodriguez I, Alejo RPD, Cortijo M, Ruiz-Cabello J. COMSPIRA: A Common Approach to Spiral and Radial MRI. Concepts in Magnetic Resonance Part B 2003;20B(1):40-44.
71. Gurney PT, Hargreaves BA, Nishimura DG. Design and analysis of a practical 3D cones trajectory. Magn Reson Med 2006;55(3):575-582.
72. Altbach MI, Trouard TP, Gmitro AF. Radial MRI techniques for obtaining motion-insensitive high-resolution images with variable contrast. IEEE International Symposium on Biomedical Imaging 2002:125-128.
73. Katoh M, Spuentrup E, Buecker A, Schaeffter T, Stuber M, Gunther RW, Botnar RM. MRI of coronary vessel walls using radial k-space sampling and steady-state free precession imaging. AJR Am J Roentgenol 2006;186(6 Suppl 2):S401-406.
74. Glover GH, Pauly JM. Projection reconstruction techniques for reduction of motion effects in MRI. Magn Reson Med 1992;28(2):275-289.
75. Haacke EM, Brown RW, Thompson MR, Venkatesan R. Magnetic Resonance Imaging: Physical Principles and Sequence Design. 1999:311.
76. Wong ST, Roos MS. A strategy for sampling on a sphere applied to 3D selective RF pulse design. Magn Reson Med 1994;32(6):778-784.

77. Irarrazabal P, Nishimura DG. Fast three dimensional magnetic resonance imaging. Magn Reson Med 1995;33(5):656-662.
78. Ahn CB, Cho ZH. Analysis of the eddy-current induced artifacts and the temporal compensation in nuclear magnetic resonance imaging. IEEE Trans Med Imaging 1991;10(1):47-52.
79. Lauzon ML, Rutt BK. Effects of polar sampling in k-space. Magn Reson Med 1996;36(6):940-949.
80. Haacke EM, Brown RW, Thompson MR, Venkatesan R. Magnetic Resonance Imaging: Physcial Principles and Sequence Design. 1999:340.
81. Shu Y, Riederer SJ, Bernstein MA. Three-dimensional MRI with an undersampled spherical shells trajectory. Magn Reson Med 2006;56(3):553-562.
82. Block KT, Uecker M, Frahm J. Undersampled radial MRI with multiple coils. Iterative image reconstruction using a total variation constraint. Magn Reson Med 2007;57(6):1086-1098.
83. Peters DC, Derbyshire JA, McVeigh ER. Centering the projection reconstruction trajectory: reducing gradient delay errors. Magn Reson Med 2003;50(1):1-6.
84. Ching-Ming L. Reconstructing NMR images from projections under inhomogenous magnetic field and non-linear field gradients. Physics in Medicine and Biology 1983;28(8):925-938.
85. Duyn JH, Yang Y, Frank JA, van der Veen JW. Simple correction method for k-space trajectory deviations in MRI. J Magn Reson 1998;132(1):150-153.
86. Coggins BE, Zhou P. Polar Fourier transforms of radially sampled NMR data. J Magn Reson 2006;182(1):84-95.
87. Sullivan JD. A fast sinc function gridding algorithm for fourier inversion in computer tomography. IEEE TRANSACTIONS ON MEDICAL IMAGING 1985;4(4):200-206.
88. Beatty PJ, Nishimura DG, Pauly JM. Rapid gridding reconstruction with a minimal oversampling ratio. IEEE Trans Med Imaging 2005;24(6):799-808.
89. Pauly J. Non-cartesian reconstruction. http://wwwstanfordedu/class/ee369c/.
90. Jackson J, Meyer C, Nishimura D, Macovski A. Selection of a convolution function for Fourier inversion using gridding. IEEE TRANSACTIONS ON MEDICAL IMAGING 1991;10(3):473-478.
91. Bernstein MA, King KF, Zhou XJ. Handbook of MRI Pulse Sequences. 2004:510.
92. Pipe JG, Menon P. Sampling density compensation in MRI: rationale and an iterative numerical solution. Magn Reson Med 1999;41(1):179-186.
93. Rasche V, Proksa R, Sinkus R, Bornert P, Eggers H. Resampling of data between arbitrary grids using convolution interpolation. IEEE Trans Med Imaging 1999;18(5):385-392.
94. Hoge RD, Kwan RK, Pike GB. Density compensation functions for spiral MRI. Magn Reson Med 1997;38(1):117-128.
95. Segers VF, Lee RT. Stem-cell therapy for cardiac disease. Nature 2008;451(7181):937-942.
96. Moretti A, Caron L, Nakano A, Lam JT, Bernshausen A, Chen Y, Qyang Y, Bu L, Sasaki M, Martin-Puig S, Sun Y, Evans SM, Laugwitz KL, Chien KR. Multipotent embryonic isl1+ progenitor cells lead to cardiac, smooth muscle, and endothelial cell diversification. Cell 2006;127(6):1151-1165.
97. Abdel-Latif A, Bolli R, Tleyjeh IM, Montori VM, Perin EC, Hornung CA, Zuba-Surma EK, Al-Mallah M, Dawn B. Adult bone marrow-derived cells for cardiac repair: a systematic review and meta-analysis. Arch Intern Med 2007;167(10):989-997.
98. Lee P, Golay X. In-Vivo Tracking of Super-Paramagnetic Iron Oxide (SPIO) - Labeled Mesenchymal Stem Cells with Positive Contrast. World Molecular Imaging Congress 2008.
99. Schneider JE, Cassidy PJ, Lygate C, Tyler DJ, Wiesmann F, Grieve SM, Hulbert K, Clarke K, Neubauer S. Fast, high-resolution in vivo cine magnetic resonance imaging in normal and failing mouse hearts on a vertical 11.7 T system. J Magn Reson Imaging 2003;18(6):691-701.
100. Bertini I, Luchinat C. Relaxation. Coordination Chemistry Reviews 1996;150:77-110.

101. Ebert SN, Taylor DG, Nguyen HL, Kodack DP, Beyers RJ, Xu Y, Yang Z, French BA. Noninvasive tracking of cardiac embryonic stem cells in vivo using magnetic resonance imaging techniques. Stem Cells 2007;25(11):2936-2944.
102. Himes N, Min JY, Lee R, Brown C, Shea J, Huang X, Xiao YF, Morgan JP, Burstein D, Oettgen P. In vivo MRI of embryonic stem cells in a mouse model of myocardial infarction. Magn Reson Med 2004;52(5):1214-1219.
103. Oude Engberink RD, van der Pol SM, Dopp EA, de Vries HE, Blezer EL. Comparison of SPIO and USPIO for in vitro labeling of human monocytes: MR detection and cell function. Radiology 2007;243(2):467-474.
104. Cao F, Lin S, Xie X, Ray P, Patel M, Zhang X, Drukker M, Dylla SJ, Connolly AJ, Chen X, Weissman IL, Gambhir SS, Wu JC. In vivo visualization of embryonic stem cell survival, proliferation, and migration after cardiac delivery. Circulation 2006;113(7):1005-1014.
105. Cohen B, Dafni H, Meir G, Harmelin A, Neeman M. Ferritin as an endogenous MRI reporter for noninvasive imaging of gene expression in C6 glioma tumors. Neoplasia 2005;7(2):109-117.
106. Muja N, Bulte JW. Magnetic resoannce imaging of cells in experimental disease models. Progress in Nuclear Magnetic Resonance Spectroscopy 2009;55:61-77.
107. Cheung JS, Chow AM, Hui ES, Yang J, Tse HF, Wu EX. Cell number quantification of USPIO-labeled stem cells by MRI: an in vitro study. Conf Proc IEEE Eng Med Biol Soc 2006;1:476-479.
108. Pawelczyk E, Arbab AS, Chaudhry A, Balakumaran A, Robey PG, Frank JA. In vitro model of bromodeoxyuridine or iron oxide nanoparticle uptake by activated macrophages from labeled stem cells: implications for cellular therapy. Stem Cells 2008;26(5):1366-1375.
109. Rad AM, Arbab AS, Iskander AS, Jiang Q, Soltanian-Zadeh H. Quantification of superparamagnetic iron oxide (SPIO)-labeled cells using MRI. J Magn Reson Imaging 2007;26(2):366-374.
110. Kuhlpeter R, Dahnke H, Matuszewski L, Persigehl T, von Wallbrunn A, Allkemper T, Heindel WL, Schaeffter T, Bremer C. R2 and R2* mapping for sensing cell-bound superparamagnetic nanoparticles: in vitro and murine in vivo testing. Radiology 2007;245(2):449-457.
111. Grove JE, Bruscia E, Krause DS. Plasticity of bone marrow-derived stem cells. Stem Cells 2004;22(4):487-500.
112. Lunde K, Solheim S, Aakhus S, Arnesen H, Abdelnoor M, Egeland T, Endresen K, Ilebekk A, Mangschau A, Fjeld JG, Smith HJ, Taraldsrud E, Grogaard HK, Bjornerheim R, Brekke M, Muller C, Hopp E, Ragnarsson A, Brinchmann JE, Forfang K. Intracoronary injection of mononuclear bone marrow cells in acute myocardial infarction. N Engl J Med 2006;355(12):1199-1209.
113. Strauer BE, Brehm M, Zeus T, Kostering M, Hernandez A, Sorg RV, Kogler G, Wernet P. Repair of infarcted myocardium by autologous intracoronary mononuclear bone marrow cell transplantation in humans. Circulation 2002;106(15):1913-1918.
114. Zhao LR, Duan WM, Reyes M, Keene CD, Verfaillie CM, Low WC. Human bone marrow stem cells exhibit neural phenotypes and ameliorate neurological deficits after grafting into the ischemic brain of rats. Exp Neurol 2002;174(1):11-20.
115. Azizi SA, Stokes D, Augelli BJ, DiGirolamo C, Prockop DJ. Engraftment and migration of human bone marrow stromal cells implanted in the brains of albino rats--similarities to astrocyte grafts. Proc Natl Acad Sci U S A 1998;95(7):3908-3913.
116. Jendelova P, Herynek V, Urdzikova L, Glogarova K, Kroupova J, Andersson B, Bryja V, Burian M, Hajek M, Sykova E. Magnetic resonance tracking of transplanted bone marrow and embryonic stem cells labeled by iron oxide nanoparticles in rat brain and spinal cord. J Neurosci Res 2004;76(2):232-243.
117. Bos C, Delmas Y, Desmouliere A, Solanilla A, Hauger O, Grosset C, Dubus I, Ivanovic Z, Rosenbaum J, Charbord P, Combe C, Bulte JW, Moonen CT, Ripoche J, Grenier N. In vivo MR

imaging of intravascularly injected magnetically labeled mesenchymal stem cells in rat kidney and liver. Radiology 2004;233(3):781-789.
118. Weisskoff RM, Zuo CS, Boxerman JL, Rosen BR. Microscopic susceptibility variation and transverse relaxation: theory and experiment. Magn Reson Med 1994;31(6):601-610.
119. Hoehn M, Kustermann E, Blunk J, Wiedermann D, Trapp T, Wecker S, Focking M, Arnold H, Hescheler J, Fleischmann BK, Schwindt W, Buhrle C. Monitoring of implanted stem cell migration in vivo: a highly resolved in vivo magnetic resonance imaging investigation of experimental stroke in rat. Proc Natl Acad Sci U S A 2002;99(25):16267-16272.
120. Kircher MF, Allport JR, Graves EE, Love V, Josephson L, Lichtman AH, Weissleder R. In vivo high resolution three-dimensional imaging of antigen-specific cytotoxic T-lymphocyte trafficking to tumors. Cancer Res 2003;63(20):6838-6846.
121. Jackson J, Chapon C, Jones W, Hirani E, Qassim A, Bhakoo K. In vivo multimodal imaging of stem cell transplantation in a rodent model of Parkinson's disease. J Neurosci Methods 2009;183(2):141-148.
122. Shapiro EM, Skrtic S, Sharer K, Hill JM, Dunbar CE, Koretsky AP. MRI detection of single particles for cellular imaging. Proc Natl Acad Sci U S A 2004;101(30):10901-10906.
123. Hinds KA, Hill JM, Shapiro EM, Laukkanen MO, Silva AC, Combs CA, Varney TR, Balaban RS, Koretsky AP, Dunbar CE. Highly efficient endosomal labeling of progenitor and stem cells with large magnetic particles allows magnetic resonance imaging of single cells. Blood 2003;102(3):867-872.
124. Stuckey DJ, Carr CA, Martin-Rendon E, Tyler DJ, Willmott C, Cassidy PJ, Hale SJ, Schneider JE, Tatton L, Harding SE, Radda GK, Watt S, Clarke K. Iron particles for noninvasive monitoring of bone marrow stromal cell engraftment into, and isolation of viable engrafted donor cells from, the heart. Stem Cells 2006;24(8):1968-1975.
125. Josephson L, Tung C-H, Moore A, Weissleder R. High-Efficiency Intracellular Magnetic Labeling with Novel Superparamagnetic-Tat Peptide Conjugate. Bioconjugate Chemistry 1999;10(2):186-191.
126. Paxinos G, Watson C. The rat brain in stereotaxic coordinates: the coronal sections. 6th Edition Academic Press 2006.
127. von zur Muhlen C, von Elverfeldt D, Moeller JA, Choudhury RP, Paul D, Hagemeyer CE, Olschewski M, Becker A, Neudorfer I, Bassler N, Schwarz M, Bode C, Peter K. Magnetic resonance imaging contrast agent targeted toward activated platelets allows in vivo detection of thrombosis and monitoring of thrombolysis. Circulation 2008;118(3):258-267.
128. Shapiro EM, Sharer K, Skrtic S, Koretsky AP. In vivo detection of single cells by MRI. Magn Reson Med 2006;55(2):242-249.
129. Vreys R, Vande Velde G, Krylychkina O, Vellema M, Verhoye M, Timmermans JP, Baekelandt V, Van der Linden A. MRI visualization of endogenous neural progenitor cell migration along the RMS in the adult mouse brain: validation of various MPIO labeling strategies. Neuroimage;49(3):2094-2103.
130. Bishop GM, Robinson SR. Quantitative analysis of cell death and ferritin expression in response to cortical iron: implications for hypoxia-ischemia and stroke. Brain Res 2001;907(1-2):175-187.

CHAPTER FOUR

REAL-TIME DETECTION OF CARDIAC GLUCOSE METABOLISM WITH DYNAMIC NUCLEAR POLARIZED (DNP) ^{13}C

4.1 Overview

Dynamic nuclear polarization is a novel technique that has the capability to multiply the magnetic resonance signal of a ^{13}C-labeled compound by at least 10,000 times (1). This opened up the path for real-time in-vivo characterization of glucose metabolism in the heart (2,3). In this chapter, we first present the utilization of DNP [1-^{13}C] pyruvate in the measurement of intracellular pH in the heart, followed by an investigation into the function of acetyl-carnitine as a transient fuel store in myocardial carbohydrate metabolism. The possibility to study necrosis upon onset of ischaemia, via infusion of [1, 4-^{13}C] labeled fumarate, is then discussed. Finally, we venture beyond MR spectroscopy into metabolic imaging, as a prelude into visualizing the biological processes that are critical in the energy production in the heart. All the work in this chapter was accomplished in the Cardiac Metabolism Research Group at the University of Oxford.

4.2 Probing Cardiac Metabolic Activity with Steady-State ^{13}C NMR/MRS

Probing of biological processes in physiology with magnetic resonance has been an ongoing activity for decades. Dynamic ^{13}C nuclear magnetic resonance spectroscopy (MRS) allows absolute metabolic flux along a particular metabolic pathway to be determined. As ^{13}C-enriched substrate is metabolized, the ^{13}C label is transferred to its metabolic intermediates. The labeling pattern is dependent on the chemistry of the enzyme reactions, and the rate of labeling is determined by flux through the pathway and the pool sizes of the intermediates (4). From the ^{13}C MRS spectra, resonances attributable to the specific carbon atoms of particular intermediates are identified by their chemical shifts. The area of the resonance peak is

proportional to the ^{13}C content of the particular carbon site, and the fractional enrichment can be calculated if the intermediate pool size is known. The ^{13}C NMR technique permits data to be acquired continuously and non-destructively while metabolism is in progress. Hence integrated biochemical and physiological responses of the tissue to external stimuli may be explored.

An important application of ^{13}C NMR is the evaluation of oxidative metabolic activity within a tissue, as a measure of functional activity that cannot be readily obtained under normal circumstances (e.g. brain). For a fundamental understanding of how ^{13}C studies can be applied to monitor metabolic flux in such systems, the data from studies in the heart have provided particular insight. Infusion of [^{13}C]–enriched substrates allow the metabolic activity of the tricarboxylic acid cycle (TCA) to be monitored in the intact heart. Using ^{13}C NMR, Malloy et al measured the fractional enrichment of [2-^{13}C] acetyl-CoA entering the cycle and the relative activities of the oxidative versus the anaplerotic pathways in the perfused rat heart (5). Neurohr and co-workers demonstrated the feasibility of detecting ^{13}C-enriched glutamate signals from the heart of an open-chested guinea pig during intravenous infusion of [2-^{13}C] acetate (6). ^{13}C NMR thus provides a useful methodology to investigate in-vivo metabolic activity in a non-invasive manner.

4.2.1 Low Detection Sensitivity in ^{13}C NMR

The biggest obstacle in the use of steady-state ^{13}C NMR for metabolic probing is its extremely low detection sensitivity. To understand the reasons for this limitation and elucidate the need for hyperpolarization, it is worth discussing the MR signal intensity *S*,

which is proportional to concentration of ^{13}C nuclei [^{13}C], γ and spin polarization P as given in eqn. (4.1). The intrinsic low sensitivity of ^{13}C detection can be partially attributed to its low ratio that is only a quarter of that in proton (10.71 MHz T^{-1}). Coupled with a low natural abundance of 1.1%, it appears that detecting ^{13}C with NMR becomes extremely difficult to perform under normal conditions. Spin polarization reflects the inequality between parallel (N^+) and anti-parallel (N^-) spins, parallel being aligned in the same direction as the main magnetic field $\overrightarrow{B_0}$, and is given by eqn. (4.2) and (4.3) for a spin ½ nucleus. At normal body temperature of 310 K and clinical field strength of 3 T, polarization at thermal equilibrium is merely 2.5×10^{-6} for ^{13}C while it is 9.9×10^{-6} for ^{1}H. The quadrupled discrepancy is due to the gyromagnetic ratio difference. The low natural abundance of ^{13}C could be alleviated in part by using ^{13}C-labeled compounds. Even with such unique atomic composition however, the low physiological concentration of metabolites (usually less than 1 mM) severely limits its detection with ^{13}C NMR, not to mention ^{13}C MRI.

$$MR\ Signal, S \propto \gamma_{13C} \cdot P \cdot \left[^{13}C\right] \tag{4.1}$$

$$Spin\ Polarization\ , P = \left(\frac{N^+ - N^-}{N^+ + N^-}\right) \tag{4.2}$$

$$P = \tanh\left(\frac{\gamma \hbar B_0}{2k_B T}\right) \tag{4.3}$$

4.2.2 Hyperpolarized ^{13}C Compounds for Signal Enhancement

Despite the low signal of ^{13}C compounds, its large range of chemical shifts in various microenvironments has made it an important nucleus in analytical NMR, particularly for molecules of biological origin. For successful implementation, it is imperative that the demand for much higher SNR must be met. Referring to eqn (4.1), the only factor that can be adjusted with technology is the polarization. Advancing to higher field strength while maintaining an extremely low temperature appears to be the easiest solution for polarization enhancement. A straightforward 'brute' force approach does exactly that by cooling the ^{13}C sample to liquid helium temperature (4 K) at a very high magnetic field (20 T) which increases the polarization by 1000 times (7). Unfortunately, 1000 times signal increase is still insufficient for clinical application, notwithstanding the impractical low temperatures that are required.

Unity polarization indicates the occupation of a single energy state by all nuclei (i.e. 100% polarization). Therefore theoretically it should be possible to achieve an enhancement of 400,000 times in ^{13}C polarization at 3 T. At thermal equilibrium, the Zeeman energy gap between the two discrete energy levels in a spin-½ system is very small,$\Delta E = \gamma \hbar B_0$, and thus there is no energy advantage for nuclei to occupy either energy state. The Boltzmann's distribution of spins is then almost equal between the two energy levels and polarization is low, as implied by eqn. (4.2). Hyperpolarization is the method employed to upset this balance by reordering the nuclei to occupy one energy level, as shown in figure 4.1. This allows transient non-equilibrium whereby one energy state contains many more nuclei than the other, effectively boosting the polarization and overcoming the sensitivity handicap.

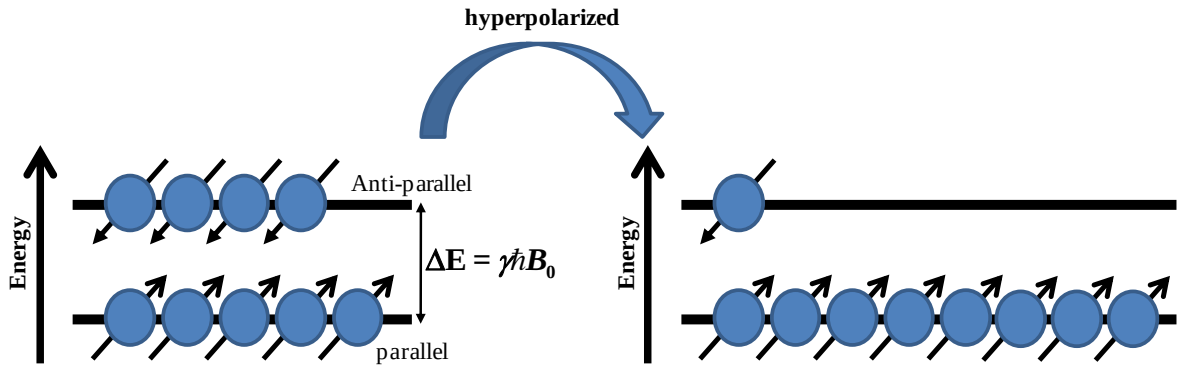

Figure 4.1: The imbalance of spin-occupied energy states upon hyperpolarization.

Many technological advances in the past two decades have occurred to make hyperpolarization feasible for applications in physiological examination, primarily optical pumping (8,9), parahydrogen induced polarization (PHIP) (10,11) and dynamic nuclear polarization (1,12). Optical pumping involves the passing of circularly polarized light from lasers at suitable resonant frequencies along an outer magnetic field through cells containing the noble gas (^{129}Xe or ^{3}He) together with either an alkali-metal vapor or metastable atoms. The angular momentum of the laser is absorbed and causes polarization of the total spin of the vapor or metastable gas. Thus, a 'pumping' of atoms having an anti-parallel spin state into more parallel-oriented spins takes place. The polarization is then transferred from the vapor or metastable atoms to the noble-gas atoms (13). This polarization enhancement technique has been particularly beneficial in the investigation of pulmonary (14,15). The PHIP technique on the other hand involves the use of parahydrogen, which are isomers of hydrogen molecules with an anti-symmetric nuclear state. They have a total nuclear spin of 0 and thus do not exhibit an NMR signal. In the late 1980s, Bowers and Weitekamp discovered that the catalytic hydrogenation of small organic molecules with parahydrogen led to a high ordered spin state conspicuously showing up by the observation of very large NMR signals

for the corresponding protons (16,17). The non-equilibrium proton spin order can be converted to longitudinal polarization of a nearby ^{13}C molecule either by means of diabatic-adiabatic field-cycling method (11) or by a sequence of rf pulses (18). The resultant highly polarized ^{13}C compound, with polarization elevated by at least 100,000 times, is an effective contrast medium that combines the long T_1 of ^{13}C with a high concentration of the NMR active nucleus, thus enabling a considerable degree of signal enhancement (19). The hyperpolarized state is transient though as the polarization will strive to return to the thermal equilibrium level at a rate governed by the T_1 relaxation time. The loss of polarization due to T_1-relaxation leads to signal decay with time and is non-recoverable. T_1 strongly depends on the chemical structure and environment of the hyperpolarized compound, and for ^{13}C it can typically range from a few seconds to several minutes.

4.3 Dynamic Nuclear Polarization (DNP)

A nascent hyperpolarization method is the use of dynamic nuclear polarization, which is based on polarizing the nuclear spins in the solid-state. The rationale behind DNP is obvious from eqn. (4.3). The thermal equilibrium polarization for ^{13}C is very low at 0.1 % under moderate conditions (1 K and 3 T) compared to the electrons, which are polarized to >90% owing to their much larger γ (6.73×10^7 versus 1.76×10^{11} rad s^{-1} T^{-1} respectively). The DNP technique effectively transfers the high polarization of electron spins to coupled nuclear spins (20). Although pioneering work by Jeffries, Abraham and Goldman in the 1950s opened up insights on nuclear polarization (21,22), the method's requirement for nuclei to occupy the solid-state, at extremely low temperatures, prevented its application in biology. Fortunately, in 2003, iconic work by Ardenkjaer-Larsen and his coworkers solved this problem with a method to dissolve DNP-polarized samples and yet retain virtually all of the solid-state

polarization. By combining solid-state DNP and dissolution techniques, they enabled nuclear polarization of 40%, thus enhancing sensitivity by 45,000 times together with in-vivo stability of approximately 1 min (1). In the following subsections, I briefly describe the physical mechanism behind DNP and outline the experimental procedures involved in a typical DNP-^{13}C NMR experiment.

4.3.1 Dynamic Nuclear Polarization Mechanism

Consider a sample of MR-active nuclei that is doped with a source of fixed paramagnetic impurities. When microwave irradiation of frequency ω is applied at or near the electronic Larmor frequency of the impurities ω_e, electron-nuclear coupling occurs and leads to electron-nuclear transitions, which enhance the absolute nuclear polarization (22). The magnitude of enhancement, mechanism of polarization and the conditions which result in maximum enhancement depend on the nature of the electron-nuclear interactions.

An Overhauser effect occurs when electron-nuclear interactions are time-dependent on a scale comparable to $1/\omega_e$, and the enhancement maximizes when the irradiation frequency ω is equal to ω_e. It has been observed in alkali metals, semiconductors, and in organic radicals such as coal (23). A solid-state effect (also known as solid effect) occurs in solids containing fixed paramagnetic centers, where the electron nuclear interactions are time-independent. Consider an assembly of nuclear spins I = ½ of Larmor frequency ω_n embedded in a diamagnetic solid that contains a few paramagnetic impurities with electronic spins S = ½ of Larmor frequency ω_e, coupled to neighboring nuclear spins by dipolar interactions. Since $\gamma_e \gg \gamma_n$, therefore $\omega_e \gg \omega_n$. In an environment with a strong magnetic field and

extremely low temperature (T ~ 1.2 K), virtually all electrons occupy the lower energy state, in accordance with the Boltzmann distribution, but it is not the case with the ^{13}C nuclei due to their much lower γ. When external microwave radiation is applied at a frequency $\omega = \omega_e \pm \omega_n$, electrons will possess sufficient energy to flip up to the next higher energy level, accompanied by either a simultaneous flip up of a nucleus to its higher energy-level (a 'flip-flip', which occurs at the frequency $\omega_e + \omega_n$) or flop down of a nucleus to the lower energy level (a 'flip-flop', at the frequency $\omega_e - \omega_n$). Flip-flip and flip-flop transitions are depicted in figure 4.2 (22). These transitions are so-called 'forbidden transitions' because their probability of occurrence is minimal without microwave excitation. Because the electronic relaxation rate is several orders of magnitudes faster than the corresponding nuclear relaxation rate, each electron can undergo transitions with many nuclei. With continued irradiation, nuclear polarization builds towards an enhanced value. Polarization enhancement is negative and becomes optimal at $\omega = \omega_e + \omega_n$, whereas it is positive at $\omega = \omega_e - \omega_n$ (23). The other mechanism that enhances polarization is the thermal-mixing effect, which occurs in solids with fixed paramagnetic centers. When the broadening of the electron paramagnetic resonance (EPR) line becomes comparable to the nuclear Larmor frequency ω_n, the nuclear Zeeman system is coupled to the electron broadening system, The polarization corresponding to this broadening system can thus be enhanced by irradiating at the electronic Larmor frequency ω_e. Then because of electron-nuclear coupling, the nuclear Zeeman polarization also becomes enhanced. The overall polarization enhancement is a sum of solid-state and thermal mixing effects and it has been demonstrated that 100% polarization is possible with the DNP technique (24).

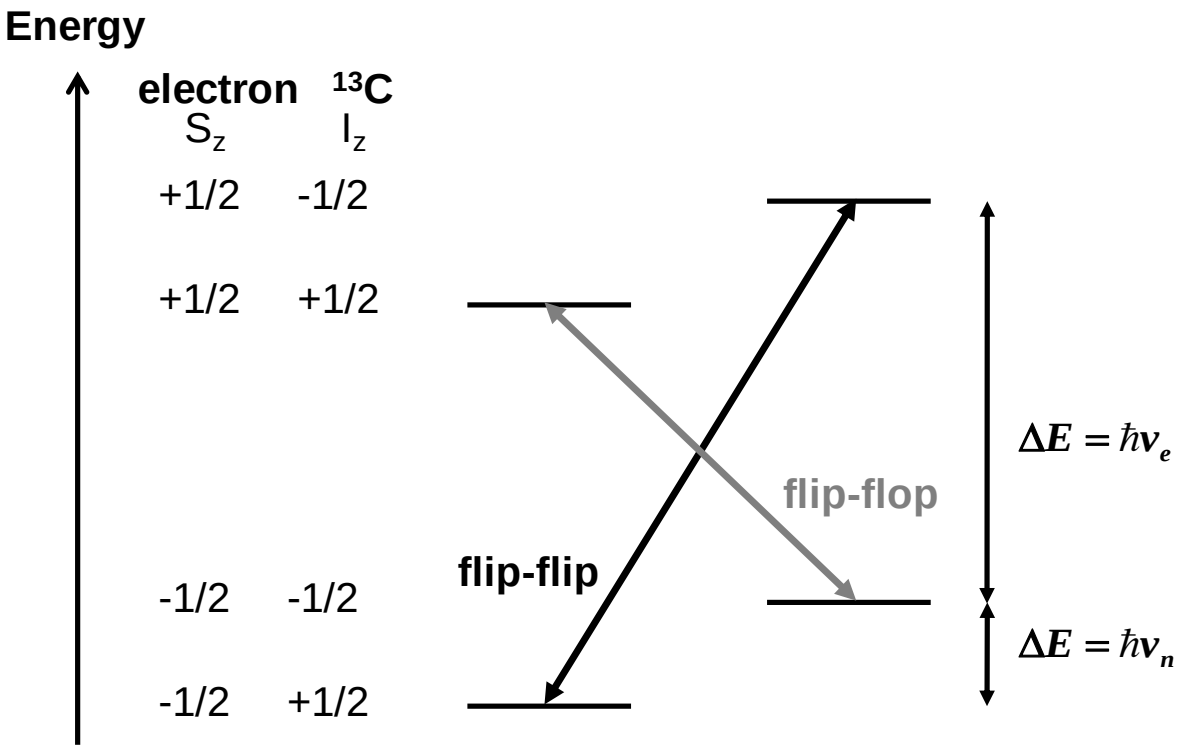

Figure 4.2: A schematic of the electron-nuclear transitions of the solid effect in a magnetic field. S_z and I_z denotes the spin of electron and nuclei respectively. '+' indicates parallel while '-' denotes anti-parallel orientation. At a low temperature T ~ 1.2 K, all electrons are at the lower energy level (S_z = -1/2). Microwave irradiation at $\omega = \omega_e - \omega_n$ excites electrons to the higher energy-state and leads to a 'flip-flop' transition in which the nuclei are transferred from the high to the low energy states, resulting in a positive signal enhancement. On the other hand, microwave irradiation at $\omega = \omega_e + \omega_n$ leads to a 'flip-flip' transition in which the nuclei are excited into higher energy state, resulting in a negative signal enhancement.

4.3.2 Liquid-State DNP

A hyperpolarized solid-state organic molecule cannot be delivered efficiently into the circulation and it must be converted into a liquid state, with minimal loss in polarization. To create a highly polarized liquid-state ^{13}C biological sample, the compound is first doped with a source of single-electron substance and then subjected to microwave irradiation within a super-cooled (~1.4 K) 3T magnet. For this thesis, the compound used to study the metabolic fate of exogenously infused pyruvate consists of [1-^{13}C] pyruvic acid was mixed with a small concentration of paramagnetic centers known as triarylmethyl (trityl) radical OXO63 (25). An optimal dose of the radical is important because an excess of paramagnetic centers hastens nuclear relaxation (preventing polarization build-up) (1) whereas a deficiency results in slow polarization (26). The helium-cooled environment is meant to force all electrons to occupy the lower energy-state, which increases the total 'flipping' transitions. It has been suggested that a minute addition of gadoterate meglumine (Gd-DOTA) could be further added in order to boost polarization enhancement. It is hypothesized that the Gd^{3+} chelated ions shorten the electronic T_1 in the sample and allow each electron to polarize more nuclei (26), though it is yet to be confirmed. A microwave sweep to identify the appropriate frequency for positive polarization enhancement is displayed in Figure 4.3a, which occurs at 94.139GHz. Figure 4.3b illustrates a typical dynamic polarization build-up of the [1-^{13}C] pyruvic acid/ OXO63/Gd^{3+} sample at 94.139GHz with microwave power of 100mW. Dynamic nuclear polarization is carried out in a commercial hyperpolarizer system ('Hypersense') from Oxford Instruments and is normally completed within an hour. A picture of the instruments is shown in figure 4.3c. Main components of the hyperpolarizer consist of a 3.35T magnet with a sample insert that is cooled to 1.1K during DNP, a microwave generator for irradiation and a pressurized dissolution system (1). During dissolution, the hyperpolarized sample is dissolved in an alkaline buffer (NaOH) and heated to body

temperature. An 80 mM solution of sodium pyruvate with a net polarization of ~30% and pH between 7.0 – 7.8 is then obtained. Figure 4.3d illustrates a schematic diagram of the process in a routine experiment with the hyperpolarized biological probe.

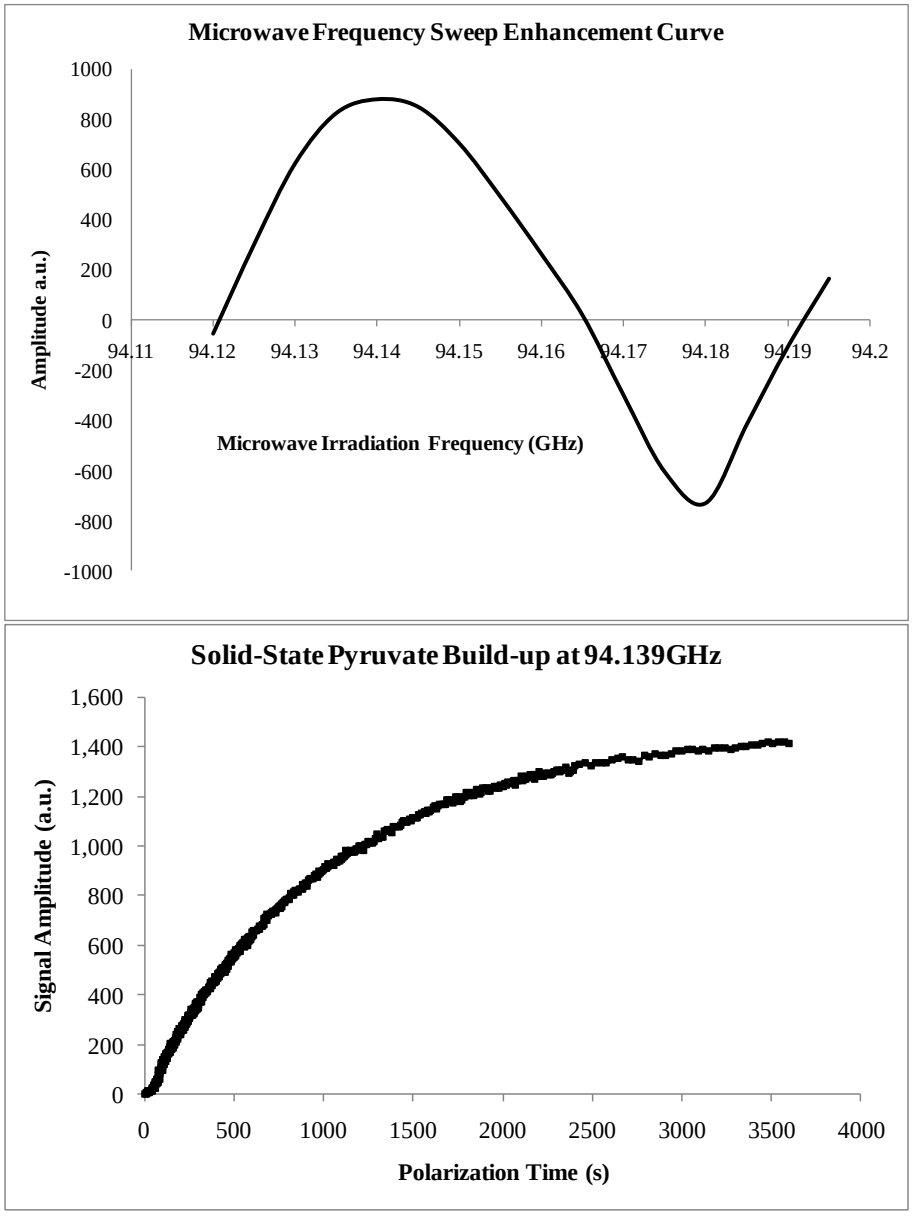

Figure 4.3: (A) Microwave frequency sweep to identify the optimal frequency for positive enhancement of polarization in a [1-^{13}C]-pyruvic acid/OXO63/Gd3^{+} sample. (B) The corresponding polarization build-up at frequency = 94.139GHz.

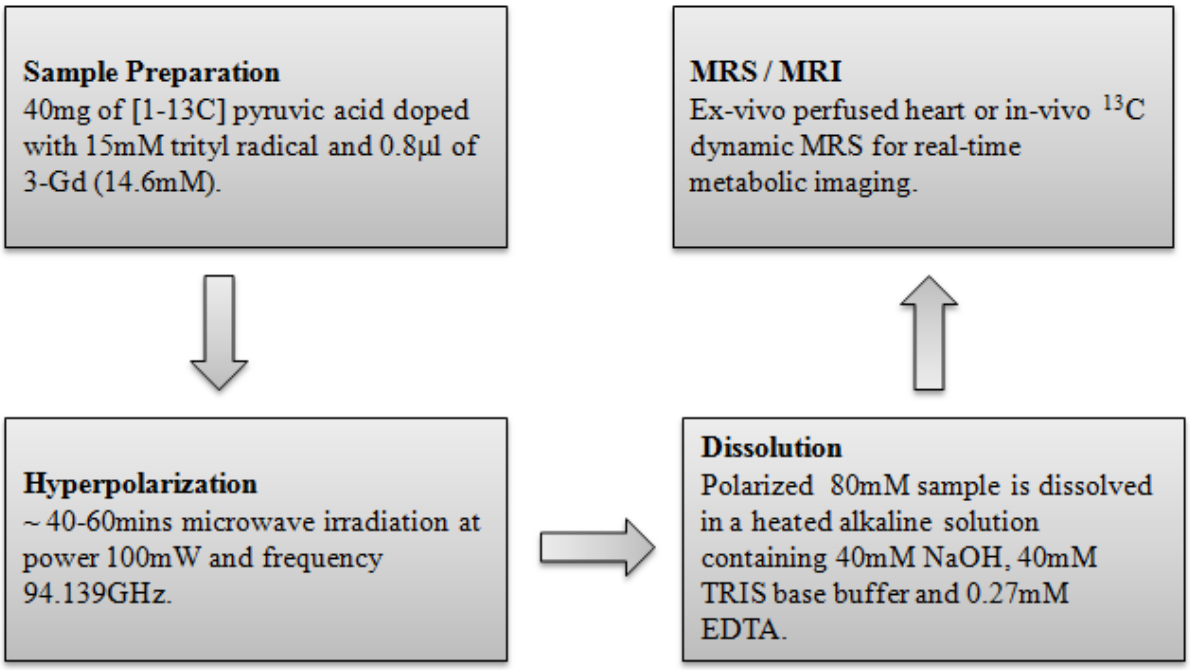

Figure 4.3c: DNP polarizer at the Cardiac Metabolism Research Group in the University of Oxford. To maximize the limited lifetime of the hyperpolarized sample, the hyperpolarizer is placed juxtaposition to the 11.7T vertical bore MRI system. (d) A typical process flow utilizing hyperpolarized pyruvic acid as a metabolic tracer.

4.4 Energy Generation in the Heart

Heart muscle is both consumer and provider of energy. It consumes energy locked in the chemical bonds of fuels through their controlled combustion and converts chemical energy into mechanical energy. The heart also provides energy in the form of substrates and oxygen both for itself and to the rest of the body. It is a center of immense metabolic activity because adenosine 5'-triphosphate (ATP), the chemical energy available, has to be continually re-synthesized from its breakdown products, adenosine 5'-diphosphate (ADP) and inorganic phosphate (P_i). The greater the cardiac output, the higher the ATP turnover rate. Since the heart's contractile activity essentially controls nutrition delivery to the rest of the body, it is unsurprising that the heart produces and uses 35 kg of ATP daily, more than 100 times its own weight and more than 10,000 times the amount of ATP stored in the heart for impromptu hydrolysis (27). Additionally, it consumes 10% of O_2 in the body, despite accounting for only 0.5% of body weight. Impairment in energy transfer in the heart is thus detrimental to proper physiological functioning of the human body.

In the heart, the direction of most enzyme-catalyzed reactions is catabolic, which is the breaking down of large macromolecular fuel complexes into smaller molecules, liberating the energy stored in the chemical bonds in the process. Biochemists have found it convenient to group the breakdown of substrates into three stages, as illustrated in Figure 4.4 (28). The first stage involves the breakdown of substrates into acetyl-CoA via fatty acid β-oxidation, glucose or amino-acids metabolism. In the second stage, acetyl-CoA units are oxidized in the Krebs or TCA cycle to CO_2. Four pairs of electrons are transferred (three to NAD+ and one to FAD) for each acetyl group that is oxidized. Then ATP is generated as electrons flow from the reduced forms of these carriers to O_2 in a process known as oxidative phosphorylation.

More than 90% of the ATP generated by the degradation of foodstuffs is formed in this third stage. For this thesis, we delivered hyperpolarized ^{13}C-labeled pyruvate into the heart and track its metabolic fate. Thus we are more interested on the oxidative decarboxylation of pyruvate into acetyl-CoA, as well as its subsequent downstream biochemical processes in the TCA cycle. We shall follow the catabolism of pyruvate into the Krebs cycle, with particular attention paid on metabolic regulation via control of (1) amount of enzymes, (2) their catalytic activities and (3) substrate accessibility. The investigation of acetyl-carnitine as a temporary storage compartment of acetyl-units at the end of Stage 1, before incorporation into the TCA cycle, is also explored.

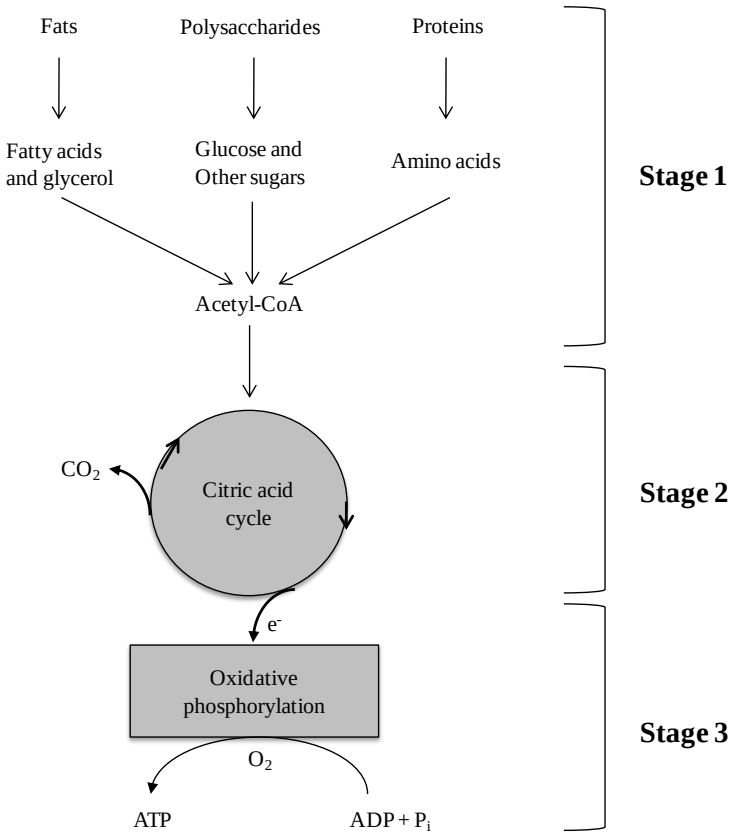

Figure 4.4: The three stages of energy transfer in heart muscle consist of intermediary metabolism, Krebs citric acid cycle and the respiratory chain. The aim of intermediary metabolism is the production of acetyl-CoA for oxidation in the Krebs cycle, and ultimately ATP synthesis.

4.4.1 Metabolic Fate of Pyruvate

Pyruvate is the downstream metabolic product of glucose via the glycolytic pathway and is a central metabolic intermediate that can either be further oxidized or used as a building block. Its metabolic fate is summarized in figure 4.5, where its downstream metabolites and the enzymes that are involved in the biochemical processes are displayed. This three-carbon α-keto acid is a major metabolic junction governing the flow of molecules in metabolism. It can be reduced into lactate, catalyzed by the enzyme lactate dehydrogenase (LDH). This pathway generates NAD^+ and enables continual operation of glycolysis under anaerobic conditions. Another readily reversible reaction in the cytosol is the transamination of pyruvate to alanine, an amino acid. Transamination is a major link between amino acid and carbohydrate metabolism. The third fate of pyruvate is its anaplerotic role, whereby it undergoes carboxylation to become oxaloacetate inside the mitochondria. This pathway serves as a source of replenishment of intermediates in the citric cycle. When a paucity of oxaloacetate occurs and the citric acid cycle is slowed, acetyl-CoA activates pyruvate carboxylase to accelerate the synthesis of oxaloacetate. A fourth, perhaps most important fate of pyruvate is its oxidative decarboxylation to acetyl-CoA. This irreversible reaction inside mitochondria is a decisive reaction in metabolism because it commits the carbon atoms of carbohydrates and amino acids to oxidation in the citric acid cycle or synthesis into lipids. The pyruvate dehydrogenase complex (PDH), which catalyzes this irreversible funneling, is stringently regulated by multiple allosteric interactions and covalent modifications. Pyruvate is rapidly converted into acetyl-CoA only if ATP is needed or if two-carbon fragments are required for the synthesis of lipids.

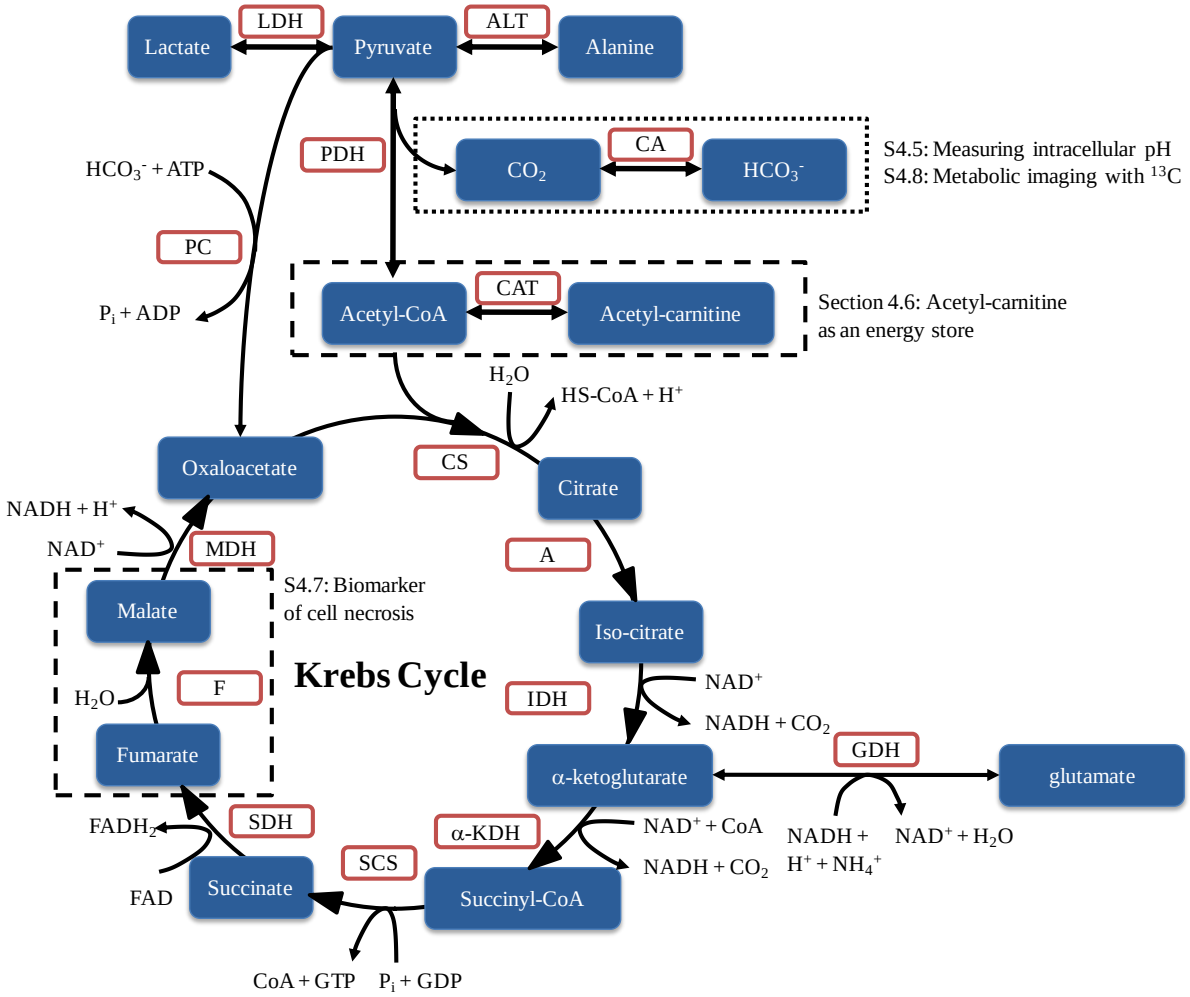

Figure 4.5: Principle biochemical pathways depicting the metabolic fate of pyruvate. Metabolite substrates are in blue boxes whereas catalytic enzymes are in red boxes. The metabolic processes that are investigated in this thesis are in dashed boxes together with the respective sections which the reader is referred to. Abbreviations for the various enzymes, electron transport carriers and acceptors can be found in Appendix A.

4.4.2 NMR Spectroscopy of [1-^{13}C] and [2-^{13}C] – Labeled Pyruvate

The heightened sensitivity enabled by hyperpolarized ^{13}C nuclei offers the possibility of using non-invasive NMR spectroscopy to measure fluxes through individual enzyme catalyzed reactions (29,30). [1-^{13}C] pyruvate has been used successfully to probe pyruvate dehydrogenase activity and lactate production. Aberrations in these biochemical processes appear to reflect pathophysiology and thus they have been proposed as potential biomarkers of diseases. Schroeder et al demonstrated the feasibility of real-time in-vivo assessment of pyruvate dehydrogenase flux in fasted and diabetic rats (3). By utilizing the generation of bicarbonate ($H^{13}CO_3^-$) as an indicator of PDH flux, they were able to detect a 65% reduction in the conversion of pyruvate to acetyl-CoA in STZ-induced rats, and established a negative correlation between bicarbonate production and disease severity. Lactate accumulation in the heart has also been shown to be a metabolic indicator of cardiac ischaemia (2). Albers and co-workers observed increasing hyperpolarized lactate production in prostate cancer development and proposed its utilization as a biomarker of tumor progression (31). Day et al hypothesized that the reduction in lactate production in tumors is due to tumor cell death and proposed using lactate dehydrogenase flux to assess the effectiveness of chemotherapy (32).

Normal cardiac function is dependent on a constant rate of ATP resynthesis by mitochondrial oxidative phosphorylation and, to a much lesser extent, glycolysis. Oxidation of fatty acids is responsible for about 60–90% of the resynthesized ATP, with the balance coming from the oxidation of pyruvate that is derived from glycolysis and lactate uptake (33). Cardiac ATP production is controlled largely by the rate at which the Krebs cycle operates (28). The chief fuel input to the Krebs cycle is the 2-carbon acetyl-CoA molecule, which is produced from oxidation of fatty acids, ketone bodies or glucose via glycolysis and oxidative

decarboxylation of pyruvate. Some mechanisms that lead to energetic imbalances in heart disease could thus be studied by simultaneously monitoring the source and the fate of glucose-derived acetyl-CoA in the heart. DNP hyperpolarized [2-^{13}C] pyruvate fulfils this role by offering real-time assessment of Krebs cycle metabolism using ^{13}C MRS. Metabolic responses to physiological perturbation such as ischaemia has been demonstrated to be directly measurable with 1 second temporal resolution (2).

To probe the downstream metabolic processes of DNP hyperpolarized pyruvate, ^{13}C label is either at the 1st or 2nd carbon position, dependent on the biochemical pathway of interest. In Section 4.5, we utilized [1-^{13}C] pyruvate to study the inter-conversion between bicarbonate and carbon dioxide in order to examine the role of carbonic anhydrase (CA) mediation in regulating intracellular pH. Real-time metabolic imaging to visualize PDH and CA activities, upon infusion of [1-^{13}C] pyruvate, are discussed in Section 4.8. [2-^{13}C] pyruvate on the other hand is used in the investigation of acetyl-carnitine role in myocardial carbohydrate metabolism, and that is discussed in Section 4.6. Although it appears that dual-labeling could improve experimental efficiency by measuring metabolic fluxes of the above processes in one attempt, it is technically very challenging because the chemical shifts of metabolites range widely and a wide receiver bandwidth is necessary, which reduces the spectral resolution. In addition, some metabolites such as lactate and glutamate have very similar chemical shifts (183.2 and 183.7 ppm respectively), and their overlapping spectra could convolute the analysis. An exception is the hydration of dual-labeled [1,4-$^{13}C_2$]fumarate, which produces [1,4-$^{13}C_2$]malate with two distinct resonances. We investigate the potential application of [1,4-$^{13}C_2$]fumarate as a biomarker of necrosis in the ischaemic heart in Section 4.7.

4.5 Measuring Intracellular pH in the Heart using Hyperpolarized Carbon Dioxide and Bicarbonate: a ^{13}C and ^{31}P Magnetic Resonance Spectroscopy Study

The aim of this study was to evaluate the potential of hyperpolarized [1-^{13}C]pyruvate to measure intracellular pH (pH_i) in healthy and diseased heart with ^{13}C magnetic resonance spectroscopy. PDH flux was measured before and after ischaemia and with CA activity inhibited. Mathematical modeling was implemented to assess the conditions whereby the $H^{13}CO_3^-/^{13}CO_2$ ratio can be used reliably for pH_i quantification in the rat heart.

This work has recently been published in Cardiovascular Research (34) and is a collaborative effort between Cardiac Metabolism Research Group and the Proton Transport Group at the Department of Physiology, Anatomy and Genetics in the University of Oxford, and the Cancer Research UK Cambridge Research Institute. The manuscript was prepared by Dr. Marie A. Schroeder.

4.5.1 Introduction

In myocardial ischaemia, anaerobic glycolysis increases in the heart, producing intracellular protons and lactic acid that accumulate in the intra- and extracellular spaces (35). Some of the acid reacts with HCO_3^- to form CO_2, which adds to any CO_2 generated by residual oxidative metabolism. Accumulation of protons, lactic acid and CO_2 in the ischaemic heart decrease intracellular pH from normal physiological levels of around 7.1-7.2 (36). Transient acidosis during ischaemia may be beneficial though and it exerts temporary cardio-protection by conserving ATP for ion transport (37). However, prolonged ischaemia reduces ATP production and leads to weakened Na^+, K^+ -ATPase activity, which increases myocardial Na^+

levels. Elevated Na^+ inhibits Ca^{2+} extrusion via the Na^+/Ca^{2+} exchanger, thus raising myocardial Ca^{2+} and damaging the myocardium. A measure of intracellular pH would thus open up insights into the state of acidosis in the ischaemic heart and allow assessment of therapeutic interventions on ATP production.

The gold standard of measuring intracellular pH in the isolated perfused heart is ^{31}P magnetic resonance spectroscopy (38), based on the chemical shift in inorganic phosphate (P_i) peak (39,40). However, ^{31}P MRS cannot measure cardiac pH_i in-vivo because the presence of 2,3-diphosphoglycerate (2,3-DPG) in the ventricular blood contaminates the myocardial P_i peak (38,41). It has been demonstrated recently that detection of hyperpolarized $^{13}CO_2$ is possible upon intravenous infusion of $H^{13}CO_3^-$ and their ratio has been used to map the extracellular pH in tumors (42) according to the Henderson-Hasselbach equation, where pK_a is the acid-dissociation constant of CO2, which is 6.15 in the Krebs-Henseleit buffer (43).

$$pH = pK_a + log\left(\frac{\left[H^{13}CO_3^-\right]}{\left[^{13}CO_2\right]}\right) \quad (4.4)$$

Since both hyperpolarized $H^{13}CO_3^-$ and $^{13}CO_2$ are detectable with ^{13}C MRS when [1-^{13}C] pyruvate is broken down via PDH (29,44), we could perhaps measure intracellular pH with this probe, provided the following conditions are met:

(1) Chemical exchange between $^{13}CO_2$ and $H^{13}CO_3^-$ catalyzed by carbonic anhydrase must be slow and

(2) Simultaneous detection of $^{13}CO_2$ and $H^{13}CO_3^-$ in the same cellular compartment.

pH can be reliably measured in tumors because of the high CA activity on the surface cells (45) and within erythrocytes (46), and the slow, transporter-mediated cellular uptake of infused bicarbonate (47). These conditions though may not apply in cardiac myocytes because the metabolically generated CO_2 diffuses rapidly from the mitochondria into the cytosol, and subsequently into the extracellular space (48). HCO^{3-} may also be removed from the cell via Na^{+}-HCO^{3-} co-transporter and the Cl^{-}/HCO^{3-} exchanger (43). Intracellular CA activity in cardiac myocytes is normally low (49) and could be further depressed in ischaemia (50,51). In addition, PDH flux post-ischaemia must be sufficiently high to enable MRS detection of $H^{13}CO_3^{-}$ and $^{13}CO_2$ prior to decay of the hyperpolarized ^{13}C MR signal.

4.5.2 Materials and Methods

Isolated Perfused Rat Heart

All investigations conformed to the Guide for the Care and Use of Laboratory Animals published by the US National Institutes of Health (NIH Publication No. 85-23, revised 1996), the Home Office Guidance on the Operation of the Animals (Scientific Procedures) Act, 1986 (HMSO), and to institutional guidelines. Male Wistar rats (~300 g) were anaesthetized using a 0.7 mL i.p. injection of pentobarbital sodium (200mg/mL Euthatal). The beating hearts were quickly removed and arrested in the ice-cold Krebs–Henseleit perfusion buffer, and the aorta was cannulated for perfusion in re-circulating retrograde Langendorff mode at a constant 85 mmHg pressure and 37°C temperature. The Krebs–Henseleit bicarbonate perfusion buffer contained 1.2 mM inorganic phosphate (KH_2PO_4), 11 mM glucose, and 2.5 mM pyruvate and was aerated with a mixture of 95% oxygen (O_2) and 5% carbon dioxide (CO_2) to give a final pH of 7.4 at 37°C. The broad-spectrum CA inhibitor, 6-ethoxyzolamide (ETZ), was dissolved in dimethyl-sulfoxide (DMSO) and added to the perfusate to achieve a

final concentration of 100 mM (with DMSO < 0.01% of total buffer volume). ETZ was expected to evenly distribute throughout the intra- and extracellular spaces to inhibit all cardiac CA isoforms.

Control Protocol

Isolated hearts (n = 6) were perfused for 30 min at 85 mmHg. For the initial 20 min, ^{31}P MRS was used to measure pH_i. After that, hyperpolarized [1-^{13}C]pyruvate was infused and the progress of ^{13}C-labeled compounds was followed using ^{13}C MRS.

Inhibition of Carbonic Anhydrase with ETZ

Hearts (n = 5) were perfused for 10 min in normal buffer, after that they were switched to buffer containing 100mM ETZ. ^{31}P MRS was performed for 20 min (10 min before and 10 min after switch over to ETZ-containing buffer). 10 min after the start of ETZ perfusion, hyperpolarized [1-^{13}C]pyruvate was infused and MRS was switched from ^{31}P to ^{13}C.

Reperfusion following ischaemia

Hearts (n = 12) were perfused for 30 min, followed by 10 min of global ischaemia, and 15 min reperfusion. ^{31}P MRS spectra were acquired for 20 min immediately before and 9 min during ischaemia. Hyperpolarized [1-^{13}C]pyruvate was infused immediately after ischaemia. In some hearts (n = 6), ^{31}P MRS was performed throughout the reperfusion period. In other hearts (n = 6), ^{13}C MRS was performed for 2 min during initial reperfusion with hyperpolarized [1-^{13}C]pyruvate, followed by 10 min of ^{31}P MR spectral acquisition.

Magnetic Resonance Spectroscopy

^{31}P MR spectra were acquired at 202.5 MHz using a 30° RF pulse and a repetition delay of 0.25s. The phosphocreatine (PCr) resonance was set the reference at 0 ppm. Each spectrum consisted of 120 transients, giving a total acquisition time of 30 s. As these partially saturated spectra had shorter repetition times than the longitudinal relaxation time of ^{31}P nuclei, an unsaturated spectrum was initially acquired from the hearts using a 90° pulse with repetition time of 15 s and 40 transients, and an acquisition time of 10 min. The unsaturated spectra were used to correct metabolite concentrations for the effects of saturation. Acquisition of ^{13}C MR spectra commenced immediately after infusion of hyperpolarized [1-^{13}C]pyruvate and [1-^{13}C]pyruvate infusion continued throughout acquisition. Spectra were acquired with 1 s temporal resolution over 2 min (excitation flip angle = 30°, 120 acquisitions). Spectra were centered at 150 ppm and referenced to the [1-^{13}C] pyruvate resonance at 171 ppm, and 4096 points were acquired over a bandwidth of 100 ppm.

Data Analysis

Carbon-13

Cardiac ^{13}C MR spectra were analyzed using the AMARES algorithm, as implemented in the jMRUI software package (52). Spectra were DC offset corrected based on the last half of acquired points and peaks corresponding with [1-^{13}C]pyruvate and its metabolic derivatives were fitted assuming a Lorentzian line shape, initial peak frequencies, relative phases, and linewidths. For spectra acquired from perfused rat hearts, the maximum peak area of each metabolite over the 2 min of acquisition was determined for each series of spectra and expressed as a percentage of the maximum [1-^{13}C]pyruvate resonance. The rate of signal

production for each metabolite, in percent per second (%.s^{-1}), was measured as the slope of the mean metabolite increase over the first 5 s following its appearance, over which time the metabolite signal increased linearly. Additionally, a first-order exponential signal decay term was fitted to each metabolite peak from the point of maximum signal over the course of signal decay. Decay of the hyperpolarized signal depends on the intrinsic spin–lattice relaxation of the nucleus, production and consumption rates of the metabolite, and metabolite washout, and may therefore provide information about metabolite accumulation in the states of no-flow ischaemia and CA inhibition. Average time courses for $H^{13}CO_3^-$, $^{13}CO_2$, and their sum were calculated for all hearts for further data analysis. $H^{13}CO_3^-$ plus $^{13}CO_2$, normalized to the maximum pyruvate peak area to allow for any differences in polarization, was used as a qualitative indicator of PDH flux. The average $H^{13}CO_3^-$ and $^{13}CO_2$ time courses were inserted into an applied form of the Henderson–Hasselbalch equation:

$$pR = 6.15 + log\left(\frac{\left[H^{13}CO_3^-\right]}{\left[^{13}CO_2\right]}\right) \quad (4.5)$$

The output of Eq. (4.5) is a variable pR which should, under the two conditions outlined in Section 4.5.1, measures pH_i. Upon the initial arrival of [1-^{13}C]pyruvate, the relative proportions of $^{13}CO_2$ and $H^{13}CO_3^-$ (and thus pR) equilibrated over several seconds to reach a steady-state value. The calculated pR was fit to a first-order exponential equation to determine the steady-state value and time constant.

Phosphorus-31

Cardiac ^{31}P MR spectra were analyzed using the AMARES algorithm in the jMRUI software package. Spectra were corrected for DC offset using the last half of acquired points. The PCr, P_i, α-, β-, and γ-ATP resonances were fitted assuming a Lorentzian line shape, peak

frequencies, relative phases, line widths, and J-coupling parameters. pH_i was calculated from the P_i chemical shift (40). Absolute ^{31}P metabolite concentrations were calculated using an ATP concentration of 10.6 mM from the first γ-ATP peak area (53) and expressing all other ATP and PCr peak areas relative to this area (54).

Statistical methods

Data are given as mean ± standard error. Statistical significances between pre- and post-ischaemic groups, and pre-ischaemic and ETZ-perfused groups, were assessed using a paired Student's t-test. Statistical significance was considered at $P < 0.05$.

4.5.3 Results

Myocardial Energetics in Isolated Perfused Heart

Cardiac function and ^{31}P MR spectra were characteristic of the isolated rat heart during pre-ischaemia, ischaemia, and reperfusion (36). Pre-ischaemia, the average [ATP] was 10.6±0.7 mM and [PCr] was 19.7±0.9 mM (Figure 4.6). Two minutes after stopping coronary flow, [PCr] decreased to 3.2 mM, and remained at 1.1–2.1 mM for the remainder of ischaemia. The rate of [ATP] hydrolysis during ischaemia was 0.14±0.10 mM/min. Five minutes after reperfusion; PCr had recovered to 17.6±1.9 mM, whereas ATP remained at 8.2±2.5 mM. Perfusion with ETZ had no effect on [ATP] or [PCr] throughout the perfusion protocol. Prior to ETZ perfusion, hearts had an average PCr of 17.8±1.9 mM and ATP of 10.6±0.5 mM. During ETZ perfusion, the average [PCr] was 18.0±1.5 mM and [ATP] was 10.3±0.9 mM.

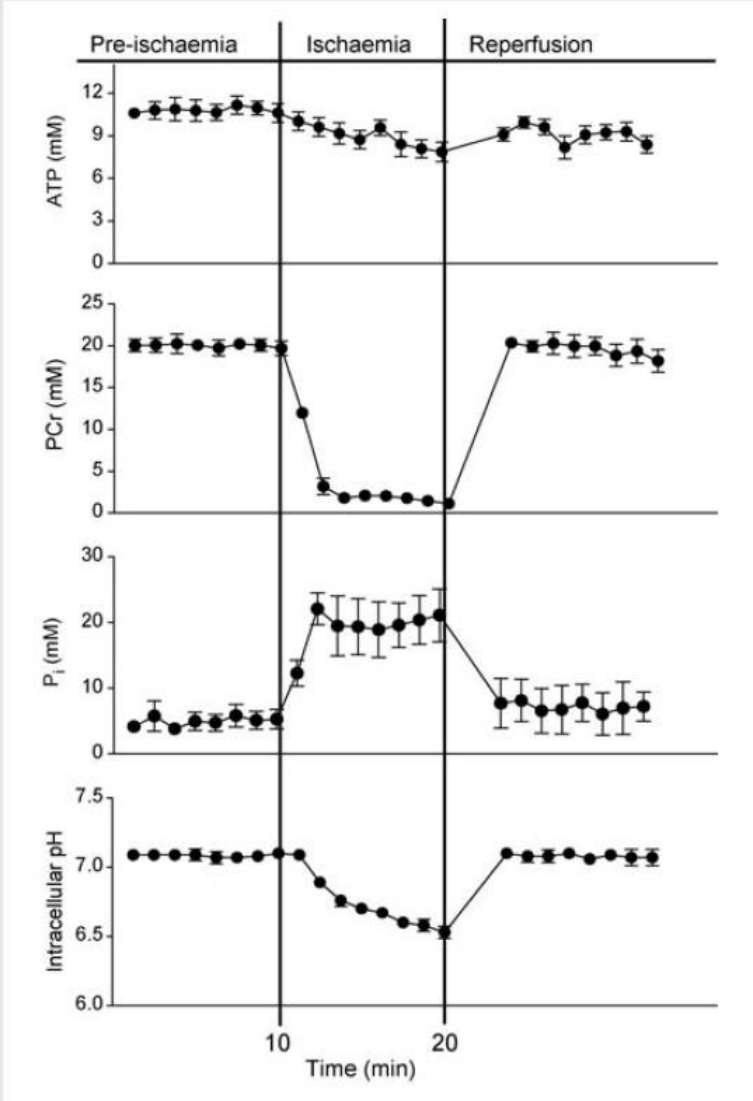

Figure 4.6: Changes in ATP, PCr, P_i and pH_i, before, during and after ischaemia. ATP levels gradually decreased during ischaemia and after reperfusion, partially recovered to pre-ischaemia levels. PCr levels rapidly decreased at the onset of ischaemia and rapidly recovered to pre-ischaemic levels after reperfusion. P_i rapidly increased at the onset of ischaemia and rapidly decreased to pre-ischaemic levels after reperfusion. pH_i gradually deceased from 7.07 to 6.49 during ischaemia and rapidly recovered to pre-ischaemia levels following reperfusion.

PDH flux in Isolated Perfused Heart

A representative spectrum of [1-^{13}C]pyruvate in the perfused heart, and the typical kinetic progression of [1-^{13}C]pyruvate metabolites, is shown in Figure 4.7. Following infusion of [1-^{13}C]pyruvate into control hearts, [1-^{13}C]lactate (183.2 ppm), $H^{13}CO_3^-$ (160.9 ppm), and [1-^{13}C]alanine (176.5 ppm) were clearly detectable with high signal compared with the baseline. A resonance corresponding to $^{13}CO_2$ was also visible, with 1 s temporal resolution, at a chemical shift of 124.5 ppm. The initial rates of production and the maximum peak areas for the [1-^{13}C]pyruvate-derived metabolites, in pre-ischaemic, ETZ, and reperfused hearts, are given in Table 4.1. The maximum peak areas of $H^{13}CO_3^-$, $^{13}CO_2$, and their sum were not significantly different from baseline when [1-^{13}C]pyruvate was infused into the myocardium upon reperfusion. However, the initial rate of $H^{13}CO_3^-$ plus $^{13}CO_2$ production was 54% slower upon reperfusion, compared with the pre-ischaemic myocardium, as indicated by the slope of the reperfusion peaks shown in Figure 4.8. Additionally, the decay rate of hyperpolarized $^{13}CO_2$ signal was 30% faster in reperfused hearts than in pre-ischaemic hearts ($P < 0.001$), indicating enhanced CO_2 washout upon re-flow after ischaemia. ETZ had no significant effect on the initial rate of $H^{13}CO_3^-$ plus $^{13}CO_2$ production, or the maximum peak area of the sum of $H^{13}CO_3^-$ and $^{13}CO_2$, compared with pre-ischaemic hearts (Figure 4.8). However, ETZ increased the maximum $^{13}CO_2$ peak area by four-fold, whereas decreasing the maximum $H^{13}CO_3^-$ peak area by two-fold (Table 4.1, $P < 0.001$). Additionally, the decay rate of hyperpolarized $^{13}CO_2$ signal was 19% faster in reperfused hearts than in pre-ischaemic hearts ($P < 0.05$), possibly indicating enhanced CO_2 diffusion out of myocytes in the absence of CA activity.

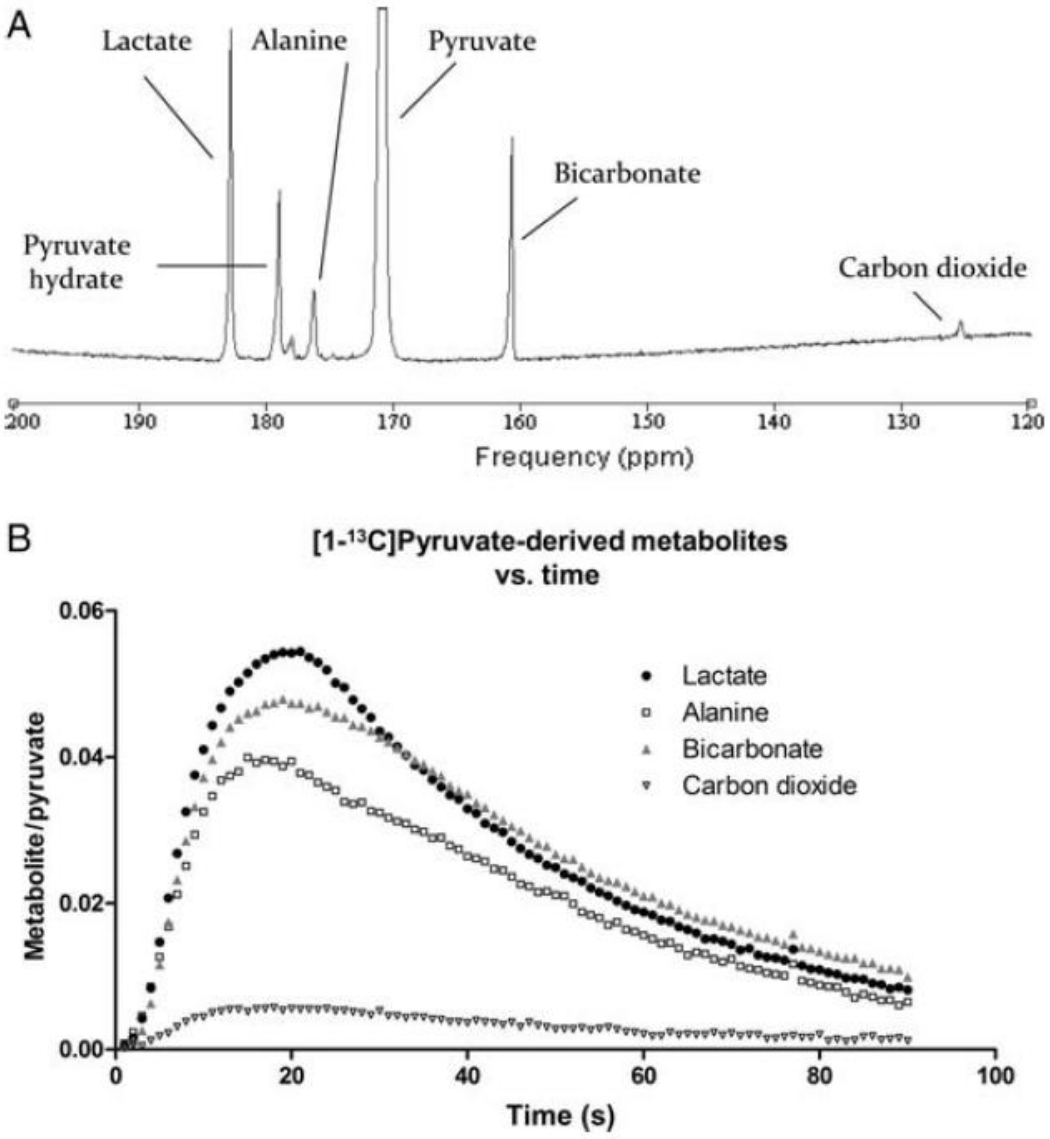

Figure 4.7: (A) Representative spectrum acquired during hyperpolarized [1-^{13}C] pyruvate infusion into the isolated perfused heart. Five single 1 s spectra were summed to yield this spectrum, acquired using a 30° rf pulse. (B) Changes in the metabolic products of [1-^{13}C] pyruvate in pre-ischaemic heart (n = 6).

	[1-^{13}C]Lactate			[1-^{13}C]Alanine		
	Pre-ischaemia	**Reperfusion**	**ETZ**	**Pre-ischaemia**	**Reperfusion**	**ETZ**
Max. metabolite/pyruvate (%)	6 ± 1	31 ± 3†	7 ± 2	4.2 ± 0.3	3.5 ± 0.2	5.7 ± 0.4
Initial production rate (% / s)	0.7 ± 0.1	4.4 ± 0.4†	0.7 ± 0.2	0.43±0.09	0.28 ± 0.03	0.7 ± 0.01
Decay, τ (s)	35 ± 4	22.3 ± 0.2*	41 ± 5	39 ± 2	41 ± 1	43 ± 7
	$H^{13}CO_3^-$			$^{13}CO_2$		
	Pre-ischaemia	**Reperfusion**	**ETZ**	**Pre-ischaemia**	**Reperfusion**	**ETZ**
Max. metabolite/pyruvate (%)	4.7 ± 0.6	3.8 ± 0.4	2.1± 0.2*	0.60±0.06	0.70 ± 0.06	2.6±0.2†
Initial production rate (% / s)	0.49±0.06	0.21 ± 0.04*	0.14±0.02*	0.06±0.02	0.053±0.007	0.31±0.03†
Decay, τ (s)	43 ± 4	35 ± 2	44 ± 4	48 ± 2	33 ± 2†	39 ± 3*

Table 4.1: Metabolite levels and kinetic parameters from ^{13}C MR spectra in pre-ischaemia, reperfused and ETZ-perfused isolated hearts. Data are expressed means ± SEM. All metabolite levels and initial production rates are expressed as a percentage of maximum [1-^{13}C] pyruvate signal. Significant difference from pre-ischaemic hearts: *P < 0.05, †P < 0.001.

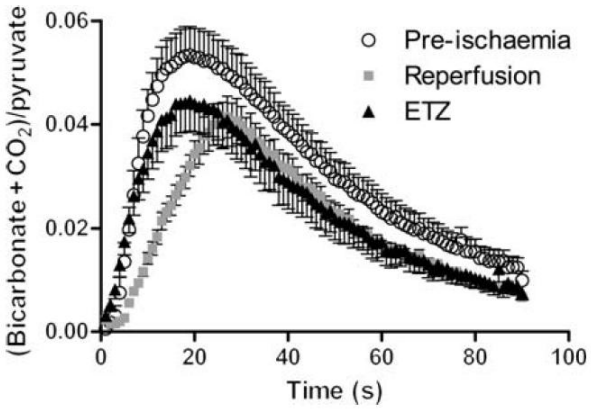

Figure 4.8: Comparison of the time courses for the sum of the bicarbonate and carbon dioxide peaks, normalized to the maximum value of pyruvate area. The maximum peak area did not change following either intervention, compared with control. Following ischaemia, the initial slope of the curve was significantly reduced.

Measurement of pH_i in the isolated perfused heart

Figure 4.9A shows the changes in $H^{13}CO_3^-$ and $^{13}CO2$, which were used for the calculation of pR. When hyperpolarized pyruvate reached the isolated heart, metabolically generated $H^{13}CO_3^-$ and $^{13}CO_2$ were out of equilibrium for 5 s before pR reached a steady-state value of 7.12±0.10 (Figure 4.9B). Fully relaxed ^{31}P measurements, acquired in the pre-ischaemic heart, gave a pH_i of 7.07±0.02. The pH_i measured using ^{31}P MRS and the 95% confidence interval are overlaid on the ^{13}C results in Figure 4.9B. ^{31}P MRS confirmed that CA inhibition with ETZ had no effect on steady-state myocardial pH_i (pH_i of 7.02±0.03 before ETZ treatment and 7.00±0.04 after ETZ treatment). Perfusion with [1-^{13}C]pyruvate and ETZ generated more $^{13}CO_2$ than $H^{13}CO_3^-$ (Figure 4.9C) with no change in total $H^{13}CO_3^-$ plus $^{13}CO_2$. The pR, calculated from the $H^{13}CO_3^-/^{13}CO_2$ ratio, stabilized within 20 s to a steady-state pR of 6.21±0.13 (Figure 4.9D). Thus, inhibition of CA activity slowed CO_2–HCO_3^- conversion, as shown by the lengthening of the out-of-equilibrium period, but also by the steady-state pR which was 0.79 pH units below the pH_i measured using ^{31}P MRS.

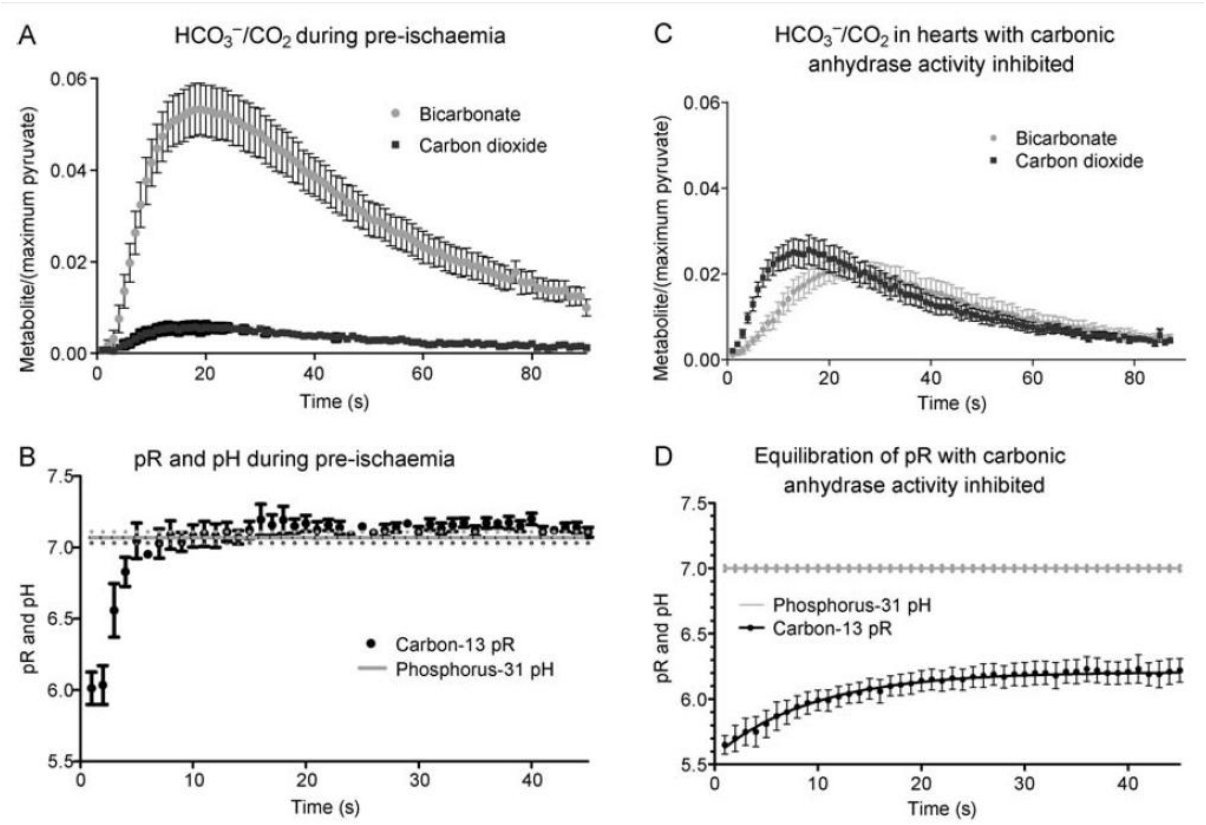

Figure 4.9: (A) The bicarbonate and carbon dioxide, both normalized to maximum pyruvate peak area, vs. time in control hearts (n = 6). The point-by-point ratio of these species was used to calculate pR. (B) Measurement of pR based on $H^{13}CO_3^-/^{13}CO_2$ in control hearts compared with measurement of pH_i using ^{31}P MRS in the same group of hearts. (C) The bicarbonate and carbon dioxide, both normalized to maximum pyruvate peak area, in hearts perfused with the CA inhibitor ETZ (n = 5). (D) Measurement of pR based on $H^{13}CO_3^-/^{13}CO_2$ in ETZ-perfused hearts compared with measurement of pH_i using ^{31}P MRS in the same group of hearts. The steady-state pR approached 6.21, a value which underestimated the true pHi of the heart by 0.79 pH units.

In reperfused hearts, ^{31}P MRS revealed that pH_i recovered from a value of 6.49±0.04 at the end of ischaemia to 7.04±0.13, at a rate of 0.73 pH units/min during the 45 s immediately after reflow (Figure 4.10). In hearts reperfused with hyperpolarized [1-^{13}C]pyruvate, the pR from the $H^{13}CO_3^-/^{13}CO_2$ ratio was the same as pH_i from ^{31}P MRS after 15 s of reperfusion. After 45 and 75 s, both ^{13}C and ^{31}P measurements gave almost identical pH_i measurements (^{13}C: 7.01±0.01 at 45 s and 6.98±0.02 at 75 s; ^{31}P: 7.04±0.13 at 45 s and 7.00±0.04 at 75 s).

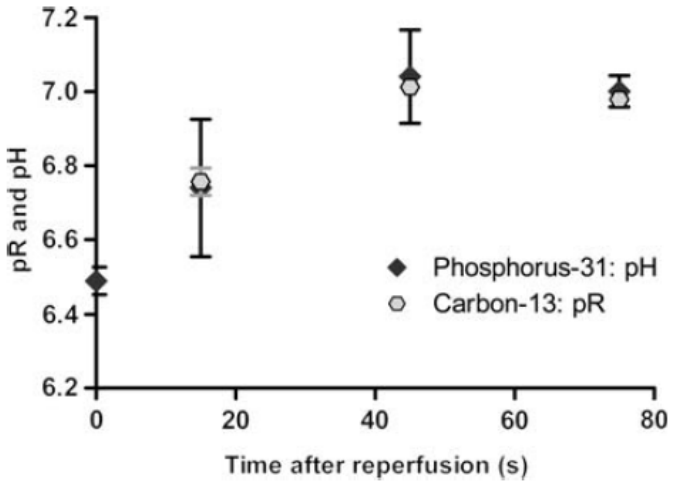

Figure 4.10: Comparison of the pR measurements made in reperfused hearts using the $H^{13}CO_3^-/^{13}CO_2$ ratio and the pH_i measurements made using ^{31}P MRS. The x-axis shows the time after reperfusion with hyperpolarized [1-^{13}C] pyruvate. The ^{31}P measurement at t = 0 equals the pH_i following 10 min of simulated ischaemia. Each pR measurement was calculated as the average of 30 s of spectra, acquired 15 s before and after the equivalent ^{31}P measurement to allow for direct comparison.

4.5.4 Discussion

PDH Flux before and after ischaemia

To study the CO_2/HCO_3^- equilibrium, PDH flux must be sufficient to generate MR-detectable levels of $^{13}CO_2$. Therefore, our first aim was to determine the effect of ischaemia on pyruvate oxidation. In the isolated rat heart perfused with pyruvate alone or pyruvate and fatty acids, ischaemia has been found to decrease PDH activity and glucose oxidation for several minutes following reperfusion (44,55,56). Here, 10 min of total global ischaemia decreased the rate of production of $H^{13}CO_3^-$ plus $^{13}CO_2$ from 0.57±0.06 to 0.26±0.05%.s^{-1}, indicating a decrease in the initial rate of pyruvate oxidation, and thus inhibition of PDH activity in reperfusion. However, a significant decrease in the total $H^{13}CO_3^-$ and $^{13}CO_2$ produced was not observed, suggesting that PDH flux recovered to control levels within 30 s. Most importantly, sufficient $^{13}CO_2$ was produced at the start of reperfusion to allow the $H^{13}CO_3^-/^{13}CO_2$ ratio to be measured, which may be used to estimate pHi.

$H^{13}CO_3^-$ / $^{13}CO_2$ equilibrium as a measure of cardiac pHi

We converted the $H^{13}CO_3^-$ / $^{13}CO_2$ ratio in the isolated perfused rat heart into a variable, pR, using the Henderson–Hasselbalch equation. At steady-state, pR in the isolated perfused rat heart was 7.12±0.1, to the pHi of 7.07±0.02 measured using ^{31}P MRS. These values are similar to those of Merritt et al. (44), and with pH_i measured by others using ^{31}P MRS (40,41,48,53,57). Thus, hyperpolarized [1-^{13}C]pyruvate can be used to obtain an accurate, non-invasive measurement of cardiac pH_i. As a first test of the suitability of pR to measure pH_i, we inhibited cardiac CA activity in perfused rat hearts, without altering pH_i. We found a significant difference between the steady-state pR of 6.21 and the pH_i of 7.01 determined

using ^{31}P MRS. Low pH_i, such as that observed during myocardial ischaemia, inhibits CA activity (50,51). Thus, the $H^{13}CO_3^-/^{13}CO_2$ ratio would not be a good measure of pH_i in the ischaemic/reperfused heart without correction for low CA activity.

4.5.5 Limitations of the study

To measure pH_i using [1-^{13}C] pyruvate, it is essential that the metabolically generated $H^{13}CO_3^-$ and $^{13}CO_2$ resonances can be accurately quantified above the baseline noise. At a physiological pH of 7, the $H^{13}CO_3^-$ resonance is 10-fold larger than the $^{13}CO_2$ resonance, so $^{13}CO_2$ quantification requires efficient hyperpolarization, high PDH flux, and careful data acquisition. An increase in achievable polarization, from the 30% observed here to 60%, has recently been reported and will aid $^{13}CO_2$ quantification (58). Also, strategic data acquisition after the ^{13}C equilibration period, over a shorter duration and with a higher excitation flip angle may further increase the $^{13}CO_2$ signal.

A second limitation of this study is the fact that the hyperpolarized label cannot directly distinguish between metabolites located in the intra- and extracellular spaces. We can be certain that virtually the entire detected $H^{13}CO_3^-$ and $^{13}CO_2$ signal was produced within the myocardium. However, it is possible that trace amounts of $^{13}CO_2$ may have diffused out of the myocardium and were subsequently hydrated to form $H^{13}CO_3^-$ spontaneously by extracellular cardiac CA. However, we believe that the contribution of the extracellular $H^{13}CO_3^-$ and $^{13}CO_2$ signal to our pH_i measurement was small because: (i) in vivo spectroscopic ^{13}C images acquired of the heart (59) have indicated that $H^{13}CO_3^-$ is confined to the myocardium, a region dominated by the intracellular space; (ii) in the perfused heart, high

coronary flow rates (20 mL/ min) would have rapidly removed hyperpolarized metabolites, and (iii) the close agreement between pR measured with ^{13}C and pH_i measured with ^{31}P in the perfused heart indicated minimal contamination from extracellular $H^{13}CO_3^-$ and $^{13}CO_2$, as these species would have equilibrated according the pH_o of 7.4.

4.5.6 Conclusion

Currently, the non-invasive measurement of cardiac pH_i in humans is not direct, because blood 2, 3-DPG signal overlies the myocardial P_i signal. Here, we have shown that in the presence of endogenous CA activity, the $H^{13}CO_3^-$/ $^{13}CO_2$ ratio accurately measured pH_i in the isolated perfused heart. Consequently, it seems that metabolically generated $H^{13}CO_3^-$ and $^{13}CO_2$ may offer an alternative technique for the non-invasive measurement of pH_i in normal hearts, and in diseased hearts with normal or elevated CA activity (53). Future work will involve correlating in vivo measurements of the $H^{13}CO_3^-$ / $^{13}CO_2$ ratio with pH_i measurements made using invasive, blood-removed or open-chest techniques.

Since acidosis is a characteristic feature of ischaemia, assessment of ischaemic heart disease in humans is another potentially useful application of a non-invasive pH_i calculation using the $H^{13}CO_3^-$ / $^{13}CO_2$ ratio. We observed excellent agreement between pH_i measured using ^{31}P MRS and pR measured using ^{13}C MRS in the reperfused myocardium when pH_i was > 6.74 (Figure 4.10). However, multiple factors shift pR relative to pH_i, including inhibition of CA activity at low pH_i and stimulation of membrane transport during reperfusion following ischaemia (60,61). Pharmaceutical agents, such as cariporide, inhibit membrane ion transport and have been used clinically to reduce ischaemia–reperfusion injury (62), but also block CA.

Therefore, the use of the $H^{13}CO_3^-$ / $^{13}CO_2$ ratio to measure pH_i may not be valid in ischaemic, acidic hearts, and in patients with ischaemic heart disease who use drugs that inhibit membrane ion transport. Additionally, it is reasonable to expect that intracellular CA expression and activity may be either reduced or increased in other forms of cardiomyopathy (63). Correction of pR to pH_i will require full characterization of CA activity in each pathophysiological state.

4.6 The Dynamic Roles of Acetylcarnitine in Myocardial Carbohydrate Metabolism: An In Vivo Study

Previous studies have indicated that mitochondrial acetylcarnitine, produced from acetyl-CoA via carnitine acetyltransferase (CAT), may be involved in balancing the glucose-fatty acid cycle in the heart. We used hyperpolarized [2-^{13}C]pyruvate, in concert with magnetic resonance spectroscopy (MRS), to monitor the incorporation of pyruvate dehydrogenase (PDH)-derived acetyl-CoA into the acetylcarnitine pool and the Krebs cycle, in real-time and in vivo. Our results demonstrated that CAT out-competes citrate synthase for pyruvate-derived acetyl-CoA in the healthy heart, with only a fraction directly oxidized via the Krebs cycle. While the critical role of PDH in balancing the glucose-fatty acid cycle is undisputed, CAT and acetylcarnitine also regulate the contribution of carbohydrates to cardiac ATP production.

The manuscript has been prepared by Dr. Marie A. Schroeder and is in the midst of submission for publication.

4.6.1 Introduction

Adenosine triphosphate (ATP) is the only immediate source of energy for the heart, and cardiac ATP production is controlled largely by the rate at which the Krebs cycle operates. In normal hearts, Krebs cycle flux is maintained by continual citrate synthase-mediated condensation of acetyl CoA with oxaloacetate to form citrate. Acetyl CoA is produced from the oxidation of fatty acids, ketone bodies, or glucose via glycolysis and the enzyme pyruvate dehydrogenase (PDH) (64). The marked variability in the roles of glucose and fatty acids as cardiac fuels has been described as t he glucose-fatty acid cycle (65).

PDH catalyses the irreversible oxidation of pyruvate to form acetyl CoA, NADH and CO_2, and is fundamental in balancing the relative contributions of glucose and fatty acid oxidation to cardiac ATP production. Normally, 60-90% of cardiac ATP is derived from fatty acids, and accordingly several PDH-mediated mechanisms exist to preserve fatty acid oxidation at the expense of glucose oxidation. In hearts chronically exposed to elevated free fatty acids, both protein expression and activity of pyruvate dehydrogenase kinase (PDK) are increased (66), phosphorylating and thus inactivating PDH (67). Acutely, PDK inhibits PDH activity in the presence of fatty acid oxidation end-products (acetyl CoA and NADH) (68), and PDH flux can be reduced directly by high acetyl CoA/CoA and NADH/NAD+ ratios (69).

Despite the central role of fatty acid oxidation in cardiac energy production, metabolic flexibility remains the key characteristic enabling the heart to meet its high ATP demand (70). For example, during aerobic exercise and after eating, glucose and other carbohydrates become important cardiac fuels (71,72). The PDH enzyme complex responds to increases in

cardiac workload and carbohydrate supply via the associated enzyme pyruvate dehydrogenase phosphatase (PDP), which dephosphorylates and thus activates PDH in environments of increased mitochondrial $Ca^{2+,}$ Mg^{2+} and insulin (73,74). High levels of mitochondrial pyruvate also activate PDH by inhibiting PDK (75). Increased pyruvate oxidation without a concomitant decrease in fatty acid oxidation, however, could theoretically inhibit further PDH flux via accumulation of acetyl CoA and subsequent end-product inhibition. Intuitively, to enable increases in carbohydrate oxidation, there must be a regulatory pathway ensuring that pyruvate-derived acetyl CoA is either buffered, or oxidized preferentially to fatty acids.

In a recent study (2), we used hyperpolarized [2-^{13}C] pyruvate as a metabolic tracer in the isolated heart to observe the relationship between PDH flux and Krebs cycle metabolism in real time, using ^{13}C magnetic resonance spectroscopy (MRS). As anticipated we observed conversion of pyruvate into the Krebs cycle intermediates citrate and glutamate. However, we also observed that a substantial fraction of pyruvate oxidized by PDH was converted to acetylcarnitine. Acetylcarnitine is produced by carnitine acetyltransferase (CAT), which is stimulated by mitochondrial acetyl CoA and carnitine (76). Our observation in the intact heart was consistent with the previous work of Lysiak et al., who reported that in heart mitochondria, acetyl CoA derived from pyruvate is particularly accessible to CAT, and that a greater proportion of acetylcarnitine is produced from pyruvate-derived acetyl CoA than from fatty acid-derived acetyl CoA (77). More recent studies have contributed evidence suggesting that acetylcarnitine may be an integral component of cardiac carbohydrate oxidation. It has been suggested that the acetylcarnitine pool may store acetyl units exceeding Krebs cycle requirements, to buffer rapid increases in substrate demand, and to release free CoA for maintenance of PDH flux (78,79). Further, Saddik et al. have proposed that myocardial

acetylcarnitine may serve as a precursor of cytosolic malonyl CoA, an inhibitor of fatty acid uptake (80). This pathway would provide pyruvate oxidation with a direct route to inhibit fatty acid oxidation.

These results point to clear involvement of CAT and the acetylcarnitine pool in regulating the glucose-fatty acid cycle alongside PDH. However, the nature of the dynamic relationship that exists in vivo between acetylcarnitine, pyruvate oxidation, fatty acid oxidation, and Krebs cycle flux has yet to be determined. The aim of this study was to use hyperpolarized [2-^{13}C] pyruvate as a metabolic tracer to examine the role of CAT in facilitating oxidative carbohydrate metabolism in the heart. We determined the metabolic fate of pyruvate-derived acetyl CoA by following its production and subsequent relative conversion into either acetylcarnitine or citrate in the isolated perfused heart.

Our results have demonstrated that more than half of all the pyruvate-derived acetyl CoA that enters the Krebs cycle does not immediately condense with oxaloacetate, but rather, is first incorporated into the acetylcarnitine pool. The unique metabolic position of CAT enables its role in buffering the supply of acetyl units to the instantaneous cardiac demand. Further, this study has contributed to evidence that the acetylcarnitine pool may be fundamental in maintaining PDH flux, by both increasing PDH activity and facilitating feedback inhibition of fatty acid uptake.

4.6.2 Materials and Methods

Trityl radical was obtained from GE-Healthcare (Amersham, UK). [2-^{13}C] pyruvic acid and all other compounds were obtained from Sigma (Gillingham, UK). Investigations conformed to Home Office Guidance on the Operation of the Animals (Scientific Procedures) Act, 1986 (HMSO) and to institutional guidelines.

[2-^{13}C] Pyruvate preparation

[2-^{13}C]pyruvic acid (40 mg), mixed with a 15 mM concentration of trityl radical and a trace amount of Dotarem, was polarized with 45 min of microwave irradiation. The sample was subsequently dissolved in a heated, pressurized alkaline solution to yield sodium [2-13C]pyruvate with a polarization of ~20% and physiological temperature and pH.

Saturation transfer experiments

Five male Wistar rat hearts (heart weight ~1 g) were perfused in the Langendorff mode, in a protocol identical to that previously described in the previous section. Three experiments were then performed in each perfused heart: 1) control, 2) acetylcarnitine saturation, and 3) control-saturation (Figure 3).

1) Hyperpolarized [2-^{13}C]pyruvate was diluted to 2.5 mM and delivered to the heart, and ^{13}C metabolites were detected as normal, with a 1-s temporal resolution over the course of 2-min (TR = 1 s, excitation flip angle = 30°, 120 acquisitions, sweep width, 180 ppm; acquired points, 4096; frequency centered at 125 ppm). The precise frequency of the [1-^{13}C]acetyl-carnitine resonance was noted.

2) After a second dose of ^{13}C was polarized (45 min), 2.5 mM [2-^{13}C]pyruvate was again delivered to the heart, and ^{13}C spectra were acquired as before while saturation was continually applied (described below) exactly to the [1-^{13}C]acetyl-carnitine resonance as determined in the previous experiment (~175 ppm).

3) A third dose of 2.5 mM [2-^{13}C]pyruvate was delivered to the heart, and a control-saturation experiment was performed: ^{13}C spectra were acquired while saturation was applied off resonance at ~187 ppm. The location of this pulse replicated the frequency separation between the [1-^{13}C]citrate and [1-^{13}C]acetyl-carnitine peaks, and ensured that the saturation pulse bandwidth was narrow enough to prevent any confounding saturation of the [1-^{13}C]citrate resonance.

To achieve continuous saturation, a cascade of eight SNEEZE pulses (81) was applied exactly at the acetylcarnitine frequency. Each SNEEZE pulse had a time-bandwidth product of 5.82 and 100 ms duration, with 100 μs interval between pulses. The effective full-width half-maximum bandwidth was ~160 Hz when tested on a sample of acetone.

MR data analysis

All cardiac ^{13}C spectra were analyzed using the AMARES algorithm as implemented in the jMRUI software package. Quantified peak areas were normalized to peak [2-^{13}C]pyruvate signal, plotted against time, and the maximum peak area of each metabolite was determined for each set of spectra.

In acetylcarnitine saturation experiments, spectra were summed over the 50 s following pyruvate arrival at the perfused heart to yield a single spectrum with peak heights for [1-

^{13}C]citrate, [5-^{13}C]glutamate, [1-^{13}C]acetylcarnitine and [1-^{13}C]pyruvate. These single spectra were then quantified as described above, and used for subsequent analyses.

Statistical methods

Values are reported ± SEM, and all analyses were performed in GraphPad Prism (GraphPad, La Jolla, California). All statistical differences within groups were assessed using one-way ANOVA with a post-hoc Tukey's Multiple Comparison Test. Statistical significance was considered at the $p < 0.05$ level.

4.6.3 Results

Acetylcarnitine saturation experiments

The acetylcarnitine resonance was selectively saturated to crush the MR signal in all nuclei incorporated into the acetylcarnitine pool, without affecting biochemistry. By analyzing the effect of acetylcarnitine saturation on the magnitude of the citrate resonance, we could qualitatively distinguish the fractions of [2-^{13}C]pyruvate-derived acetyl CoA that were 1) converted immediately into citrate, 2) converted into acetylcarnitine and stored, and 3) converted into acetylcarnitine prior to rapid re-conversion to acetyl-CoA and incorporation into the Krebs cycle.

To ensure that the low-SNR citrate and glutamate peaks were quantified accurately, 50 spectra acquired with 1 s temporal resolution were summed, starting with the spectrum at which infused [2-^{13}C] pyruvate first arrived at the heart. Therefore, the magnitudes of the

acetylcarnitine, citrate, and glutamate peaks reflected the amount of ^{13}C accumulated in each metabolite pool over 50 s. To ensure that the saturation pulse had no independent effects on the citrate peak, a control saturation experiment was performed in each heart, as detailed in Figure 4.11.

The acetylcarnitine saturation pulse was completely effective, reducing the magnitude of the acetylcarnitine peak by 99.5% compared with control experiments. Further, the control saturation experiments confirmed that the saturation pulse had a sufficiently low bandwidth to avoid RF effects on the citrate peak. Selective saturation of the acetylcarnitine peak reduced the magnitude of the citrate peak by 63%. This result indicated that of all the [2-^{13}C]pyruvate-derived acetyl CoA that was incorporated into the Krebs cycle over a 50 s time period, 63% was initially converted into acetylcarnitine, prior to release from the acetylcarnitine pool as acetyl CoA and incorporation into the Krebs cycle. The remaining 37% of [1-^{13}C]citrate unaffected by saturation was produced from [2-^{13}C]pyruvate-derived acetyl CoA that immediately condensed with citrate synthase. This effect was also observed as a 51% reduction in the magnitude of the glutamate resonance compared with controls.

In a further set of experiments the citrate resonance was selectively saturated. No reduction in the acetylcarnitine resonance was seen, indicating that there was no reverse pathway for [1-^{13}C]citrate conversion to acetylcarnitine.

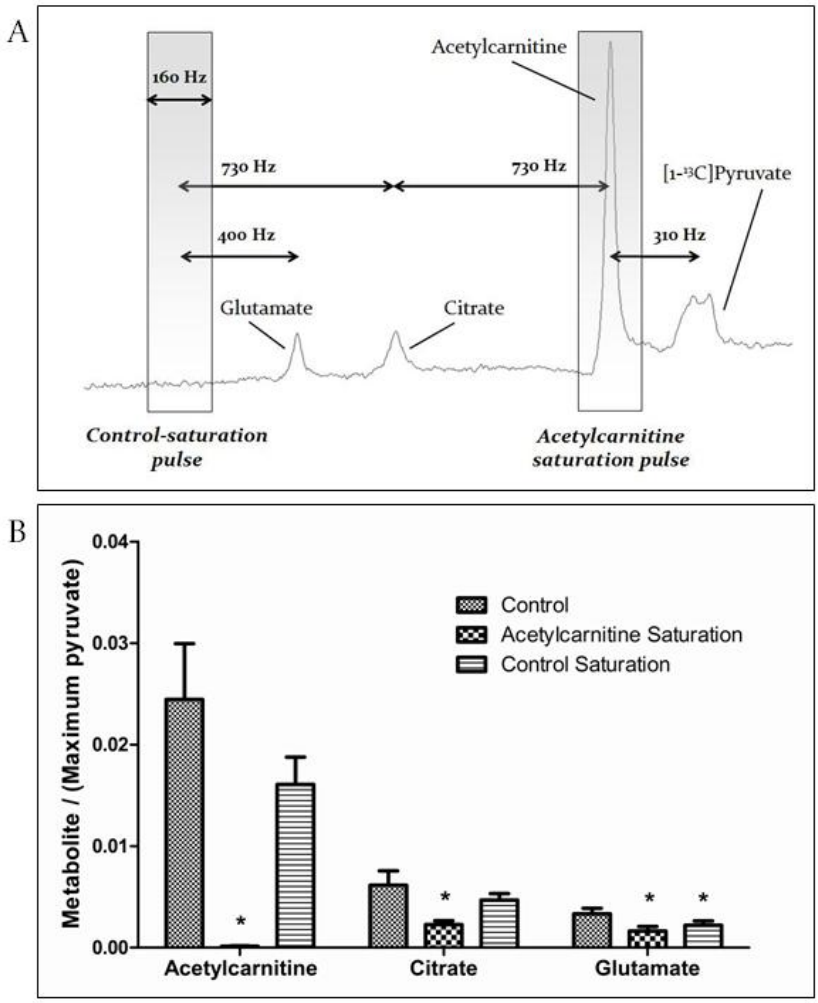

Figure 4.11: Design and results of the acetylcarnitine saturation experiments. A) Control data were acquired to identify the exact frequency of the acetylcarnitine peak. An example control spectrum is shown. Next, a saturation pulse (gray box: 160 Hz bandwidth) was applied continuously to the acetylcarnitine resonance, which was 730 Hz downstream of citrate. Finally, the same pulse was applied 730 Hz upstream of citrate as a control to ensure that citrate was not affected by RF saturation. B) Acetylcarnitine saturation crushed the ^{13}C signal from the acetylcarnitine pool, and significantly reduced the citrate and glutamate peaks. The control-saturation experiment confirmed that acetylcarnitine saturation had no effect on citrate. Glutamate, which was 330 Hz nearer to the saturation pulse than citrate, was significantly reduced by RF effects.

4.6.4 Discussion

In healthy hearts, the careful regulation of the glucose-fatty acid cycle is considered to encourage rapid incorporation of all acetyl CoA produced into the Krebs cycle. Further, the relative fractions of acetyl CoA derived from either β-oxidation or PDH are thought to reflect the contribution of each substrate to cardiac ATP production. However, in this study, we observed that 63% of the pyruvate-derived acetyl CoA incorporated into the Krebs cycle was first reversibly converted to acetylcarnitine by CAT. An even greater proportion of the pyruvate-derived acetyl groups were stored as acetylcarnitine for a time exceeding the duration of our experiment, as evidenced by the large [1-^{13}C]acetylcarnitine peak area relative to either [1-^{13}C]citrate or [5-^{13}C]glutamate.

It has been suggested that acetylcarnitine may serve as a precursor of cytosolic malonyl CoA, thus enabling feedback inhibition of fatty acid uptake by high levels of pyruvate oxidation (80). This hypothesis remains difficult to prove, due to technological limitations that prevent specific measurement of the cytosolic and mitochondrial fractions of acetyl CoA and malonyl CoA (82). However, tentative support has been provided by this study and others, which when considered together, suggest that supply of pyruvate-derived mitochondrial acetyl CoA, production of [1-^{13}C]acetylcarnitine, and whole-myocyte levels of malonyl CoA correlate in the heart (64,80,82,83). These data advance the possibility that acetylcarnitine exported out of the mitochondria may offer an important source of cytosolic acetyl CoA in the heart, providing a link between mitochondrial acetylcarnitine and cytosolic malonyl CoA production (80). The proposed mechanism of acetylcarnitine dynamics is illustrated in Figure 4.12.

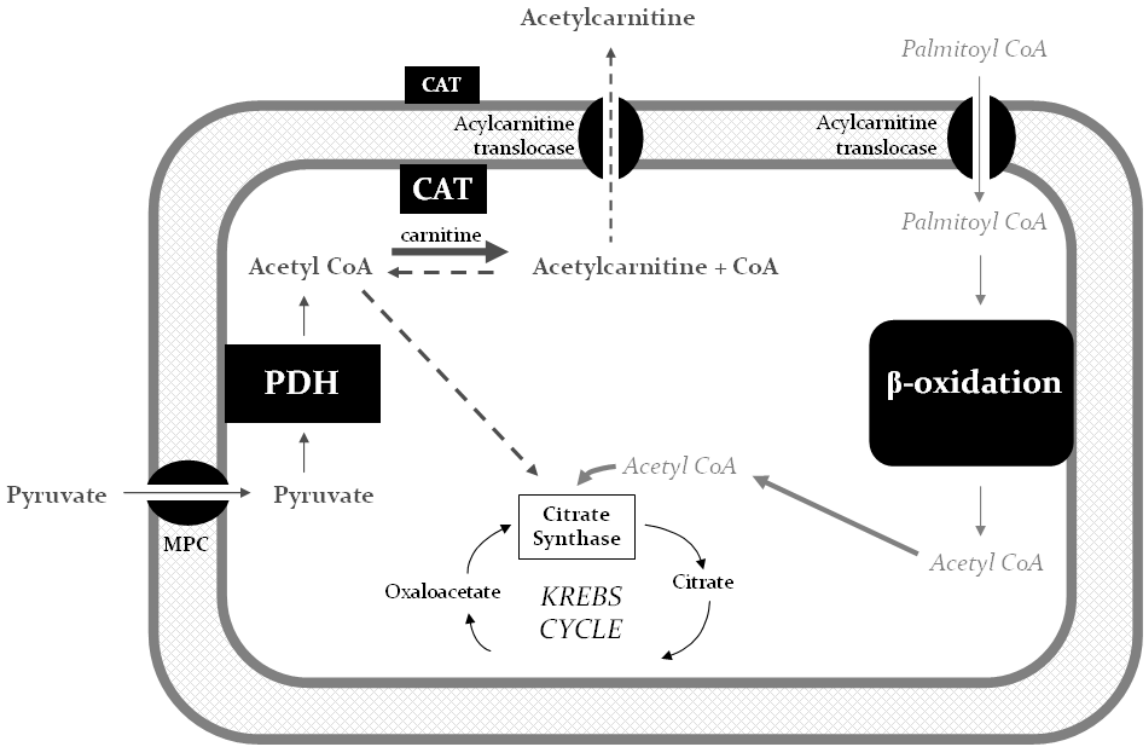

Figure 4.12: Proposed mechanism describing the dynamics of acetylcarnitine involvement in the glucose-fatty acid cycle. Acetyl CoA produced by fatty acid β-oxidation and PDH are compartmentalized into distinct pools with divergent metabolic fates. Acetyl CoA from β-oxidation is closely coupled to citrate synthase, while acetyl CoA from PDH has 2 parallel metabolic fates: incorporation into the Krebs cycle, or conversion to acetylcarnitine. Depending on oxidative demand, acetylcarnitine may rapidly re-convert into acetyl CoA (within several seconds), provide acetyl group storage in the long term, or leave the mitochondria to provide cytosolic acetyl CoA.

4.6.5 Conclusion

The link revealed between pyruvate-derived acetyl CoA and CAT indicates that acetyl CoA produced by PDH and β-oxidation exist as functionally compartmentalized pools with divergent metabolic fates. The critical role of PDH in balancing contributions of pyruvate and fatty acids to acetyl CoA production is undisputed; however, this study has demonstrated that CAT and acetylcarnitine also have key roles in regulating the contribution of carbohydrates to cardiac ATP production. Therefore, CAT activation via carnitine supplement may offer a useful metabolic therapy in cardiac diseases which are characterized by mismatched glycolysis and glucose oxidation, such as pressure-overload hypertrophy (79).

4.7 Investigation of Metabolically Generated Hyperpolarized [1, 4 - ^{13}C] Malate from [1, 4 - ^{13}C] Fumarate as a Biomarker of Necrosis in the Ischemic Heart

Cardiac ischaemia induces necrosis and apoptosis of myocytes, which are distinct mechanisms of cell death (84). Ischaemic necrosis is characterized by ATP depletion, cell swelling and loss of membrane integrity, whereas apoptosis usually requires energy, and is associated with cell shrinkage and phagocytosis without loss of membrane integrity. Prolonged or acute ischaemia destroy myocytes via necrosis. Recently, Gallagher and co-workers have demonstrated the detection of hyperpolarized [1,4-$^{13}C_2$]malate, the downstream metabolite produced from an infusion of [1,4-$^{13}C_2$]fumarate, with ^{13}C magnetic resonance spectroscopy in a murine lymphoma tumor. After etoposide treatment, they observed a 2.4 fold increase in hyperpolarized [1,4-$^{13}C_2$]malate and attributed it to tumor cell necrosis

causing a breakdown in membrane integrity. Thus the increase in the hydration of hyperpolarized fumarate to malate appears to be a potential biomarker of necrosis. The purpose of this study was thus to investigate whether hyperpolarized fumarate could be used as a biomarker of necrosis in the ischaemic rat heart. Hyperpolarized [1,4-$^{13}C_2$]fumarate is delivered into the isolated perfused heart before ischaemia, immediately upon reperfusion and 30 min post-reperfusion. Results showed obvious enhancement in maximum peak of [1,4-$^{13}C_2$]malate in the time-courses and significant changes in the initial rate of malate production after reperfusion.

4.7.1 Introduction

Myocardial ischaemia is a pathological process that results in extensive necrosis. The deprivation of oxygen and nutrition triggers cellular and sub-cellular alterations, which accompany a progressive reduction in ATP production (85,86). The characteristic pattern of ischemic cell injury involves fluid and electrolyte alterations, with loss of K^+ and Mg^{2+} and accumulation of water, Na^+, Cl^-, H^+ (acidosis), and Ca^{2+}; cytoplasmic, organellar, and cellular swelling with plasma membrane blebbing; and margination and clumping of nuclear chromatin. These cellular changes are due to progressive impairment of membrane composition, structure, and function (85,87). The compromised membrane permeability then allows the unregulated influx of divalent and trivalent cations, including calcium. Subsequently, the swollen cells develop physical defects (holes) in their cell membranes and rupture. These features of cell injury with cell swelling have been shown to involve cardiac myocytes subjected to hypoxia in vitro and cardiac muscle during the evolution of myocardial infarction in vivo (85,88). The underlying cellular membrane damage to

ischaemic myocytes is the basis for the diagnosis of myocardial infarction by pathology laboratory and nuclear cardiology methods (87).

Fumarate is a metabolite derived from the oxidation of succinate in the Krebs cycle. It is then reversibly hydrated to become malate in the reaction catalyzed by fumarase. In in-vitro necrotic cells, Gallagher et al have established a correlation between rate of malate production and percentage of cells that lost plasma membrane integrity, using hyperpolarized [1,4-$^{13}C_2$]fumarate as the probe (89). They modeled the ^{13}C label flux transfer between fumarate and malate, and noticed a 19 times increase in the forward rate constant in etoposide-treated lymphoma cells. In-vivo, 2.4 and 2.5 times increases were observed in the epotoside-treated mice in the forward and reverse fluxes respectively, together with a 59% increase in maximum malate signal. The enhanced fluxes and malate production indicated an increase in the concentration of fumarase available to its substrates, as a result of degradation in membrane integrity. The aim of this work is to investigate the possibility for detection of necrosis in the ischaemic/reperfused heart with hyperpolarized [1,4-$^{13}C_2$]fumarate.

4.7.2 Material & Methods

Polarization of [1,4-^{13}C]Fumaric Acid (89)

All chemicals were obtained from Sigma/Aldrich unless stated otherwise. [1,4-$^{13}C_2$]fumaric acid (3.23 mmol; Cambridge Isotope Laboratories) was dissolved in 8.74 mmol of DMSO containing 11.48 μmol of a trityl radical (AH111501; GE Healthcare) and 0.48 μmol of a gadolinium chelate [Gd-3; GE Healthcare]. The solution was sonicated and centrifuged, and a 40 mg aliquot was hyperpolarized by using a method similar to that described (1,3). Briefly,

the sample was cooled to ~1.2K while irradiated with microwaves at 93.139 GHz and 100mW for 1 h and then dissolved in 6mL of buffer containing 40 mM phosphate, 50 mM sodium chloride, and 40 mM sodium hydroxide, pH 7.4 at 10 bar and 180 °C. The resulting solution contained 20 mM [1,4-$^{13}C_2$]fumarate, which was then cooled to ~37 °C and diluted to 2.5 mM before perfusion into the isolated rat heart.

Control Protocol

Isolated hearts (n = 6) were perfused for 30 min at 85 mmHg. After this, hyperpolarized [1,4-$^{13}C_2$]fumarate was infused and the progress of ^{13}C-labelled compounds was followed using ^{13}C MRS.

Reperfusion following ischaemia

Hearts (n = 5) were perfused for 30 min, followed by 10 min of global ischaemia, and 30 min reperfusion. Hyperpolarized [1,4-$^{13}C_2$]fumarate was infused immediately after ischaemia. ^{13}C MRS was performed for 2 min with hyperpolarized [1,4-$^{13}C_2$]fumarate in two stages, initial reperfusion and 30mins after continuous reperfusion.

Magnetic Resonance Spectroscopy

Acquisition of ^{13}C MR spectra commenced immediately after infusion of hyperpolarized [1,4-$^{13}C_2$]fumarate and the infusion continued throughout acquisition. Spectra were acquired with 1 s temporal resolution over 2 min (excitation flip angle = 30°, 120 acquisitions). Spectra were centered at 175 ppm and referenced to the [1,4-$^{13}C_2$]fumarate resonance at 175

ppm, and 4096 points were acquired over a bandwidth of 100 ppm. The area under each peak was used to calculate the concentrations of labeled metabolites. [1,4-$^{13}C_2$]fumarate produces a single peak, whereas [1,4-$^{13}C_2$] malate gives two resonances (181.2 and 182 ppm) and these were combined to produce a single signal intensity measurement.

Data Analysis

Carbon-13

Cardiac ^{13}C MR spectra were analyzed using the AMARES algorithm, as implemented in the jMRUI software package (52). Spectra were DC offset corrected based on the last half of acquired points and peaks corresponding with [1,4-$^{13}C_2$]fumarate and its metabolic derivatives were fitted assuming a Lorentzian line shape, initial peak frequencies, relative phases, and line-widths. For spectra acquired from perfused rat hearts, the maximum peak area of each metabolite over the 2 min of acquisition was determined for each series of spectra and expressed as a percentage of the maximum [1,4-$^{13}C_2$] fumarate resonance. The rate of signal production for each metabolite, in percent per second (%.s^{-1}), was measured as the slope of the mean metabolite increase over the first 5 s following its appearance, over which time the metabolite signal increased linearly. Additionally, a first-order exponential signal decay term was fit to each metabolite peak from the point of maximum signal over the course of signal decay. Decay of the hyperpolarized signal depends on the intrinsic spin–lattice relaxation of the nucleus, production and consumption rates of the metabolite, and metabolite washout, and may therefore provide information about metabolite accumulation in the states of control, initial reperfusion and 30 min after continuous reperfusion.

Statistical methods

Data are given as mean ± standard error. Statistical significances between pre-ischaemic and immediate reperfused groups, and pre-ischaemic and 30 min continuous reperfused groups, were assessed using a paired Student's t-test. Statistical significance was considered at $P < 0.05$.

4.7.3 Results

[1,4-$^{13}C_2$]Malate Spectra and Time-Course

A representative spectrum of hyperpolarized [1,4-$^{13}C_2$]fumarate in the isolated perfused heart and the kinetic progression of [1,4-$^{13}C_2$]malate is shown in Figure 4.13a. Following infusion of [1,4-$^{13}C_2$]fumarate into control hearts, [1-^{13}C]malate (181.2 ppm) and [4-^{13}C]malate (180 ppm) were clearly detectable with high signal compared with the baseline. The maximum peak area, initial rate of production and the decay time constant for the [1,4-$^{13}C_2$]malate in pre-ischaemic, initial reperfused and 30mins continuous reperfused hearts are shown in Table 4.2. The corresponding graphs with means ± SEM are illustrated in Figure 4.14.

Although there is an uptrend of maximum malate peak area after ischaemia, their differences are not significant. The initial production rate of [1,4-$^{13}C_2$]malate significantly increases by 143% immediately after ischaemia (from 0.07 ± 0.01% to 0.17 ± 0.04%) and 157% after 30 min reperfusion (from 0.07 ± 0.01% to 0.18 ± 0.07%) ($p < 0.05$). There are no significant changes in the decay constants, as indicated by the slope in Figure 4.13b.

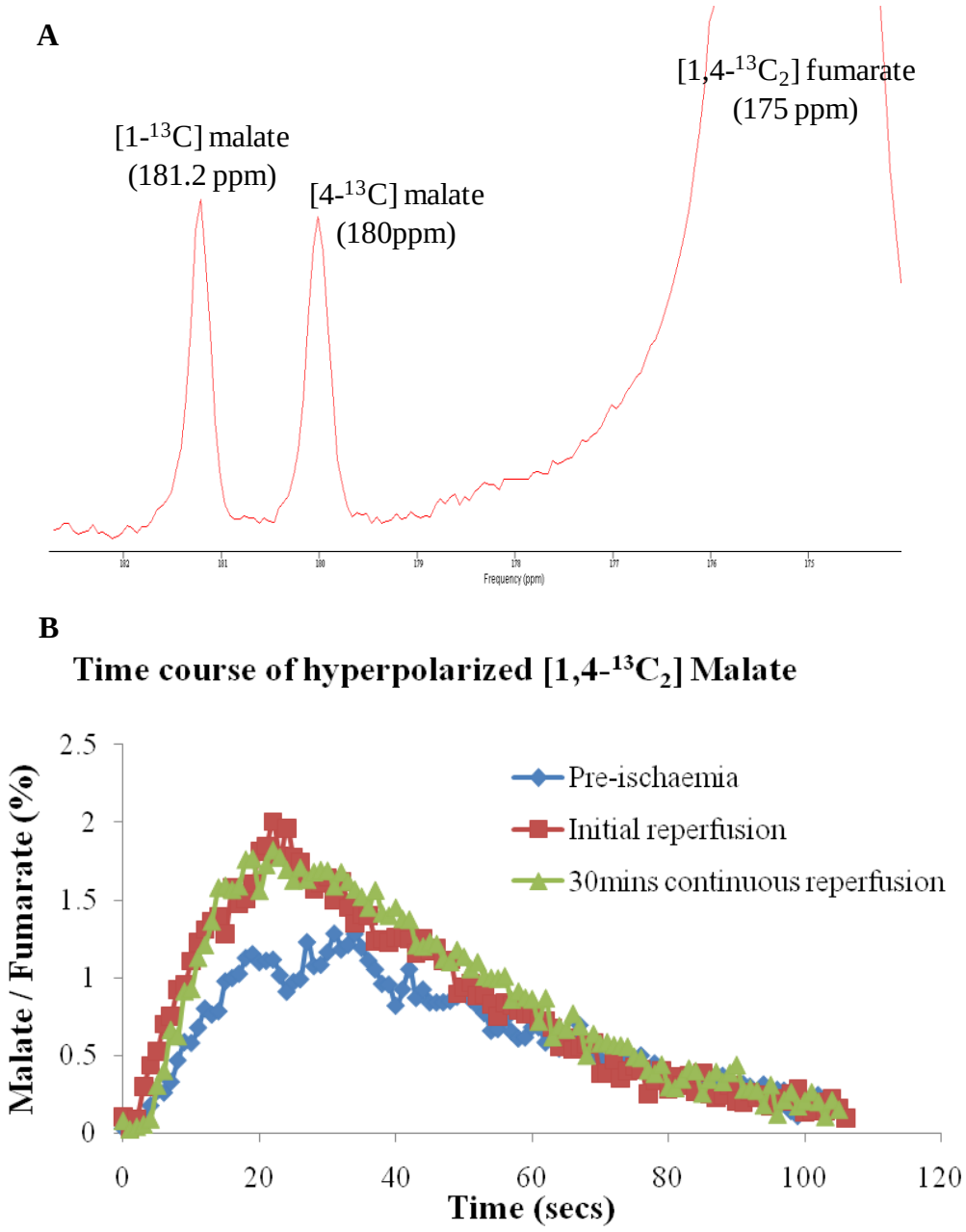

Figure 4.13: (A) Representative spectrum acquired during hyperpolarized [1,4-$^{13}C_2$] fumarate infusion into the isolated perfused heart. (B) Representative time-course of [1,4-$^{13}C_2$] malate before ischaemia, immediately upon reperfusion and 30mins post reperfusion.

	[1,4-$^{13}C_2$] Malate		
	Pre-ischemia	**Reperfusion**	**30 min after reperfusion**
Max. malate / fumarate (%)	2.9 ± 0.7	3.9 ± 0.6	5.1 ± 1.1
Initial production rate (% / s)	0.07 ± 0.01	0.17 ± 0.04 *	0.18 ± 0.07*
Decay, τ (s)	41.1 ± 0.2	38.9 ± 1.9	51 ± 4.5

Table 4.2: Metabolic levels and kinetic parameters from ^{13}C MR spectrum in pre-ischaemia, initial reperfused and 30 min post-reperfused isolated hearts (n = 5). * indicates $p < 0.05$.

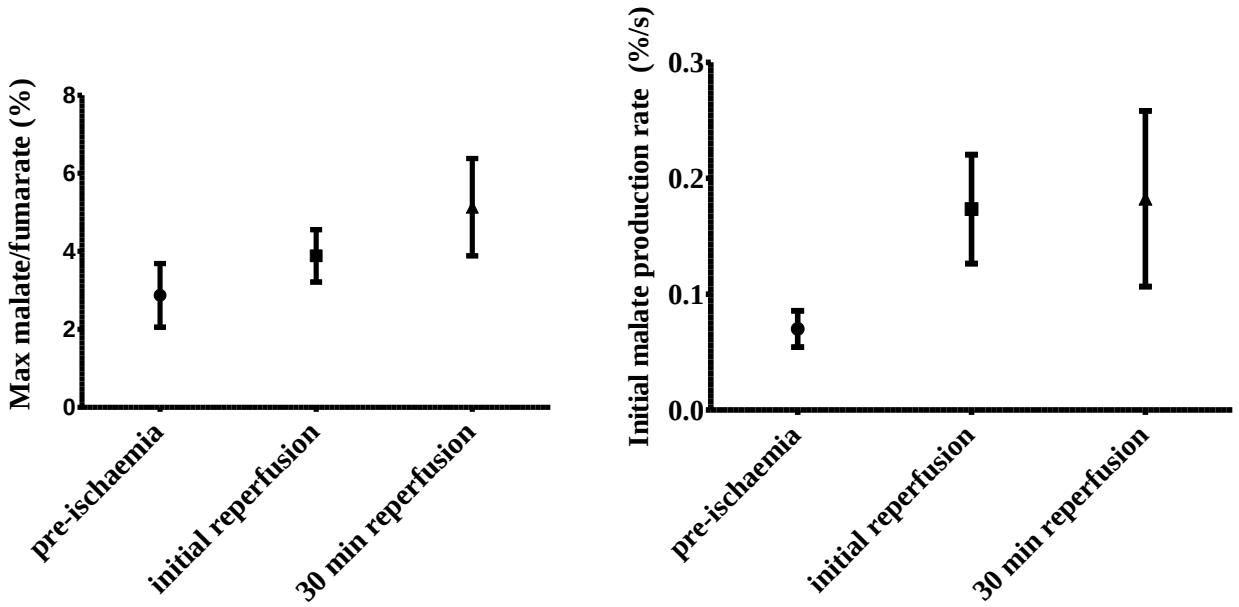

Figure 4.14: Changes in maximum malate peak area and initial malate production rate, before ischaemia, upon reperfusion and 30mins post-reperfusion.

4.7.4 Discussion

To study the onset of cell death with ischaemia, we have introduced 10 min of global ischaemia to the isolated rat heart. Immediately after ischaemia, we reperfused the heart with hyperpolarized fumarate, and demonstrated that the production of [1,4-$^{13}C_2$]malate can be detected in real-time. ^{13}C MR spectroscopic measurements showed a significant increase in

malate production rate, probably due to a higher fumarate-malate flux. The underlying mechanism could be increased substrate uptake by the cardiomyocytes or escape of fumarase into the extracellular matrix (89), either of which indicates compromised cellular membrane permeability. After 30 min reperfusion, the initial rate of malate production stabilized, which indicated an arrest in necrosis, preventing further myocardium damage. Thus cell death did not appear to proliferate. Nonetheless, ischaemia triggers the activation of a series of signaling molecules such as caspases and tumor-necrosis factor-α that inevitably lead to cell death of injured myocytes (90). Besides, growing evidence has surfaced suggesting that apoptosis is induced upon onset of ischaemia and is accelerated when the ischaemic heart is reperfused, further triggering a cascade of apoptotic signaling pathways (91-93). An example of such an apoptogenic protein is cytochrome c, which is released by the mitochondria during ischaemia. Cytochrome c has been known to activate caspases, inhibit mitochondrial respiratory chain activity and produce free radical in the mitochondria (92). If the heart is kept under prolonged ischaemia, ATP depletion will limit caspase activation and cause widespread necrosis (94). But if the heart is reperfused, cytochrome c release and caspase activation that occurred during the previous ischaemic period will trigger further caspase activation at reperfusion, potentially causing widespread apoptosis (95,96). Myocyte apoptosis in the reperfused heart has been demonstrated in both animal models (96,97) and humans (98,99). Despite the intense interest on the role of apoptosis in pathology of cardiovascular disease such as ischaemic heart disease, majority of cell death occurred via necrosis (85,86,100). The decay time constant did not differ significantly between pre-ischaemic and reperfused hearts even though malate production increased. This could be due to the activation of malate dehydrogenase by the high malate concentration, resulting in an increased forward flux to oxaloacetate (101), enabling efficient metabolism of the excess malate.

In this study, we did not perform histology to confirm the onset of necrosis. The fractionation of cell death attributable to necrosis and apoptosis was also not verified. Establishing a quantitative correlation between metabolism of hyperpolarized fumarate and necrosis severity would improve interpretation and add diagnostic value. There appeared to be no change in maximum peak area of hyperpolarized malate, contrary to the 59% increase seen in treated tumor (89). This warrants further investigation.

4.7.5 Conclusion

We have demonstrated the utilization of hyperpolarized [1,4-$^{13}C_2$]fumarate as a potential positive contrast agent of necrosis in the isolated perfused heart. Further quantification such as fumarase and malate dehydrogenase kinetics, in addition to histological verification of cell death are required to strengthen its robustness as a biomarker of necrosis in the ischemic heart.

4.8 Real-Time Metabolic Imaging with Chemical Shift MRI

The emergence of hyperpolarized ^{13}C techniques shifts the paradigm in the study of metabolism from steady-state to real-time, offering us unprecedented insight into the bioenergetics and cellular dynamics in pathology. ^{13}C MRS is currently the main workhorse that provides this information. It enables high detection sensitivity (provided ^{13}C label is sufficiently polarized) and ease of operation (normally single-pulse acquisitions would suffice). With the exception of isolated perfused organs such as the heart and liver, in-vivo detected signal with ^{13}C MRS origins from the tissue of interest as well as its surrounding environment. The derived metabolic time-course is thus somewhat corrupted and there is a risk of drawing the wrong conclusions. In addition, pathology rarely progresses homogenously throughout the organ but rather via regional deterioration. As we advance into the domain of personalized medicine, therapeutic drugs would have to be target–specific and precise in locating targets. A mapping of metabolic activity throughout the diseased organ is thus essential for accurate localization of abnormal metabolism and tissue degeneration. In addition, metabolic imaging could also provide new information on disease progression such as proliferation, and aid in pathodiagnosis and disease staging.

The advent of hyperpolarized MRI began with the use of optically pumped noble gases such as ^{3}He (102-104) and ^{129}Xe (105,106) in the 1990s, primarily in lung perfusion studies where ^{1}H MRI is inferior in signal-to-noise ratio (107). In addition, since the resonance frequency of ^{129}Xe depends on its physical phase (gaseous or liquid) (108) and the local microenvironment (109), it has been exploited to reveal regional pO_2 in the blood (110) as well as monitor the dynamics of ^{129}Xe when transported from alveoli to the pulmonary blood (111), from which information about the diffusing capacity of the lung can be obtained. For metabolic imaging,

^{13}C is the choice of label since carbon is present in all organic molecules and the ^{13}C label chemical shift is directly related to its molecular structure. An injectable hyperpolarized solution could be used to visualize part of the vascular system (11), to map physiological parameters (112,113) or probe metabolic pathways (114). The DNP method is a general technique that may be applied to all nuclei (^{1}H, ^{13}C, ^{15}N etc.) Real-time metabolic imaging with DNP [1-^{13}C]pyruvate has been demonstrated in murine muscles (115) and swine myocardium (114) in-vivo. The resulting lactate and alanine biodistribution maps allow the distinction of regions with different lactate dehyodrogenase (LDH) and alanine transaminase (ALT) fluxes. Since lactate production is effectively a biomarker of tumor viability (31,116) and cardiac ischaemia (2), metabolic CSI could provide assessment in both function and spatial proliferation of the diseases.

Oxidative decarboxylation of DNP hyperpolarized [1-^{13}C]pyruvate, mediated by the pyruvate dehydrogenase (PDH) complex, is a critical reaction that produces acetyl-CoA for ATP synthesis and also the byproducts NADH and [1- ^{13}C]carbon dioxide ($^{13}CO2$). $^{13}CO_2$ is in a pH-dependent equilibrium with bicarbonate ($H^{13}CO_3^-$) and observation of $H^{13}CO_3^-$ production has been shown to be an effective biomarker of real-time, in vivo PDH flux (3). Thus, the capability to visualize these metabolites in vivo allows us to probe metabolic processes that are critical to energy production and the physiological condition of the heart. However, to fully understand the changes observed in vivo it is useful to be able to study a model system where the exact parameters of the system can be carefully controlled. The perfused rat heart has been used as such a model system for many years, but the limitations of a small heart size and the resulting requirement for high spatial resolution have so far prevented metabolic imaging of the perfused heart with hyperpolarized [1-^{13}C]pyruvate. In this study, we aimed to demonstrate the feasibility of mapping the spatial distribution of

hyperpolarized pyruvate, lactate, alanine and bicarbonate in the perfused rat heart via the implementation of a rapid, high spatial resolution, chemical shift imaging approach. Technical considerations including the limited polarization lifetime of ^{13}C label as well as optimization of pulse sequence for optimal SNR will be discussed.

4.8.1 Limited T_1 Lifetime of the Hyperpolarized Pyruvic Acid (CSI)

Although hyperpolarized ^{13}C biomolecules allow unprecedented access into the dynamics of metabolic activity, their short T_1 effectively limit signal acquisition and provide only a small window of opportunity to probe their metabolic fate. Dependent on the biochemical pathway of interest, that window might be restrictively short. Thus the longitudinal relaxation time is an extremely critical factor in real-time metabolic investigation. In addition, each RF pulse applied during MR spectroscopy removes some polarization, and thus a compromise has to be met between getting sufficient SNR and following the temporal evolution of metabolites. A RF power calibration of hyperpolarized [1-^{13}C]pyruvate would provide both the T_1 and the appropriate flip angle to adopt. To do that, a dummy dissolution of [1-^{13}C]pyruvate followed by ^{13}C MRS was carried out. A total of 60 acquisitions were done, first 30 readings had a RF attenuation factor of 30 dB and the next 30 had 24 dB. Repetition time was 1 s. We fitted the acquired signal S into eqn. (4.6), where A is a constant and assuming an exponential decay in polarization. The acquired and fitted results are displayed in Figure 4.15. The estimated T_1 value is ~50 seconds and flip angle is ~5°. Thus CSI imaging has to be completed within 50-60 s.

$$S = A sin\theta \left(e^{\frac{-1}{T_1}} cos\theta \right) \tag{4.6}$$

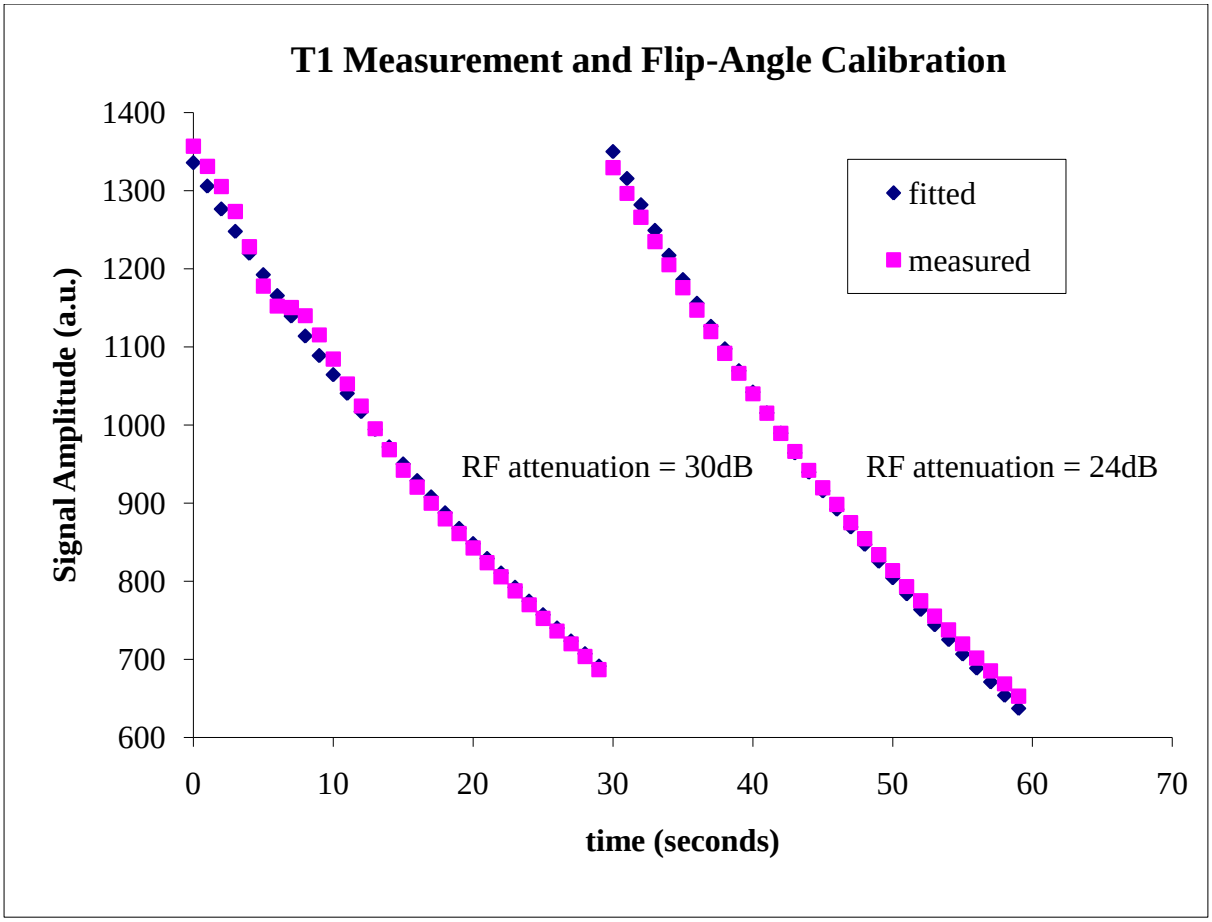

Figure 4.15: T_1 measurement and flip angle calibration of sinc pulse for chemical shift imaging of metabolites, upon dissolution of hyperpolarized [1-^{13}C] pyruvate.

4.8.2 Materials and Methods

Isolated Heart Perfusion

Rat hearts (n=3) were rapidly excised from male Wistar rats (~350 g) and perfused in the recirculating retrograde Langendorff mode and then placed in the centre of an 11.7 T, vertical bore MRI scanner (Bruker-Biospin, Germany).

Chemical Shift Imaging

A 2D gradient-echo CSI pulse sequence was implemented with acquisition begun 18 s after the start of infusion following identification of an optimal imaging window in the 1D spectroscopy time course. A single CSI image with centric phase encoding was acquired axially through the middle of the heart over a time-course of 64 s with TR = 250 ms, TE = 0.85 ms, FA = 25°, SW = 40 ppm, SP = 512, FOV = 24 x 24 mm, matrix = 16 x 16, slice thickness = 5 mm. Post-processing with Matlab included zero-filling the data to 128 x 128, 2D Fourier Transformation and automatic detection of the resonance of each metabolite to generate metabolic maps of pyruvate, lactate, alanine and bicarbonate. A reference proton image was acquired with a FLASH imaging sequence (matrix = 128 x 128, TR = 100 ms, TE = 1.28 ms and slice thickness = 1 mm).

4.8.3 Results

^{13}C MR Spectroscopy

The time course in Figure 4.16 illustrates the temporal evolution of hyperpolarized lactate, alanine and bicarbonate following infusion of pyruvate. All metabolites reached their peak amplitude at approximately 20 s after the start of infusion. Therefore subsequent CSI imaging was chosen to begin at t = 18 s so that the centre of k-space coincided with the peak amplitudes of the metabolites. The imaging window is shown boxed in Figure 4.16.

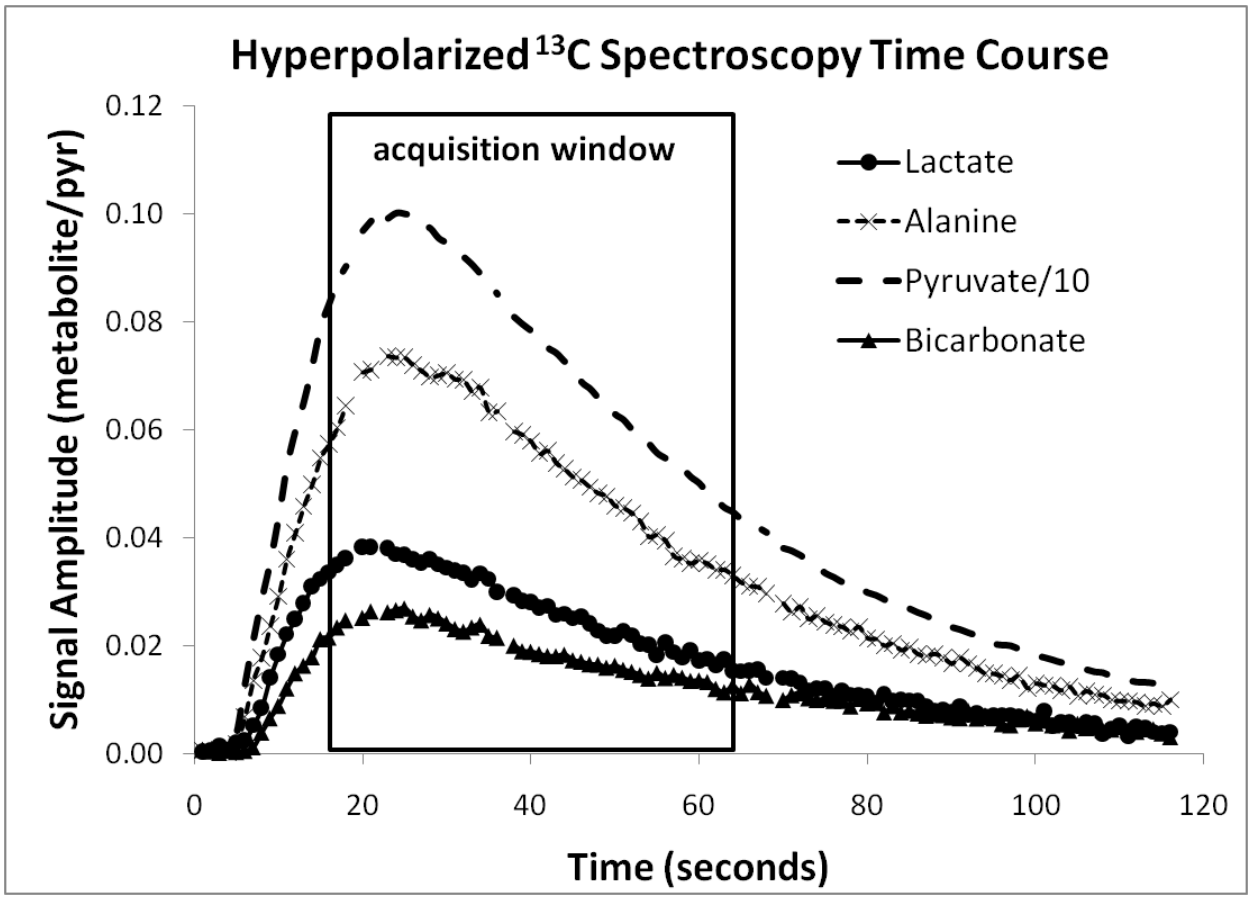

Figure 4.16: Metabolic time course of the infused [1-13C]pyruvate and its derivatives [1-^{13}C]lactate, [1-^{13}C]alanine and H$^{13}CO_3$-. The imaging window is overlaid on the plot.

Gradient-echo Chemical Shift Imaging

Figure 4.17 shows the axial proton image along with the metabolite maps for pyruvate, lactate, alanine and bicarbonate. The left and right ventricles are highlighted on the metabolite maps by the dotted lines. The peak pyruvate signal is seen just outside the heart at the location of perfusion buffer drainage. All other metabolites are localized within the contracting left ventricular tissue.

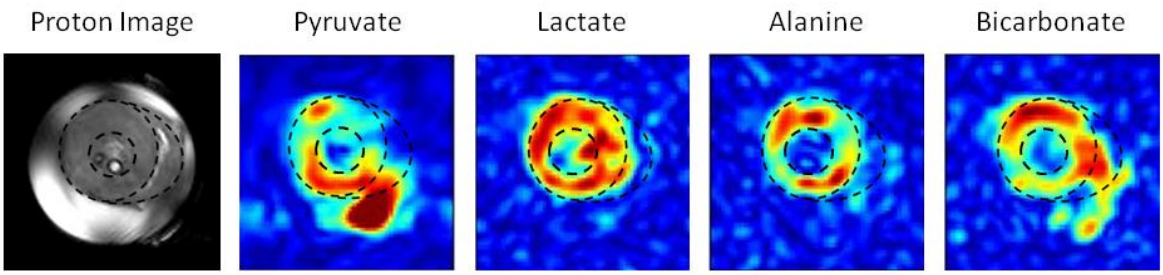

Figure 4.17: Metabolic images of [1-^{13}C]pyruvate, [1-^{13}C]lactate, [1-^{13}C]alanine and $H^{13}CO_3^-$ in the perfused heart along with a reference proton image. The dotted lines indicate the borders of the left and right ventricles.

4.8.4 Discussion

We have demonstrated the capability of metabolic imaging with DNP [1-^{13}C]pyruvate as substrate in the isolated perfused heart. Even though the oxidative carboxylation of 5 mM pyruvate yields a $H^{13}CO3^-$ signal that was only 3% of maximum pyruvate peak, it was still feasible to obtain a bicarbonate distribution map. A previous study has found that production of $H^{13}CO_3^-$ correlates with the severity of diabetes (3) and thus the ability to map bicarbonate distribution in the perfused heart would further enlighten the pathophysiology of the diabetic heart. Unfortunately, the $^{13}CO_2$ signal was insufficient for imaging (~0.6% of [1-^{13}C]pyruvate); otherwise an intracellular pH map could be obtained according to our study in Section 4.5. An alternative method to map pH distribution is an infusion of hyperpolarized $H^{13}CO_3^-$ instead, which has been shown to produce substantial $^{13}CO_2$ (42). Thus it appears that $^{13}CO_2$ signal has to increase by at least 5 times in the isolated perfused heart to permit detection with CSI. According to eqn. (4.1), the most direct way to achieve that, partially at least, would be to increase polarization. Johannesson and co-workers have demonstrated the almost 3 times enhancement in [1-^{13}C]pyruvate polarization by increasing polarizing

magnetic field from 3.35 T to 4.64 T (58). The biggest hurdle though is that polarization time is tripled as well.

Metabolic activity of lactate dehydrogenase in the reduction of pyruvate into lactate is clearly mapped with CSI. This facility would be beneficial in mapping the extent of myocardial damage in ischaemic hearts, in which lactate metabolism increases by 5-fold upon reperfusion (see Table 4.1). In addition, Golman et al has demonstrated that lactate production from pyruvate in pigs is compromised in regions of myocardial cell death after 15 min occlusion, and that could also be mapped with CSI (59). It has also been proposed that the pyruvate map could be used for qualitative perfusion assessment in the diseased heart (114). The visualization of alanine in the isolated perfused myocardium has been shown to be feasible. It has been demonstrated that regions in the heart that are still viable after induction of ischaemia continue to exhibit transamination of pyruvate into alanine (59). Therefore the presence of alanine acts as a biomarker of cell viability.

Limited by the finite polarization of hyperpolarized metabolites as well as the smaller gyromagnetic ratio of ^{13}C, resolution was restricted to 1.5 x 1.5 x 5 mm^3 to achieve sufficient SNR. In addition, each metabolite map obtained in this work was an average signal in 50 sec of its time-course and did not portray the dynamics of metabolism. Thus for metabolic maps to accurately interpret the physiological response of the heart to hyperpolarized pyruvate, rapid real-time CSI is necessary. In order to increase precision in metabolic mapping and achieve higher spatial resolution, customized pulse sequences that consider the T_1 and T_2 relaxation times in different regions and compartments of the myocardium should be adopted. For example, Mansson and coworkers demonstrated a potential multiple-echo steady-state

free-precession (SSFP) sequence that could perform doubly as well in terms of spatial resolution and reduce scan time by four-fold, compared to a gradient-echo CSI pulse sequence (117). Optimizing the acquisition time window, adopting variable flip angles scheme, 3D spatial acquisition and using an appropriate sampling strategy (e.g. EPI) are some of the improvements that could better image quality (118,119).

4.8.5 Conclusion

Hyperpolarized ^{13}C chemical shift imaging allows 2D visualization of pyruvate metabolism in the isolated perfused heart. Localized metabolic maps, such as the bicarbonate map, provide real-time spatial information on energy production in the myocardium. A spatial resolution, before zero-filling, of approximately 11 µl permits localized detection of metabolism throughout the left ventricle. Future work will include reducing the TR and extending the imaging window to allow for the acquisition of multiple images or 3D acquisitions.

4.9 Chapter Conclusion

In this chapter, we have demonstrated the versatility and competency of hyperpolarized ^{13}C biomolecules to study the dynamic metabolism of the heart. Tracking intracellular pH_i changes during ischaemia offers a real-time insight into the pH homeostasis mechanism within cardiac myocytes. We have also explored the potential of hyperpolarized fumarate as a biomarker of cellular necrosis as well as enabled spatial metabolic mapping in perfused hearts. Advancement of dynamic nuclear polarization technique to increase polarization will facilitate more precise measurements and quantification, corroborating the results that were achieved. Increased availability of ^{13}C-labeled compounds will permit investigation of a wider range of metabolic pathways and allow real-time monitoring of therapeutic intervention efficacy.

4.10 Chapter References

1. Ardenkjaer-Larsen JH, Fridlund B, Gram A, Hansson G, Hansson L, Lerche MH, Servin R, Thaning M, Golman K. Increase in signal-to-noise ratio of > 10,000 times in liquid-state NMR. Proc Natl Acad Sci U S A 2003;100(18):10158-10163.
2. Schroeder MA, Atherton HJ, Ball DR, Cole MA, Heather LC, Griffin JL, Clarke K, Radda GK, Tyler DJ. Real-time assessment of Krebs cycle metabolism using hyperpolarized 13C magnetic resonance spectroscopy. FASEB J 2009;23(8):2529-2538.
3. Schroeder MA, Cochlin LE, Heather LC, Clarke K, Radda GK, Tyler DJ. In vivo assessment of pyruvate dehydrogenase flux in the heart using hyperpolarized carbon-13 magnetic resonance. Proc Natl Acad Sci U S A 2008;105(33):12051-12056.
4. Brindle KM. NMR methods for measuring enzyme kinetics in-vivo. PRogress in NMR Spectroscopy 1986;20:257-293.
5. Malloy CR, Sherry AD, Jeffrey FM. Carbon flux through citric acid cycle pathways in perfused heart by 13C NMR spectroscopy. FEBS Lett 1987;212(1):58-62.
6. Neurohr KJ, Barrett EJ, Shulman RG. In vivo carbon-13 nuclear magnetic resonance studies of heart metabolism. Proc Natl Acad Sci U S A 1983;80(6):1603-1607.
7. Frossati G. Polarization of 3He, D2 (and possibly 129Xe) using cryogenic techniques. Nuclear Instrument Methods A 1998;402:479-483.
8. Bouchiat M, Carver T, CM V. Nuclear polarization in 3He gas induced by optical pumping and dipolar exchange. Phys Rev Lett 1960;5:373-375.
9. Colegrove F, Schearer L. Polarization of 3He gas by optical pumping. Phys Rev 1963;132:2561-2572.
10. Natterer J, Bargon J. Parahydrogen induced polarization. Progress in Nuclear Magnetic Resonance Spectroscopy 1997;31:293-315.
11. Golman K, Axelsson O, Johannesson H, Mansson S, Olofsson C, Petersson JS. Parahydrogen-induced polarization in imaging: subsecond (13)C angiography. Magn Reson Med 2001;46(1):1-5.
12. Mansson S, Johansson E, Magnusson P, Chai CM, Hansson G, Petersson JS, Stahlberg F, Golman K. 13C imaging-a new diagnostic platform. Eur Radiol 2006;16(1):57-67.
13. Kauczor H, Surkau R, Roberts T. MRI using hyperpolarized noble gases. Eur Radiol 1998;8(5):820-827.
14. Moller HE, Chen XJ, Saam B, Hagspiel KD, Johnson GA, Altes TA, de Lange EE, Kauczor HU. MRI of the lungs using hyperpolarized noble gases. Magn Reson Med 2002;47(6):1029-1051.
15. Salerno M, Altes TA, Mugler JP, 3rd, Nakatsu M, Hatabu H, de Lange EE. Hyperpolarized noble gas MR imaging of the lung: potential clinical applications. Eur J Radiol 2001;40(1):33-44.
16. Bowers CR, Weitekamp DP. Parahydrogen and synthesis allow framatically enhanced nuclear alignment. Journal of American Chemical Society 1987;109:5541-5542.
17. Bowers CR, Weitekamp DP. Transformation of symmetrization order to nuclear-spin magnetization by chemical reaction and nuclear magnetic resonance. Phys Rev Lett 1986;57(21):2645-2648.
18. Johannesson H, Axelsson O, Karlsson M, Goldman M. Methods to convert parahydrogen spin order into heteronuclei polarization for in-vivo detection. Proc 21st Annual Meeting ESMRMB 2004:144.
19. Goldman M, Johannesson H, Axelsson O, Karlsson M. Hyperpolarization of 13C through order transfer from parahydrogen: a new contrast agent for MRI. Magn Reson Imaging 2005;23(2):153-157.
20. Abragam A, Goldman M. Principles of dynamic nuclear polarization. Reports Progress in Physics 1978;41:395.

21. Jeffries CD. Polarization of nuclei by resonance saturation in paramagnetic crystals. Phys Rev 1957;106:164-165.
22. Abraham M, MacCausland MAH, Robinson FNH. Dynamic Nuclear Polarization. Phys Rev Lett 1959;2:449-451.
23. Wind RA, Duijvestin MJ, Van der Lugt C, MAnenschijn A, Vriend J. Applications of dynamic nuclear polarization in 13C NMR in solids. PRogress in NMR Spectroscopy 1985;17:33-67.
24. Boer WD, Nijnikoski TO. Dynamic proton polarization in propanediol below 0.5 K. Nuclear Instruments and Methods 1974;114:495-498.
25. Fielding AJ. Applied Magnetic Resonance. 2005 2005;28:231-238.
26. Ardenkjaer-Larsen JH, Macholl S, Jóhannesson H. Dynamic Nuclear Polarization with Trityls at 1.2 K. Applied Magnetic Resonance 2008;34(3-4):509.
27. Mitchell MB, Winter CB, Locke-Winter CR, Banerjee A, Harken AH. Cardiac preconditioning does not require myocardial stunning. Ann Thorac Surg 1993;55(2):395-400.
28. Taegtmeyer H. Energy metabolism of the heart: from basic concepts to clinical applications. Curr Probl Cardiol 1994;19(2):59-113.
29. Merritt ME, Harrison C, Storey C, Jeffrey FM, Sherry AD, Malloy CR. Hyperpolarized 13C allows a direct measure of flux through a single enzyme-catalyzed step by NMR. Proc Natl Acad Sci U S A 2007;104(50):19773-19777.
30. Kohler SJ, Yen Y, Wolber J, Chen AP, Albers MJ, Bok R, Zhang V, Tropp J, Nelson S, Vigneron DB, Kurhanewicz J, Hurd RE. In vivo 13 carbon metabolic imaging at 3T with hyperpolarized 13C-1-pyruvate. Magn Reson Med 2007;58(1):65-69.
31. Albers MJ, Bok R, Chen AP, Cunningham CH, Zierhut ML, Zhang VY, Kohler SJ, Tropp J, Hurd RE, Yen YF, Nelson SJ, Vigneron DB, Kurhanewicz J. Hyperpolarized 13C lactate, pyruvate, and alanine: noninvasive biomarkers for prostate cancer detection and grading. Cancer Res 2008;68(20):8607-8615.
32. Day SE, Kettunen MI, Gallagher FA, Hu DE, Lerche M, Wolber J, Golman K, Ardenkjaer-Larsen JH, Brindle KM. Detecting tumor response to treatment using hyperpolarized 13C magnetic resonance imaging and spectroscopy. Nat Med 2007;13(11):1382-1387.
33. Opie LH. Metabolism of the heart in health and disease. 3. Am Heart J 1969;77(3):383-410.
34. Schroeder MA, Swietach P, Atherton HJ, Gallagher FA, Lee P, Radda GK, Clarke K, Tyler DJ. Measuring intracellular pH in the heart using hyperpolarized carbon dioxide and bicarbonate: a 13C and 31P magnetic resonance spectroscopy study. Cardiovasc Res.
35. Opie LH. Myocardial ischemia--metabolic pathways and implications of increased glycolysis. Cardiovasc Drugs Ther 1990;4 Suppl 4:777-790.
36. Garlick PB, Radda GK, Seeley PJ. Studies of acidosis in the ischaemic heart by phosphorus nuclear magnetic resonance. Biochem J 1979;184(3):547-554.
37. Bing OH, Brooks WW, Messer JV. Heart muscle viability following hypoxia: protective effect of acidosis. Science 1973;180(92):1297-1298.
38. Frohlich O, Wallert MA. Methods of measuring intracellular pH in the heart. Cardiovasc Res 1995;29(2):194-202.
39. Hoult DI, Busby SJ, Gadian DG, Radda GK, Richards RE, Seeley PJ. Observation of tissue metabolites using 31P nuclear magnetic resonance. Nature 1974;252(5481):285-287.
40. Bailey IA, Williams SR, Radda GK, Gadian DG. Activity of phosphorylase in total global ischaemia in the rat heart. A phosphorus-31 nuclear-magnetic-resonance study. Biochem J 1981;196(1):171-178.
41. Katz LA, Swain JA, Portman MA, Balaban RS. Intracellular pH and inorganic phosphate content of heart in vivo: a 31P-NMR study. Am J Physiol 1988;255(1 Pt 2):H189-196.
42. Gallagher FA, Kettunen MI, Day SE, Hu DE, Ardenkjaer-Larsen JH, Zandt R, Jensen PR, Karlsson M, Golman K, Lerche MH, Brindle KM. Magnetic resonance imaging of pH in vivo using hyperpolarized 13C-labelled bicarbonate. Nature 2008;453(7197):940-943.

43. Leem CH, Lagadic-Gossmann D, Vaughan-Jones RD. Characterization of intracellular pH regulation in the guinea-pig ventricular myocyte. J Physiol 1999;517 (Pt 1):159-180.
44. Merritt ME, Harrison C, Storey C, Sherry AD, Malloy CR. Inhibition of carbohydrate oxidation during the first minute of reperfusion after brief ischemia: NMR detection of hyperpolarized 13CO2 and H13CO3. Magn Reson Med 2008;60(5):1029-1036.
45. Swietach P, Vaughan-Jones RD, Harris AL. Regulation of tumor pH and the role of carbonic anhydrase 9. Cancer Metastasis Rev 2007;26(2):299-310.
46. Hoffman DW, Henkens RW. The rates of fast reactions of carbon dioxide and bicarbonate in human erythrocytes measured by carbon-13 NMR. Biochem Biophys Res Commun 1987;143(1):67-73.
47. Madshus IH. Regulation of intracellular pH in eukaryotic cells. Biochem J 1988;250(1):1-8.
48. Vandenberg JI, Carter ND, Bethell HW, Nogradi A, Ridderstrale Y, Metcalfe JC, Grace AA. Carbonic anhydrase and cardiac pH regulation. Am J Physiol 1996;271(6 Pt 1):C1838-1846.
49. Leem CH, Vaughan-Jones RD. Out-of-equilibrium pH transients in the guinea-pig ventricular myocyte. J Physiol 1998;509 (Pt 2):471-485.
50. Kernohan JC. The Ph-Activity Curve of Bovine Carbonic Anhydrase and Its Relationship to the Inhibition of the Enzyme by Anions. Biochim Biophys Acta 1965;96:304-317.
51. Khalifah RG. The carbon dioxide hydration activity of carbonic anhydrase. I. Stop-flow kinetic studies on the native human isoenzymes B and C. J Biol Chem 1971;246(8):2561-2573.
52. Naressi A, Couturier C, Devos JM, Janssen M, Mangeat C, de Beer R, Graveron-Demilly D. Java-based graphical user interface for the MRUI quantitation package. MAGMA 2001;12(2-3):141-152.
53. Cross HR, Clarke K, Opie LH, Radda GK. Is lactate-induced myocardial ischaemic injury mediated by decreased pH or increased intracellular lactate? J Mol Cell Cardiol 1995;27(7):1369-1381.
54. Murray AJ, Lygate CA, Cole MA, Carr CA, Radda GK, Neubauer S, Clarke K. Insulin resistance, abnormal energy metabolism and increased ischemic damage in the chronically infarcted rat heart. Cardiovasc Res 2006;71(1):149-157.
55. Lewandowski ED, White LT. Pyruvate dehydrogenase influences postischemic heart function. Circulation 1995;91(7):2071-2079.
56. Lopaschuk GD, Spafford MA, Davies NJ, Wall SR. Glucose and palmitate oxidation in isolated working rat hearts reperfused after a period of transient global ischemia. Circ Res 1990;66(2):546-553.
57. Brindle KM, Rajagopalan B, Williams DS, Detre JA, Simplaceanu E, Ho C, Radda GK. 31P NMR measurements of myocardial pH in vivo. Biochem Biophys Res Commun 1988;151(1):70-77.
58. Johannesson H, Macholl S, Ardenkjaer-Larsen JH. Dynamic Nuclear Polarization of [1-13C]pyruvic acid at 4.6 tesla. J Magn Reson 2009;197(2):167-175.
59. Golman K, Petersson JS, Magnusson P, Johansson E, Akeson P, Chai CM, Hansson G, Mansson S. Cardiac metabolism measured noninvasively by hyperpolarized 13C MRI. Magn Reson Med 2008;59(5):1005-1013.
60. Vaughan-Jones RD, Spitzer KW, Swietach P. Intracellular pH regulation in heart. J Mol Cell Cardiol 2009;46(3):318-331.
61. Vandenberg JI, Metcalfe JC, Grace AA. Mechanisms of pHi recovery after global ischemia in the perfused heart. Circ Res 1993;72(5):993-1003.
62. Scholz W, Albus U, Counillon L, Gogelein H, Lang HJ, Linz W, Weichert A, Scholkens BA. Protective effects of HOE642, a selective sodium-hydrogen exchange subtype 1 inhibitor, on cardiac ischaemia and reperfusion. Cardiovasc Res 1995;29(2):260-268.
63. Alvarez BV, Johnson DE, Sowah D, Soliman D, Light PE, Xia Y, Karmazyn M, Casey JR. Carbonic anhydrase inhibition prevents and reverts cardiomyocyte hypertrophy. J Physiol 2007;579(Pt 1):127-145.

64. Stanley WC, Recchia FA, Lopaschuk GD. Myocardial substrate metabolism in the normal and failing heart. Physiol Rev 2005;85(3):1093-1129.
65. Randle PJ, Garland PB, Hales CN, Newsholme EA. The glucose fatty-acid cycle. Its role in insulin sensitivity and the metabolic disturbances of diabetes mellitus. Lancet 1963;1(7285):785-789.
66. Sugden MC, Holness MJ. Recent advances in mechanisms regulating glucose oxidation at the level of the pyruvate dehydrogenase complex by PDKs. Am J Physiol Endocrinol Metab 2003;284(5):E855-862.
67. Linn TC, Pettit FH, Reed LJ. Alpha-keto acid dehydrogenase complexes. X. Regulation of the activity of the pyruvate dehydrogenase complex from beef kidney mitochondria by phosphorylation and dephosphorylation. Proc Natl Acad Sci U S A 1969;62(1):234-241.
68. Cooper RH, Randle PJ, Denton RM. Stimulation of phosphorylation and inactivation of pyruvate dehydrogenase by physiological inhibitors of the pyruvate dehydrogenase reaction. Nature 1975;257(5529):808-809.
69. Hansford RG, Cohen L. Relative importance of pyruvate dehydrogenase interconversion and feed-back inhibition in the effect of fatty acids on pyruvate oxidation by rat heart mitochondria. Arch Biochem Biophys 1978;191(1):65-81.
70. Taegtmeyer H, Golfman L, Sharma S, Razeghi P, van Arsdall M. Linking gene expression to function: metabolic flexibility in the normal and diseased heart. Ann N Y Acad Sci 2004;1015:202-213.
71. Collins-Nakai RL, Noseworthy D, Lopaschuk GD. Epinephrine increases ATP production in hearts by preferentially increasing glucose metabolism. Am J Physiol 1994;267(5 Pt 2):H1862-1871.
72. Owen OE, Mozzoli MA, Boden G, Patel MS, Reichard GA, Jr., Trapp V, Shuman CR, Felig P. Substrate, hormone, and temperature responses in males and females to a common breakfast. Metabolism 1980;29(6):511-523.
73. Caruso M, Maitan MA, Bifulco G, Miele C, Vigliotta G, Oriente F, Formisano P, Beguinot F. Activation and mitochondrial translocation of protein kinase Cdelta are necessary for insulin stimulation of pyruvate dehydrogenase complex activity in muscle and liver cells. J Biol Chem 2001;276(48):45088-45097.
74. McCormack JG, Halestrap AP, Denton RM. Role of calcium ions in regulation of mammalian intramitochondrial metabolism. Physiol Rev 1990;70(2):391-425.
75. Pratt ML, Roche TE. Mechanism of pyruvate inhibition of kidney pyruvate dehydrogenasea kinase and synergistic inhibition by pyruvate and ADP. J Biol Chem 1979;254(15):7191-7196.
76. Neely JR, Morgan HE. Relationship between carbohydrate and lipid metabolism and the energy balance of heart muscle. Annu Rev Physiol 1974;36:413-459.
77. Lysiak W, Toth PP, Suelter CH, Bieber LL. Quantitation of the efflux of acylcarnitines from rat heart, brain, and liver mitochondria. J Biol Chem 1986;261(29):13698-13703.
78. Renstrom B, Liedtke AJ, Nellis SH. Mechanisms of substrate preference for oxidative metabolism during early myocardial reperfusion. Am J Physiol 1990;259(2 Pt 2):H317-323.
79. Schonekess BO, Allard MF, Lopaschuk GD. Propionyl L-carnitine improvement of hypertrophied heart function is accompanied by an increase in carbohydrate oxidation. Circ Res 1995;77(4):726-734.
80. Saddik M, Gamble J, Witters LA, Lopaschuk GD. Acetyl-CoA carboxylase regulation of fatty acid oxidation in the heart. J Biol Chem 1993;268(34):25836-25845.
81. Freeman R. Shaped radiofrequency pulses in high resolution NMR. Journal of Progress in Nuclear Magnetic Resonance Spectroscopy 1998;32:59-106.
82. King KL, Okere IC, Sharma N, Dyck JR, Reszko AE, McElfresh TA, Kerner J, Chandler MP, Lopaschuk GD, Stanley WC. Regulation of cardiac malonyl-CoA content and fatty acid oxidation during increased cardiac power. Am J Physiol Heart Circ Physiol 2005;289(3):H1033-1037.

83. Goodwin GW, Taegtmeyer H. Regulation of fatty acid oxidation of the heart by MCD and ACC during contractile stimulation. Am J Physiol 1999;277(4 Pt 1):E772-777.
84. Searle J, Kerr JF, Bishop CJ. Necrosis and apoptosis: distinct modes of cell death with fundamentally different significance. Pathol Annu 1982;17 Pt 2:229-259.
85. Buja LM, Eigenbrodt ML, Eigenbrodt EH. Apoptosis and necrosis. Basic types and mechanisms of cell death. Arch Pathol Lab Med 1993;117(12):1208-1214.
86. Majno G, Joris I. Apoptosis, oncosis, and necrosis. An overview of cell death. Am J Pathol 1995;146(1):3-15.
87. Buja LM, Entman ML. Modes of myocardial cell injury and cell death in ischemic heart disease. Circulation 1998;98(14):1355-1357.
88. Reimer KA, Ideker RE. Myocardial ischemia and infarction: anatomic and biochemical substrates for ischemic cell death and ventricular arrhythmias. Hum Pathol 1987;18(5):462-475.
89. Gallagher FA, Kettunen MI, Hu DE, Jensen PR, Zandt RI, Karlsson M, Gisselsson A, Nelson SK, Witney TH, Bohndiek SE, Hansson G, Peitersen T, Lerche MH, Brindle KM. Production of hyperpolarized [1,4-13C2]malate from [1,4-13C2]fumarate is a marker of cell necrosis and treatment response in tumors. Proc Natl Acad Sci U S A 2009;106(47):19801-19806.
90. Gurevitch J, Frolkis I, Yuhas Y, Paz Y, Matsa M, Mohr R, Yakirevich V. Tumor necrosis factor-alpha is released from the isolated heart undergoing ischemia and reperfusion. J Am Coll Cardiol 1996;28(1):247-252.
91. Gottlieb RA, Burleson KO, Kloner RA, Babior BM, Engler RL. Reperfusion injury induces apoptosis in rabbit cardiomyocytes. J Clin Invest 1994;94(4):1621-1628.
92. Borutaite V, Brown GC. Mitochondria in apoptosis of ischemic heart. FEBS Lett 2003;541(1-3):1-5.
93. Veinot JP, Gattinger DA, Fliss H. Early apoptosis in human myocardial infarcts. Hum Pathol 1997;28(4):485-492.
94. Eguchi Y, Shimizu S, Tsujimoto Y. Intracellular ATP levels determine cell death fate by apoptosis or necrosis. Cancer Res 1997;57(10):1835-1840.
95. Borutaite V, Jekabsone A, Morkuniene R, Brown GC. Inhibition of mitochondrial permeability transition prevents mitochondrial dysfunction, cytochrome c release and apoptosis induced by heart ischemia. J Mol Cell Cardiol 2003;35(4):357-366.
96. Bialik S, Cryns VL, Drincic A, Miyata S, Wollowick AL, Srinivasan A, Kitsis RN. The mitochondrial apoptotic pathway is activated by serum and glucose deprivation in cardiac myocytes. Circ Res 1999;85(5):403-414.
97. Black SC, Huang JQ, Rezaiefar P, Radinovic S, Eberhart A, Nicholson DW, Rodger IW. Co-localization of the cysteine protease caspase-3 with apoptotic myocytes after in vivo myocardial ischemia and reperfusion in the rat. J Mol Cell Cardiol 1998;30(4):733-742.
98. Olivetti G, Abbi R, Quaini F, Kajstura J, Cheng W, Nitahara JA, Quaini E, Di Loreto C, Beltrami CA, Krajewski S, Reed JC, Anversa P. Apoptosis in the failing human heart. N Engl J Med 1997;336(16):1131-1141.
99. Saraste A, Pulkki K, Kallajoki M, Henriksen K, Parvinen M, Voipio-Pulkki LM. Apoptosis in human acute myocardial infarction. Circulation 1997;95(2):320-323.
100. Chakrabarti S, Hoque AN, Karmazyn M. A rapid ischemia-induced apoptosis in isolated rat hearts and its attenuation by the sodium-hydrogen exchange inhibitor HOE 642 (cariporide). J Mol Cell Cardiol 1997;29(11):3169-3174.
101. Gelpi JL, Dordal A, Montserrat J, Mazo A, Cortes A. Kinetic studies of the regulation of mitochondrial malate dehydrogenase by citrate. Biochem J 1992;283 (Pt 1):289-297.
102. MacFall JR, Charles HC, Black RD, Middleton H, Swartz JC, Saam B, Driehuys B, Erickson C, Happer W, Cates GD, Johnson GA, Ravin CE. Human lung air spaces: potential for MR imaging with hyperpolarized He-3. Radiology 1996;200(2):553-558.

103. Bachert P, Schad LR, Bock M, Knopp MV, Ebert M, Grossmann T, Heil W, Hofmann D, Surkau R, Otten EW. Nuclear magnetic resonance imaging of airways in humans with use of hyperpolarized 3He. Magn Reson Med 1996;36(2):192-196.
104. Ebert M, Grossmann T, Heil W, Otten WE, Surkau R, Leduc M, Bachert P, Knopp MV, Schad LR, Thelen M. Nuclear magnetic resonance imaging with hyperpolarised helium-3. Lancet 1996;347(9011):1297-1299.
105. Mugler JP, 3rd, Driehuys B, Brookeman JR, Cates GD, Berr SS, Bryant RG, Daniel TM, de Lange EE, Downs JH, 3rd, Erickson CJ, Happer W, Hinton DP, Kassel NF, Maier T, Phillips CD, Saam BT, Sauer KL, Wagshul ME. MR imaging and spectroscopy using hyperpolarized 129Xe gas: preliminary human results. Magn Reson Med 1997;37(6):809-815.
106. Albert MS, Tseng CH, Williamson D, Oteiza ER, Walsworth RL, Kraft B, Kacher D, Holman BL, Jolesz FA. Hyperpolarized 129Xe MR imaging of the oral cavity. J Magn Reson B 1996;111(2):204-207.
107. Ruppert K, Brookeman JR, Hagspiel KD, Mugler JP, 3rd. Probing lung physiology with xenon polarization transfer contrast (XTC). Magn Reson Med 2000;44(3):349-357.
108. Miller KW, Reo NV, Schoot Uiterkamp AJ, Stengle DP, Stengle TR, Williamson KL. Xenon NMR: chemical shifts of a general anesthetic in common solvents, proteins, and membranes. Proc Natl Acad Sci U S A 1981;78(8):4946-4949.
109. Wagshul ME, Button TM, Li HF, Liang Z, Springer CS, Zhong K, Wishnia A. In vivo MR imaging and spectroscopy using hyperpolarized 129Xe. Magn Reson Med 1996;36(2):183-191.
110. Wolber J, Cherubini A, Leach MO, Bifone A. Hyperpolarized 129Xe NMR as a probe for blood oxygenation. Magn Reson Med 2000;43(4):491-496.
111. Mansson S, Wolber J, Driehuys B, Wollmer P, Golman K. Characterization of diffusing capacity and perfusion of the rat lung in a lipopolysaccaride disease model using hyperpolarized 129Xe. Magn Reson Med 2003;50(6):1170-1179.
112. Johansson E, Olsson LE, Mansson S, Petersson JS, Golman K, Stahlberg F, Wirestam R. Perfusion assessment with bolus differentiation: a technique applicable to hyperpolarized tracers. Magn Reson Med 2004;52(5):1043-1051.
113. Johansson E, Mansson S, Wirestam R, Svensson J, Petersson JS, Golman K, Stahlberg F. Cerebral perfusion assessment by bolus tracking using hyperpolarized 13C. Magn Reson Med 2004;51(3):464-472.
114. Golman K, Petersson JS. Metabolic imaging and other applications of hyperpolarized 13C1. Acad Radiol 2006;13(8):932-942.
115. Golman K, in 't Zandt R, Thaning M. Real-time metabolic imaging. Proc Natl Acad Sci U S A 2006;103(30):11270-11275.
116. Golman K, Zandt RI, Lerche M, Pehrson R, Ardenkjaer-Larsen JH. Metabolic imaging by hyperpolarized 13C magnetic resonance imaging for in vivo tumor diagnosis. Cancer Res 2006;66(22):10855-10860.
117. Månsson S, Leupold J, Wieben O, In't Zandt R, Magnusson P, Johansson E, Petersson J. Metabolic Imaging with Hyperpolarized 13C and Multi-Echo, Single-Shot RARE. Proc 14th Annual Meeting ISMRM 2006 2006:584.
118. Yen YF, Kohler SJ, Chen AP, Tropp J, Bok R, Wolber J, Albers MJ, Gram KA, Zierhut ML, Park I, Zhang V, Hu S, Nelson SJ, Vigneron DB, Kurhanewicz J, Dirven HA, Hurd RE. Imaging considerations for in vivo 13C metabolic mapping using hyperpolarized 13C-pyruvate. Magn Reson Med 2009;62(1):1-10.
119. Mayer D, Yen YF, Tropp J, Pfefferbaum A, Hurd RE, Spielman DM. Application of subsecond spiral chemical shift imaging to real-time multislice metabolic imaging of the rat in vivo after injection of hyperpolarized 13C1-pyruvate. Magn Reson Med 2009;62(3):557-564.

THESIS CONCLUSION

In this thesis, we have demonstrated the versatility of magnetic resonance imaging to cross boundaries from physiological to cellular and down to molecular dimensions. Qualitative and quantitative perfusion imaging in the mouse pancreas allows differentiation of microvascular environment between pathology and normal tissue, and could perhaps serve as biomarkers of abnormal angiogenesis or impaired glucose response. Cellular tracking with high positive contrast facilitates in-vivo visualization of transplanted cells and could boost success rate of cellular therapy. Metabolic processes and fluxes in the heart could be detected in real-time using the hyperpolarized ^{13}C- labeled biomolecules, and serve as robust biomarkers of ischemia and necrosis. From molecular to functional imaging, the diversity of information provided by MRI is unparalleled by other imaging modality and it would indeed become the mainstay technology in the advancement of molecular medicine.

BIBLOGRAPHY

I was born on 29th September 1977 in Singapore. I was educated at Victoria School and Victoria Junior College from 1990 to 1996, after which I served two and a half years as a soldier in the Republic of Singapore Army.

From August 1998 to May 2002, I studied electrical engineering at the National University of Singapore and specialized in semiconductor technology. I spent a year as an exchange student at the University of Wuppertal in Germany under the supervision of Professor Ludwig Joseph Balk. My study research project titled 'Integrated Circuit Failure Analysis with Scanning Thermal Microscopy' was completed in May 2002. Subsequently I graduated from the National University of Singapore with First Class Honors in Electrical Engineering.

From June 2002 to July 2006 I worked as a research and development engineer in a wafer foundry. In August 2006 I received a PhD scholarship from the Agency of Science, Technology and Research in Singapore and commenced my candidature at the National University of Singapore. The focus of my study was to implement MRI pulse sequences for cellular and molecular imaging in small animals, with a 9.4 T preclinical scanner at the Singapore Bioimaging Consortium (SBIC). From October 2008 to September 2009, I had the opportunity to work with Dr. Damian Tyler from the Cardiac Metabolism Research Group at the University of Oxford. It was there where I acquired skills and knowledge pertaining to glucose metabolism studies with hyperpolarized carbon-13. This thesis was supervised by Sir George Radda from Singapore Bioimaging Consortium, A-STAR, Singapore.

Appendix A

Abbreviations for enzymes and other biochemical compounds

Enzymes	
LDH	Lactate dehydrogenase
ALT	Alanine transaminase
PC	Pyruvate decarboxylase
CA	Carbonic anhydrase
PDH	Pyruvate dehyrogenase
CAT	Carnitine acetyltransferase
CS	Citrase synthase
A	Aconitase
IDH	Isocitrate dehydrogenase
a-KDH	α-Ketoglutarate dehydrogenase complex
GDH	Glutamate dehydrogenase
SCS	Succinyl CoA Synthase
SDH	Succinate dehydrogenase
F	Fumarase
MDH	Malate dehydrogenase
Energy Carriers	
ATP	Adenosine triphosphate
ADP	Adenosine diphosphate
GTP	Guanosine triphosphate
GDP	Guanosine diphosphate
Electron Acceptors	
NAD^+	Nicotinamide adenine dinucelotide
FAD	Flavin adenine dinucelotide
Electron Carriers	
NADH	reduced NAD^+
FADH	reduced FAD

LIST OF PUBLICATIONS

PUBLICATIONS

[1] Schroeder MA, Swietach P, Atherton HJ, Gallagher FA, **Lee P**, Radda GK, Clarke K, Tyler DJ. Measuring intracellular pH in the heart using hyperpolarized carbon dioxide and bicarbonate: a 13C and 31P magnetic resonance spectroscopy study. Cardiovasc Res;86(1):82-91

[2] Zheng B, **Lee PTH**, Golay X. High Sensitivity Cerebral PErfusion Mapping in Mice by kbGRASE-FAIR at 9.4 T. NMR Biomed 2010; IN PRESS

ISMRM ABSTRACTS

[1] Coolen BF, **Lee P**, Golay X. Optimized MRI parameters for positive contrast detection of iron-oxide labeled cells using double-echo Ultra-short echo time (d-UTE) sequences. Proc Intl Soc Mag Reson Med 2007:1224.

[2] **Lee P**, Golay X, Radda G. Dynamic Perfusion Study of Mouse Pancreas with an Intravascular Contrast Agent. Proc Intl Soc Mag Reson Med 2009:2057.

[3] **Lee P**, Zheng B, Radda G, Padmanabhan P, Bhakoo K. In-Vivo Positive Contrast Tracking of Bone Marrow Stem Cells Labeled with IODEX-TAT-FITC Nanoparticles. Proc Intl Soc Mag Reson Med 2010:2760

[4] **Lee P**, Riegler J, Price A, Lythgoe MF, Golay X. A multi-echo technique for positive contrast detection of SPIO-labeled cells at 9.4T. Proc Intl Soc Mag Reson Med 2010:497.

[5] **Lee P**, Schroeder M, Ball D, Clarke K, Radda G, Tyler D. Metabolic Imaging of the Perfused Rat Heart Using Hyperpolarized [1-13C]Pyruvate. Proc Intl Soc Mag Reson Med 2010:2733.

[6] Schroeder MA, Swietach P, **Lee P**, Gallagher FA, Rowlands B, Supuran CT, Brindle KM, Vaughan-Jones RD, Radda GK, Clarke K. The Role of Cardiac Carbonic Anhydrases In Vivo: A Hyperpolarised 13C MR Study. Proc Intl Soc Mag Reson Med 2010:3552.

[7] Schroeder MA, Atherton HJ, **Lee P**, Dodd MS, Cochlin LE, Clarke KE, Radda GK, Tyler DJ. Hyperpolarised [2-13C]Pyruvate Uniquely Reveals the Role of Acetylcarnitine as a Mitochondrial Substrate Buffer in the Heart. Proc Intl Soc Mag Reson Med 2010:3269.

WORLD MOLECULAR IMAGING CONGRESS ABSTRACTS

[1] **Lee P**, Golay X. In-Vivo Tracking of Super-Paramagnetic Iron Oxide (SPIO) - Labeled Mesenchymal Stem Cells with Positive Contrast. World Molecular Imaging Congress 2008:1048.

[2] **Lee P**, Golay X. Enhanced detection of SPIO-labeled stem cells with Z-shim ultrashort echo time (ZUTE). World Molecular Imaging Congress 2009:415.